Department of Signal
Theory and Communications

UNIVERSITAT POLITÈCNICA DE CATALUNYA
BARCELONATECH

Ph.D. Thesis Dissertation

Contribution to the characterization of interferometric radiometers devoted to Earth observation: application to the MIRAS/SMOS payload

Author
Verónica González Gambau

Ph.D. Thesis Advisors
Prof. Francesc Torres Torres
Dr. Nuria Duffo Úbeda

Remote Sensing Laboratory
Dept. Teoria del Senyal i Comunicacions
Universitat Politècnica de Catalunya

Barcelona, May 2012

Contents

Abstract

The variability of soil moisture and ocean salinity controls the continuous exchange of water between the oceans, the atmosphere and the land. Therefore, the accurate and periodic measurements of these geophysical variables are paramount to improve the climate change prediction and extreme-event forecasting. However, until very recently, global measurements of these parameters with a suitable spatial and temporal resolution have not been available.

Real aperture radiometers have been frequently used for Earth observation applications. Nevertheless, for space-borne sensors at a low Earth orbit, the requirements on spatial resolution and coverage, at the operating frequencies (L-band), would require an unfeasibly large antenna. Conversely, synthetic aperture radiometry achieves high resolution using an array of small antennas, becoming a sound alternative to real aperture radiometry at low microwave frequencies.

The ESA's SMOS (Soil Moisture and Ocean Salinity) mission, successfully launched on November 2009, is the first mission ever attempted to frequently and globally measure soil moisture over the continents and sea surface salinity over the oceans. The single payload of the mission, the MIRAS (Microwave Imaging Radiometer by Aperture Synthesis) instrument, is the first space-borne L-band two dimensional synthetic aperture radiometer. This completely new type of instrument implies a technological challenge, for which the development of a detailed error model definition, dedicated calibration and image reconstruction algorithms have been needed.

The calibration of MIRAS tackles all activities devoted to retrieve the SMOS scientific products from raw data measurements with the accuracy required by the scientific community. Characterization activities, mainly performed prior to the beginning of the in-orbit operation, have been required to develop and test the calibration activities.

Within the framework of the SMOS mission, this Ph.D. Thesis is focused on the characterization of the interferometric radiometers devoted to Earth observation. The main contributions of this Thesis, which are directly related to the MIRAS payload performance assessment, are: (i) the definition of tests for the characterization campaigns, data processing methods and success criteria and (ii) the development of calibration algorithms and tools to fine-tune the instrument in order to fully achieve the system requirements and therefore the scientific requirements of the mission.

Most of the work has been done in the framework of the MIRAS/SMOS Pre-Commissioning Phase activities and it has been completed in the framework of the Commissioning Phase preparatory work. Calibration tools and techniques developed for the MIRAS ground characterization have been adapted to fulfill in-orbit instrument characterization during the first months of the Commissioning Phase and contributed to the development and consolidation of the SMOS operational level-1 processing.

Resumen

La variabilidad de la humedad del suelo y de la salinidad de los océanos controla el continuo intercambio de agua entre los océanos, la atmósfera y la tierra. Por tanto, la obtención de medidas precisas y periódicas de estas dos variables geofísicas es fundamental para la mejora de la predicción del cambio climático y de la previsión de desastres naturales. Sin embargo, hasta hace muy poco no se disponía de medidas globales de estos parámetros con la resolución temporal y espacial necesaria para este tipo de aplicaciones.

Los radiómetros de apertura real se han utilizado frecuentemente para aplicaciones de observación de la Tierra. Sin embargo, para sensores situados en órbitas bajas, los requerimientos de resolución espacial y cobertura, a la frecuencia de trabajo (banda L), implicarían el uso de una antena de unas dimensiones que no son viables tecnológicamente. Por el contrario, la radiometría de apertura sintética permite obtener una alta resolución utilizando un array de pequeñas antenas, convirtiéndose en una sólida alternativa a la radiometría de apertura real para frecuencias bajas de microondas.

La misión SMOS, de la Agencia Espacial Europea, lanzada con éxito en Noviembre de 2009, es la primera misión para la medida frecuente y global de la humedad del suelo y la salinidad de los océanos. La única carga útil de la misión, el instrumento MIRAS, es el primer radiómetro de apertura sintética en dos dimensiones que es lanzado al espacio. Este tipo de instrumento, completamente novedoso, implica todo un reto tecnológico, por lo que han sido necesarios la definición de un modelo detallado de errores y el desarrollo de algoritmos específicos de calibración e inversión de imagen.

La calibración del radiómetro MIRAS comprende todas las actividades dedicadas a recuperar los productos científicos de SMOS a partir de los datos crudos con la precisión requerida por la comunidad científica. Para poder desarrollar y probar las actividades de calibración ha sido preciso realizar campañas de caracterización del instrumento, llevadas a cabo en tierra principalmente.

En el marco de la misión SMOS, esta tesis se centra en la caracterización de radiómetros interferométricos para la observación de la Tierra. Las principales contribuciones de esta tesis, relacionadas directamente con la evaluación de las prestaciones del radiómetro MIRAS, son: (i) la definición de las medidas para las campañas de caracterización, métodos de procesado de datos y criterios de éxito y (ii) el desarrollo de algoritmos de calibración y herramientas que permitan el ajuste del intrumento para cumplir los requerimientos del sistema y por lo tanto, los requerimientos científicos de la misión.

La mayor parte de este trabajo se ha realizado en el marco de las actividades previas al lanzamiento de la misión y se ha completado en el marco del trabajo preparatorio de la fase de comisionado (primeros meses de medidas en órbita). Las herramientas de calibración y las técnicas desarrolladas para la caracterización en tierra del instrumento se han adaptado para completar la caracterización del instrumento durante los primeros meses en órbita, contribuyendo al procesado de nivel 1 operacional.

Chapter 1

Introduction

The scope of the doctoral Thesis proposed herein is the characterization of interferometric radiometers devoted to Earth observation. It particularly contributes to characterizing and assessing the system performance of the ESA's SMOS single payload: the Microwave Imaging Radiometer by Aperture Synthesis (MIRAS). This chapter justifies the scientific and technological interest of this work within the SMOS mission, describes the motivation of this Thesis and the context in which it has been developed.

1.1 Motivation

Nowadays, climate change and extreme-event forecasting are top priority research fields for most developed countries. Scientific community has demonstrated that geophysical variables such as soil moisture and ocean salinity allow improving the knowledge of the water cycle and the meteorological modeling. However, until very recently, global measurements of these parameters with a suitable spatial and temporal resolution were not available, and both sea surface salinity and soil moisture in-situ measurements were very sparsely distributed.

During the last years, the interest in interferometric aperture synthesis for Earth observation has increased. Many applications require spatial and temporal resolutions not attained using real aperture radiometers. Microwave interferometry observation represents a solid alternative to real aperture radiometry at low microwave frequencies since it may provide higher spatial resolutions, as it was first proposed by C. Swift and R. McIntosh in the 80's [Swift & McIntosh, 1983].

SMOS (Soil Moisture and Ocean Salinity) is the second Earth Explorer opportunity mission of the ESA's Living Planet Program [Silvestrin *et al.*, 2001]. It is the first mission ever attempted to frequently and globally measure two main geophysical parameters: soil moisture over land surfaces [Kerr *et al.*, 2001, 2010] and surface salinity over the oceans [Font *et al.*, 2004, 2010]. Hence, SMOS mission is a direct response to the current lack of

global observations of these two parameters and will contribute to enhance climate and hazardous events forecasting.

SMOS unique payload is a totally innovative instrument: MIRAS, the first space-borne L-band two dimensional synthetic aperture radiometer [Martín-Neira & Goutoule, 1997, McMullan *et al.*, 2008]. MIRAS technology is based on concepts first developed in radio-astronomy [Thompson *et al.*, 1986]. However, in radio-astronomy the imaged targets are point sources while Earth observation deals with an extended source of radiation. This technological challenge implies the development of a detailed error model definition, dedicated calibration and image reconstruction algorithms, issues throughly addressed in [Camps, 1996, Ribó i Vedrilla, 2005, Corbella *et al.*, 2009a].

All the activities needed to retrieve the final products with the accuracy required by the scientific community are comprised in the calibration procedures. Likewise, characterization and system performance assessment activities, mainly performed before launch after payload integration, are required to assure a proper development of the calibration activities. This is the scope of this Ph.D. Thesis which is aimed to the characterization of interferometric radiometers devoted to Earth observation.

This research focuses on the characterization of the MIRAS/SMOS instrument, mainly on its capability to synthesize images of the Earth's surface with a radiometric accuracy (spatial error) and radiometric resolution (error over time) that achieve SMOS scientific requirements [SMOS, 2003a]. System performance evaluation is based on the statistics of the retrieved brightness temperature error. Scientific requirements have been translated into radiometric constraints, which, in turn, imply electrical and technological requirements. These can be directly applied to the visibility samples [SMOS, 2003b, Torres *et al.*, 2007, Corbella *et al.*, 2000b]. MIRAS compliance to these requirements is then directly related to the instrumental errors in the visibility samples (Fig. 1.1), which are directly translated into image distortion (the so-called pixel-bias). Hence, the characterization of the instrument performance is paramount to achieving SMOS scientific objectives.

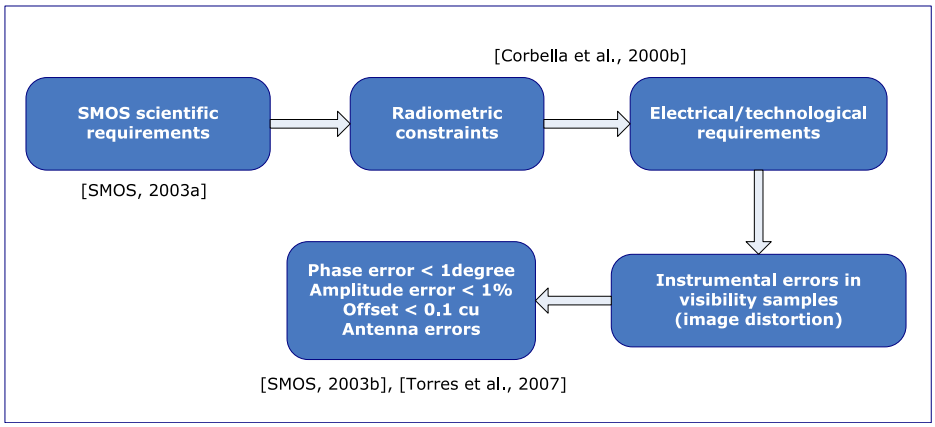

Figure 1.1: Relationship between scientific and electrical/technological requirements.

1.2 Context of the Thesis

The research performed during this Thesis has been carried out within the frame of the Passive Remote Sensing group of the Universitat Politècnica de Catalunya (UPC) SMOS activities. This group has been involved in the SMOS mission since the MIRAS payload conception, in 1993, taking part in the MIRAS/SMOS concept, in the development of calibration and image inversion algorithms and also in the scientific aspects of the mission. Many field experiments have been performed by this research group in the framework of SMOS preparatory activities, both dealing with sea surface salinity and soil moisture measurements. Further information can be found in http://www.tsc.upc.edu/prs.

The SMOS Barcelona Expert Centre on Radiometric Calibration and Ocean Salinity (SMOS-BEC), founded in 2007, is a joint initiative of the Spanish Research Council (CSIC) and the Universitat Politècnica de Catalunya in order to contribute to ground segment activities (http://www.smos-bec.icm.csic.es/). The last stage of this Thesis has been carried out as part of the SMOS-BEC team, providing support to higher level activities.

The Spanish company EADS-CASA Espacio has been the SMOS/MIRAS payload prime contractor leading a space mission in the framework of a joint French/Spanish program under ESA management for the first time ever. EADS-CASA Espacio has been responsible for the MIRAS payload development and integration and the execution of the on-ground characterization tests. Ground processing aspects and the SMOS Level-1 Prototype Processor (L1PP) have been developed by Deimos Engenharia (Portugal) [Gutierrez *et al.*, 2007]. In parallel, an independent processing chain has been developed by the UPC Remote Sensing Group: the MIRAS Testing Software (MTS) [Corbella *et al.*, 2008a]. Both softwares have allowed to process MIRAS data from raw measurements up to brightness temperature maps in near real time.

Most of the research of this Thesis has been carried out in the framework of the MIRAS/SMOS Pre-Commissioning Phase activities. The author has worked in close collaboration with ESA and EADS-CASA Espacio during the on-ground characterization of the instrument that took place in the Netherlands at ESA's Maxwell anechoic chamber within the so called Image Validation Tests (SMOS-IVT) and also the RACT tests at Thales Alenia Space, in Cannes, after the payload integration to the platform. During the first months of Commissioning Phase, the author took part of the data processing team at ESAC (European Space Astronomy Centre) facilities, jointly with ESA, EADS-CASA, Deimos and UPC personnel.

Specifically, this research has been developed in the framework of the following projects and contracts:

- 2009-2010: *"UPC SMOS Commissioning activities"*. European Space Agency, subcontractor of EADS-CASA Espacio.

- 2008-2010: MIDAS-5. *"Microwave measurement analysis devoted to SMOS algorithm development". Ministerio de Educación y Ciencia Plan Nacional I+D+I ESP2007-65667-C04-02/FEDER*

- 2008: *"RACT Tests in Cannes".* CCN European Space Agency, subcontractor of EADS-CASA Espacio.

- 2007-2011: *"Specific collaboration agreement between the Universitat Politècnica de Catalunya and the Consejo Superior de Investigaciones Científicas to found the SMOS-Barcelona Expert Centre on Radiometric Calibration and Ocean Salinity (SMOS-BEC)".* UPC and CSIC-ICM.

- 2007-2008: *"UPC Pre-commissioning activities".* European Space Agency, subcontractor of EADS-CASA Espacio.

- 2005-2008: MIDAS-4. *"Calibration of the measurements provided by the MIRAS/ SMOS instrument and retrieval of salinity and soil moisture maps".* Ministerio de Educación y Ciencia Plan Nacional I+D+I ESP2005-06823-C05-02.

1.3 Objectives

As outlined in the previous section, this PhD. Thesis focuses on the assessment and characterization of interferometric radiometers devoted to Earth observation. It particularly contributes to the MIRAS/SMOS payload system performance characterization. The major objectives of this Thesis are listed below:

- Contribution to the definition of tests, data processing methods and success criteria for MIRAS on-ground characterization. The author has participated, as part of the UPC data processing team, in the following campaigns:

  - ◇ Thermal characterization at ESA-ESTEC Large Space Simulator (LSS) in April 2007.
  - ◇ Image Validation tests (IVT) at ESA-ESTEC Maxwell anechoic chamber during May-June 2007.
  - ◇ Platform integration tests at Thales Alenia Space, Cannes (France) in April 2008.

- Development of algorithms and calibration tools in order to achieve the electrical and technological requirements applied to the visibility samples, such as tracking phase errors due to orbital temperature gradients and checking the consistency of the amplitude calibration. These techniques and calibration tools have been validated from on-ground characterization measurements.

- Comprehensive data analysis of MIRAS on-ground characterization tests. As part of this analysis, the development of dedicated software tools that allow processing and analyzing all the instrument system performance tests was foreseen. These tools were afterwards updated for the MIRAS/SMOS Commissioning Phase analysis (in-orbit measurements).

These main tasks had lead to some additional more specific activities, such as:

- Contribution to the development of specific features of MIRAS Testing Software, developed by UPC Remote Sensing team.
- Development of dedicated software devised to automatically process and generate most of the data needed for the different analysis of the on-ground characterization tests and in-orbit operation measurements.
- Participation in the cross-checking of data products at the different processing levels between the official SMOS Level-1 Prototype processor (L1PP) and the UPC MIRAS Testing Software (MTS) in order to consolidate the final products of both, achieving a high degree of confidence in the data provided by the SMOS processor up to Level-1A products (calibrated visibilities).

1.4 Thesis outline

This Thesis is organized as follows:

Chapter 1 describes the motivation of this Thesis, justifies its scientific and technological interest within the SMOS mission and presents the context in which it has been carried out.

Chapter 2 is devoted to the MIRAS/SMOS payload. First, microwave radiometry fundamentals are reviewed and the state-of-the-art of microwave radiometry for Earth observation is introduced. MIRAS operating principle and the main subsystems integrating the instrument are also outlined.

Chapter 3 is focused on MIRAS/SMOS In-Orbit Calibration Plan (IOCP) [Brown *et al.*, 2008]. Calibration procedures applied to MIRAS in order to correct the visibility samples from instrumental errors are introduced. In addition, this chapter gives an insight into MIRAS in-orbit calibration current baseline and its main calibration products.

Chapter 4 is devoted to assessing the MIRAS instrument performance on-ground. Characterization campaigns in which the author has actively participated jointly with ESA and EADS-CASA Espacio are described. The tools and algorithms developed

to meet the electrical and technological mission requirements applied to the visibility samples are tested and validated. The following specific issues are addressed in detail:

- SMOS data handling and representation
- Phase errors due to temperature gradients along the orbit
- Consistency of the amplitude calibration
- MIRAS/SMOS RFI and electromagnetic compatibility between the payload and the platform
- Assessment of the instrument stability

These calibration tools have led to fine tuning the instrument in order to fully comply with the mission requirements [SMOS, 2003b]. Corrections and auxiliary parameters derived from these analysis have been included in the L1PP first and then consolidated in the Level-1 Operational Processor (L1OP) as data to be used when in-orbit calibration is not available. In addition, some of the outcomes have also contributed to the definition and the assessment on the frequency of some calibration sequences.

Chapter 5 assesses the performance of an alternative calibration method to the MIRAS amplitude calibration current baseline. This technique, the one-point calibration, is proposed as an alternative method for: (i) PMS (Power Measurement System) absolute calibration during external events (in an all-LICEF mode) and (ii) tracking the PMS gain drifts due to the orbital temperature swings.

Chapter 6 analyzes the first in-orbit measurements, performed during SMOS Commissioning Phase, devoted to fulfill the MIRAS characterization. Results of applying the algorithms and tools developed for on-ground characterization are presented. Corrections and auxiliary parameters derived from in-orbit measurements have been used to update the calibration algorithms.

Chapter 7 summarizes the main conclusions as well as the original contributions of this work. Future lines of research are also outlined.

Chapter 2

MIRAS/SMOS Payload

MIRAS/SMOS payload is the first 2D aperture synthesis radiometer for spaceborne Earth observation. Interferometric imaging radiometers measure the cross correlation between the signals received by each pair of antennas forming an array. These measurements are known as visibility samples and develop into a brightness temperature image, in an ideal case, by means of an inverse Fourier transform. This is the operating principle of MIRAS. In this chapter, fundamentals on microwave radiometry and different types of radiometers are sketched. Focusing on the MIRAS instrument, interferometers operating principle, architecture and main integrating subsystems are detailed.

2.1 Theoretical background on microwave radiometry

All materials at a finite absolute temperature radiate electromagnetic energy. Radiometry is the field of science and engineering which analyzes the electromagnetic radiation emitted by the bodies. The relationship between the brightness temperature measured by the antenna and the emissivity of the materials is reviewed in this section.

2.1.1 Brightness and power collected by an antenna

The power radiated by a source per unit solid angle and per unit area is known as brightness $B(\theta, \phi)$ and its units are $[Wsr^{-1}m^{-2}]$,

$$B(\theta, \phi) = \frac{F_t(\theta, \phi)}{A_t}, \tag{2.1}$$

where $F_t(\theta, \phi)$ stands for the radiation intensity of the transmitting antenna $[Wsr^{-1}]$ and $A_t[m^2]$ corresponds to the total radiating area.

The power [W] collected by a lossless antenna surrounded by a distribution of incident

power $B(\theta, \phi)$ is given by

$$P = BA_r \frac{A_t}{R^2}, \tag{2.2}$$

where A_r is the effective area of the receiving antenna and R is the distance between the radiating target and the receiving antenna. This expression can also be written as a function of the transmitting antenna solid angle

$$P = BA_r\Omega_t. \tag{2.3}$$

The spectral brightness $B_f(\theta, \phi)$ is defined as the brightness per unit bandwidth df and its units are $[Wsr^{-1}m^{-2}Hz^{-1}]$. In general, the total power collected by an antenna with effective aperture A_r and radiation pattern $F_n(\theta, \phi)$ over a bandwidth Δf from an extended source with spectral brightness $B_f(\theta, \phi)$ along the direction (θ, ϕ) is given by

$$P = \frac{A_r}{2} \int_f^{f+\Delta f} \iint_{4\pi} B_f(\theta, \phi) F_n(\theta, \phi)\, d\Omega\, df, \tag{2.4}$$

where Δf is the bandwidth of the receiving antenna and the $1/2$ factor takes into account that thermal emission is unpolarized and therefore the antenna, which is sensitive to a single polarization, will detect only half of the total incidence power.

2.1.2 Thermal microwave radiation

Planck's Blackbody radiation law

Normally, part of the incident radiation upon a body or a surface is absorbed and the remainder part is reflected. Blackbodies are ideal materials absorbing all incoming radiation at all frequencies (without reflection). A blackbody at thermodynamic equilibrium should re-emit all absorbed energy. Therefore, a blackbody can be considered a perfect absorber and also a perfect emitter.

The spectral brightness of blackbodies B_f as a function of temperature and frequency is given by the Planck's radiation law (Fig. 2.1)

$$B_f(f, T) = \frac{2hf^3}{c^2} \left(\frac{1}{e^{hf/kT} - 1} \right), \tag{2.5}$$

where $h = 6.63 \cdot 10^{-34} J \cdot s$ is the Planck's constant, f [Hz] is the frequency, $c[m/s]$ is the velocity of light, $T[K]$ is the absolute physical temperature and $k = 1.38 \cdot 10^{-23} J \cdot K^{-1}$ stands for the Boltzmann's constant.

At microwave frequencies ($f < 117GHz$), the term $hf/kT \ll 1$ and then, expression in (2.5) simplifies to the Rayleigh-Jeans law

$$B_f(f, T) \simeq \frac{2f^2kT}{c^2} = \frac{2kT}{\lambda^2}, \tag{2.6}$$

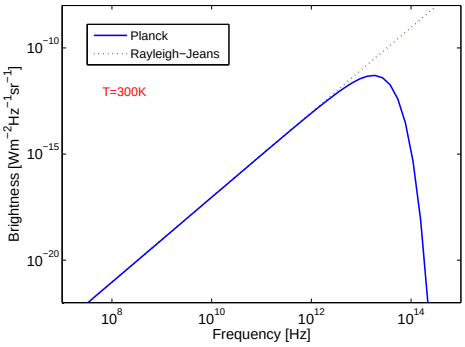

Figure 2.1: Planck's radiation law and its approximation for microwave frequencies (Rayleigh-Jeans law), considering a physical temperature $T = 300K$.

where the λ term corresponds to the wavelength. This expression is mathematically simpler than (2.5) and the deviation error is smaller than 1% for $f < 117GHz$ and $T = 300K$.

Brightness of a blackbody at a physical temperature T and bandwidth Δf in the microwave region is defined by

$$B_{bb} = B_f(f,T)\cdot \Delta f = \frac{2kT}{\lambda^2}\Delta f. \tag{2.7}$$

Therefore, the power collected by an antenna with radiation pattern $F_n(\theta,\phi)$ enclosed by a blackbody at a constant physical temperature T is given by (2.4) and (2.7)

$$P_{bb} = \frac{A_r}{2}\int_f^{f+\Delta f}\iint_{4\pi}\frac{2kT}{\lambda^2}F_n(\theta,\phi)\,d\Omega\,df. \tag{2.8}$$

If the receiver bandwidth is narrow enough to consider the brightness approximately constant, equation (2.8) yields

$$P_{bb} = kT\Delta f\frac{A_r}{\lambda^2}\iint_{4\pi}F_n(\theta,\phi)\,d\Omega, \tag{2.9}$$

where the integral corresponds to the definition of the antenna solid angle Ω_p, in such a way that the equation (2.9) simplifies to

$$P_{bb} = kT\Delta f. \tag{2.10}$$

Note that there is a linear relationship between power and temperature.

Brightness temperature and emissivity

Grey bodies, that is, real materials, emit less than blackbodies since they do not absorb all the incoming radiation upon them. This energy is partly reflected and partly absorbed and then re-emitted. The brightness of a grey body $B(\theta, \phi)$ at microwave frequencies is dependent on the direction and is defined similarly to (2.7)

$$B(\theta, \phi) = \frac{2k}{\lambda^2} T_B(\theta, \phi) \Delta f, \tag{2.11}$$

where $T_B(\theta, \phi)$ is known as brightness temperature, defined as the temperature that a blackbody should have in order to emit the brightness $B(\theta, \phi)$.

The brightness of a material relative to the brightness of a blackbody at the same physical temperature is defined as the emissivity:

$$e(\theta, \phi) = \frac{B(\theta, \phi)}{B_{bb}} = \frac{T_B(\theta, \phi)}{T}. \tag{2.12}$$

Since real materials emit less than blackbodies, $B(\theta, \phi) \leq B_{bb}$, therefore $0 \leq e(\theta, \phi) \leq 1$. A material with $e = 0$ is a perfect reflector (as for example, a lossless conductor) while a material with $e = 1$ is a perfect absorber (blackbody). Hence, the brightness temperature of a material $T_B(\theta, \phi)$ is always lower than or equal to its physical temperature T.

The emissivity depends on several parameters such as the electrical properties of the body/material, the angle of the observation, the roughness of the surface, the polarization and the frequency. For the measurement of soil moisture and ocean salinity, the sensitivity of the dielectric constant to these geophysical parameters is maximum in the L-band range frequencies. In addition, in this band the atmosphere can be considered lossless (transparent).

Antenna temperature

The power [W] collected by an antenna is the sum of all contributions from the elementary emitters. As aforementioned, the relationship between the power received by the antenna and the brightness is given by

$$P = \frac{A_r}{2} \iint_{4\pi} B(\theta, \phi) F_n(\theta, \phi) \, d\Omega. \tag{2.13}$$

The apparent temperature T_{AP} is an equivalent temperature related to the total brightness incident over the antenna $B_i(\theta, \phi)$:

$$B_i(\theta, \phi) = \frac{2k}{\lambda^2} T_{AP}(\theta, \phi) \Delta f. \tag{2.14}$$

At this point, it is important to mention that the term brightness temperature refers to the self-emitted radiation from a surface or a body whereas apparent temperature makes reference to the radiation incident upon the antenna.

Different contributions to the noise power incident upon the antenna can be distinguished (see Fig. 2.2):

- Brightness temperature from the observed scene to which the antenna is pointing (T_B), attenuated by the atmosphere ($L_a(\theta)$). This is the major contribution.
- Atmospheric upward radiation (T_{UP})
- Atmospheric downward radiation reflected by the Earth's surface (T_{SC})

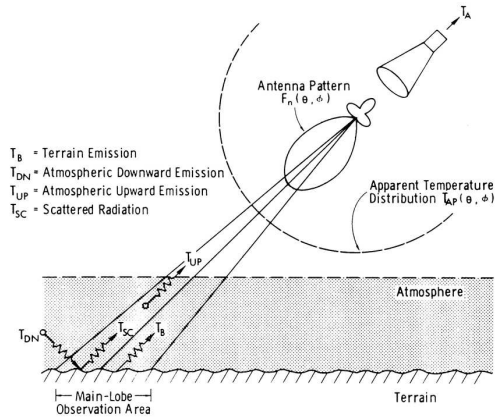

Figure 2.2: Relationships between antenna temperature T_A, brightness temperature T_B and apparent temperature T_{AP}, from [Ulaby *et al.*, 1981], page 202.

Therefore, the apparent temperature can be defined as

$$T_{AP}(\theta,\phi) = \frac{1}{L_a(h,\theta,\phi)}\left(T_B(\theta,\phi) + T_{SC}(\theta,\phi)\right) + T_{UP}(\theta,\phi), \tag{2.15}$$

where L_a is the attenuation of the atmosphere. However, in the $1-10$ GHz frequency range, the atmosphere can be considered lossless and therefore in expression (2.15), the main contribution is the emission from the terrain. A small contribution from the sky background reflected on the Earth's surface can be subtracted from the measurements. Therefore, expression (2.13) can be written as

$$P = k\Delta f \iint_{4\pi} T_B(\theta,\phi)\frac{A_r(\theta,\phi)}{\lambda^2}F_n(\theta,\phi)\,d\Omega = kT_A\Delta f, \tag{2.16}$$

and therefore, the antenna temperature [K] is given by:

$$T_A = \frac{P}{k\cdot\Delta f}. \tag{2.17}$$

Therefore, the antenna temperature is given by

$$T_A = \frac{1}{\Omega_p} \iint_{4\pi} T_B(\theta, \phi) F_n(\theta, \phi)\, d\Omega, \tag{2.18}$$

being $F_n(\theta, \phi)$ the radiation pattern and Ω_p the antenna equivalent solid angle.

Three special cases are shown next:

- When the brightness temperature is constant, for example inside an anechoic chamber, the antenna temperature matches the brightness temperature.

- In case of a quasi-point source, as for example in radio-astronomy, the brightness temperature of the point source is equal to T_S at the position (θ_S, ϕ_S) and null elsewhere. In this case, the antenna temperature depends on the ratio of antenna and source solid angles and therefore on the distance antenna-source

$$T_A = \frac{\Omega_S}{\Omega_p} T_S \cdot F_n(\theta_S, \phi_S) \tag{2.19}$$

- In case of an extended source pointed to by a narrow beam-width antenna, as it is the case of Earth observation, the antenna temperature is equal to the brightness temperature of the spot pointed to by the antenna boresight. It is independent of the distance antenna-source.

2.1.3 Microwave radiometers

Real Aperture radiometers

This type of radiometers are frequently used in field experiments, as for example in the framework of the SMOS preparatory activities. Two types of real aperture radiometers are described in this section: total power and Dicke radiometers. A particular type of Dicke radiometer, known as noise injection radiometer, improves the stability of the measurement. MIRAS uses 3 noise injection radiometers. Additionally, each receiver in MIRAS has a PMS (Power Measurement System) which acts as a total power radiometer (see section 2.4.2).

Total power radiometer (TPR)

This is the simplest real aperture radiometer. In a TPR, the antenna is connected to a superheterodyne receiver (bandwidth B, total gain G) followed by a power detector and a low-pass filter (Fig. 2.3(a)). The average of the output voltage is given by

$$V_{out} = G_s \left(T_A + T_R\right) = G_s T_{sys}, \tag{2.20}$$

being T_A the antenna temperature, T_R the receiver equivalent noise temperature, T_{sys} the system input noise temperature and G_s the average system power gain. Any offset is assumed to be zero in this section for the sake of simplicity.

The radiometric sensitivity is defined as the smallest change in the antenna radiometric temperature which can be detected by the radiometer. The radiometric sensitivity of an ideal TPR, taking into account exclusively the measurement uncertainty due to noise fluctuations, is given by

$$\Delta T = \frac{T_A + T_R}{\sqrt{B\tau}} = \frac{T_{sys}}{\sqrt{B\tau}}, \tag{2.21}$$

being B the receiver noise equivalent bandwidth and τ the integration time, which is related to the post-detection low pass-filter.

Due to gain fluctuations at rates larger than the integration time in the receiving chain, the radiometric sensitivity gets worse, since changes in the gain are interpreted as antenna temperature variations

$$\Delta T = T_{sys}\left[\frac{1}{B\tau} + \left(\frac{\Delta G_s}{G_s}\right)^2\right]^{\frac{1}{2}}. \tag{2.22}$$

Moreover, slow gain fluctuations (at rates lower than τ) in real aperture radiometers need to be corrected by means of periodic calibrations, which require an accurate knowledge of the system's response to two calibration standards (hot and cold loads).

Dicke radiometer

The principle of a Dicke radiometer consists of measuring not directly the antenna temperature T_A but the difference between this magnitude and a reference temperature T_{REF}. Basically, a Dicke radiometer is a TPR with two additional elements (Fig. 2.3(b)):

- A switch at the receiver input to periodically change between the measurement of the scene and a constant reference noise source T_{REF}.
- A synchronous demodulator between the square law detector and the low-pass filter.

The switching frequency is selected so that over a period the system gain can be assumed constant. Therefore, the gain is the same for the half cycle in which the receiver is connected to the antenna and the half cycle in which it is connected to the reference noise source. The output voltage is given by

$$V_{OUT} = \frac{1}{2}G_s\left(T_A - T_{REF}\right). \tag{2.23}$$

Note that, the system gain is multiplied by the difference between the antenna and the reference temperature (which is in the same order as T_A), being less affected by the instabilities.

The radiometric sensitivity of a Dicke radiometer is given by

$$\Delta T = \left[\frac{2\left(T_A + T_R\right)^2 + 2\left(T_{REF} + T_R\right)^2}{B\tau} + \left(\frac{\Delta G_S}{G_S} \right)^2 \left(T_A - T_{REF}\right)^2 \right]^{\frac{1}{2}}. \tag{2.24}$$

In case of a balanced Dicke radiometer, $T_A = T_{REF}$, so that gain variation effects are eliminated. Then, equation (2.24) reduces to

$$\Delta T = \frac{2\left(T_A + T_R\right)}{\sqrt{B\tau}} = 2\Delta T_{IDEAL} \tag{2.25}$$

where ΔT_{IDEAL} stands for the theoretical sensitivity of an ideal TPR and the factor 2 indicates that T_A is only observed for half the period.

The main drawback of this type of radiometer with respect to an ideal TPR is the loss of radiometric sensitivity due to the reduced effective integration time. In addition, if the antenna temperature and the reference noise temperature are not equal, gain fluctuations are not completely compensated.

Noise Injection radiometer

A particular type of Dicke radiometer in which the output voltage always equals zero is the Noise Injection Radiometer (NIR). In this type of radiometers a given amount of noise (T_I) is added to its output so that $T'_A = T_A + T_I = T_{REF}$ and therefore, it is independent on the gain and reference noise temperature fluctuations. This condition is accomplished using a loop so that the reference temperature and the antenna temperature are equal. A block diagram is presented in Fig. 2.3(c).

$$V_{OUT} = \frac{1}{2} G_s \left(T'_A - T_{REF}\right) = 0. \tag{2.26}$$

And the radiometric sensitivity of a noise injection radiometer can be computed from

$$\Delta T = 2\frac{T'_A + T_R}{\sqrt{B\tau}} = 2\frac{T_{REF} + T_R}{\sqrt{B\tau}}. \tag{2.27}$$

Radiometric sensitivity of a NIR is similar to that of Dicke's. However, NIR has the advantage of being a zero detection system (more accurate) and giving continuous measurements of the scene.

Further information about real aperture radiometers can be found in [Ulaby *et al.*, 1981] and [Skou, 1989].

Synthetic aperture radiometers

Unlike real aperture radiometers, synthetic aperture radiometers do not measure directly the brightness temperature image but the visibility samples, that is, the cross-correlation

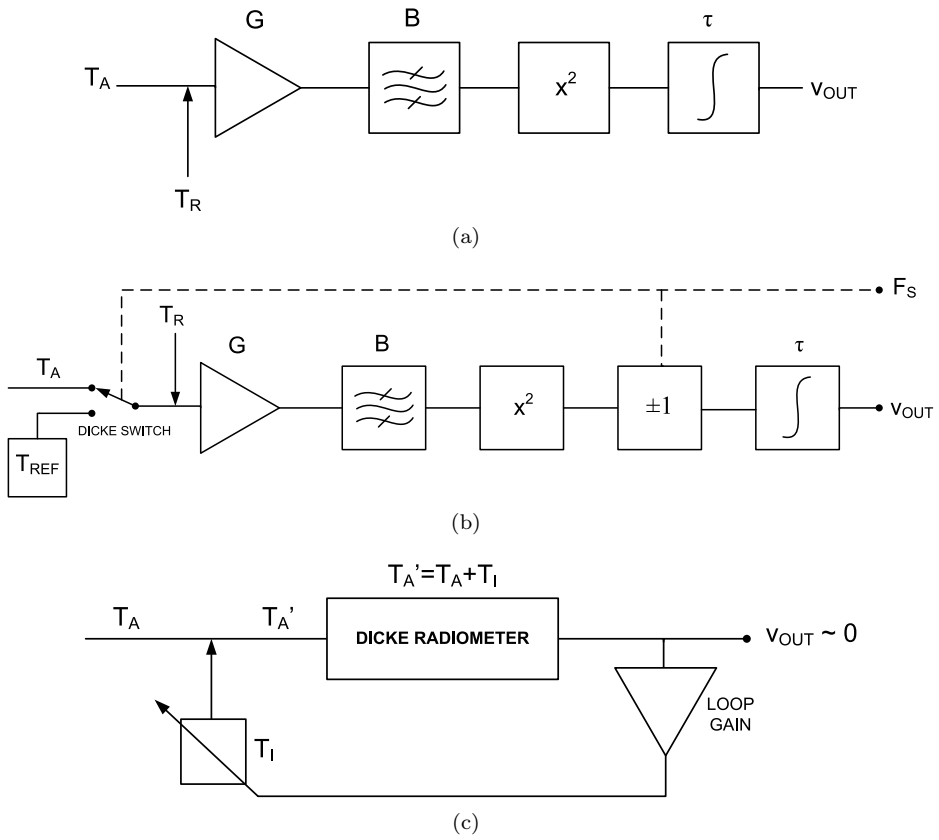

Figure 2.3: Block diagrams of real radiometers, from [Skou, 1989]: (a) Total power radiometer (TPR), (b) Dicke radiometer, (c) Noise injection radiometer (NIR).

between the signals collected by many pairs of antennas located at different relative distances. These visibility samples need to be corrected from instrumental errors. After that, brightness temperature images are retrieved by inversion of the measured visibility function. Section 2.4.1 further develops the synthetic aperture radiometry concept particularized to the MIRAS instrument.

2.2 Microwave radiometry for Earth observation

Real aperture radiometers have been frequently used for Earth observation applications. However, for space-borne sensors at a low Earth orbit, requirements on spatial resolution and coverage would entail, at high operating wavelengths, a too large antenna using real aperture techniques. Synthetic aperture radiometry for Earth observation is an alternative to real aperture radiometry at low microwave frequencies with high resolution, as it was first proposed by C. Swift and R. McIntosh in 1983 [Swift & McIntosh, 1983].

Passive interferometry was first developed in Radio-astronomy [Thompson *et al.*,

1986]. This technique was used, for example, in the Very Large Array (VLA), formed by twenty-seven 25-meter diameter dish antennas that together comprised a Y-shaped radio telescope system located in Socorro, New Mexico [Napier *et al.*, 1983].

However, the application of this technique to Earth observation presented several technological challenges. Main differences between both applications come from the observed scene, which consists of point sources in Radio-astronomy (visibility amplitude practically constant), and of extended sources in the case of Earth observation. Point sources imaging allows the use of highly directive antennas (oriented to point to the source) with an accurate measurement of the antenna patterns in the field of view. On the contrary, Earth observation requires a wider field of view and individual antenna patterns must be taken into account in the inversion procedure. Moreover, the antenna spacing is shorter in order to prevent the aliasing in the image reconstruction process, which increases the antenna coupling and self-interferences. These differences led to the development of more complex calibration and image retrieval algorithms. These issues were thoroughly addressed in [Camps, 1996, Ribó i Vedrilla, 2005, Corbella *et al.*, 2009a].

The first instrument devoted to Earth observation using interferometric aperture synthesis was ESTAR (Electronically Steered Thinned Array Radiometer), developed at NASA/Goddard Space Flight Center in the 90's. This L-band airborne radiometer, devoted to soil moisture remote sensing, uses a hybrid configuration: real aperture antennas for along-track direction and interferometric aperture synthesis for across-track. ESTAR allowed to validate the 1D aperture synthesis concept [Le Vine *et al.*, 2001]. Next step in the development of this instrument was the evolution from ESTAR (aperture synthesis only in one dimension, one polarization and analog processing) to 2D-STAR, a dual-polarized L-band airborne radiometer with aperture synthesis in two dimensions and digital processing [Le Vine *et al.*, 2007].

In the early 90's, ESA undertook within the Earth Living Planet Program the first interferometric aperture radiometer using two dimensions devoted to Earth observation: the MIRAS instrument [Martín-Neira & Goutoule, 1997, Camps, 1996, McMullan *et al.*, 2008]. Its scientific objectives are devoted to globally provide soil moisture and ocean salinity maps from space (see section 2.3). Considering the novelty of the instrument technology, the development of an airborne demonstrator was key to test the technology to be applied in MIRAS. EADS-CASA Espacio led the development of AMIRAS (Airborne Microwave Imaging Radiometer by Aperture Synthesis), a small scale airborne prototype of MIRAS [Martín-Neira *et al.*, 2008a], in the framework of the MDPP-3 project (MIRAS Demonstrator Pilot Project, stage 3) sponsored by ESA.

Previous stages allowed the development of the required hardware overcoming technical problems. Receivers and calibration subsystems integrated in AMIRAS are similar to the elements on the MIRAS instrument. This feature has allowed assessing the instrument system performance as well as its limitations. The IEEC (Institut d'Estudis Espacials de Catalunya) was responsible for the development of the Electronic Ground

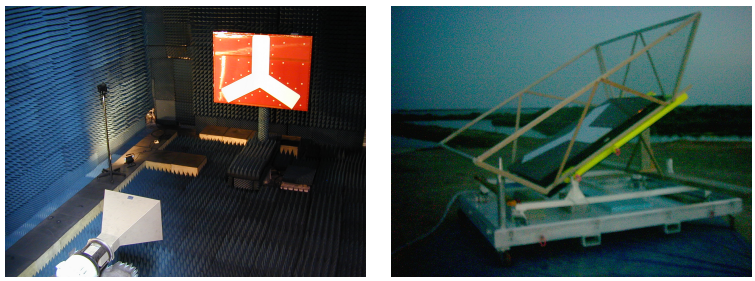

(a) (b)

(c)

Figure 2.4: AMIRAS instrument (a) during antenna pattern characterization at UPC anechoic chamber, (b) prepared for sky map imaging at IRTA facilities, (c) installed on the HUT skyvan, ready for the airborne campaigns over Finland.

Segment Equipment (EGSE) [Ribó i Vedrilla, 2005]. Characterization of the instrument performance was carried out by UPC and IEEC (see Fig. 2.4(a)) [Beraza *et al.*, 2006]. After that, first outdoor experiments were undertaken in 2006 at IRTA (Institut de Recerca i Tecnologia Agroalimentarias) facilities, located at the Ebro River Delta. Its main objective was to obtain an image of the Milky Way with AMIRAS (Fig. 2.4(b)) for the first time [Duffo *et al.*, 2007]. Figure 2.5(a) shows the measured image of the Milky Way. In the last stage, AMIRAS was boarded in a skyvan of the LST/HUT (Laboratory of Space Technology, Helsinki University of Technology) and data from several flights over the Pensaari island (Finland) at the beginning of Lohja lake were acquired (Fig. 2.4(c)). These images demonstrated AMIRAS capability to image water-land transitions (2.5(b)) [Corbella *et al.*, 2009a]. From these field experiments, calibration methods and image reconstruction algorithms foreseen for MIRAS instrument were assessed and validated. However, AMIRAS is not the only MIRAS airborne demonstrator. A second demonstrator, HUT-2D, was developed by Helsinki University of Technology (TKK). It is compounded by 36 receivers in a U-shape geometry. HUT-2D contributed mainly to testing different calibration techniques focused on the reference radiometer (NIR), that is, on the absolute amplitude calibration method foreseen for SMOS [Rautiainen *et al.*, 2008].

Currently, there are several missions devoted to Earth observation in progress us-

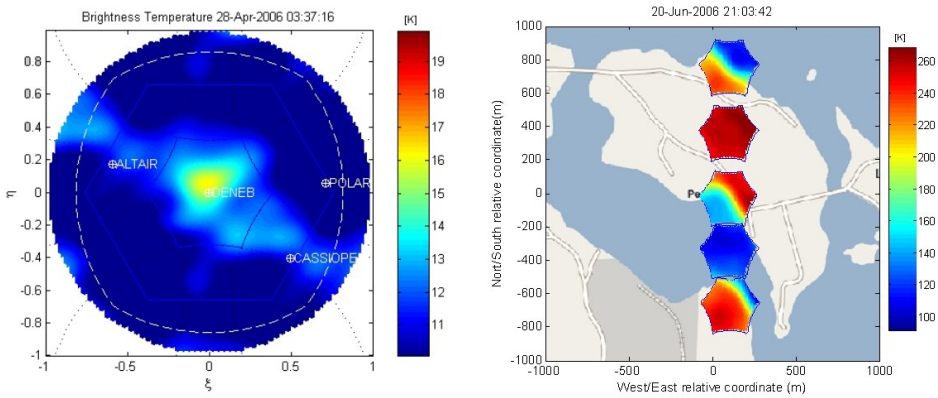

(a) (b)

Figure 2.5: First 2D images with AMIRAS (a) Milky Way: image of Deneb in the whole space. The positions of Altair and Cassiopeiae in the Galaxy are shown for reference. (b) Pensaari island imaging obtained during the flights. From [Duffo *et al.*, 2007, Corbella *et al.*, 2009a].

ing interferometric aperture synthesis. The development of a 2D interferometer called GeoSTAR (Geostationary Synthetic Thinned Aperture Radiometer) is underway at JPL (Jet Propulsion Laboratory) and at GSFC (Goddard Space Flight Center) within NASA's Instrument Incubator Program. Its goal is the measurement of the atmospheric parameters at microwave frequencies with high spatial resolution from a geostationary orbit (geosounder). A GeoSTAR prototype has been used to test the technology and demonstrate the concept feasibility [Lambrigtsen *et al.*, 2007]. GeoSTAR has been proposed to be the payload of the PATH (Precipitation and All-weather Temperature and Humidity) mission, being the first passive microwave sensor in a geostationary orbit. Another geostationary atmospheric sounder is GAS, which is currently under development by Saab Space AB and Omnisys AB, Sweden, and funded by the European Space Agency (ESA). Initial breadboard results for the hardware development have been already obtained [Christensen *et al.*, 2007]. The next phase of the mission is the construction of the GAS demonstrator.

As it has been aforementioned, SMOS is an Earth Explorer mission. A SMOS follow-on operational mission is currently under study. Based on the experience of the current mission, improvements in several technological and scientific aspects are being evaluated. If the mission goes ahead, CSSAR (Center of Space Science and Applied Research) has been proposed as responsible for an auxiliary radiometer, a one dimensional Full Polarization Interferometric Radiometer (FPIR). It would contribute to enhance sea surface salinity retrievals by means of sea-surface roughness estimation collocated with radiometer data [Yan *et al.*, 2007]. Regarding technological features, L-band receivers with parallel H and V channels and a higher frequency rate are envisaged for MIRAS-2. Both improvements will allow to increase the radiometric sensitivity of the instrument. In addition, the

distance between adjacent antennas will be reduced in order to increase the field of view. Potential improvements for SMOSops have been tested in a demonstrator developed at UPC by Ramos-Pérez et al., the SA-PAU (Synthetic Aperture Passive Advanced Unit) [Ramos-Pérez *et al.*, 2007].

2.3 The SMOS mission

Soil Moisture and Ocean Salinity, successfully launched on November 2, 2009 (Fig. 2.6), is the second Earth Explorer mission selected as part of the European Space Agency's (ESA) Living Planet Program [Silvestrin *et al.*, 2001, Barre *et al.*, 2008]. SMOS is the first satellite mission capable of frequently and globally measuring two main geophysical parameters: soil moisture over continental surfaces [Kerr *et al.*, 2010] and sea surface salinity over the oceans [Font *et al.*, 2010]. Additionally, the mission is expected to improve the characterization of ice and snow-covered surfaces.

(a) (b)

Figure 2.6: (a) MIRAS and Proba-2 inside the launcher. (b) MIRAS/SMOS launch on November 2, 2009, from Plesetsk Cosmodrome (Russia). Credits: ESA

Both soil moisture and ocean salinity are key parameters related to the Earth's water cycle (Fig. 2.7) and climate, since the variability in these geophysical variables controls the continuous exchange of water between the oceans, the atmosphere and the land. Sea surface salinity (SSS) relates Earth global water cycle to ocean circulation. Salinity varies mainly by evaporation/precipitation and by freezing/melting of ice in polar regions. The increase/decrease of fresh water in the ocean surface creates density gradients, which are able to drive ocean currents and modulate the climate of the continents (thermohaline circulation). The estimation of this parameter at global scale and its variability, both annual and interannual, is key for a better understanding and modeling of the ocean circulation. This leads to the detection of phenomena such as the El Niño/Southern Oscillation. Soil moisture (SM) is also a key variable in the Earth water cycle since controls the percentages of rainfall running the surface (runoff), filtering the land and evaporating from the land. It is especially valuable for improving short- and medium-term meteorological modeling, monitoring global hydrological resources and plant growth,

studying biogeochemical cycles and forecasting of hazardous events, such as floods and landslides. Therefore, this mission will contribute to an improved weather, extreme-events and seasonal-climate forecasting.

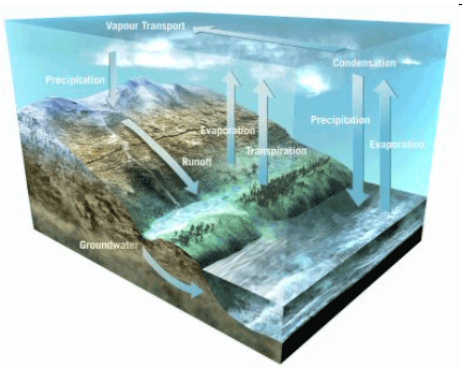

Figure 2.7: Earth's water cycle (credits: ESA).

SMOS scientific requirements for soil moisture imply providing global maps every 3 days with a spatial resolution better than 50 Km with an accuracy of 4% volumetric humidity (0.04 m^3/m^3). For sea surface salinity retrievals, maps with an accuracy of 0.1 psu (practical salinity units) and 200 km spatial resolution are expected every 30 days [SMOS, 2003a]. As secondary objectives, SMOS is expected to provide vegetation water content maps with an accuracy of $0.2kg \cdot m^{-2}$ every 6 days and provide useful data for cryosphere studies. Further information can be found in ESA-SMOS home page (www.esa.int/esaLP/LPsmos.html).

SMOS has been conceived as a demonstrator mission with a nominal (extended) lifetime of 3 (5) years. The satellite is in a low Earth orbit (at 758 km), Sun-synchronous, dawn/dusk and quasi-circular. As it has been introduced in section 2.2, SMOS carries a fully innovative type of instrument for Earth observation: the Microwave Imaging Radiometer using Aperture Synthesis (MIRAS). It is an L-band two dimensional synthetic aperture radiometer with multilook and multiangular observation and dual-polarization/full polarimetric capabilities. Section 2.4 is devoted to describe MIRAS operating principle and the subsystems which integrate the payload. EADS-CASA Espacio has led the MIRAS payload integration and the execution of the on-ground characterization tests. Other Spanish companies have been involved in different SMOS activities, such as Mier Comunicaciones, Space Department (La Garriga, Barcelona), manufacturing the MIRAS receivers. Helsinki University of Technology (HUT) and Ylinen (Finland) have developed MIRAS calibration subsystems and reference radiometers.

Regarding the ground segment, it involves both satellite operations, which are controlled by CNES (Centre National d'Études Spatiales), and data receiving, processing and storing stations. Data from the satellite are downloaded when the ground station is visible through an X-band link to the Data Processing Ground Segment (DPGS) at

ESA's European Space Astronomy Center (ESAC), in Villafranca del Castillo, Madrid (Spain). Other ESA receiving stations are: a Near-Real Time (NRT) acquisition station in Svalbard (Norway) and a Long-Term Archive (LTA) and reprocessing center in Kiruna, Sweeden. ESA distributes to the scientific community the following SMOS products:

- Raw data: observation data and telemetry as received from the satellite
- Level 0: unprocessed data containing the Earth Explorer headers
- Level 1, which is divided into three levels:
  - ◇ Level 1A: calibrated visibilities, corrected from instrumental errors.
  - ◇ Level 1B: Fourier components of brightness temperature in the antenna reference frame.
  - ◇ Level 1C: geolocated brightness temperatures, that is, swath-based maps of brightness temperature.
- Level 2: soil moisture and ocean salinity swath-based maps.

Therefore, ESA distributes as SMOS final products Level 2 soil moisture and ocean salinity satellite swath gridded data. However, many applications need global maps obtained by applying spatial and temporal averaging techniques on different satellite overpasses (Level 3) or merged products with other satellite or in situ data sources (Level 4). The CP34 (Spanish Processing Centre for level 3 and level 4 products) is formed by a Production and Distribution Centre, installed at ESAC close to DPGS, and the Barcelona Expert Centre (SMOS-BEC) hosted by ICM-CSIC. CP34 is in charge of generating and distributing global and regional maps of soil moisture, ocean salinity, and other related parameters, based on the data provided by SMOS DPGS. Further information can be found in CP34 home page (www.cp34-smos.icm.csic.es).

2.4 The payload: MIRAS

2.4.1 MIRAS operating principle

MIRAS operating principle is based on 2D interferometric aperture synthesis, as it has been previously mentioned. Cross-correlations of the signals $b_k(t)$, $b_j(t)$ collected by each pair of receivers (known as baseline), provide the samples of the visibility function (Fig. 2.8). The brightness temperature map is then obtained by a Fourier synthesis of the calibrated visibility function. The complete development of the visibility function in interferometric aperture synthesis radiometry can be found in [Corbella *et al.*, 2004]. The main concepts are summarized in this section.

Signals collected by the antennas are first band-pass filtered and then sent to the correlator. An integrator accumulates the output of the correlator during each integration

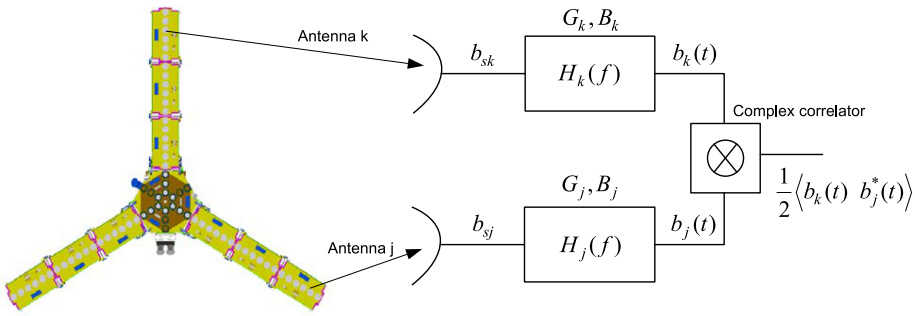

Figure 2.8: Block diagram of a single baseline relating the measurement of a visibility sample.

period (1.2 seconds). The average power of the signals at the input of the correlator is given by

$$\langle |b_k(t)|^2 \rangle = 2kG_kB_k\left(T_{Ak} + T_{Rk}\right), \tag{2.28}$$

where subindex k stands for the receiver k and a similar expression can be written for the second receiver j forming the baseline. B_k is the receiver noise equivalent bandwidth and G_k the available power gain of receiver k. The term T_{Ak} corresponds to the antenna temperature and T_{Rk} is the receiver noise temperature at the antenna plane. The sum of these terms is known as the system temperature T_{sysk}.

Complex correlation of the signals $b_k(t)$ and $b_j(t)$ at the input of the correlator can be expressed as

$$\langle b_k(t)b_j^*(t)\rangle = 2k\sqrt{G_kG_j}\sqrt{B_kB_j}V_{kj}^t, \tag{2.29}$$

being V_{kj}^t the time-domain system visibility in units of Kelvin.

Then, considering equations (2.28) and (2.29), the normalized complex correlation can be written as a function of the system temperatures and the system visibility

$$\mu_{kj} = \frac{\langle b_k(t)b_j^*(t)\rangle}{\sqrt{\langle |b_k(t)|^2\rangle\langle |b_j(t)|^2\rangle}} = \frac{V_{kj}}{\sqrt{T_{sys_k}T_{sys_j}}}. \tag{2.30}$$

The cross-correlation of the signals at the output of the receivers can also be expressed, assuming infinite integration time, as a function of the signals at the input (b_{sk}, b_{sj}) and the receivers' frequency response

$$\frac{1}{2}\langle b_k(t)b_j^*(t)\rangle = \int_0^\infty \overline{b_{sk}(f)b_{sj}^*(f)}H_k(f)H_j^*(f)\,df = \int_0^\infty kV_{kj}H_k(f)H_j^*(f)\,df, \tag{2.31}$$

where V_{kj} is the frequency-domain system visibility and can be expressed as:

$$V_{kj} = \iint_{4\pi} T_B' e^{jk\Delta r}\,d\Omega, \tag{2.32}$$

The term T'_B corresponds to the modified brightness temperature and Δr to the decorrelation time.

Substituting expressions (2.29) and (2.31) in equation (2.32), the visibility yields

$$V_{kj}^{t} = \iint\limits_{4\pi} T'_B \frac{1}{\sqrt{G_k G_j}\sqrt{B_k B_j}} \int\limits_{0}^{\infty} H_k(f) H_j^*(f) e^{jk\Delta r}\, df\, d\Omega \tag{2.33}$$

Considering the fringe washing function definition, which takes into account spatial decorrelation effects

$$\tilde{r}_{kj}(t) = \frac{1}{\sqrt{B_k B_j}\sqrt{G_k G_j}} e^{-j2\pi f_0 t} \int_0^{\infty} H_k(f) H_j^*(f) e^{j2\pi f t}\, df, \tag{2.34}$$

the system visibility of any pair of antennas measured using time-domain cross-correlation can be rewritten as:

$$V_{kj}(u_{kj}, v_{kj}) = \iint\limits_{\xi^2+\eta^2\leq 1} T'_B(\xi,\eta) \cdot \bar{\tilde{r}}_{kj}\left(-\frac{u_{kj}\xi + v_{kj}\eta}{f_0}\right) \cdot e^{-j2\pi(u_{kj}\xi + v_{kj}\eta)}\, d\xi\, d\eta \tag{2.35}$$

being $(u_{kj}, v_{kj}) = (x_j - x_k, y_j - y_k)/\lambda_0$ the set of spatial frequencies where the visibility function V_{kj} is sampled (see Fig. 2.9(a)), the term $\bar{\tilde{r}}_{kj}$ corresponds to the fringe washing function normalized to the value at the origin and f_0 is the central frequency of the receivers. Coordinates $(\xi, \eta) = (\sin\theta\cos\phi, \sin\theta\sin\phi)$ are the director cosines with respect to the (X, Y) axes. The subscript t indicating the time-domain cross-correlation is removed from now on for the sake of simplicity. $T'_B(\theta, \phi)$ is defined as the modified brightness temperature and it is related to the brightness temperature through the normalized voltage antenna patterns ($F_{n_k}(\xi,\eta)$, $F_{n_j}(\xi,\eta)$), the equivalent solid angle of the antennas (Ω_k, Ω_j) and the physical temperature mean value of receivers forming the baseline ($T_{rec_{kj}}$):

$$T'_B(\xi,\eta) = \frac{F_{n_k}(\xi,\eta) F_{n_j}^*(\xi,\eta)}{\sqrt{\Omega_k \Omega_j}} \cdot \frac{T_B(\xi,\eta) - T_{rec_{kj}}}{\sqrt{1-\xi^2-\eta^2}} \tag{2.36}$$

It must be pointed out that visibility samples in (2.35) should be corrected from instrumental errors before applying the inversion procedure to obtain the modified brightness temperatures. All the calibration procedures applied to MIRAS are comprehensively reviewed in chapter 3.

The distance between adjacent antennas is $d = 0.875\lambda$, not satisfying the Nyquist criterion ($d > \lambda_0/\sqrt{3}$). Therefore, replicas of $T_B(\xi,\eta)$ overlap with the main one producing aliasing (see Fig. 2.9(b)). The alias-free field of view (AF-FOV) is the region of non-overlapping of the unit circle aliases and it is marked in light green. The extension of this zone up to the region limited by the repetition of the Earth aliases is the extended

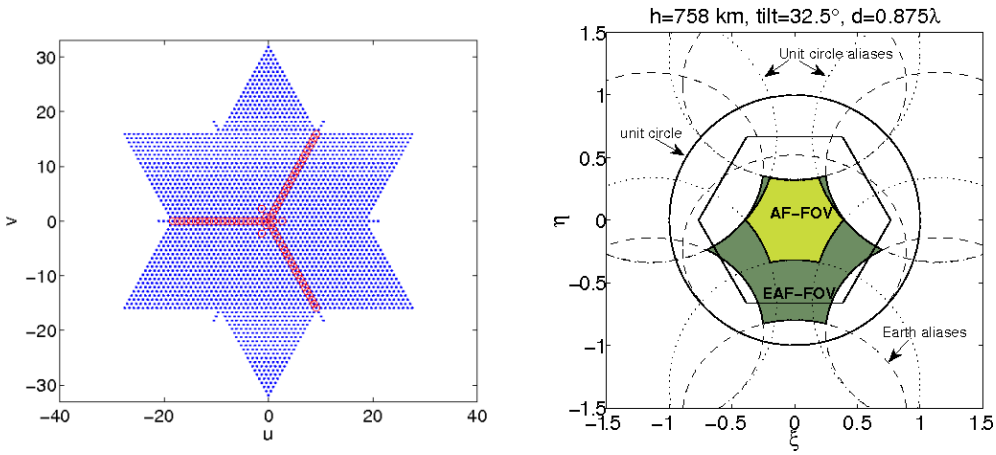

(a) (b)

Figure 2.9: (a) Spatial frequencies where the visibility is sampled. (b) The points of (ξ, η) grid where the brightness temperature is retrieved. Aliasing in the brightness temperature images. Earth disks (dashed ellipses), the unit circle (solid circle), the DFT basic period (hexagon) and the 6 closest replicas of the unit circle are also represented (dotted circles). Strict alias-free field of view (AF-FOV) is marked in light green and the extended one (EAF-FOV) in dark green.

alias-free field of view (EAF-FOV), marked in dark green. This is possible because the sky is known and it can be subtracted [Camps, 1996, Le Vine & Abraham, 2004, Camps *et al.*, 2008].

The Flat Target Response (FTR) is defined as the visibility of a completely unpolarized target having equal brightness temperature in any direction. It can be measured pointing to the cold sky (flat target) or by measuring the antenna patterns and the fringe washing function [Martín-Neira *et al.*, 2008b]. It only depends on the instrument and can be expressed as:

$$FTR_{kj} = \iint\limits_{\xi^2+\eta^2\leq 1} \frac{1}{\sqrt{1-\xi^2-\eta^2}} \frac{F_{n_k}(\xi,\eta)F^*_{n_j}(\xi,\eta)}{\sqrt{\Omega_k\Omega_j}} \cdot \bar{\bar{r}}_{kj}\left(-\frac{u_{kj}\xi + v_{kj}\eta}{f_0}\right) \cdot e^{-j2\pi(u_{kj}\xi+v_{kj}\eta)} d\xi\, d\eta \tag{2.37}$$

Several approaches to combine non-zero baselines visibility (different antennas) and visibilities measured by zero-baselines, that is, the antenna temperature, are tested to invert the visibility function in [Corbella *et al.*, 2009a]. One of them consists of inverting the incremental modified brightness temperature $\Delta T_{B_{kj}} = T_B(\xi,\eta) - T_A$, being T_A the average antenna temperature measured by the NIR units or by all the LICEFs. Therefore, the incremental visibility can be expressed, using the FTR, as

$$\Delta V_{kj}(u_{kj}, v_{kj}) = V_{kj}(u_{kj}, v_{kj}) - (T_{A_{kj}} - T_{rec_{kj}})FTR_{kj}, \tag{2.38}$$

where $T_{A_{kj}}$ is the average of the antenna temperatures of both antennas.

This technique allows to reduce the uncertainties of antenna patterns and fringe washing function, since they are scaled by the difference between the brightness temperature and antenna temperature. Results obtained from the different approaches using real data from AMIRAS can be found in [Corbella *et al.*, 2009a].

In the ideal case all the antenna patterns are equal ($F_{n_k}(\xi,\eta) = F_{n_j}(\xi,\eta)$ and $\Omega_k = \Omega_j$) and the decorrelation effects are considered negligible ($\bar{\bar{r}}_{kj} \approx 1$). Then, the modified brightness temperature map is retrieved directly from calibrated visibilities by applying an inverse Fourier transform (a first-order solution):

$$V(u,v) = \mathscr{F}\left[T'_B(\xi,\eta)\right]. \tag{2.39}$$

MIRAS, as any Y-shaped interferometer, measures the visibility samples over a hexagonal grid in the spatial frequencies domain (u,v). Therefore, a hexagonal grid (ξ,η) reciprocal of the (u,v) grid was defined to process the visibility samples by using the standard FFT techniques [Camps, 1996, Camps *et al.*, 1997].

The discretized visibility can be expressed as a linear system of equations that can be written in a matrix form

$$\overline{V} = \overline{\overline{G}} \cdot \overline{T}, \tag{2.40}$$

where the definition of V and T depends on the inversion approach, as is detailed in [Corbella *et al.*, 2009a] and the $\overline{\overline{G}}$ matrix includes the antenna patterns and the fringe washing function. $\overline{\overline{G}}$ matrix in a Y-shaped instrument like MIRAS is not squared, since the number of visibility samples and the number of (ξ,η) points are not the same. Hence, this system of equations can be solved by applying, for example a Moore-Penrose pseudo-inverse. Both inversion techniques, inverse Fourier transform and G-matrix pseudo-inverse were validated using real data from AMIRAS [Corbella *et al.*, 2009a]. After the inversion procedure, brightness temperatures at antenna frame are available.

The next step in the level 1 processing is the geolocation of the brightness temperatures over the Earth's surface. For each polarization, several observations of the same pixel at different incident angles are obtained in each overpass. Brightness temperatures at different incidence angles and polarizations are used in the retrieval algorithms of soil moisture and ocean salinity.

2.4.2 MIRAS architecture

A general description of the MIRAS instrument's architecture and a brief explanation of the main subsystems integrating the payload are presented in this section. Further details on the hardware used can be found in [McMullan *et al.*, 2008].

MIRAS instrument consists of a Y-shape synthetic aperture radiometer with receivers equally distributed along the three deployable arms, which are connected to a central

structure called hub. Each arm is divided into three segments, each one containing 6 receivers, the so-called LICEFs (LIghtweight Cost-Effective Front-ends). Each segment contains a CMN (Control and Monitoring Node) that provides power and coherent local oscillator to each LICEF receiver. In addition, three noise injection radiometers (NIRs) have been included in the central hub (see Fig. 2.10(a)). Each NIR comprises two LICEF receivers connected to a single antenna. Hence, the instrument is composed of 72 receivers but only 69 antennas. A Correlation and Control Unit (CCU), placed in the central structure, is the single interface between the payload and the services module in the platform. It generates source packets (telemetry) every integration period containing data provided by the LICEFs, NIRs, CMNs and also platform's attitude information. Received noise signal is transmitted from each LICEF to the DIgital COrrelator System (DICOS), placed in the CCU. The noise signal amplitude is measured by the PMS (Power Measurement System) of each LICEF, digitalized in the corresponding CMN and sent to the CCU, since this information is added to the telemetry. A photograph of the MIRAS instrument during the integration of the different subsystems at EADS-CASA Espacio facilities is shown in Fig. 2.10(b).

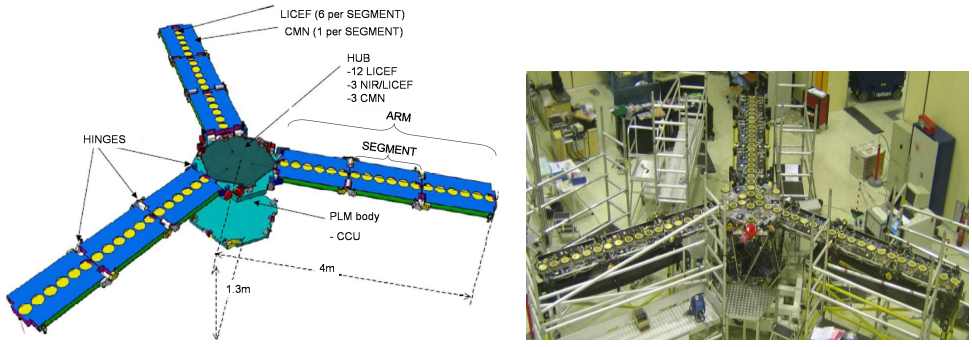

(a) (b)

Figure 2.10: MIRAS payload architecture. (a) MIRAS payload scheme, from [McMullan *et al.*, 2008]. (b) Integration of MIRAS subsystems at EADS-CASA facilities (credits: EADS-CASA Espacio).

In order to support the calibration procedure, the NIRs provide an accurate measurement of the average brightness temperature scene and also act as reference radiometers to calibrate the PMS of each receiver [Colliander *et al.*, 2007a]. Besides, a CAlibration Subsystem (CAS) [Lemmetyinen *et al.*, 2007] based on a distributed noise injection approach, allows maintaining phase and amplitude calibration track along the three arms [Torres *et al.*, 1996]. In the hub, there is a one-to-eighteen network to distribute the noise generated by the single Noise Source (NS) simultaneously to all the receivers (centralized calibration). In the arms, there is a NS located at each CMN driving a one-to-twelve network distributing the noise to the receivers in the same segment and in the adjacent one. This approach allows injecting two correlated noise levels in overlapped sets of receivers

to apply the distributed noise injection concept [Corbella *et al.*, 2005]. A thermal control subsystem composed of an active system of heaters is used to control the physical temperature drifts of each receiver and maintain them at constant operational temperature (around 22°C).

A 2D image is taken every integration period (1.2 seconds). During this time, MIRAS generates a large number of signals and telemetry data which are saved as binary files in the on-board computer. It generates for each snapshot 72 PMS voltage readings, 2556x2 correlator counts (real and imaginary part of complex correlations for the 2556 baselines), 6 NIR dicke pulse fraction, temperature readings (from sensors located in LICEFs, CAS and NIR) and control signals related to the instrument operation modes, among others.

The payload is coupled to a standard spacecraft called PROTEUS (Plate-forme Reconfigurable pour l'Observation, les Télécommunications et les Usages Scientifiques), developed jointly by the French Space Agency (CNES) and Thales Alenia Space. The platform acts as a services module containing all the subsystems needed for the correct satellite operation, such as solar arrays, GPS receiver and star tracker.

After a general description of the MIRAS instrument architecture, the subsystems integrating the payload are briefly described, focusing on those which have been key during the research of this thesis. Figure 2.11(a) shows the components of segment B3 during the integration at EADS-CASA Espacio facilities: the 6 LICEF units, the CMN, the Noise Source (NS) and the Power Divider (PD) of the calibration subsystem section corresponding to this segment.

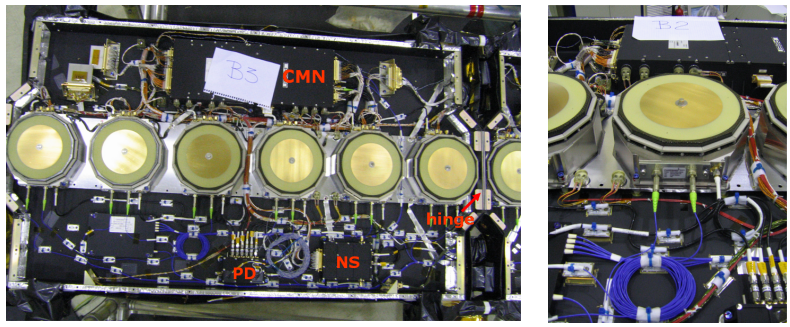

(a) (b)

Figure 2.11: (a) Architecture of B3 segment: LICEF units, the CMN and the Calibration system section corresponding to this segment. (b) Architecture of B2 segment: H, V and C ports of the LICEFs can be appreciated. Courtesy of EADS-CASA Espacio.

LICEF

Each LICEF of the MIRAS instrument comprises a radiometric receiver integrated with a dual polarization antenna. A switch allows to select between the two observation modes (H/V polarization) and the two calibration modes, that is, correlated noise injection

through the calibration subsystem (CAS) and uncorrelated noise injection (matched load). The four inputs of the receiver can be appreciated in Fig. 2.11(b). For a better understanding, a block diagram of a LICEF unit is shown in Fig. 2.12. The band pass filter in the RF circuitry allows selecting the working band (1400-1423 MHz). The mixer shifts the RF (Radio Frequency) band to the IF (Intermediate Frequency) band (8-27 MHz) using a local oscillator (LO) frequency of 1396 MHz. Outputs of each receiver correspond to in-phase (I) and quadrature (Q) components of the noise signal. One of these components is sent to the PMS, providing the amplitude (power) of the noise signal. Signals from both channels are digitally converted and sent to the central correlator unit, placed in the CCU. Each PMS converts the power of the received signal to voltage. Each one of these systems is formed by a diode detector and an integrator acting as a total power radiometer (TPR) (see section 2.1.3).

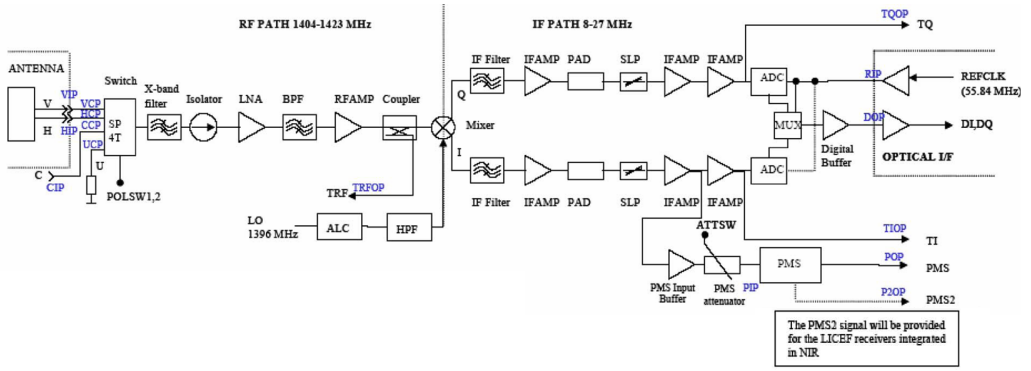

Figure 2.12: MIRAS receiver block diagram, from [McMullan *et al.*, 2008].

The LICEF antenna, as aforementioned, is a dual polarization antenna. MIRAS has two observation modes: dual polarization and full polarimetric. In the first mode, both polarizations, H and V, are sequentially measured every integration time (1.2 seconds), as it is shown in Fig. 2.13. Therefore, during each acquisition all receivers are measuring in the same polarization. In the polarimetric mode [Martín-Neira *et al.*, 2002, Ribó i Vedrilla, 2005], a switching sequence allows to measure all the possible cross-correlations, which are completed in four integration periods (Table 2.1).

MIER Comunicaciones was in charge of manufacturing the receivers. EADS-CASA designed and manufactured the antenna and the receiver band-shaping RF filter, while UPC provided key support in elaborating technical specifications.

Noise Injection Radiometer (NIR)

As commented in the previous sections, MIRAS includes three polarimetric NIRs in its central structure. NIR units are also known as zero baseline radiometers, since they are used to accurately measure the zero baseline (antenna temperature). Design, on-ground

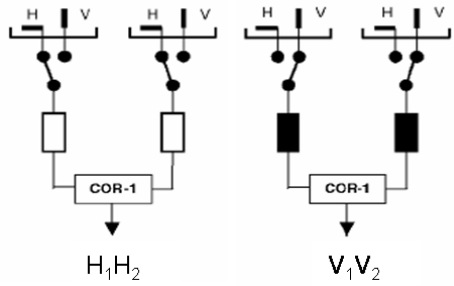

Figure 2.13: Dual polarization mode in MIRAS.

Table 2.1: Full polarimetric switching sequence [Martín-Neira *et al.*, 2002].

Integration period	Arm A	Arm B	Arm C
First epoch	H	H	H
Second epoch	V	H	H
	H	V	H
	H	H	V
Third epoch	V	V	V
Fourth epoch	H	V	V
	V	H	V
	V	V	H

characterization and in-orbit calibration scheme of these units is throughly detailed in [Colliander *et al.*, 2007a]. The NIR purpose is two-fold:

- to measure the antenna temperature of the scene, providing the MIRAS absolute reference.
- to measure the noise temperature level of the calibration system.

In addition, NIR units incorporate operational modes that allow them to form interferometric baselines with LICEF units of MIRAS, the so-called mixed baselines [Colliander *et al.*, 2005]. Each NIR unit is formed by a controller (Fig. 2.14(a))) and two LICEF receivers, one for horizontal and the other for vertical polarization (see Fig. 2.14(b)). These units are practically identical to the other receivers of MIRAS.

The controller injects the reference noise into the two receiver chains, regulating the amount of the injected noise to keep the system balanced with the antenna temperature or with the calibration noise from CAS, depending on its operation mode [Colliander *et al.*, 2007a]. Figure 2.15 shows schematic diagrams of the two main NIR operation modes: NIR-A mode for the antenna temperature measurement and NIR-R for the measurement of the CAS noise temperature levels. In the first mode, the Dicke switch commutes continuously between the antenna and a fixed load at U port (Fig. 2.15(a)). The balance between both switch inputs is performed by injecting a known additional noise temperature to the antenna signal. In this way, the effect of the fluctuations of the receiver

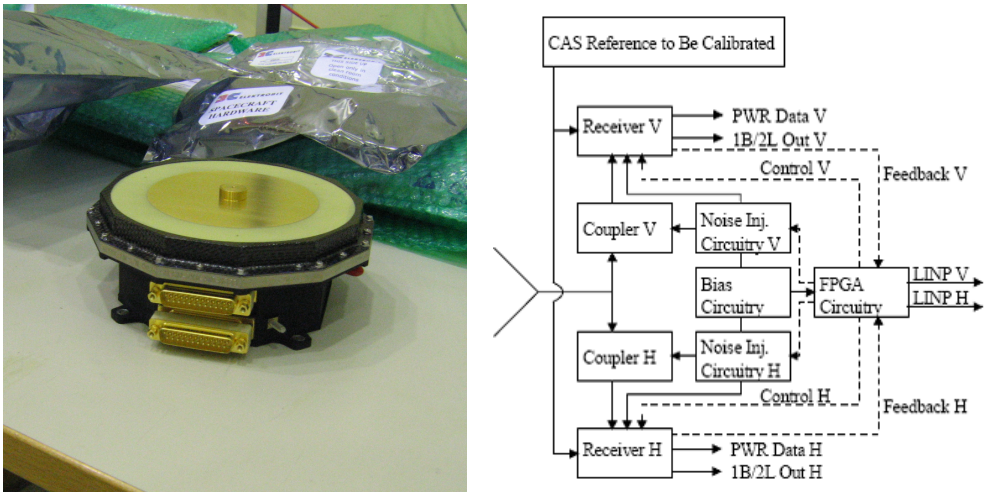

(a) (b)

Figure 2.14: (a) NIR controller (NIC) which together with two LICEF units form the NIR, courtesy of EADS-CASA Espacio. (b) Block diagram of a NIR unit, from [McMullan *et al.*, 2008]

gain can be mitigated (see section 2.1.3). In the NIR-R mode (Fig. 2.15(b)), the Dicke switch commutes between the C port of the NDN (Noise Distribution Network) and the reference branch. In this case, the balance between both switch inputs is achieved by injecting a known noise temperature to the reference temperature. Both the noise injected to the antenna path and to the reference branch need to be measured during external calibrations [Brown *et al.*, 2008].

A comprehensive description of the different NIR operational modes can be found in [Colliander *et al.*, 2007a].

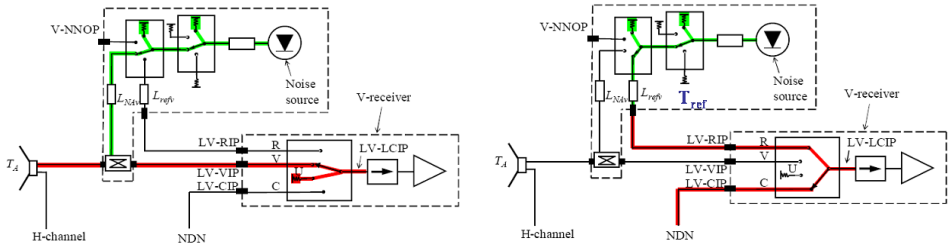

(a) (b)

Figure 2.15: NIR basic operation modes, from [Colliander *et al.*, 2007a]. (a) Measurement of the antenna temperature (NIR-A mode). (b) Measurement of the CAS noise level (NIR-R mode).

DIgital COrrelator System (DICOS)

MIRAS performs the complex correlation between the signals collected by each pair of receivers. For each baseline, two real correlators are needed. The other two correlators are redundant. In order to do that, MIRAS uses one-bit two-levels digital correlators. Quantified and sampled signals from each output of the receiver, the in-phase (I) and quadrature (Q) channels are sent to a multiplier and an integrator, as it can be seen in Fig. 2.16.

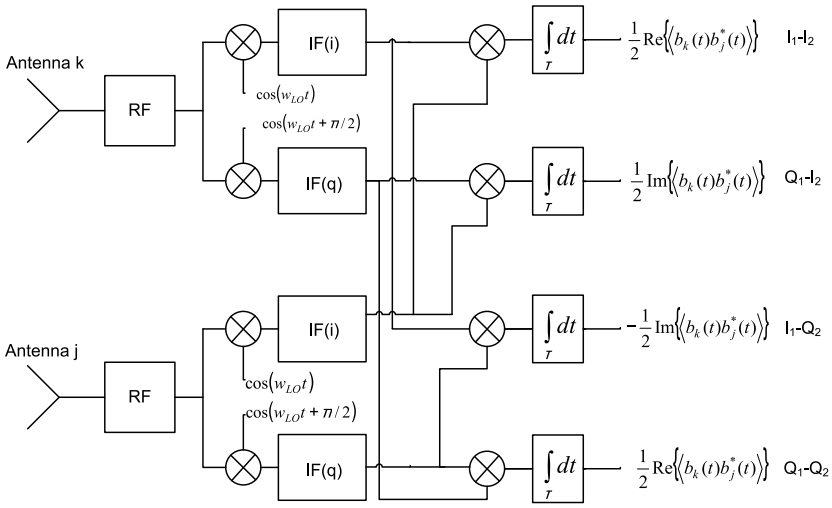

Figure 2.16: Block diagram of the complex correlator in a baseline. Only two of the four correlators are needed. The other two are redundant.

The multiplier output is equal to 1 when the two input bits are equal, acting as a XNOR gate. The integrator accumulates the number of ones every integration period. The conversion of the correlation counts to normalized complex correlations are throughly detailed in chapter 3. The digital signal produced by each LICEF is transmitted to the DIgital COrrelator System (DICOS). In this way, the 72 signals from I and Q channels are correlated with each other, providing 2556 complex correlations for each observation measurement. Besides, correlations with "all-zeroes" and "all-ones" signals are needed for self-calibration purposes [Martín-Neira *et al.*, 2004]. During internal calibration events, correlations at early and late delay lags are also computed. These correlations are needed to estimate the fringe washing function shape, which is used in the inversion procedure [Butora *et al.*, 2003, Duffo *et al.*, 2008].

Calibration Subsystem (CAS)

MIRAS calibration subsystem allows maintaining phase and amplitude calibration track along the receivers in the three arms [Torres *et al.*, 1996]. This subsystem is used to periodically inject two levels (hot and warm) of correlated noise to all the receivers. Correlated noise injection is performed during internal calibration events to calibrate the

PMS of each LICEF and also during LO phase track sequences in order to track the phase of the fringe washing function [Brown *et al.*, 2008].

In the hub, there is a one-to-eighteen network for distributing the noise generated by a single source (the nominal or the redundant one in case of failure) simultaneously to all receivers in the hub (see scheme in Fig. 2.17(a)). Each output of the NS-HUB is connected to a Power Divider (PD) placed in each segment of the hub, which distributes the noise to the receivers and the NIR units in that segment. NIR-LICEF units act as a reference radiometers in order to calibrate the PMS units in the hub (centralized calibration).

In the arms, there is a different noise source located at each segment. Each one drives a one-to-twelve network for distributing the noise to the receivers of that segment and the adjacent one, which are separated by the hinges (Fig. 2.17(b)). Hence, each individual LICEF is fed by 2 different NS, except those receivers in the third section of each arm. This technique allows injecting noise in overlapped sets of receivers to apply the distributed noise injection concept. Details on calibration concepts are addressed in chapter 3.

The NDN (Noise Distribution Network) has been throughly characterized on-ground in terms of the S-parameters, so as to correct amplitude and phase imbalance. S-parameters at unit level (NS units, PD units and cables) and noise level have been measured. In addition, the behavior of the CAS components over temperature has been characterized on-ground. Details on CAS characterization and performance can be found in [Lemmetyinen *et al.*, 2007]. In this way, the S-parameter of the complete path is obtained by cascading the four components: the NS (Fig. 2.18(a)), the cable between the NS and the PD, the PD (Fig. 2.18(b)) and the cable between the PD and the receiver. Depending on the physical temperature measured by the thermistors during calibration, the amplitude and phase of the S-parameters at that specific temperature are computed by means of a linear interpolation between the two closest temperatures. Physical temperatures of NS and PD units are available in telemetry data. However, since there are no thermistors on the cables, the physical temperature at calibration is obtained by averaging the temperatures of the two subsystems that each cable interconnect [CASA, 2007].

Control and Monitoring Node (CMN), local oscillators and thermal control

The Control and Monitoring Node (CMN) acts as a remote terminal of the CCU. In each segment, there is one CMN responsible for the control and monitoring of the signals. Its main functions are:

- Reception/transmission of commands from/to the CCU.
- Acquisition of PMS voltages and physical temperature readings.
- Control of LICEF switching and noise injection.
- Generation and distribution of the local oscillator signals.

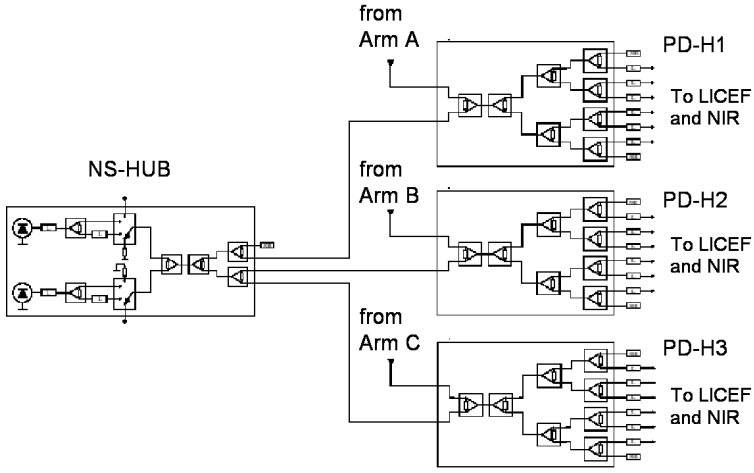

(a)

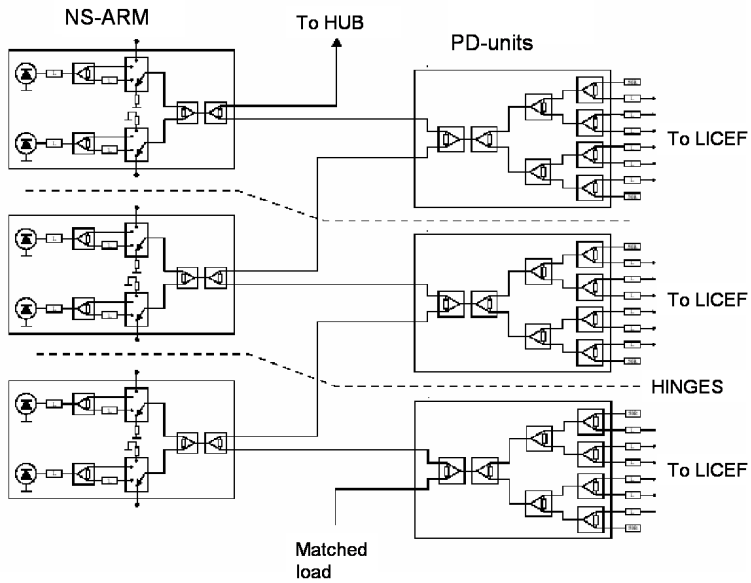

(b)

Figure 2.17: (a) Block diagram of CAS configuration in the hub. This section of the CAS is responsible for the centralized calibration. (b) Block diagram of CAS configuration in one of the arms. Sets of receivers are overlapped to allow phase and modulus calibration track along the array.

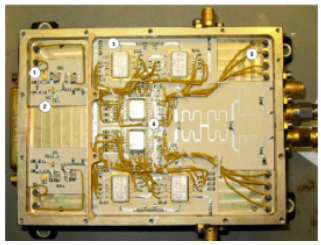

(a)

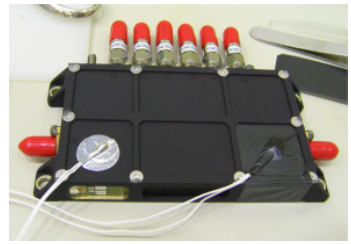

(b)

Figure 2.18: (a) The NS in the hub has 2 inputs, one for nominal and the other for redundant and 3 outputs, each one connected to the PD in each segment of the hub. Each NS in the arms has 2 inputs and 2 outputs to be connected to the PD in the same segment or to the PD in the adjacent one. (b) Each PD has 2 inputs: one for the NS in the same segment and the other one for the NS in the adjacent segment and 6 outputs, one per receiver.

- Distribution of active thermal control signals.

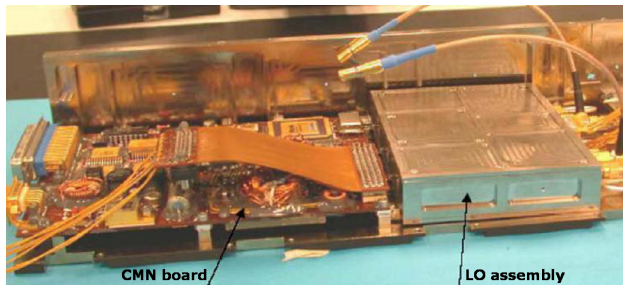

Figure 2.19: CMN and LO of a segment.

A local oscillator (LO) placed in each segment and therefore, common for the 6 receivers in the segment, synthesizes the frequency of 1396 MHz in order to shift the RF band to IF (see Fig. 2.19).

An active thermal control system is responsible for minimizing the temperature gradients between all the receivers. MIRAS has two heater systems, one nominal and other redundant. There are 12 heaters, one in each segment of the three arms and three more in the hub. Each heater is controlled by its associated CMN. Sensors distributed along the instrument acquire the physical temperatures that are sent to the CMNs to switch on/off the heaters, according to the control loop associated to that CMN. In this way, receivers are kept at a temperature around $22°C$. Correspondence between the numbering of the thermal control loops and the CMN that implements the actuation of the heater switch can be found in [Sanz & team, 2007].

Next chapter is devoted to describe all the calibration procedures needed to correct visibility samples from instrumental errors.

Chapter 3

Calibration of radiometric interferometers

Calibration of an Earth observation sensor is fundamental to obtain the scientific data products with the required accuracy. Characterization activities, mainly performed prior to the beginning of the in-orbit operation, are a requirement for the development of the calibration activities. MIRAS calibration procedures are reviewed in this chapter. MIRAS end-to-end calibration comprises all the procedures performed to obtain brightness temperature maps over the Earth's surface out of the raw data. However, this chapter is exclusively focused on giving an insight on the procedures applied to obtain the calibrated visibilities. MIRAS calibration current baseline and the main calibration products obtained from each calibration event have also been outlined. During the Commissioning Phase, timelines and frequencies of the calibration activities have been updated in order to improve the quality of the Level 1 data products during the Operational Phase.

3.1 Introduction

As it has been introduced in chapter 2, in an ideal case, an interferometric radiometer gives a multi-pixel image of brightness temperature after a Fourier Transform of the visibility samples. That is, the interferometric radiometer does not measure the brightness temperature distribution directly, as done by a real aperture radiometer, but a set of samples of its Fourier Transform. Therefore, a relative internal error correction of each single visibility must be performed before the image inversion. Besides, a common offset and gain factors can also be present in all the visibilities and hence, an external absolute calibration is also required.

The scope of this chapter is the description of the internal calibration procedures to obtain the calibrated visibility samples from MIRAS raw data. The calibrated visibility function is then inverted by the image reconstruction algorithm to get the brightness temperature as a function of the director cosines at the antenna reference plane. The main calibration procedures and methods, necessary to understand the algorithms developed within this Thesis have been compiled in the next sections. Detailed calibration procedures and further correction techniques can be found in [Corbella *et al.*, 2005] and [Torres *et al.*, 2006].

For a better understanding, a detailed block diagram of a baseline, which comprises the two receivers and the complex correlator, is shown in Fig. 3.1. In addition, the NDN (Noise Distribution Network), the reference radiometer, as well as the different planes where the calibration equations are defined, are detailed in the scheme. At this point, it is important to define the nomenclature followed to refer the calibration equations. For the system temperatures present at the system input, the first superscript indicates the switch position, while the second one refers to the reference plane. Normalized correlations and the Fringe Washing Function (FWF) term at the origin only have one subscript, indicating that these are measurements in the observation mode.

The visibility samples are corrected from instrumental errors and denormalized according to the following expression:

$$V_{kj} = \frac{\sqrt{T_{sys_k}^{AA} T_{sys_j}^{AA}}}{G_{kj}^{A}} M_{kj}^{A}, \tag{3.1}$$

where M_{kj}^{A} stands for the normalized complex correlations during observation measurements, computed from the correlator counts after the self-calibration procedure [Martín-Neira *et al.*, 2004]. The terms $T_{sys_k}^{AA}$ and $T_{sys_j}^{AA}$ correspond to the system temperature referred to the antenna plane of LICEF k and j, respectively. The term G_{kj}^{A} is the baseline complex gain also referred to the antenna plane.

The normalized complex correlations are measured by means of 1-bit digital correlators. The self-calibration procedure is applied in each measurement in order to remove the comparator offsets and quadrature errors. The Power Measurement System (PMS) available in each receiver provides a signal proportional to the input noise. The PMS must be either on-ground or in-orbit calibrated. The system temperatures in (3.1) are obtained from the PMS voltage readings, once the PMS offset (v_{off_k}) and gain (G_k^A) have been internally calibrated using the two-level four-points method [Torres *et al.*, 2003, Piironen, 2002]:

$$T_{sys_k}^{AA} = \frac{v_k^A - v_{off_k}}{G_k^A}. \tag{3.2}$$

The technique based on injecting two levels of correlated noise is also used to calibrate the baseline amplitude and phase,G_{kj}^{A}, the so-called fringe washing function term evaluated

at the origin. This term takes into account the spatial decorrelation effects due to the noise bandwidth of the receiver filters.

In addition to the outputs of the instrument (correlator counts, PMS voltages and NIR outputs), ancillary parameters are required to perform the instrument calibration. Some of them, such as LICEF switch and CAS S-parameters and the characterization of the NIR receivers, among others, have been measured by the manufacturers of the different subsystems. Others, such as the antenna inter-element phase, the correlation offsets and the sensitivity coefficients of the calibration parameters to the physical temperature have been retrieved from the instrument on-ground characterization campaigns (see chapter 4).

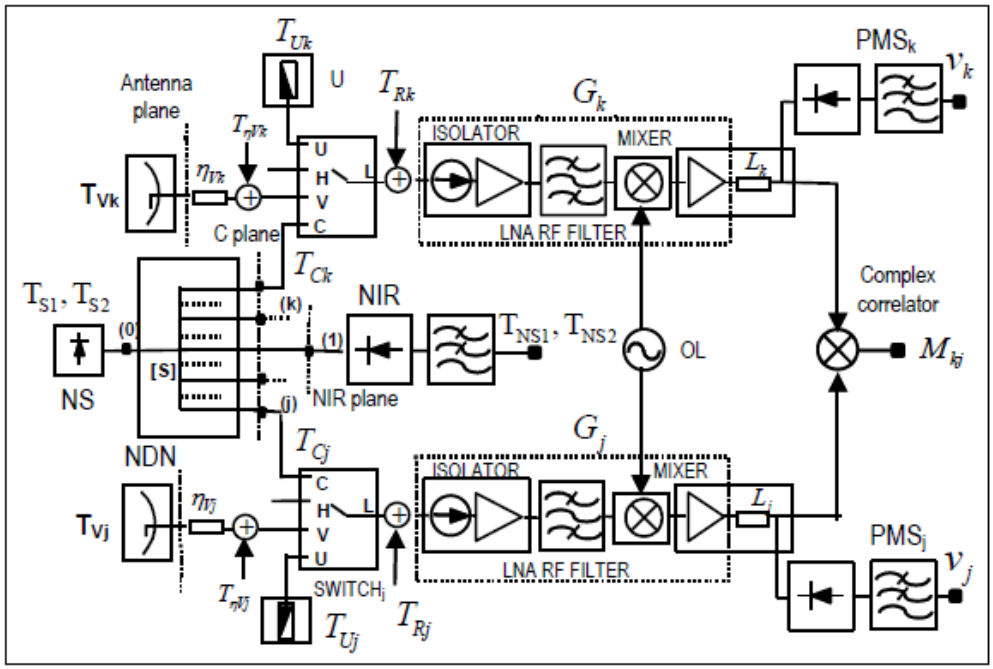

Figure 3.1: Block diagram of a single baseline, which comprises two LICEF units and a complex 1-bit correlator. The NDN, the reference radiometer and the planes where the calibration equations are defined are also indicated in the scheme.

3.2 Self-calibration

The procedure devoted to correct the comparator offsets and quadrature errors is detailed in this section. These corrections are applied to each measurement, both in calibration and observation modes.

The output of each individual cell in the DICOS (DIgital COrrelation System) is 1 when the two inputs are identical. The correlation is measured accumulating the output

during the 1.2 seconds of the integration time. At the end of this time, counts are read and the accumulator is reset. Hence, counts provided by DICOS are the number of coincidences of the corresponding two digital signals during the integration time. Digital counts (N_c) provided for each pair of receiver outputs are converted to digital correlations (Z_{kj}) using the following relation

$$Z_{kj} = 2\frac{N_c}{N_{c_{MAX}}} - 1, \tag{3.3}$$

where N_c is the number of counts, $N_{c_{MAX}}$ stands for the maximum number of counts in the integration period and digital correlation (Z_{kj}) is a real number ranging from -1 to +1. Computation of the normalized correlation of the real signals from the digital correlations requires to solve the following non-linear equation by means of an iterative process [Martín-Neira *et al.*, 2004]

$$Z_{kj} = \frac{2}{\pi}\arcsin\mu_{kj} - \frac{2}{\sqrt{1-\mu_{kj}^2}}\left(\mu_{kj}X_{01}^2 + \mu_{kj}Y_{01}^2 - 2X_{01}Y_{01}\right), \tag{3.4}$$

where the first guess is $\mu_{kj} = \sin\left(\frac{\pi}{2}Z_{kj}\right)$, which is only applicable for zero-offset comparators. The terms X_{01} and Y_{01} are parameters computed from the measured digital correlations of each signal with the fixed channel "1" (Z_1) and "0" (Z_0), respectively:

$$X_{01} = \frac{1}{4}\left(Z_0 - Z_1\right), \tag{3.5}$$

where X_{01} is related to receiver k and Y_{01} is related to receiver j. Normalized correlations (μ_{kj}) are also a real number ranging from -1 to +1.

The interferometric approach is based on the cross-correlation of the signals $b_k(t)$, $b_j(t)$ collected by each pair of receivers, as it has been mentioned in chapter 2. For a given baseline, different normalized real correlations can be found from the correlation counts

$$\mu_{kj}^{\alpha\beta} = \frac{\Re e\left[\left\langle b_k^{\alpha}(t)b_j^{\beta}(t)^*\right\rangle e^{j\Delta\phi_{LO}}\right]}{\sqrt{\left\langle\left|b_k^{\alpha}(t)\right|^2\right\rangle\left\langle\left|b_j^{\beta}(t)\right|^2\right\rangle}}, \tag{3.6}$$

where α and β denote the in-phase and/or quadrature channel of receivers k, j. The exponential term $\Delta\phi_{LO}$ varies depending on the combination of channels i, q:

$$\Delta\phi_{LO} = \begin{cases} 0 & \text{if } \alpha\beta = ii, qq \\ -\frac{\pi}{2} & \text{if } \alpha\beta = qi \\ \frac{\pi}{2} & \text{if } \alpha\beta = iq \end{cases}$$

Using the results obtained in [Corbella *et al.*, 2004], measuring the signal from the

antenna, equation (3.6) yields

$$\mu_{kj}^{\alpha\beta} = \frac{\Re e\left[e^{j\Delta\phi_{LO}}\tilde{r}_{kj}^{\alpha\beta}(0)V_{kj}\right]}{\sqrt{T_{sys_k}^{AA}T_{sys_j}^{AA}}}, \tag{3.7}$$

where $\tilde{r}_{kj}^{\alpha\beta}(0)$ indicates the fringe washing function at the origin which carries the information of the in-phase and quadrature errors and the non-separable amplitude and phase errors. Terms of system temperatures $T_{sys_k}^{AA}$ and $T_{sys_j}^{AA}$ are measured by the PMS of the receivers k and j, respectively.

The nominal and redundant normalized complex correlations are computed from normalized real correlations, respectively, as

$$\begin{aligned} \mu_{kj}^{N} &= \mu_{kj}^{ii} + j\mu_{kj}^{qi} \\ \mu_{kj}^{R} &= \mu_{kj}^{qq} - j\mu_{kj}^{iq}. \end{aligned} \tag{3.8}$$

Substituting the real normalized correlations in (3.8), for their expressions (3.7)

$$\mu_{kj}^{N} = \frac{1}{\sqrt{T_{sys_k}^{AA}T_{sys_j}^{AA}}}\left(\Re e\left[\tilde{r}_{kj}^{ii}(0)V_{kj}\right] + j\Im m\left[\tilde{r}_{kj}^{qi}(0)V_{kj}\right]\right) \tag{3.9}$$

$$\mu_{kj}^{R} = \frac{1}{\sqrt{T_{sys_k}^{AA}T_{sys_j}^{AA}}}\left(\Re e\left[\tilde{r}_{kj}^{qq}(0)V_{kj}\right] + j\Im m\left[\tilde{r}_{kj}^{iq}(0)V_{kj}\right]\right)$$

For a given baseline (k, j), the fringe washing function terms of the ii and qi signals in (3.9) can be written approximately as

$$\begin{aligned} \tilde{r}_{kj}^{ii}(0) &= |G_{kj}|e^{-j(\alpha_{kj}+Q_{kj})} \\ \tilde{r}_{kj}^{qi}(0) &= |G_{kj}|e^{-j\left(\alpha_{kj}+Q'_{kj}\right)}, \end{aligned} \tag{3.10}$$

where $|G_{kj}|$ is the modulus of the fringe washing function at the origin and α_{kj} includes the in-phase and non-separable phase errors. The terms Q_{kj} and Q'_{kj} depend on the quadrature error $(\theta_{qk}, \theta_{qj})$ of the receivers, which is estimated from the normalized correlation between the in-phase and quadrature channels of the receiver

$$Q_{kj} = \frac{\theta_{qj} - \theta_{qk}}{2}; \quad Q'_{kj} = \frac{\theta_{qj} + \theta_{qk}}{2}$$

Defining M_1 and M_2 as parameters only dependent on the quadrature error

$$M_1 = \cos(Q'_{kj}) + j\sin(Q_{kj}); \quad M_2 = \cos(Q_{kj}) + j\sin(Q'_{kj}), \tag{3.11}$$

and substituting in equation (3.9), the expression for the quadrature-corrected normalized

complex nominal and redundant correlations yields, respectively

$$\begin{aligned} M_{kj}^{N} &= \frac{1}{\cos\theta_{qj}}\left(\Re e\left[M_1\mu_{kj}^{N}\right] + j\Im m\left[M_2\mu_{kj}^{N}\right]\right) \\ M_{kj}^{R} &= \frac{1}{\cos\theta_{qj}}\left(\Re e\left[M_1^{*}\mu_{kj}^{R}\right] + j\Im m\left[M_2^{*}\mu_{kj}^{R}\right]\right), \end{aligned} \tag{3.12}$$

where subscript A has been omitted for simplicity. Equation (3.12) has been derived for the correlations measured in the observation mode. The same equation is used when correlated noise (HOT and WARM) is injected, measuring the correlation temperature, indicated as M_{kj}^{C2}, M_{kj}^{C1} (see 3.3.3).

3.3 Amplitude and phase calibration by correlated noise injection

Now, system temperatures ($T_{sys_k}^{AA}$) and the fringe washing function term at the origin (G_{kj}^{A}), also known as baseline complex gain, need to be measured in order to get the calibrated visibilities in (3.1). Amplitude and phase calibration procedures by correlated noise injection are presented in this section.

Amplitude calibration comprises the estimation of two terms: the system temperatures at the receivers input referred to the antenna plane and the baseline complex gain amplitude referred to the same plane. The computation of the system temperatures requires the PMS internal calibration of each receiver.

The phase of the baseline complex gain is also measured by means of correlated noise injection at two levels. In addition, the inter-element amplitude and phase, which can not be measured by correlated noise injection, have been computed during the on-ground characterization tests [Corbella *et al.*, 2008b].

3.3.1 PMS internal calibration

The PMS voltage output v_k of LICEF k, when an equivalent temperature T_{sys_k} is present at system input (see Fig. 3.1), considering a linear model of the PMS, is given by

$$v_k = v_{off_k} + G_k T_{sys_k}, \tag{3.13}$$

where $T_{sys_k} = T_{ext} + T_{R_k}$ includes the receiver equivalent noise temperature T_{R_k} and T_{ext} is the equivalent external temperature. PMS gain and offset are denoted by G_k and v_{off_k}, respectively.

The system temperatures at the calibration plane when correlated noise is injected at two different temperatures, HOT and WARM, are referred as $T_{sys_k}^{C_2C}$ and $T_{sys_k}^{C_1C}$, respectively. The computation of the system temperatures requires the PMS calibration of each

receiver to estimate the gain and offset. The calibration technique, also known as the two-level four-points method [Torres *et al.*, 2004, 2006], makes use of two known external temperatures and injects the noise through the NDN. T_{C1} is the so-called WARM temperature and T_{C2} is the HOT temperature ($T_{C1} < T_{C2}$). In addition, the overall system gain can be switched between two values, G_k and G_k/L_k, through an attenuator located in the signal path at a point that it does not affect T_{R_k} [Piironen, 2002].

The four PMS voltage measurements are given by

$$\begin{aligned} v_{1k} &= v_{off_k} + G_k^C T_{sys_k}^{C_1C}; \quad v_{2k} = v_{off_k} + G_k^C T_{sys_k}^{C_2C} \\ v_{3k} &= v_{off_k} + \frac{G_k^C}{L_k} T_{sys_k}^{C_1C}; \quad v_{4k} = v_{off_k} + \frac{G_k^C}{L_k} T_{sys_k}^{C_2C}, \end{aligned} \tag{3.14}$$

where the overall system gains (both G_k^C and G_k^C/L_k) are referred to the calibration plane (indicated by superscript C).

Therefore, PMS offset and gain can be readily computed from (3.14) as

$$v_{off_k} = \frac{v_{2k}v_{3k} - v_{1k}v_{4k}}{(v_{2k} - v_{4k}) - (v_{1k} - v_{3k})} \tag{3.15}$$

$$G_k^C = \frac{v_{2k} - v_{1k}}{T_{sys_k}^{C_2C} - T_{sys_k}^{C_1C}}. \tag{3.16}$$

Terms $T_{sys_k}^{C_2C}$ and $T_{sys_k}^{C_1C}$ correspond to the system temperatures HOT and WARM, respectively, at the calibration plane.

The main advantage of this relative calibration approach is that the PMS gain is computed using the difference between both system temperatures, canceling out the noise contribution of the receiver and the NDN contribution itself

$$T_{sys_k}^{C_2C} = T_{C2k} + T_{R_k}; \quad T_{sys_k}^{C_1C} = T_{C1k} + T_{R_k}. \tag{3.17}$$

From now on, the simplified scheme given in Fig. 3.2 will be used to illustrate the relative calibration approach.

The equivalent external temperatures at the calibration plane of LICEF k denoted by T_{C2k}, T_{C1k}, can be written as

$$\begin{aligned} T_{C2k} &= |S_{k0}|^2 T_{S2} + \Delta T\left(S_{k0}, T_{phk}\right) \\ T_{C1k} &= |S_{k0}|^2 T_{S1} + \Delta T\left(S_{k0}, T_{phk}\right), \end{aligned} \tag{3.18}$$

where S_{k0} corresponds to the S-parameter from the noise source to the k port of the NDN and T_{phk} is the physical temperature at k port of the NDN. The term $\Delta T\left(S_{k0}, T_{phk}\right)$ takes into account the noise contribution of the NDN itself. Similar equations to (3.18) can be derived for LICEF j.

Since the NIR is also measuring the external noise temperatures, PMS gain can be

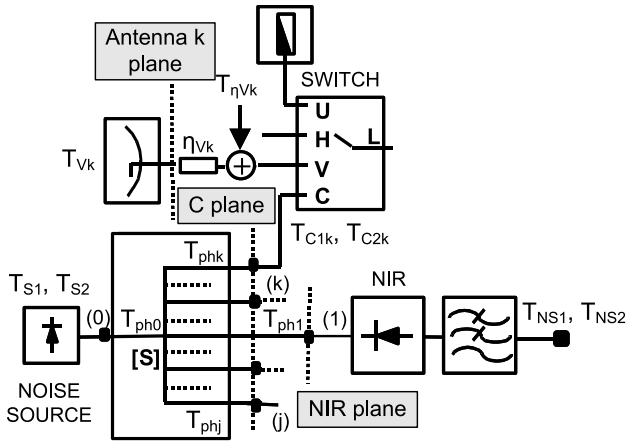

Figure 3.2: Schematic block diagram of a receiver to illustrate the relative calibration approach [Torres *et al.*, 2004].

computed relative to the difference of both temperatures measured by the reference radiometer

$$\begin{aligned} T_{NS2} &= |S_{10}|^2 T_{S2} + \Delta T'\left(S_{10}, T_{ph1}\right) \\ T_{NS1} &= |S_{10}|^2 T_{S1} + \Delta T'\left(S_{10}, T_{ph1}\right), \end{aligned} \tag{3.19}$$

where S_{10} stands for the S-parameter from the noise source to the NIR port of the NDN and T_{ph1} is the physical temperature at NIR port. The term $\Delta T'\left(S_{10}, T_{ph1}\right)$ considers the contribution of the NDN itself.

Therefore, expressions for HOT and WARM noise temperatures at the calibration port (T_{C2k} and T_{C1k}, respectively) as a function of the NIR measurements (T_{NS2} and T_{NS1}) are

$$\begin{aligned} T_{C2k} &= |S_{k0}|^2 \cdot \frac{T_{NS2} - \Delta T'\left(S_{10}, T_{ph1}\right)}{|S_{10}|^2} + \Delta T\left(S_{k0}, T_{phk}\right) \\ T_{C1k} &= |S_{k0}|^2 \cdot \frac{T_{NS1} - \Delta T'\left(S_{10}, T_{ph1}\right)}{|S_{10}|^2} + \Delta T\left(S_{k0}, T_{phk}\right), \end{aligned} \tag{3.20}$$

being the difference $T_{C2k} - T_{C1k}$ independent of the noise contribution from the receiver and the NDN itself. Substituting expressions (3.17) and (3.20) in (3.16), PMS gain as a function of the NIR measurements is given by:

$$G_k^C = \frac{v_{2k} - v_{1k}}{T_{NS2} - T_{NS1}} \frac{|S_{10}|^2}{|S_{k0}|^2}. \tag{3.21}$$

Finally, any system temperatures at the calibration plane when correlated noise is injected

can be computed using

$$T_{sys_k}^{CC} = \frac{v_k - v_{off_k}}{v_{2k} - v_{1k}} \frac{|S_{k0}|^2}{|S_{10}|^2} \left(T_{NS2} - T_{NS1}\right). \tag{3.22}$$

Once the system temperatures have been estimated using a linear model of the PMS, a second order correction is applied to the PMS voltages and PMS gain and offset are recalculated [González-Haro *et al.*, 2009].

The system temperatures needed to denormalized the visibility samples in (3.1) are referred to the antenna plane. In order to obtain them, first, system temperatures in measurement mode at calibration plane are computed as

$$T_{sys_k}^{AC} = \frac{v_k^A - v_{off_{k1}}}{G_{k_1}^C} \tag{3.23}$$

where superscript A indicates measurement by the antenna port (H or V polarization). Subscript 1 in $v_{off_{k1}}$ and $G_{k_1}^C$ terms, indicates that both PMS gain and offset have been corrected in temperature from the calibration time to the measurement instant. The temperature correction applied to the calibration parameters is detailed in section 3.5.

Finally, system temperatures in measurement mode are referred to the antenna plane by means of a plane translation

$$T_{sys_k}^{AA} = T_{sys_k}^{AC} \cdot \frac{|S_{LCk}|^2}{|S_{LAk}|^2 \cdot \eta_{Ak}}, \tag{3.24}$$

where S_{LCk} and S_{LAk} are the LICEF switch S-parameters relating C and H/V ports, respectively, with port L in receiver k (see Fig. 3.2), and η_{Ak} takes into account the antenna ohmic efficiency in H/V modes.

This approach provides a relative calibration, since all measurements are referenced to the NIR measurement of the CAS noise injection temperatures. Internal calibration can not provide absolute accuracy. Hence, external calibration events are needed to calibrate the reference for the internal calibrations (NIR absolute calibration during deep sky views) [Colliander *et al.*, 2007a, Brown *et al.*, 2008].

The receiver noise temperature, $T_{R_k}^C$, can be computed, for monitoring purposes, using the PMS gain at the calibration plane obtained in (3.21) and the U-noise measurement:

$$T_{R_k}^C = \frac{v_k^U - v_{off_k}}{G_k^C} - T_{phU_k}, \tag{3.25}$$

where v_k^U is the PMS voltage measurement and T_{phU_k} is the receiver physical temperature while U-noise is injected.

3.3.2 Baseline phase and amplitude calibration

The estimation of the baseline complex gain is also needed in the visibilities denormalization (3.1). The FWF term at the origin can be estimated at the calibration plane (G_{kj}^{C}) by means of the two-level noise injection technique for all receivers sharing a noise source (columns in Table 3.1). The convention used in the numbering of the receivers is listed in Table 3.2. Figure 3.3 shows the location of the receivers. This is the nomenclature which has been used in the results presented in this work. For the rest of the baselines, the computation of this term is performed using the distributed approach, as detailed in section 3.3.3.

Table 3.1: Distributed noise injection. NS and the corresponding LICEF units.

HUB	ARM A			ARM B			ARM C		
NS-HUB	NS-A1	**NS-A2**	NS-A3	NS-B1	**NS-B2**	NS-B3	NS-C1	**NS-C2**	NS-C3
LCF-AB-03	LCF-AB-03	LCF-A-04	LCF-A-10	LCF-BC-03	LCF-B-04	LCF-B-10	LCF-CA-03	LCF-C-04	LCF-C-10
NIR-AB-01-H	NIR-AB-01-H	LCF-A-05	LCF-A-11	NIR-BC-01-H	LCF-B-05	LCF-B-11	NIR-CA-01-H	LCF-C-05	LCF-C-11
NIR-AB-01-V	NIR-AB-01-V	LCF-A-06	LCF-A-12	NIR-BC-01-V	LCF-B-06	LCF-B-12	NIR-CA-01-V	LCF-C-06	LCF-C-12
LCF-A-01	LCF-A-01	LCF-A-07	LCF-A-13	LCF-B-01	LCF-B-07	LCF-B-13	LCF-C-01	LCF-C-07	LCF-C-13
LCF-A-02	LCF-A-02	LCF-A-08	LCF-A-14	LCF-B-02	LCF-B-08	LCF-B-14	LCF-C-02	LCF-C-08	LCF-C-14
LCF-A-03	LCF-A-03	LCF-A-09	LCF-A-15	LCF-B-03	LCF-B-09	LCF-B-15	LCF-C-03	LCF-C-09	LCF-C-15
LCF-BC-03	LCF-A-04	LCF-A-10	LCF-A-16	LCF-B-04	LCF-B-10	LCF-B-16	LCF-C-04	LCF-C-10	LCF-C-16
NIR-BC-01-H	LCF-A-05	LCF-A-11	LCF-A-17	LCF-B-05	LCF-B-11	LCF-B-17	LCF-C-05	LCF-C-11	LCF-C-17
NIR-BC-01-V	LCF-A-06	LCF-A-12	LCF-A-18	LCF-B-06	LCF-B-12	LCF-B-18	LCF-C-06	LCF-C-12	LCF-C-18
LCF-B-01	LCF-A-07	LCF-A-13	LCF-A-19	LCF-B-07	LCF-B-13	LCF-B-19	LCF-C-07	LCF-C-13	LCF-C-19
LCF-B-02	LCF-A-08	LCF-A-14	LCF-A-20	LCF-B-08	LCF-B-14	LCF-B-20	LCF-C-08	LCF-C-14	LCF-C-20
LCF-B-03	LCF-A-09	LCF-A-15	LCF-A-21	LCF-B-09	LCF-B-15	LCF-B-21	LCF-C-09	LCF-C-15	LCF-C-21
LCF-CA-03									
NIR-CA-01-H									
NIR-CA-01-V									
LCF-C-01									
LCF-C-02									
LCF-C-03									

Table 3.2: NS and the numbering assigned to the corresponding LICEF units.

HUB	ARM A			ARM B			ARM C		
NS-HUB	NS-A1	**NS-A2**	NS-A3	NS-B1	**NS-B2**	NS-B3	NS-C1	**NS-C2**	NS-C3
1	1	7	13	25	31	37	49	55	61
2	2	8	14	26	32	38	50	56	62
3	3	9	15	27	33	39	51	57	63
4	4	10	16	28	34	40	52	58	64
5	5	11	17	29	35	41	53	59	65
6	6	12	18	30	36	42	54	60	66
25	7	13	19	31	37	43	55	61	67
26	8	14	20	32	38	44	56	62	68
27	9	15	21	33	39	45	57	63	69
28	10	16	22	34	40	46	58	64	70
29	11	17	23	35	41	47	59	65	71
30	12	18	24	36	42	48	60	66	72
49									
50									
51									
52									
53									
54									

The normalized correlation when HOT (T_{S2}) and WARM (T_{S1}) noise temperatures

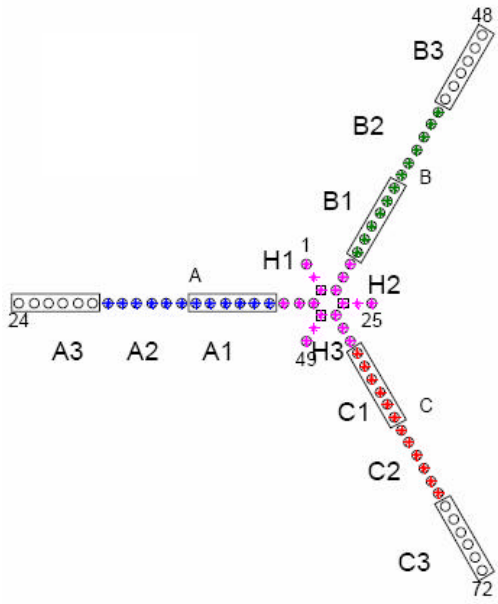

Figure 3.3: Convention used in the numbering of MIRAS receivers.

are injected through the NDN can be written as [Corbella *et al.*, 2000a]

$$M_{kj}^{C_2} = \frac{S_{k0} S_{j0}^* \left(T_{S2} - T_{ph}\right)}{\sqrt{T_{sys_k}^{C_2C} T_{sys_j}^{C_2C}}} \cdot G_{kj}^C$$
$$M_{kj}^{C_1} = \frac{S_{k0} S_{j0}^* \left(T_{S1} - T_{ph}\right)}{\sqrt{T_{sys_k}^{C_1C} T_{sys_j}^{C_1C}}} \cdot G_{kj}^C, \tag{3.26}$$

where T_{ph} is the physical temperature of the NDN.

The differential measurement removes the NDN contribution, therefore, the FWF term yields

$$G_{kj}^C = \frac{\sqrt{T_{sys_k}^{C_2C} T_{sys_j}^{C_2C}} M_{kj}^{C_2} - \sqrt{T_{sys_k}^{C_1C} T_{sys_j}^{C_1C}} M_{kj}^{C_1}}{S_{k0} S_{j0}^* \left(T_{S2} - T_{S1}\right)}. \tag{3.27}$$

System temperatures measured by the PMS while injecting HOT and WARM correlated noise at the calibration plane can be derived from equation (3.22)

$$T_{sys_k}^{C_2C} = \frac{v_{2k} - v_{off_k}}{v_{2k} - v_{1k}} \frac{|S_{k0}|^2}{|S_{10}|^2} \left(T_{NS2} - T_{NS1}\right)$$
$$T_{sys_k}^{C_1C} = \frac{v_{1k} - v_{off_k}}{v_{2k} - v_{1k}} \frac{|S_{k0}|^2}{|S_{10}|^2} \left(T_{NS2} - T_{NS1}\right), \tag{3.28}$$

and the difference between the external noise temperatures measured by the NIR

(3.19) is

$$T_{NS2} - T_{NS1} = |S_{10}|^2 \left(T_{S2} - T_{S1}\right). \tag{3.29}$$

Substituting (3.28) and (3.29) in (3.27), the expression of the baseline complex gain at the calibration plane yields

$$G_{kj}^{C} = \frac{M_{kj}^{C_2}\sqrt{\left(v_{2k} - v_{off_k}\right)\left(v_{2j} - v_{offj}\right)} - M_{kj}^{C_1}\sqrt{\left(v_{1k} - v_{off_k}\right)\left(v_{1j} - v_{offj}\right)}}{\sqrt{\left(v_{2k} - v_{1k}\right)\left(v_{2j} - v_{1j}\right)}} \frac{|S_{k0}||S_{j0}|}{S_{k0}S_{j0}^{*}}, \tag{3.30}$$

where the baseline phase and amplitude term G_{kj}^{C} depends only on the quadrature-corrected correlations at both levels of noise injection, PMS voltages and the relative phases of the NDN S-parameters (NDN phase imbalance).

Since the G_{kj}^{A} term in equation (3.1) is referred to the antenna plane, a plane translation is applied

$$G_{kj}^{A} = G_{kj}^{C} \cdot \frac{\overline{S}_{LAk}\overline{S}_{LAj}^{*}}{\overline{S}_{LCk}\overline{S}_{LCj}^{*}} \cdot e^{j(\phi_{Ak} - \phi_{Aj})}, \tag{3.31}$$

where S_{LCk} and S_{LAk} are the S-parameters of the switch from the calibration and antenna ports to the output and the overline means normalized to unit amplitude, that is $\overline{S} = S/|S|$. The terms ϕ_{Ak} and ϕ_{Aj} are the inter-element phases retrieved during on-ground measurements [Corbella *et al.*, 2008b].

3.3.3 Distributed noise injection

In large instruments, as MIRAS, the requirements on mass, volume and phase equalization of the NDN for an accurate characterization are difficult to accomplish. For this reason, a distributed noise injection approach is used [Torres *et al.*, 1996]. In the hub, there is a one-to-eighteen network to distribute the noise generated by the single noise source simultaneously to all receivers in the hub. NIR-LICEFs act as reference radiometers in order to calibrate the PMS units in the hub, so that the procedure described in the previous sections can be applied (centralized calibration). In the arms, there is a noise source located at each segment driving a one-to-twelve network to distribute the noise to the receivers in the same segment and in the adjacent one. This approach allows injecting two correlated noise levels in overlapped sets of receivers in order to keep track of a common reference phase.

A set of switches allows injecting noise in overlapping sets of receivers to apply the distributed noise injection concept. Noise is injected to the receivers in two steps (see Tables 3.1): first using the so-called even sources (NS-HUB, NS-A2, NS-B2, NS-C2), highlighted in bold in the table, and then with the odd ones (NS-A1, NS-A3, NS-B1, NS-B3, NS-C1, NS-C3). First of all, receivers in the hub are calibrated injecting correlated noise through the even NS-HUB and using the NIRs as reference. After that, receivers in the second section are calibrated using the odd noise sources in the first section of each

arm, selecting as reference those receivers which have been previously calibrated with NS-HUB. This process is repeated for the second (even NS) and third (odd NS) sections of the arms.

After the distributed noise injection, PMS gain and offset values are available for all receivers. Baseline complex gain is only measured for baselines sharing a noise source, both baselines formed by receivers in the same segment or baselines across segments (Table 3.1). Baseline complex gain for all baselines measured can be approximated by the product of two separable terms

$$G_{kj}^{C} \approx g_k e^{j\alpha_k} g_j e^{-j\alpha_j}, \tag{3.32}$$

where g_k, g_j correspond to the amplitude term of each receiver and α_k, α_j to the individual phases.

Therefore, the following expressions for the amplitude and phase can be written, respectively

$$\begin{aligned} \log\left(|G_{kj}^{C}|\right) &= \log g_k + \log g_j \\ arg\left(G_{kj}^{C}\right) &= \alpha_k - \alpha_j. \end{aligned} \tag{3.33}$$

Individual terms of amplitude and phase for all receivers can be retrieved by applying matrix pseudo-inverse to the system of equations in (3.33). In this way, the complex gain for the non-measured baselines (those which do not share a noise source) is computed using the separable amplitude and phase of receivers forming the baseline (3.32).

3.4 Residual offset correction

An undesired signal injected simultaneously to both receivers of a baseline produce a non-zero value of correlation. This is the case of the thermal noise from the local oscillator signal. Therefore, this mainly affects the receivers of the same section, since these receivers have a common local oscillator.

Residual offset of the visibilities must be reduced to the level of the required accuracy, well below the thermal noise. In order to measure and correct this residual offset from the calibrated visibilities, uncorrelated noise is periodically injected to all receivers during the long calibration events [Brown *et al.*, 2008].

This correction can be considered as having an equivalent non-zero visibility at the antenna reference plane. Visibility during the observation mode (switch to antenna) includes the visibility due to the external sources and the residual visibility offset. When the switch is commuted to the matched load, only this residual term is measured. Therefore, the final formulas to obtain the corrected visibilities are now reduced to subtract the visibility offset measured by injecting uncorrelated noise

$$V_{kj}^{A}(external) = V_{kj}^{AA} - V_{kj}^{AU}, \tag{3.34}$$

being V_{kj}^{AA} the denormalized visibility during the antenna measurement and V_{kj}^{AU} the residual visibility offset.

3.5 Temperature correction

Temperature variations of the receivers imply drifts in the PMS calibration parameters, mainly in the PMS gain and the receiver noise temperature. In consequence, MIRAS instrument is specially affected by the in-orbit physical temperature drifts. The instrument has an active thermal control subsystem (heaters) which is prepared to keep the instrument close to a nominal operation temperature of 22°C [McMullan *et al.*, 2008]. However, small temperature drifts (around 2°C peak-to-peak along the orbit) are foreseen during the in-orbit operation. For that reason, the instrument requires in-orbit temperature drift correction.

MIRAS calibration current baseline foresees internal calibration performed periodically at specific orbit locations and applying temperature drift correction between calibration events. Sensitivity coefficients of the calibration parameters to the physical temperature drifts have been computed during the on-ground thermal characterization [Corbella *et al.*, 2009b] and updated during the in-orbit operation [Corbella *et al.*, 2011]. Calibration parameters can be estimated at any measurement time using the sensitivity coefficients, as proposed in [Torres *et al.*, 2006]. Hence, values of the PMS gain and offset at the measurement point are corrected in temperature from the closest calibration using the following expressions:

$$G_k^C\left(T_{obs}\right) = G_k^C\left(T_{cal}\right)\left(1 + \frac{S_{T_{ph}}^{G_k^C}}{100}\left(T_{obs} - T_{cal}\right)\right) \tag{3.35}$$

$$v_{off_k}\left(T_{obs}\right) = v_{off_k}\left(T_{cal}\right) + S_{T_{ph}}^{v_{off_k}}\left(T_{obs} - T_{cal}\right), \tag{3.36}$$

where $S_{T_{ph}}^{G_k^C}$ and $S_{T_{ph}}^{v_{off_k}}$ are the sensitivity coefficients for the PMS gain and offset of receiver k, respectively, T_{cal} is the physical temperature at the calibration time and T_{obs} is the physical temperature at the measurement time. Note that $S_{T_{ph}}^{G_k^C}$ units are $[\%/^{o}C]$.

Sequences and timelines for MIRAS in-orbit calibration have been devised depending on the calibration parameters to be retrieved. The frequency of the different calibration events is related to their dependence on the in-orbit temperature drifts. It has been consolidated after analyzing several orbits in calibration mode during the SMOS Commissioning Phase.

3.6 In-orbit calibration plan

The detailed steps of each calibration sequence can be found in [Brown *et al.*, 2008] and are not presented in this work. However, the main calibration products that can be obtained from each calibration event are detailed as part of the payload characterization procedure. All the in-orbit calibration activities and the corresponding retrieved parameters are summarized in Table 3.3.

In order to maximize the observation time, the total time dedicated to calibration activities, both internal and external, is restricted to 1 % of the mission time [SMOS, 2003b]. Related to the stability of the calibration parameters, different calibration timelines had been defined. These calibration sequences have been modified and optimized in terms of duration along the on-ground characterization and Commissioning Phase measurements.

Regarding the internal calibration, three calibration sequences have been defined, namely, short, long and LO phase tracking sequences. From short calibration events, the PMS calibration parameters and the FWF term evaluated at the origin can be retrieved. From long calibration sequences, in addition to the same parameters as in short calibration, the visibility offsets and the FWF shape (needed in the image inversion procedure) [Butora *et al.*, 2003, Duffo *et al.*, 2008] are obtained. Fluctuations found in the PMS offset during the in-orbit operation have led to perform a short calibration every week while the frequency of the long calibration sequences is 2 months due to the stability of the parameters retrieved from them [Corbella *et al.*, 2011]. The last internal calibration sequence is the LO Phase tracking. During the thermal characterization of the instrument, the correlation phases showed a significant dependence on the LO temperature drifts (see section 3.4.7) [Martín-Neira, 2007]. This feature has led to define a calibration sequence in order to track the phase drift due to temperature variations. At present, LO calibration frequency is set to 10 minutes. However, the possibility of increasing the LO calibration frequency in order to improve the SSS retrieval is being further investigated [Gabarró *et al.*, 2011].

During the external calibration events, the instrument is pointing to the cold sky in order to calibrate the reference radiometers. Besides, the Flat Target Response [Martín-Neira *et al.*, 2008b] is obtained and the CAS is validated/updated by means of the one-point calibration (see chapter 5).

The nominal baseline for MIRAS in-orbit calibration has been thoroughly detailed in [Brown *et al.*, 2008, Corbella *et al.*, 2007]. However, during Commissioning Phase activities, dedicated tests have been performed to evaluate all the system performance and in consequence calibration events and their frequencies have been modified and/or validated. The calibration strategy to be performed during MIRAS/SMOS operational phase is detailed in Fig. 3.4.

Table 3.3: MIRAS/SMOS in-orbit calibration sequences, from [Brown *et al.*, 2008].

Event	Type	Calibration parameters
Self-calibration	Internal	Quadrature error Sampling correction
Short calibration	Internal	PMS calibration (gain and offset) FWF at the origin LICEF noise temperature
Long calibration	Internal	same parameters as in short cal. FWF shape Visibility offsets
LO Phase tracking	Internal	LO Phase tracking with temperature drifts
Deep sky views	External	NIR absolute calibration Flat Target Response CAS validation/update (one-point calibration)

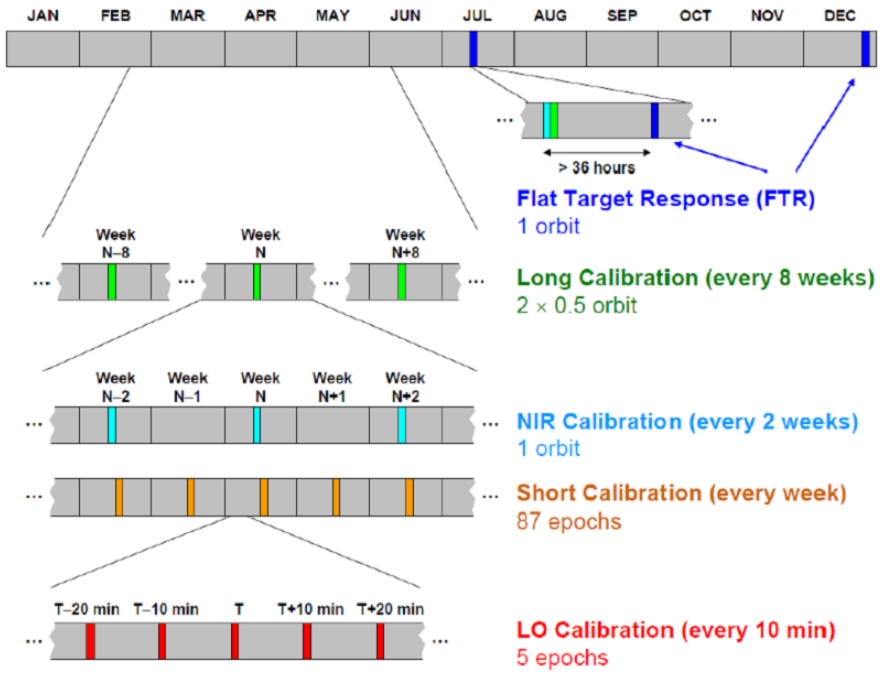

Figure 3.4: MIRAS in-orbit calibration strategy during SMOS operational phase, from [Martín-Neira *et al.*, 2011].

Chapter 4

MIRAS system performance and calibration tools

The main purpose of the MIRAS on-ground characterization was to show that the instrument could be calibrated as predicted and to produce brightness-temperature images with the required accuracy. The instrument has been successfully and extensively characterized on ground in terms of temperature drifts, image validation and RFI (Radio Frequency Interference). The system performance tests have revealed the need to develop several calibration tools to fine-tuning the instrument in order to fully comply with the mission requirements [SMOS, 2003b]. The tools and algorithms developed during this Thesis have played an important role in the MIRAS system performance calibration assessment. Main issues addressed in this chapter are related to the assessment of the amplitude and phase calibration consistency as well as the RFI and EMC (ElectroMagnetic Compatibility).

4.1 MIRAS on-ground characterization

Complex calibration procedures have been devised and implemented in order to achieve the required accuracy of the SMOS final data products [SMOS, 2003a], as detailed in Chapter 3. Calibration activities are based on an accurate on-ground characterization of the instrument during the system performance tests and IVT (Image Validation Tests). Data from this characterization are also used as the preliminary dataset for the in-orbit calibration.

One of the main objectives of the on-ground characterization has been to show that the instrument could be calibrated as predicted and produce brightness temperature images with the required accuracy. Most of the work of this Thesis has been developed in the

framework of the MIRAS/SMOS on-ground characterization and system performance tests. The overall instrument characterization has been realized in four stages, as detailed in this section, in which the author has actively participated.

4.1.1 Preliminary measurements

The SMOS payload was successfully assembled by the prime contractor, EADS-CASA Espacio (Spain) in January 2007. Preliminary tests were carried out just after the integration at EADS-Casa Espacio clean room in order to assess the payload system performance.

During the measurements in this first stage, the instrument was folded and only internal noise injection modes were feasible. Tests were mainly devoted to perform basic functionality tests aimed at checking the hardware and software operation as well as assessing the correct implementation of the internal calibration sequences. In addition, these first data provided by MIRAS were used to check the proper behavior of the data processing software.

4.1.2 Thermal characterization at ESA's Large Space Simulator

In April 2007, the instrument was placed inside the Large Space Simulator (LSS) at the ESA-ESTEC facilities for the thermal characterization process (Fig. 4.1). As in the previous stage, only measurements in noise injection modes were possible. The thermal vacuum chamber was used to set ambient temperature and pressure to emulate the space conditions during the instrument in-orbit operation.

Datasets were acquired when the instrument was temperature cycled from 5°C to 35°C approximately. These data have been used to characterize the instrument performance and the sensitivity of calibration parameters with respect to the physical temperature drifts. These sensitivity values have been used to correct the in-orbit measurements between calibration events until new values were measured in orbit.

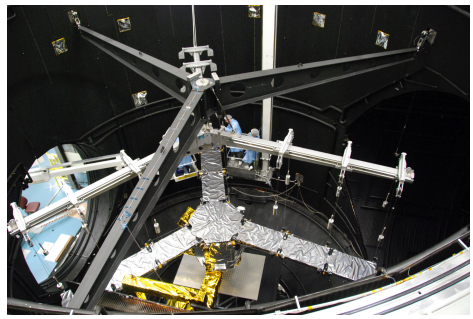

Figure 4.1: MIRAS inside the LSS during the thermal characterization. Courtesy of EADS-CASA Espacio.

4.1.3 Image Validation Tests

After the thermal characterization, MIRAS was deployed at the ESA's anechoic chamber, called Maxwell, where the first antenna measurements were acquired (Fig. 4.2). Image Validation Tests (IVT), performed during May-June 2007, included tests aimed at checking both the hardware and software operation, assessing calibration algorithms and testing imaging methods [Benito & team, 2007].

The data processing team (formed by ESA, EADS-CASA Espacio and UPC personnel) processed the measurements in quasi real time in the clean room next to Maxwell anechoic chamber (Fig. 4.3).

In particular, this campaign comprised two phases. The first one was carried out on 14^{th}, 15^{th} and 16^{th} of May 2007 and comprised, among others:

- *Calibration sequences assessment.* Aimed at checking the proper implementation of the internal and external calibration sequences [Brown *et al.*, 2008].
- *Polarization check.* Devoted to verify the definition of the PLM (Payload Module) polarization axis and test receivers switching between H and V.
- *Inter-element phase retrieval.* The objective of this test was the retrieval of the relative phase for all the antennas [Corbella *et al.*, 2008b].

The second one was performed on 31^{st} of May and from 1^{st} to 5^{th} of June 2007. Measurements in this period were mainly devised to assess the self electromagnetic compatibility as well as the instrument stability. These measurements were used in the analysis of the following properties:

- *Stability.* Long periods of measurements at constant temperature to evaluate the instrument stability with a large integration time (PMS calibration parameters and empty chamber correlation offsets).
- *Self Electromagnetic compatibility.* Tests devoted at assessing the impact on system performance of different instrument/set up configurations. Different subsystems of the payload, namely, power supply, heaters and X-band transmitter, were switch on/off in order to identify possible interferences.
- *Imaging validation.* Oriented to produce the first images of the chamber ceiling at constant temperature.

4.1.4 RACT measurements

After the successful IVT campaign, MIRAS was taken to Thales Alenia Space in Cannes (France), where the last phase of the on-ground characterization was carried out. In April 2008, just after the integration of the payload with the platform (CNES/ALCATEL

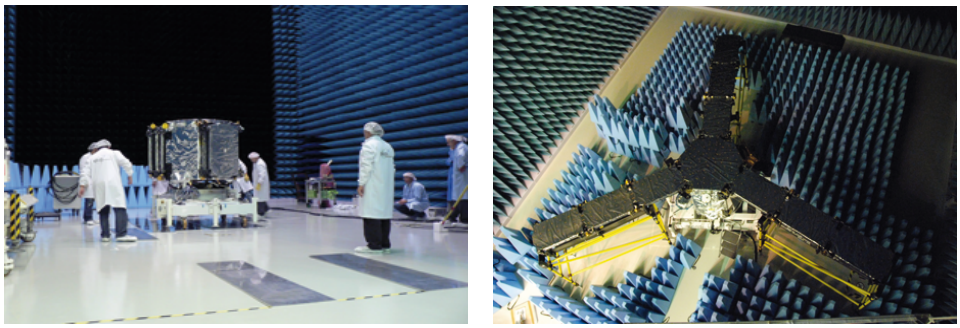

(a) Instrument deployment and installation. (b) MIRAS during IVT.

Figure 4.2: MIRAS payload at Maxwell anechoic chamber.

(a) In the clean room next to the anechoic chamber. (b) At Maxwell anechoic chamber in front of the instrument.

Figure 4.3: Near real time data processing team during IVT campaign.

PROTEUS), the author participated in several tests that were conducted to check the electromagnetic compatibility between them in the CATR anechoic chamber.

Once the payload was stabilized in temperature, tests were conducted for the platform and payload on the nominal mode. After that, both the payload and the platform were switched off and measurements for the redundant mode were acquired.

Different subsystems of the payload/platform were switched on/off while the instrument was kept in the same operation mode in order to assess the impact on the instrument performance. The effects on MIRAS measurements of the X-band transmitters, solar array rotation subsystem, star trackers, S-band transmitter and GPS were evaluated. In addition, instrument performance was evaluated and final calibration sequences were tested before the in-orbit operation.

4.2 MIRAS fast processing tool

Data processing from on-ground characterization campaigns requires the use of a software capable of dealing with SMOS data from raw to level 1A products. MIRAS fast processing tool, from now on MTS, is a software designed by the UPC Remote Sensing Group to read and process SMOS data in near real time [Corbella *et al.*, 2008a]. During this Thesis work, specific features of this software have been developed and tested.

The tool accepts raw data from the Electronic Ground Support Equipment (EGSE), which is the data format used during on-ground characterization and also the Level 0 data provided by the SMOS ground segment data acquisition system. It applies the calibration procedures detailed in chapter 3 to obtain calibrated visibilities (level 1A) and finally horizontal and vertical brightness temperature maps (level 1C).

At this point, a block diagram of MTS is presented, detailing the products obtained in the different processing levels (Fig. 4.4). These products and most of the intermediate results are saved into disk for further analysis and post-processing.

Besides, MTS includes a graphical user interface (Fig. 4.5) to monitor in real time any data product depending on the different processing levels. This feature has been of utmost importance in order to check the system performance in quasi real time during the on-ground measurements. Taking advantage of this interactivity, the user can choose different options in terms of selecting receivers/baselines using a given criteria, measurements corresponding to specific instrument settings, a given calibration sequence and dual/full antenna measurements among others in order to analyze specific instrument modes and datasets. In addition, any data selected by the user can be saved as an image using Portable Network Graphics (PNG) format and exported to a spreadsheet application [González-Gambau *et al.*, 2008c].

Following the block diagram in Fig. 4.4, the first step in the processing classifies the input data stream (level 0) according to the measurement type (correlation, PMS, temperatures, control signals, etc.). The result is used as input for processing next level, involving the correction of the quadrature error and comparator offset, obtaining the quadrature corrected normalized correlations Mkj (level 0A) [Corbella *et al.*, 2005, Martín-Neira *et al.*, 2004]. The calibrated visibility (level 1A) is computed after the denormalization using the system temperatures calibrated by the two-level four-points method [Torres *et al.*, 2006]. Level 1A product is the input for the image reconstruction process, resulting in the brightness temperature at the antenna reference plane (level 1B) [Corbella *et al.*, 2009a]. Finally, level 1C products contain the geolocated brightness temperatures.

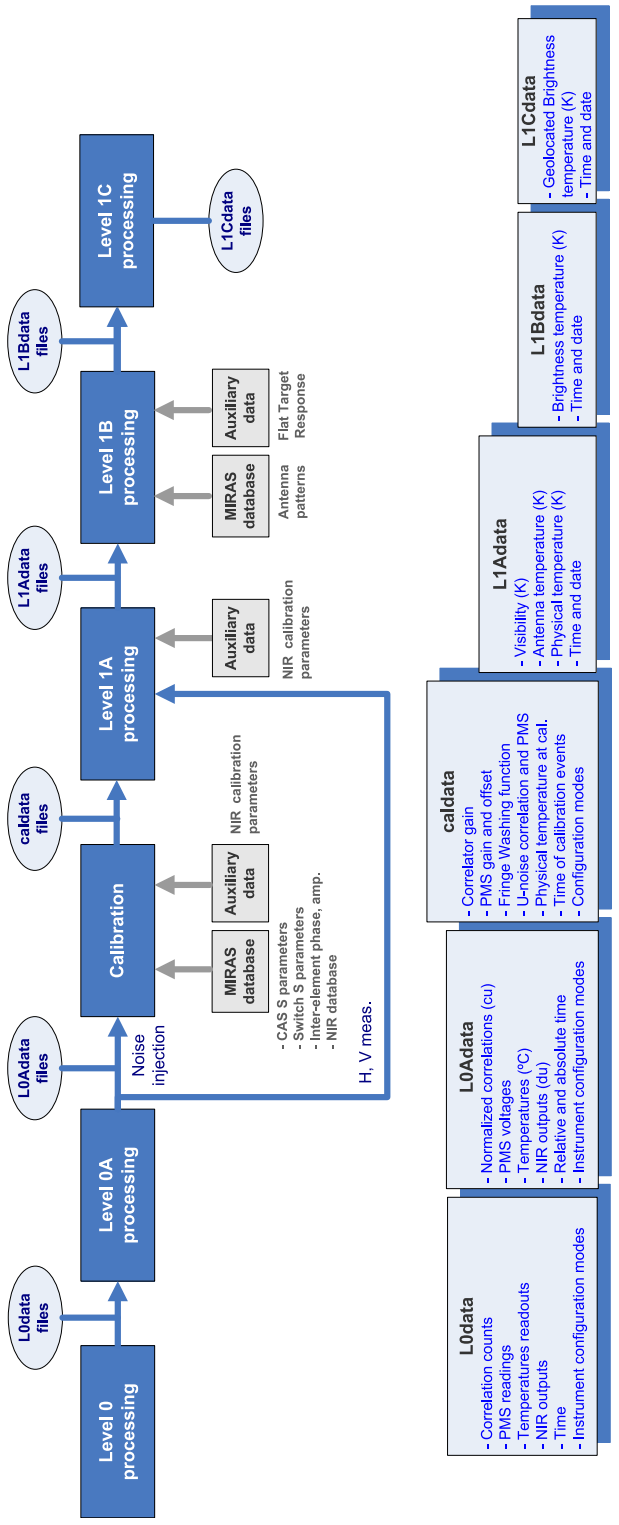

Figure 4.4: Block diagram of MTS, developed by the UPC Remote Sensing Group [Corbella *et al.*, 2008a].

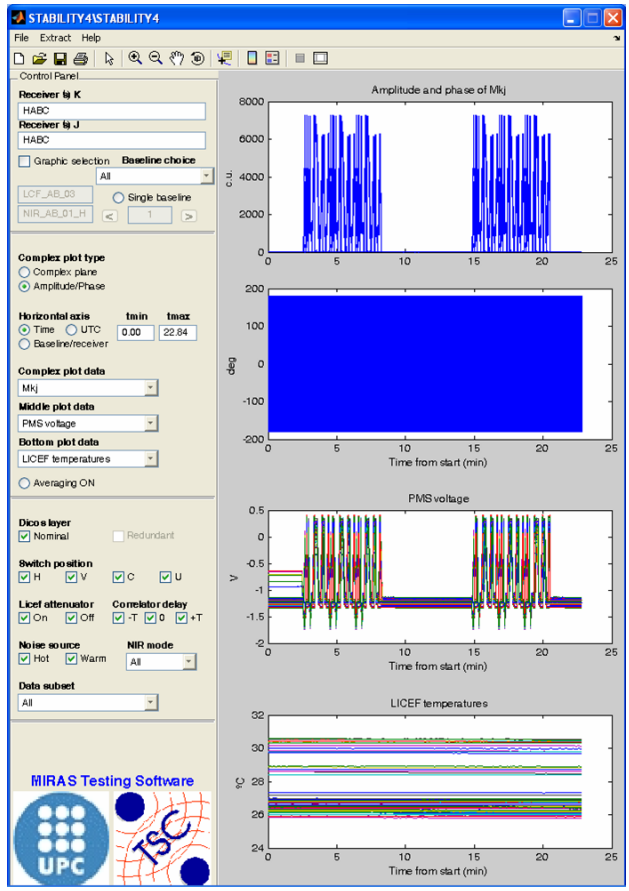

Figure 4.5: User graphical interface of the MTS interactive package developed by the UPC Remote Sensing Group [Corbella *et al.*, 2008a].

4.2.1 Dedicated software packages

Based on the different analysis and requirements of the on-ground characterization campaigns, dedicated software packages have been devised during the development of this Thesis to support a comprehensive analysis of the system performance in each of the stages.

All these tools are based on the data products at the different processing levels provided by the MTS. Among other minor contributions to fine-tuning the MTS, the main contributions are:

- Success criteria tool
- Calibration consistency tool
- Phase track tool

These tools are comprehensively described in the following sections.

MIRAS Fast Processing tool and the dedicated software packages have been successfully used to characterize the payload performance during the LSS and the IVT tests at ESA-ESTEC facilities and also during the electromagnetic compatibility tests performed at Thales Alenia Space just after the payload and the platform integration. The graphical user interface of the software package used during the IVT campaign is shown in Fig. 4.6. This software has been used to automatically process and generate all the significant parameters and statistics needed for the analysis of each one of the tests.

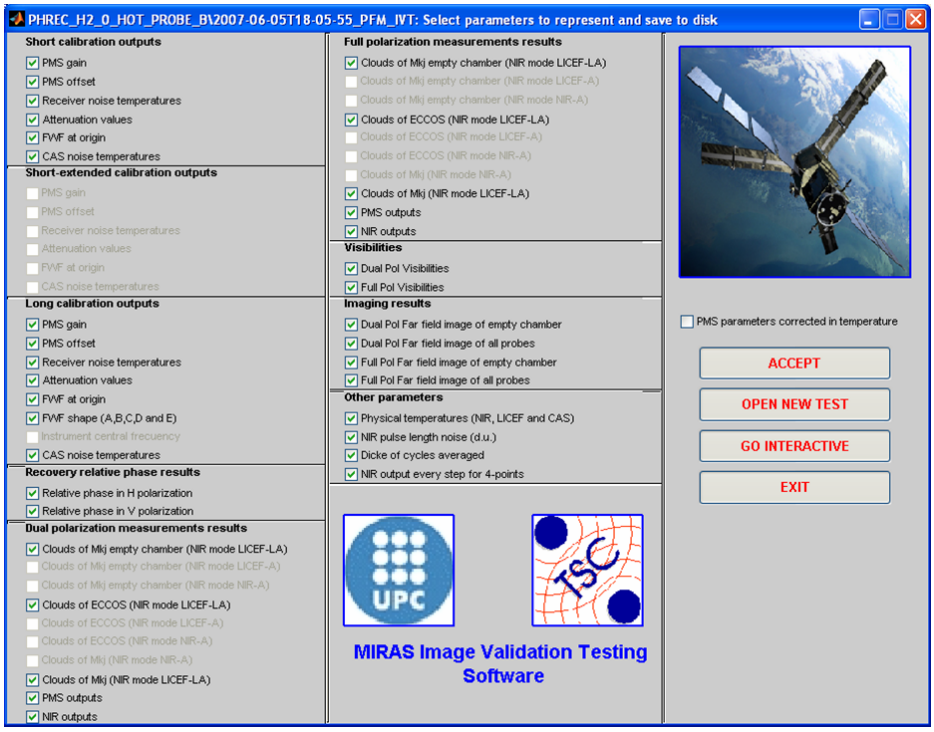

Figure 4.6: User graphical interface of the IVT software package, developed to automatically generate and compute statistics of the relevant parameters in each one of the tests.

A comprehensive process of data products cross-validation at the different processing levels (up to level 1A) between the official SMOS Level-1 Prototype Processor (L1PP) [Gutierrez *et al.*, 2007] and the MTS (two independent softwares) has being performed in order to achieve a high degree of confidence on the SMOS L1 data products.

4.3 MIRAS/SMOS RFI and EMC tests

As part of the system performance characterization, a set of tests devoted to evaluate the self Radio Frequency Interferences (RFI) and the self Electromagnetic Compatibility (EMC) of the instrument were performed at the ESA's Maxwell anechoic chamber. To the

same purpose, similar tests were carried out at Thales Alenia Space in Cannes (France), in this case with the payload integrated to the platform.

In these tests, different subsystems of the payload and the platform were switched on/off while the instrument was measuring the anechoic chamber background in a specific configuration keeping a constant temperature. The impact of the differences in the instrument/setup configuration on the measurements collected by MIRAS was then analyzed.

Visibility samples are denormalized and corrected from instrumental errors using the normalized correlations and system temperatures referred to the antenna plane, which are computed using the antenna PMS gain referred to that plane and voltage readings [Torres *et al.*, 2006]. In consequence, any perturbation on the normalized correlations and/or the antenna PMS voltage readings affects to the visibility samples.

The development of a dedicated data processing tool as well as a comprehensive analysis have allowed the assessment of the impact of different instrument configurations/set ups on MIRAS system performance.

4.3.1 Success Criteria tool

A major problem to easily evaluate the impact of any change in the set up configuration or instrument operating conditions is the large number of measurements to deal with, since MIRAS generates 2556 complex correlations from all possible baselines and 72 PMS voltage readings in each acquisition (1.2 seconds).

The Success Criteria Tool is a dedicated data processing tool conceived and developed within this Thesis to process and easily assess the impact of any perturbation on MIRAS system performance from the data products provided by the MTS. For that reason, it has been designed to accomplish the following requirements:

- It must manage a large number of measurements.
- It must deal with random magnitudes: PMS voltages and correlator outputs.
- The tool must clearly identify small perturbations embedded in noise, that may affect only a few receivers and/or baselines.
- It should present the main outcomes in a simple format (a few plots showing the overall system performance) and in quasi-real time in order to ease a preliminary analysis during the tests execution.

The tool compares the statistical properties of the nominal measurement (reference) with those of the measurement under perturbation. It checks if the changes in the statistics of both sets of measurements are below a threshold defined as the success criteria.

The criteria have been defined for the mean (4.1) and the standard deviation (4.2):

$$\left|\overline{X}_{meas} - \overline{X}_{ref}\right| < \mathrm{std}\left(X_{ref}\right) \tag{4.1}$$

$$\mathrm{std}\left(X_{meas}\right) < \overline{\mathrm{std}\left(X_{ref}\right)} + 3 \cdot \mathrm{std}\left(\mathrm{std}\left(X_{ref}\right)\right) \tag{4.2}$$

where X_{ref} stands for the magnitudes in the reference measurement and X_{meas} represents the same magnitudes in the case of the measurement under perturbation. The overline notation indicates the mean value of the corresponding variable.

The outputs of each test show the results in a straightforward format. Graphic files show the comparison of the statistic properties of normalized complex correlations and PMS voltages with the success criteria. In addition to this, baselines and/or receivers non-compliant with the success criteria are listed in excel files to ease troubleshooting.

4.3.2 Data analysis and results

During MIRAS RFI and EMC tests, all the measurements were acquired keeping the instrument in the same mode and measuring in dual polarization the anechoic chamber background at constant temperature. Similar number of acquisitions in both instrument configurations/set ups has allowed comparing statistically the measurements. All tests have been analyzed in quasi real time in order to assess if there was any problem in each set of measurements.

The most relevant outcomes of this analysis are presented in order to illustrate the system performance and its dependence on electromagnetic perturbations. It must be pointed out that most of the tests show that variations in the statistics between the nominal measurement and the measurement under perturbation are within the expected uncertainty. However, in some of the tests, marginal effects on correlations and/or PMS voltages have been detected by means of the Success Criteria tool [González-Gambau *et al.*, 2008a,e].

Concerning the heaters test, results correspond to the expected ones for a test where the perturbation (red dots) produces a negligible impact in the statistics of normalized correlations (Fig. 4.7) and PMS voltages (Fig. 4.8) in relation to the success criteria (blue dots). The changes in the mean and the standard deviation for the test under perturbation are within the expected measurement uncertainty in a set of 100 samples at 1.2 s correlation time and 0.18 s PMS integration time.

In the analysis of the X-band transmitter test performed after the integration, two periods have been assessed. One of them when the transmitter is sending stuffing packets to synchronize with the ground station (before and after data transmission) and another while scientific data is being dumped. The impact on normalized correlations provided by the instrument during the switching on of the nominal X-band transmitter can be clearly observed, both in the mean and in the standard deviation (Fig. 4.9). Table

4.1 lists marginal baselines which are non-compliant with the success criteria. It must be pointed out that these baselines are formed by at least one of the receivers located near the transmitter. Besides, baselines affected in H (Figs. 4.9(a) and 4.9(b)) and V polarizations (Figs 4.9(c) and 4.9(d)) are not the same, indicating coupling by the antenna. However, this effect can be avoided since it is not present when using a redundant transmitter included in the platform (Fig. 4.11). Regarding the period during data transmission there was no interference at all, neither for the nominal X-band transmitter (Fig. 4.10) nor for the redundant one (Fig. 4.12). This was one of the main reasons to fly MIRAS in redundant configuration after launch.

Table 4.1: Non-compliant baselines during nominal X-band transmitter switching on.

$M_{kj}H$			$M_{kj}V$		
Receiver k	Receiver j	*std*	Receiver k	Receiver j	*std*
LCF-A-03	LCF-CA-03	3.3189	LCF-A-01	LCF-C-03	3.2315
LCF-A-04	LCF-CA-03	3.2080	LCF-A-15	LCF-C-04	3.1948
LCF-A-06	LCF-CA-03	3.2425	LCF-B-02	LCF-C-10	3.2006
LCF-BC-03	LCF-CA-03	3.3808	LCF-B-04	LCF-C-03	3.2527
LCF-B-02	LCF-CA-03	3.3214	LCF-CA-03	LCF-C-02	3.4273
LCF-B-03	LCF-CA-03	3.6225	LCF-CA-03	LCF-C-03	4.2456
LCF-B-04	LCF-CA-03	4.0031	LCF-CA-03	LCF-C-04	3.6160
LCF-B-04	LCF-C-01	3.2511	LCF-CA-03	LCF-C-09	3.4513
LCF-B-06	LCF-B-20	3.2225	LCF-CA-03	LCF-C-10	3.3593
LCF-B-19	LCF-B-20	3.2185	LCF-C-02	LCF-C-03	3.5424
LCF-B-21	LCF-C-21	3.1842	LCF-C-02	LCF-C-04	3.4632
LCF-CA-03	LCF-C-02	3.2072	LCF-C-02	LCF-C-09	3.2561
LCF-CA-03	LCF-C-04	3.2152	LCF-C-03	LCF-C-04	4.2856
LCF-CA-03	LCF-C-05	3.3408	LCF-C-03	LCF-C-09	3.3741
LCF-CA-03	LCF-C-09	3.2602	LCF-C-03	LCF-C-10	3.4230
LCF-CA-03	LCF-C-19	3.1959	LCF-C-04	LCF-C-09	3.2697
LCF-C-06	LCF-C-12	3.1836	LCF-C-04	LCF-C-10	3.2890

Other possible source of interferences is the Solar Array Driver Mechanism (SADM). Two different mechanisms have been assessed: 1 degree step and continuous rotation. In both tests, complex correlations are not affected by the movement of the rotation system. However, it is important analyzing the PMS voltage results in the 1 degree rotation test. Reference measurement was acquired in full polarization mode while measurement during the subsystem rotation was taken in dual mode. For this reason, a measurement acquired 7 hours apart from the measurement under perturbation has been used as reference in the analysis. Success criteria for the mean (Figs. 4.13(a) and 4.13(c)) and the standard deviation (Figs. 4.13(b) and 4.13(d)) show a high variation in the PMS voltages. The origin of this changes is probably due to the PMS gain drift, since the temperature between both tests was changed around $1°C$.

Finally, all the platform subsystems in the nominal side capable of producing interferences were switched off. For simplicity, results from each individual test are not presented. Instead, the comparison between the configuration with all subsystems off and the measurements acquired while all the platform subsystems were on reveals that no impact on correlations (Fig. 4.14) nor on PMS voltages (Fig. 4.15) can be detected. These results permit to ensure that the nominal side of the platform is not affecting MIRAS system

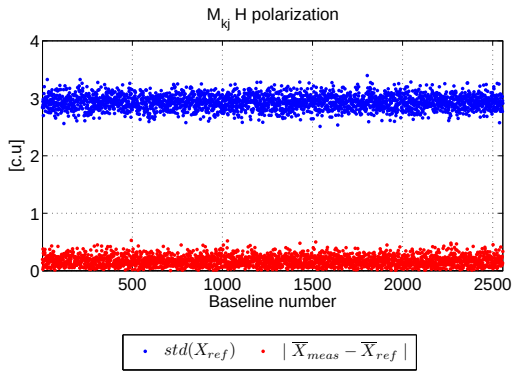

(a) Mean H polarization

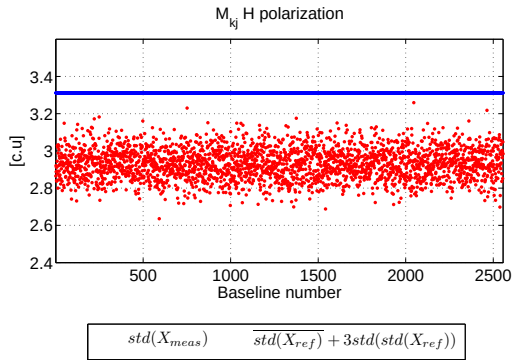

(b) Standard deviation H polarization

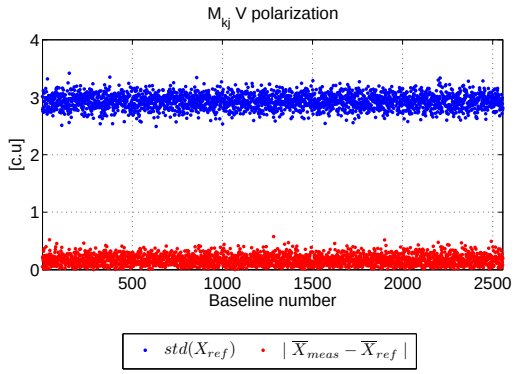

(c) Mean V polarization

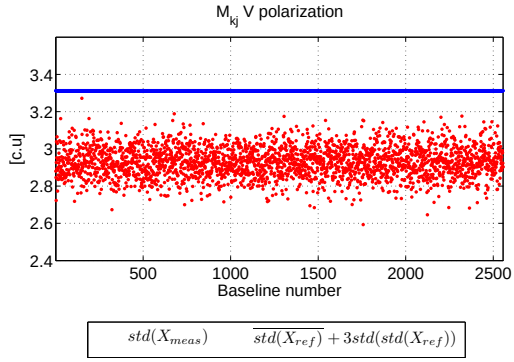

(d) Standard deviation V polarization

Figure 4.7: Success criteria for the normalized correlations during heaters test.

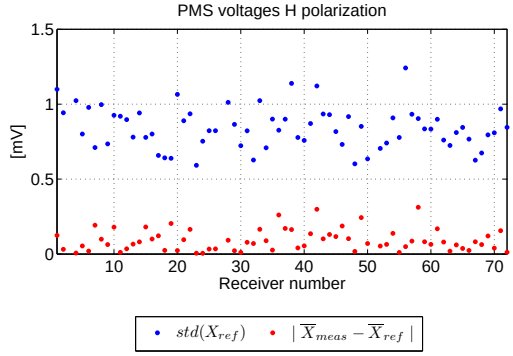

(a) Mean H polarization

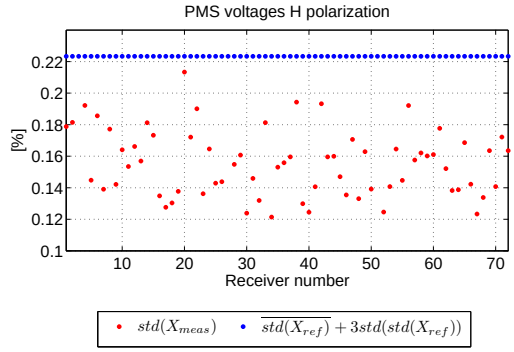

(b) Standard deviation H polarization

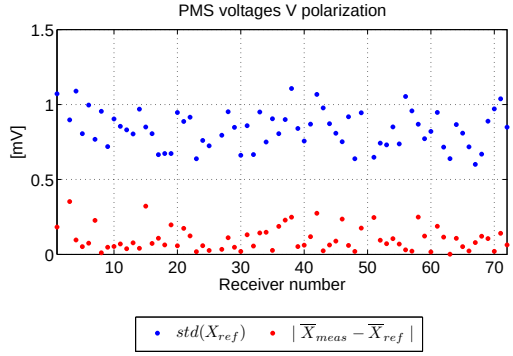

(c) Mean V polarization

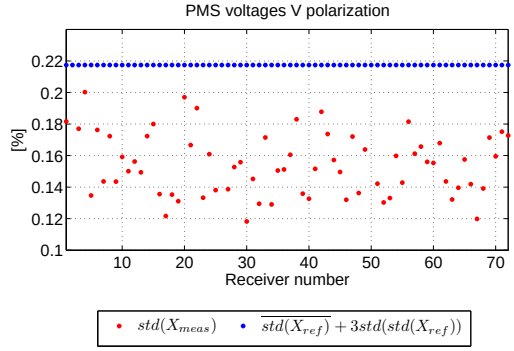

(d) Standard deviation V polarization

Figure 4.8: Success criteria for the power detector voltages during heaters test.

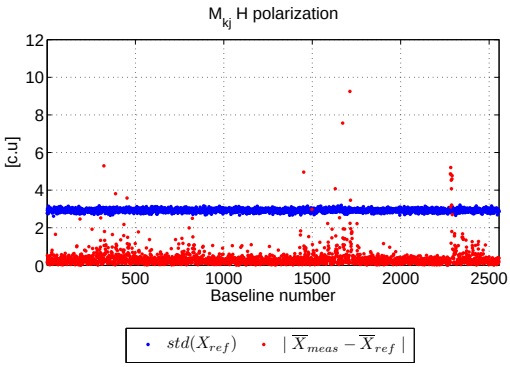

(a) Mean H polarization

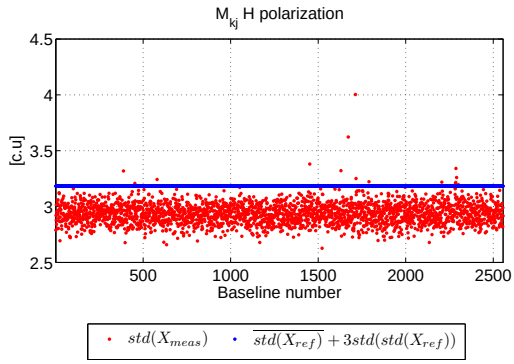

(b) Standard deviation H polarization

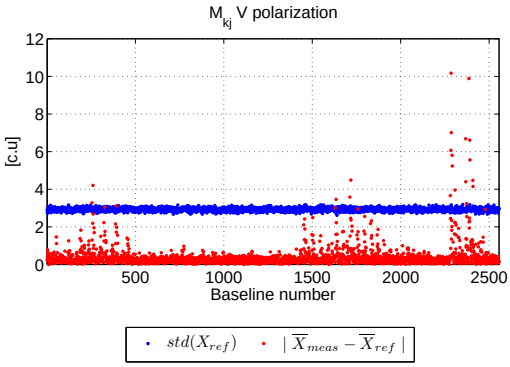

(c) Mean V polarization

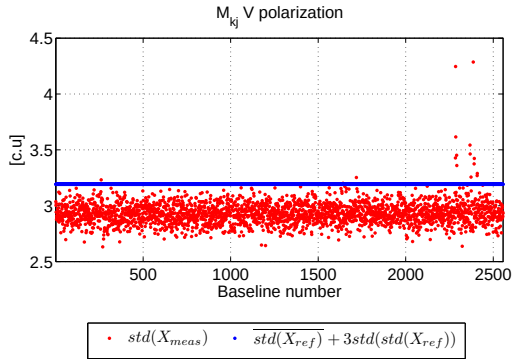

(d) Standard deviation V polarization

Figure 4.9: Success criteria for the normalized correlations during nominal X-band transmitter switching on (stuffing).

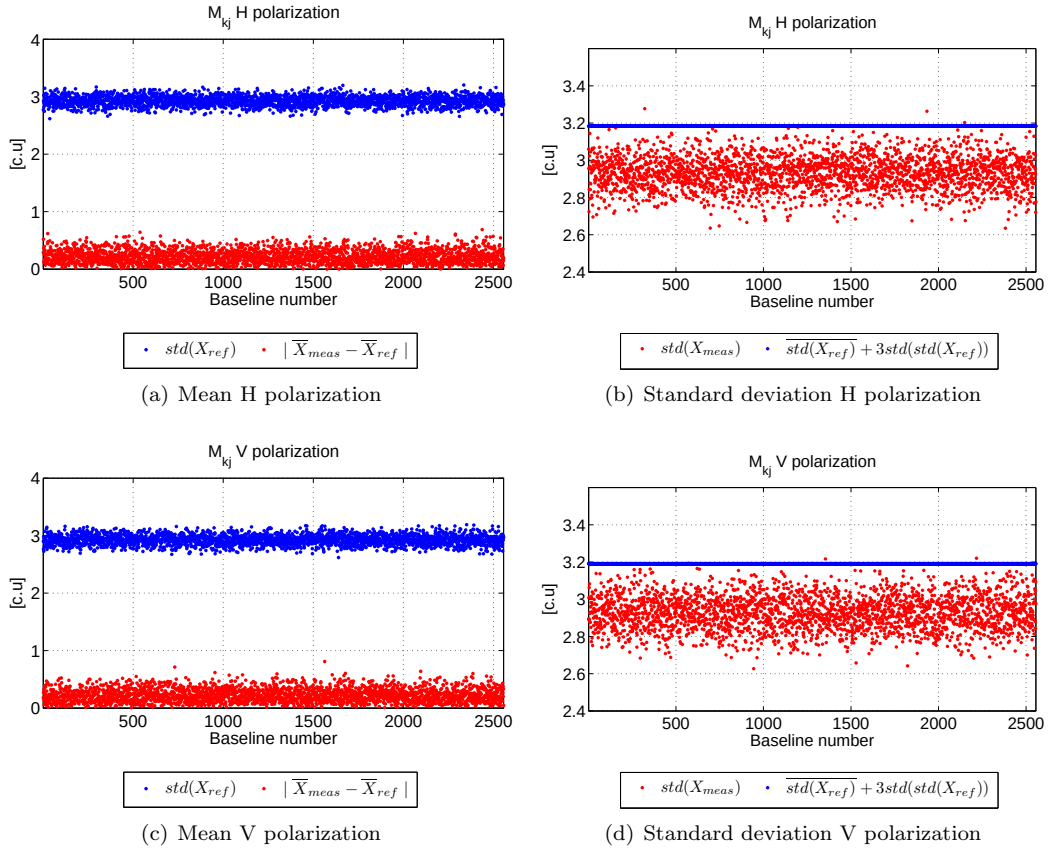

(a) Mean H polarization

(b) Standard deviation H polarization

(c) Mean V polarization

(d) Standard deviation V polarization

Figure 4.10: Success criteria for the normalized correlations during nominal X-band transmitter data transmission.

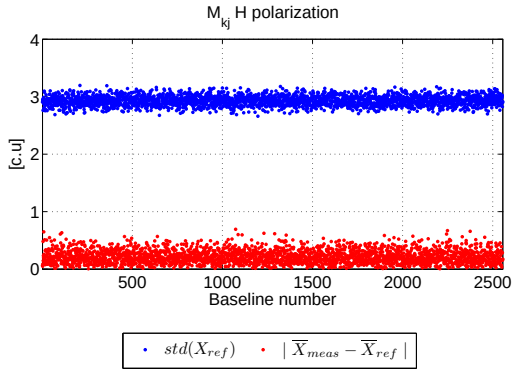

(a) Mean H polarization

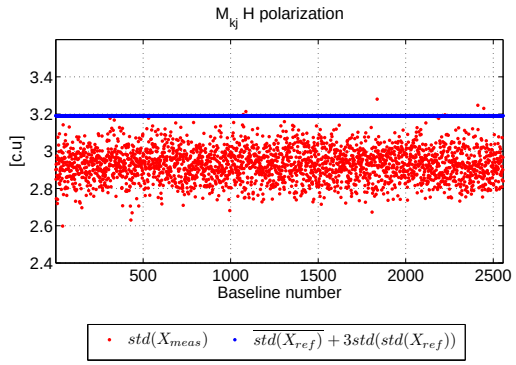

(b) Standard deviation H polarization

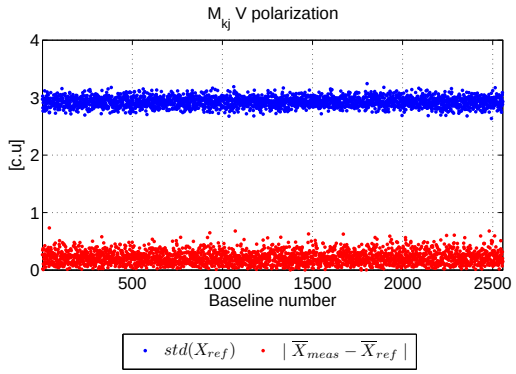

(c) Mean V polarization

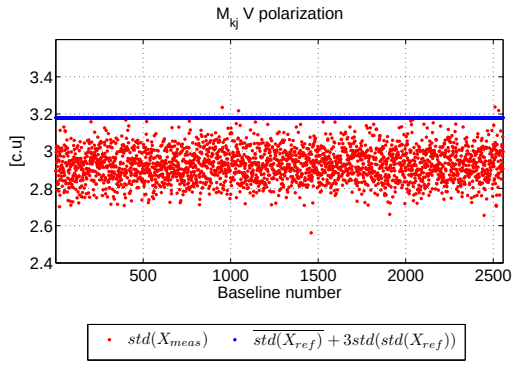

(d) Standard deviation V polarization

Figure 4.11: Success criteria for the normalized correlations during redundant X-band transmitter switching on (stuffing).

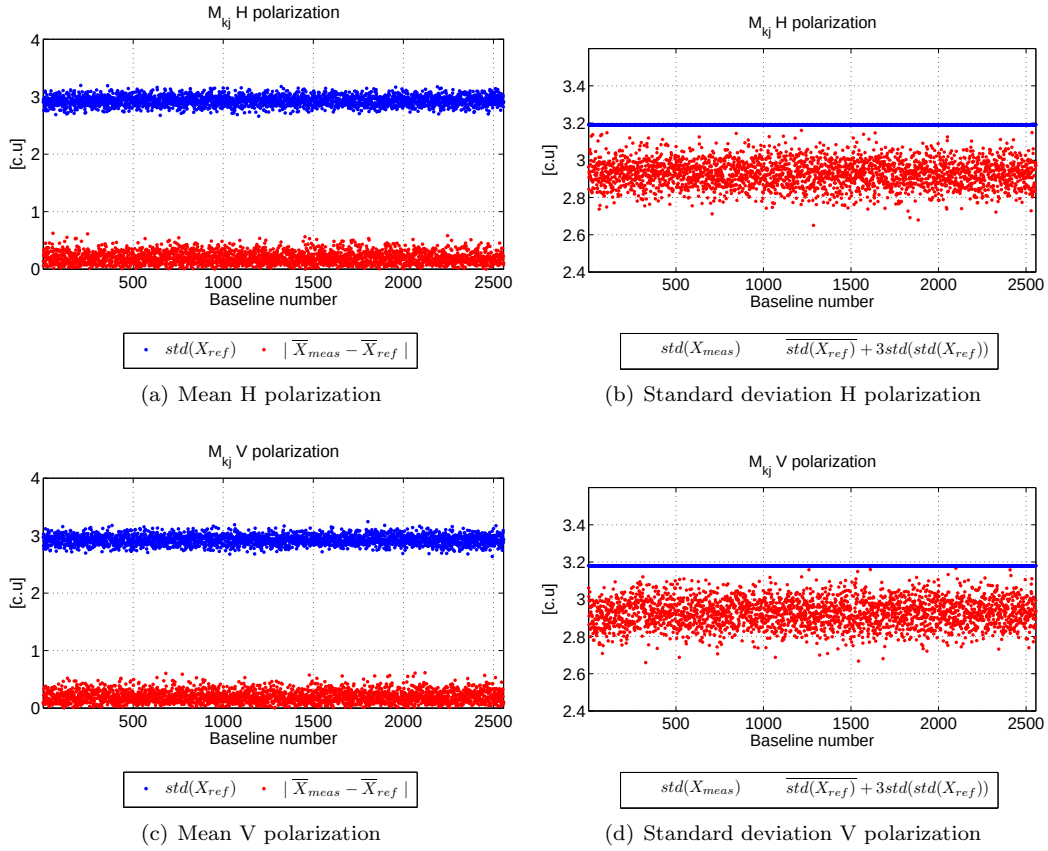

(a) Mean H polarization

(b) Standard deviation H polarization

(c) Mean V polarization

(d) Standard deviation V polarization

Figure 4.12: Success criteria for the normalized correlations during redundant X-band data transmission.

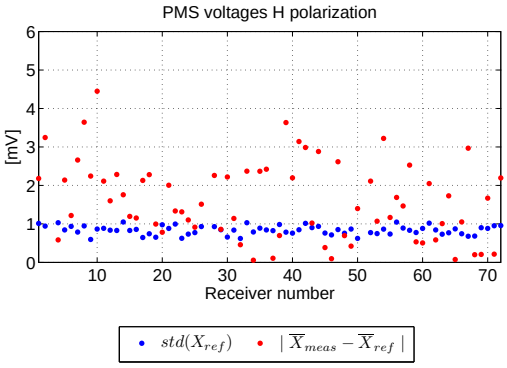

(a) Mean H polarization

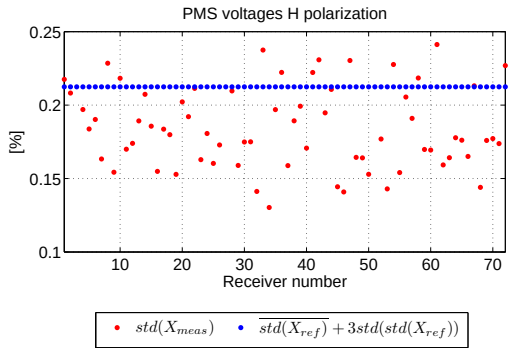

(b) Standard deviation H polarization

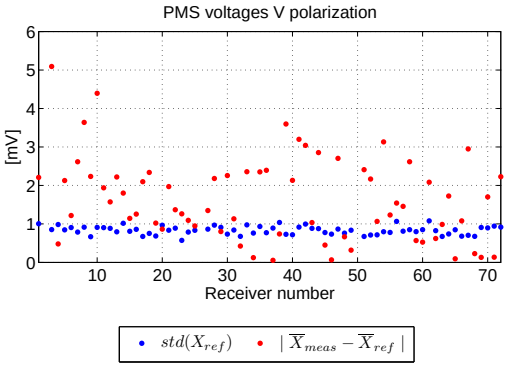

(c) Mean V polarization

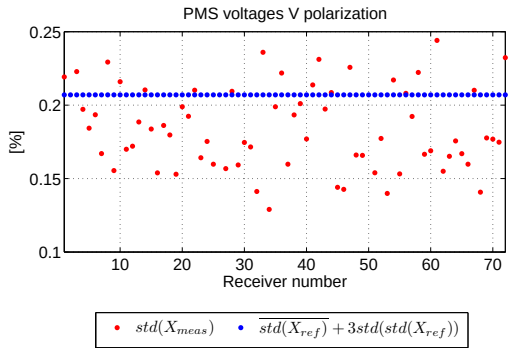

(d) Standard deviation V polarization

Figure 4.13: Success criteria for the PMS voltages in solar array 1 degree step compatibility test.

performance. A similar analysis in the redundant configuration of the platform shows that any subsystem of the platform is not affecting the PMS voltages (Fig. 4.17) nor the complex correlations, as appreciated in Fig. 4.16.

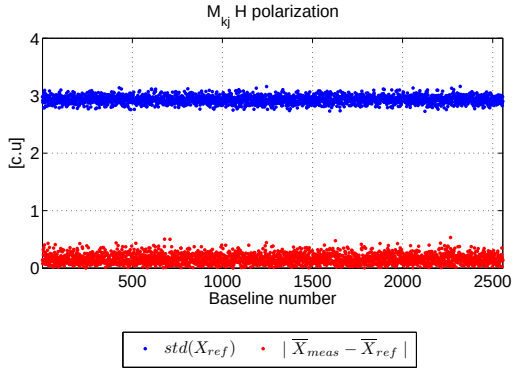

(a) Mean H polarization

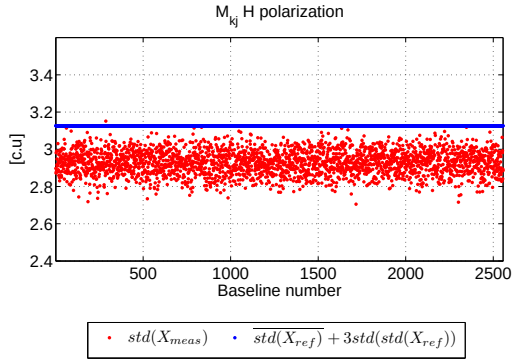

(b) Standard deviation H polarization

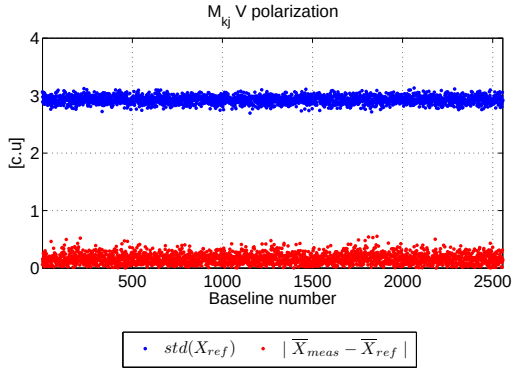

(c) Mean V polarization

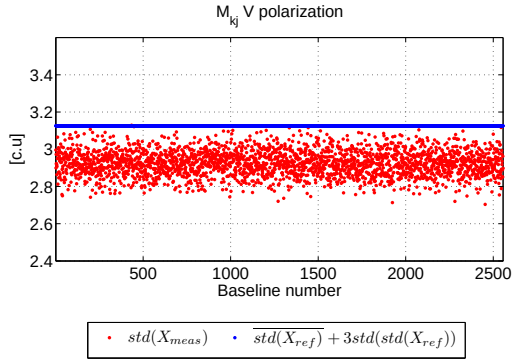

(d) Standard deviation V polarization

Figure 4.14: Success criteria for the normalized correlations comparing measurements with all subsystems OFF and those with all subsystems ON. Nominal mode of the platform.

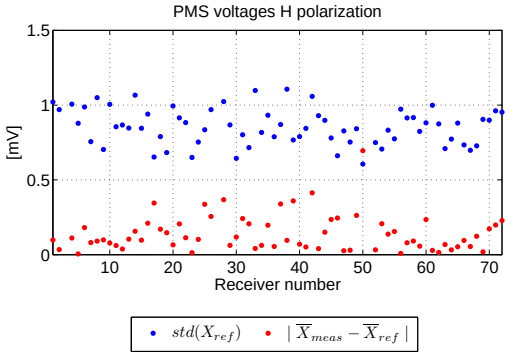

(a) Mean H polarization

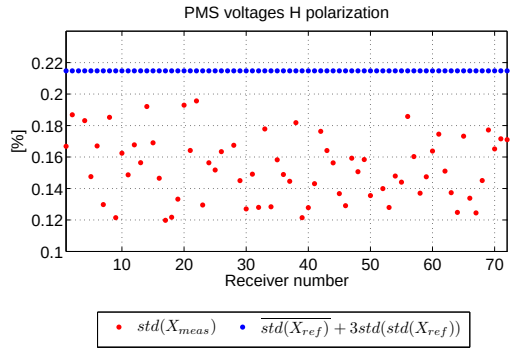

(b) Standard deviation H polarization

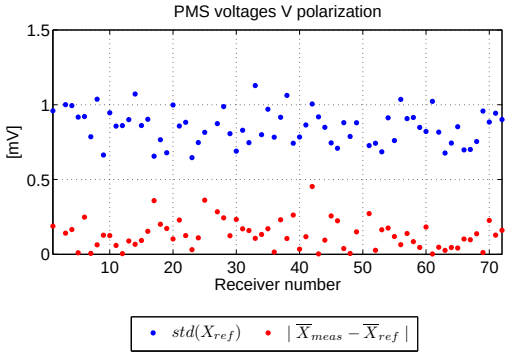

(c) Mean V polarization

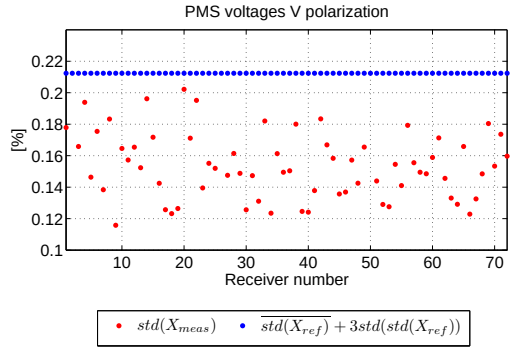

(d) Standard deviation V polarization

Figure 4.15: Success criteria for the PMS voltages comparing measurements with all subsystems OFF and those with all subsystems ON. Nominal mode of the platform.

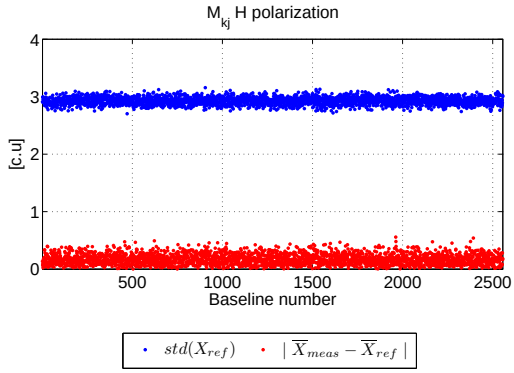

(a) Mean H polarization

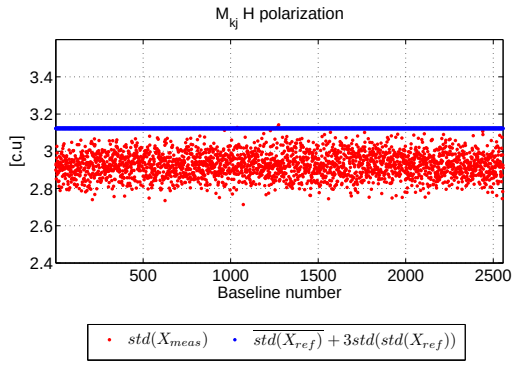

(b) Standard deviation H polarization

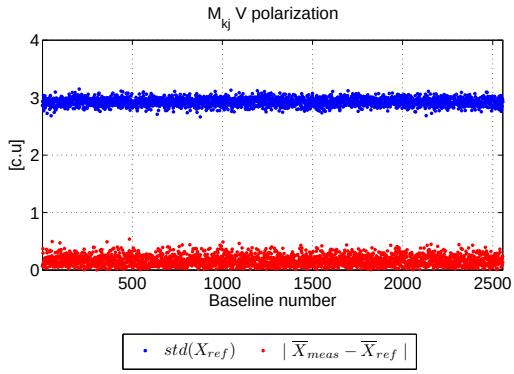

(c) Mean V polarization

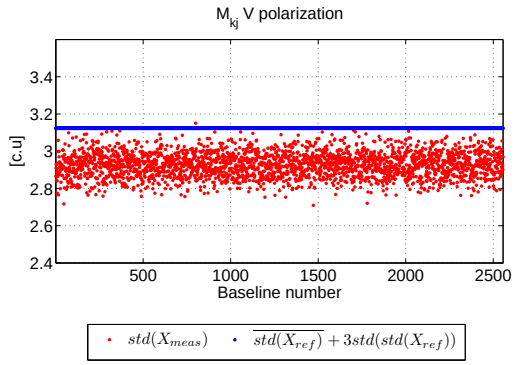

(d) Standard deviation V polarization

Figure 4.16: Success criteria for the normalized correlations comparing measurements with all subsystems OFF and those with all subsystems ON. Redundant mode of the platform.

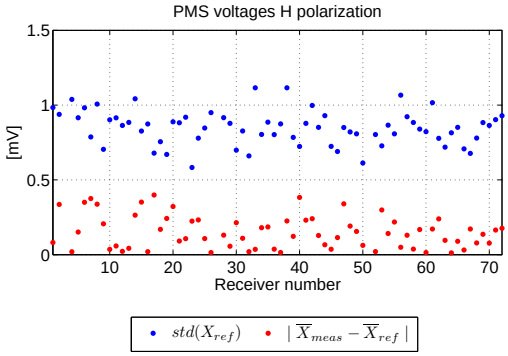

(a) Mean H polarization

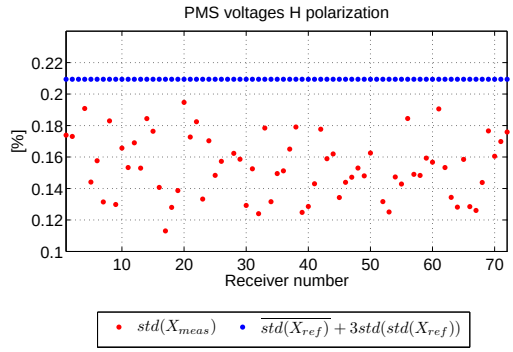

(b) Standard deviation H polarization

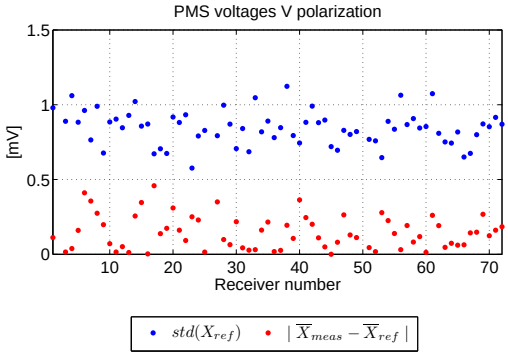

(c) Mean V polarization

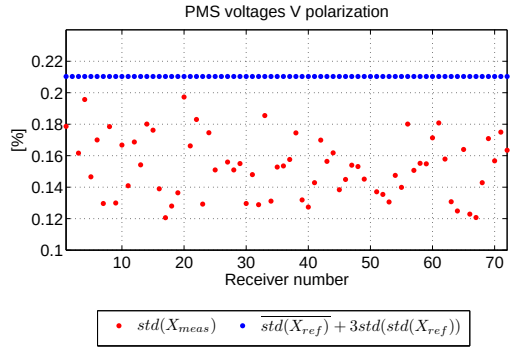

(d) Standard deviation V polarization

Figure 4.17: Success criteria for the PMS voltages comparing measurements with all subsystems OFF and those with all subsystems ON. Redundant mode of the platform.

4.3.3 Conclusions

MIRAS/SMOS RFI and EMC tests have shown that the payload presents a very robust performance in front of electromagnetic perturbations and/or extreme operating conditions. The Success Criteria tool has been extensively and successfully used during the analysis of the EMC tests performed at ESA's Maxwell anechoic chamber during the IVT campaign and also during RACT tests at Thales Alenia Space, once the instrument was integrated to the platform. Several instrument configurations (heaters ON/OFF, power supply maximum/minimum) and all the subsystems in the platform, such as the star tracker, the GPS, the X-band and S-band transmitters and the solar arrays have been assessed, both in the nominal and redundant configurations. The tool has also allowed detecting marginal effects on the correlations and/or PMS voltages at mean and/or standard deviation level depending on the nature of the perturbations.

The conclusion of all compatibility tests performed shows that there is no source of major interference nor with the platform nor with the other subsystems of the payload. There is only marginal interferences from the nominal X-band transmitter during the switching on. This effect is not critical, but it has been overcome by using the redundant X-band transmitter. Therefore, the redundant configuration is recommended for MIRAS in-orbit operation.

4.4 Amplitude calibration consistency

The consistency of the amplitude calibration is a key issue comprehensively investigated in the framework of this Thesis, in which a method to easily assess the self-consistency of the amplitude calibration coefficients used in the MIRAS instrument has been developed. The approach takes advantage of the internal calibration intrinsic properties to provide a good estimation of the amplitude errors after the calibration procedures [Corbella *et al.*, 2005].

4.4.1 Rationale and methodology

The rationale of the amplitude self-consistency tool is based on a quite simple principle. When all PMS units in a section are fed by the same noise source, the difference in the system temperatures at their inputs between both noise injection levels (HOT and WARM) must be the same, except for the Noise Distribution Network (NDN) imbalance. This assertion is based on the differential measurement of the system temperatures that removes both the noise contribution from the individual receivers and from the NDN itself. In principle, this imbalance can be compensated, since the NDN has been throughly characterized on ground [Lemmetyinen *et al.*, 2007, Colliander *et al.*, 2007b]. However, residual errors have been found to be significant.

The tool provides, for a set of LICEF units, the fractional deviation of the difference in system temperatures relative to the mean of all receivers. Only the relative path differences from the reference radiometers to the receivers are needed. The absolute value of the noise injected by each one of the sources is measured by the three NIR units. This feature allows to equalize the different noise injection levels of each noise source when the measurements are considered at a common virtual reference port [González-Gambau *et al.*, 2008b]. Therefore, the fractional deviation out from the amplitude self-consistency tool is a direct estimator of the PMS gain uncertainty and, in consequence, of the visibility amplitude errors (pixel bias).

At this point, it must be considered that MIRAS uses a distributed noise injection scheme to keep amplitude and phase calibration track along the arms reducing the size of the NDN [Torres *et al.*, 1996]. All receivers are fed by two noise sources (one even and other odd, as explained in chapter 3) except those receivers in the third section of each arm (Fig. 4.18). Hence, the self-consistency tool provides, for the LICEF units driven twice, the fractional deviation in the difference of system temperatures for both noise sources.

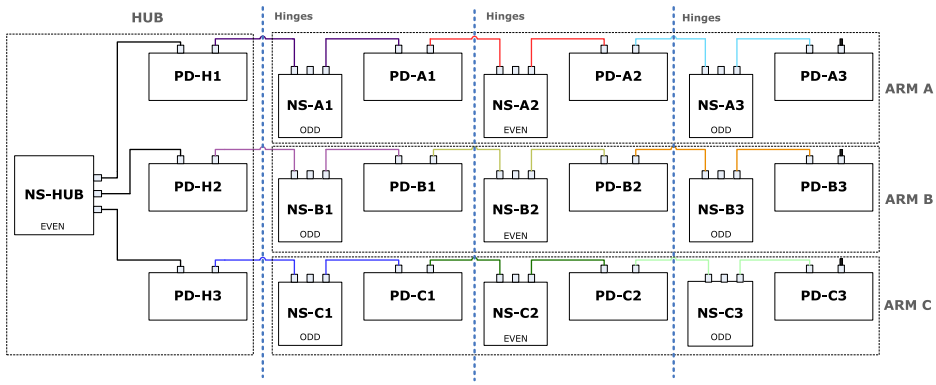

Figure 4.18: Noise distribution network scheme.

The methodology used can be formulated as follows:

- *Calibrate each PMS by means of the one-point calibration.* This calibration approach is independent of the NDN (chapter 5).

- *Define a common virtual reference port (CIP_r)*

  The S-parameter between the common virtual reference port and port 0 of the NDN, S_{r0}, has been defined as the mean value of all the NDN S-parameters.

- *Measure the system temperature differences at CIP_i port* (NDN output port i)

$$T_{sysk_i}^{HOT} - T_{sysk_i}^{WARM} = \frac{v_{2k} - v_{1k}}{G_k^C}, \tag{4.3}$$

where v_{2k}, v_{1k} are the PMS voltages while HOT and WARM correlated noise injection and G_k^C is the PMS gain calibrated using the one-point approach.

- *Translate the difference of system temperatures from CIP_i to CIP_r port for each noise source*

  All receivers fed by the same noise source NS_i (see Fig. 4.18) should measure the same for this difference:

$$T_{sysk_{ir}}^{HOT} - T_{sysk_{ir}}^{WARM} = \left(T_{sysk_i}^{HOT} - T_{sysk_i}^{WARM}\right) \frac{|S_{r0}|^2}{|S_{k0_i}|^2}, \tag{4.4}$$

  where the subscript i indicates the noise source, S_{k0_i} corresponds to the S-parameter between calibration plane of receiver k and the port 0 of the NDN for NS_i and S_{r0} is the S-parameter between the common virtual reference port and port 0 of the NDN. The term $T_{sysk_i}^{HOT} - T_{sysk_i}^{WARM}$ is the difference of system temperatures measured by the PMS of receiver k when is fed by NS_i at CIP plane.

- *Define a common equivalent noise source*

  The difference $T_{sysk_{ir}}^{HOT} - T_{sysk_{ir}}^{WARM}$ related to each noise source can be equalized using the ratio between the mean value of this magnitude for all the sources and the mean value for each noise source:

$$T_{sysk_r}^{HOT} - T_{sysk_r}^{WARM} = \left(T_{sysk_{ir}}^{HOT} - T_{sysk_{ir}}^{WARM}\right) \frac{\left\langle T_{sysk_{ir}}^{HOT} - T_{sysk_{ir}}^{WARM} \right\rangle_{allNS}}{\left\langle T_{sysk_{ir}}^{HOT} - T_{sysk_{ir}}^{WARM} \right\rangle_{NS_i}} \tag{4.5}$$

  This normalization is performed just for representation purposes to have each set of 12 LICEFs with an equivalent noise source level.

4.4.2 PMS calibration consistency tool

In order to test the tool and assess the instrument performance, PMS subsystems have been characterized taking into account the ground characterization of each LICEF unit.

The tool computes the difference in the system temperatures measured by each PMS, which has been calibrated by means of the alternative one-point calibration approach [Torres *et al.*, 2008], explained in Chapter 5. One of the major reasons supporting the use of this technique is that allows calibrating the PMS subsystem independently of the NDN imbalance. Therefore, this calibration approach permits to assess possible systematic errors in the NDN S-parameters to improve the current calibration baseline using CAS and NIR. In addition, this method removes the PMS gain dependence with the receiver position in the arm, an effect which has been observed with the current calibration baseline.

The convention used in the numbering of the receivers has been explained in Table 3.2, in chapter 3. Results presented from now on use this numbering and the vertical dashed lines separate from left to right the receivers in the following sections: AB, arm A, BC, arm B, CA, arm C.

The output of the consistency tool for both configurations of the NS, nominal and redundant, is presented in percent and in dB in Fig. 4.19. Errors in system temperature retrievals for nominal and redundant NS are clearly grouped in clouds of six receivers. This effect is associated to the NS output at which are connected: receivers in the same CMN as the NS and receivers separated by the arm hinges (Fig. 4.18). A peak to peak PMS gain calibration dispersion of about 6% in nominal and 8% in redundant is observed.

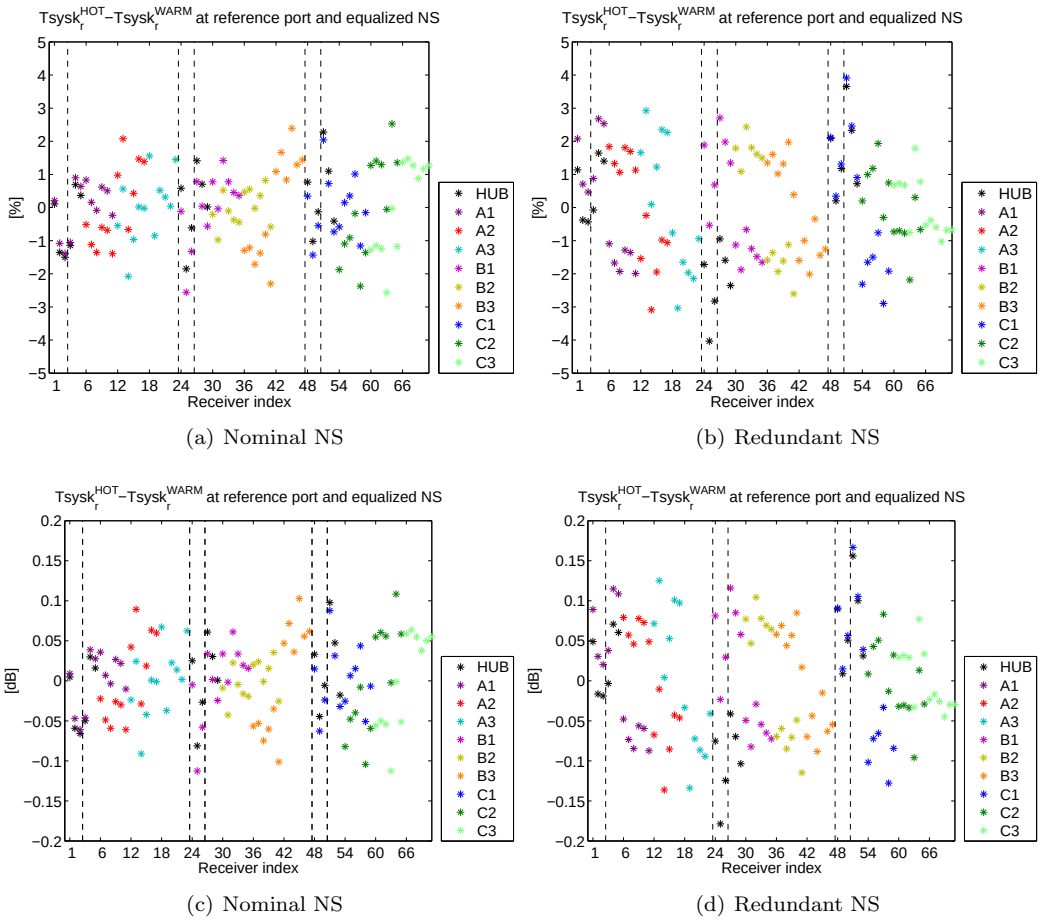

(a) Nominal NS

(b) Redundant NS

(c) Nominal NS

(d) Redundant NS

Figure 4.19: Difference of system temperatures at the reference port, once the noise injection levels related to each NS have been equalized for comparison. Top plots: in percent; bottom: in dB; left: nominal NS; right: redundant NS. This difference is a measure of the NDN residual errors after the imbalance correction by means of the NDN S-parameters measurements.

Systematic errors are different depending on the NS configuration (nominal or redun-

Table 4.2: Arms NS S-parameters imbalance.

		$A1$	$A2$	$A3$	$B1$	$B2$	$B3$	$C1$	$C2$	$C3$
Amp. [dB]	Nom.	0.1685	0.2177	0.1459	0.2123	0.1877	0.1729	0.1834	0.1729	0.2437
	Red.	0.1022	0.1134	0.0436	0.0784	0.0826	0.0074	0.1236	0.0663	0.1541
	Imb.	-0.0663	-0.1043	-0.1023	-0.1339	-0.1051	-0.1655	-0.0598	-0.1066	-0.0896
Phase [deg]	Nom.	1.4765	1.3621	0.9011	2.1343	0.6594	1.4082	1.3058	2.0985	2.1688
	Red.	2.3101	2.2163	1.5063	2.5459	1.685	2.1702	2.4644	3.0247	3.1623
	Imb.	0.8336	0.8542	0.6052	0.4116	1.0256	0.7620	1.1586	0.9262	0.9935

dant). This fact leads to check the NS S-parameters imbalance, since the rest of the network is common for both configurations. According to the NS configuration (see an example of a NS in the arms in Fig 4.20), it is possible that $S_{31} \neq S_{32}$ and $S_{41} \neq S_{42}$. However, since there is a common point at the input of the second power divider (Fig. 4.20), the imbalance between outputs should be the same for the nominal input (Test port 1) and the redundant one (Test port 2)

$$S_{42} - S_{32} = S_{41} - S_{31}[dB]. \tag{4.6}$$

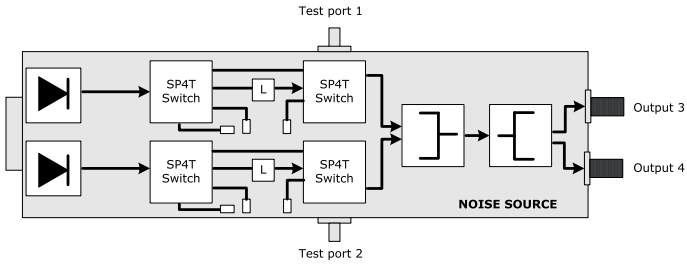

Figure 4.20: Arm Noise Source scheme.

Amplitude and phase imbalance consistency have been checked from the MIRAS database (Table 4.2). The tag Nom. indicates the difference between both outputs for the nominal input. Similarly, the tag Red. refers to the difference between outputs for the redundant port. Imbalance corresponds to the difference between both terms in the equivalence (4.6). A systematic discrepancy of about 0.1 dB in amplitude and 1 degree in phase has been detected. Note that the self-consistency tool only deals with amplitude errors. Phase errors have been taken into account by means of the IVT relative phases estimation [Corbella *et al.*, 2008b].

This systematic error is not easy to identify from the NS S-parameters imbalance (Table 4.2), since it is masked by random errors. However, the calibration consistency tool benefits from averaging all the calibration sequences. From results in Fig. 4.19, the

following preliminary outcomes can be pointed out:

- In redundant configuration, the NS output connected to the hinge cable is systematically 0.14 dB (3.5%) larger than the output connected to LICEF units in the same CMN.

- In nominal configuration, the NS output connected to the hinge cable is between 0.05 dB (1.2%) and 0.12 dB (3%) lower than the output connected to LICEF units in the same CMN.

- It does not seem an error in the computation of the cable losses through the hinge, since the cable is the same for both configurations.

- Errors revealed by the calibration consistency tool are in agreement with the NS S-parameters imbalance detailed in Table 4.2.

- These errors are large with respect to 1% amplitude errors in the calibration requirements [SMOS, 2003b, Torres *et al.*, 2007]. The PMS gain dependence on the arm position using the distributed calibration that has been revealed during the IVT tests could be caused by these errors, since calibration references are translated from one CMN to another based on a good knowledge of the NDN S-parameters.

Based on the PMS calibration self-consistency tool results, a mathematical amplitude correction factor can be retrieved to overcome the systematic errors presented by receivers fed by the same NS. Amplitude correction factors have been computed for each output of the NS (for each group of 6 receivers) and for both NS configurations:

$$factor_{NS\ output\ i} = \frac{\langle (T^{HOT}_{sysk_r} - T^{WARM}_{sysk_r}) \rangle_{all}}{\langle (T^{HOT}_{sysk_r} - T^{WARM}_{sysk_r}) \rangle_{6\ receivers\ NS\ output\ i}}. \tag{4.7}$$

For the NS in the arms, two amplitude correction factors have been retrieved, one for the output connected to the hinge cable (output 3 in Fig. 4.20) and the other for the output connected to the receivers in the same segment (output 4). Regarding the NS in the Hub, three amplitude correction factors (outputs 3, 4 and 5) have been retrieved from the consistency tool output. All the correction factors are summarized in Table 4.3.

S-parameters amplitude correction factors to be applied as a cascaded S-parameter at the NDN output are given by

$$S_{k0}|_{corrected} = \frac{S_{k0}}{\sqrt{f_{k0}}}, \tag{4.8}$$

where the term f_{k0} are the corresponding factors in Table 4.3 in linear units.

The differences $T^{HOT}_{sysk_r} - T^{WARM}_{sysk_r}$ after applying the amplitude correction factors are shown in Fig. 4.21 for both configurations. Now, the error presents a random distribution

Table 4.3: Amplitude correction factors from the Calibration Consistency tool for nominal and redundant configurations.

	Amplitude correction factors from Calibration Consistency tool [dB]									
	HUB	$A1$	$A2$	$A3$	$B1$	$B2$	$B3$	$C1$	$C2$	$C3$
3	-0.0244	0.0137	0.0411	0.0293	0.0214	0.0149	0.0679	-0.0131	0.0668	0.0585
Nom. 4	0.0277	-0.0136	-0.0407	-0.0292	-0.0213	-0.0149	-0.0669	0.0131	-0.0658	-0.0577
5	-0.0031									
3	-0.0786	-0.0660	-0.0636	-0.0685	-0.0633	-0.0698	-0.0510	-0.0890	-0.0247	-0.0237
Red. 4	-0.0170	0.0670	0.0646	0.0696	0.0642	0.0709	0.0516	0.0908	0.0248	0.0238
5	0.0973									

with much lower dispersion (around 4% peak-to-peak). This dispersion includes the S-parameter dispersion after temperature drift correction, the error and drift from factory PMS calibration parameters and the compensation for temperature PMS drift. These results were very promising since amplitude errors are below 1% (1σ) calibration requirements [SMOS, 2003b, Torres *et al.*, 2007] and absolute calibration of the NIR units during the in-orbit operation led to the improvement of these results using the same technique [Corbella *et al.*, 2011].

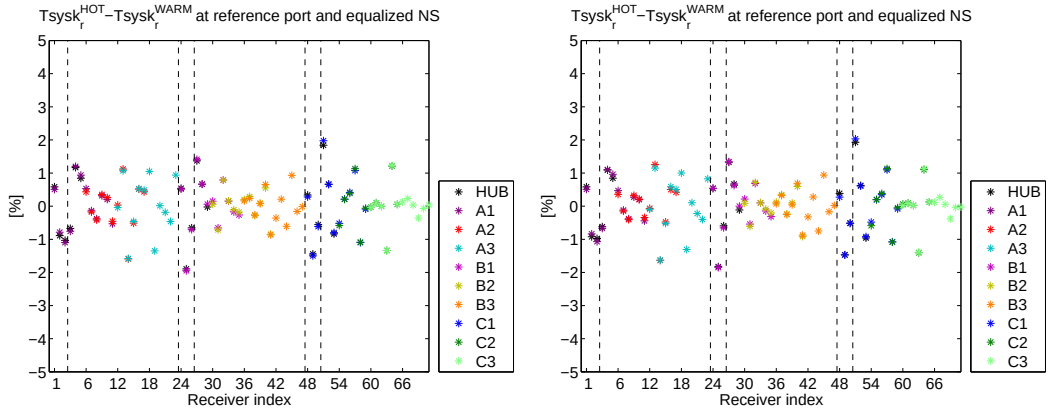

(a) Nominal NS (b) Redundant NS

Figure 4.21: Consistency tool output after applying the amplitude correction factors.

4.4.3 NIR consistency tool

During the internal calibration, NIR units are measuring the two noise temperatures (HOT and WARM) to be injected to each receiver through the NDN. These reference

temperatures are used to calibrate the LICEF units in the Hub, except those acting as NIR. The difference of the reference temperatures should be the same for all 6 NIR channels, except for the NDN S-parameters imbalance.

Based on the PMS calibration consistency tool, the consistency of the NIR measurements is assessed by referring all them to a virtual reference NDN output:

$$|S_{r0}|^2 = \langle |S_{i0}|^2 \rangle_{6NIR}, \tag{4.9}$$

being S_{i0} the S-parameter between the noise diode and the NDN output at NIR_i and S_{r0} the S-parameter between the common virtual port and port 0 of the NDN. This last value is given by the mean of the 6 NIR S-parameters. Therefore, NDN S-parameters imbalance can be removed by comparing the 6 NIR measurements of HOT and WARM CAS noise temperatures at the virtual reference port

$$T^{HOT}_{sys_{N\,r}} - T^{WARM}_{sys_{N\,r}} = \left(T^{HOT}_{sys_N} - T^{WARM}_{sys_N}\right) \cdot \frac{|S_{r0}|^2}{|S_{i0}|^2}. \tag{4.10}$$

Figure 4.22 shows the results from the NIR consistency tool for nominal and redundant configurations. It must be pointed out that during on-ground measurements, the accuracy of the NIR noise sources is based on a ground calibration since NIR sky calibration was not feasible inside the anechoic chamber. External calibration events during in-orbit measurements [Brown *et al.*, 2008] allowed the improvement of the NIR absolute calibration, reducing the dispersion of the NIR units results.

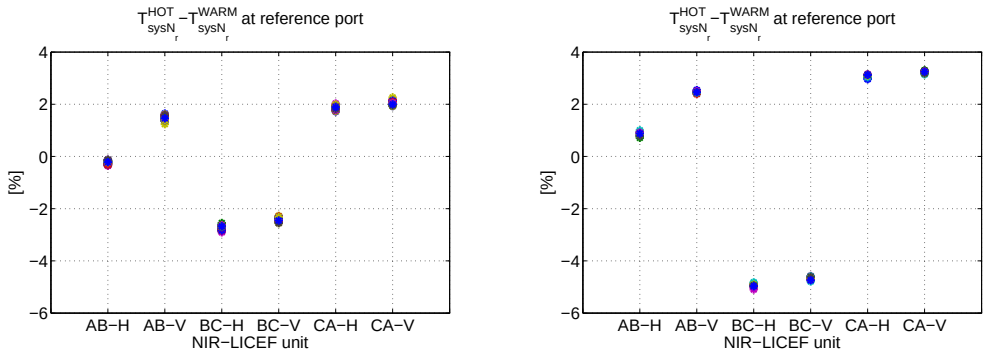

(a) Nominal NS (b) Redundant NS

Figure 4.22: Relative error in CAS noise temperatures retrieval computed using the NIR Consistency tool.

4.4.4 Impact of the amplitude correction factors application

This section is devoted to analyze the impact of the amplitude correction factors from the calibration consistency tool on the calibration parameters. LICEF noise temperatures re-

trieved from the distributed noise injection method (see chapter 3) are shown in nominal and redundant configurations (Fig. 4.23). The dependence of the receiver noise temperatures with the LICEF position in the arms can be clearly observed. The difference of this parameter between both configurations (see Fig. 4.24) reveals that the problem is associated to the CAS S-parameters at PD/NS level.

The same analysis is performed after applying the amplitude correction factors from calibration consistency tool (Table 4.3). In this case, similar values are retrieved both in nominal and redundant configurations (Fig. 4.25), as expected. It must be pointed out that receiver noise temperatures are, after the correction, independent on the LICEF position in the arms and always lower than 2.5 K (see Fig. 4.26).

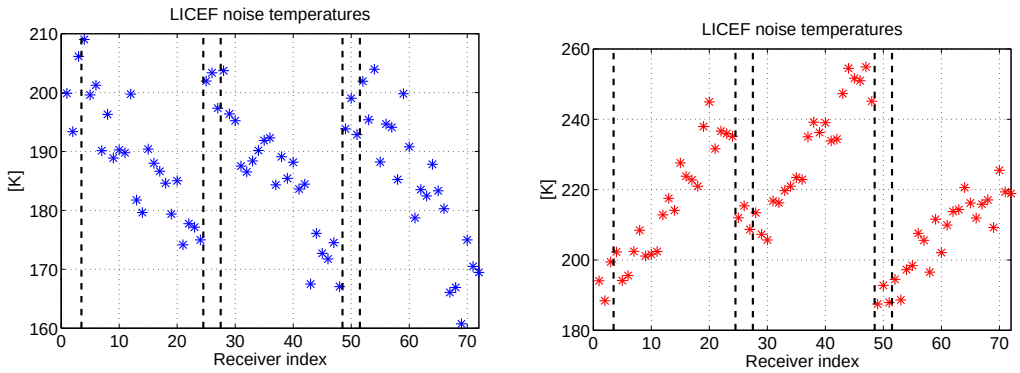

(a) Nominal configuration (b) Redundant configuration

Figure 4.23: LICEF noise temperatures by distributed noise injection before applying the amplitude correction factors.

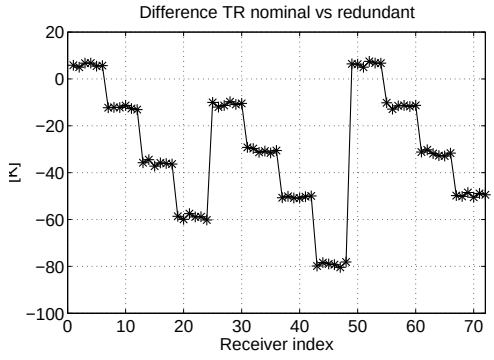

Figure 4.24: Difference of LICEF noise temperatures between nominal and redundant configurations before applying the amplitude correction factors.

A similar analysis has been performed to assess the impact of the correction on the PMS gain calibration. The relative difference between the PMS gain computed using the two-level four-points method (calibration baseline, as given in (3.16)) and the one

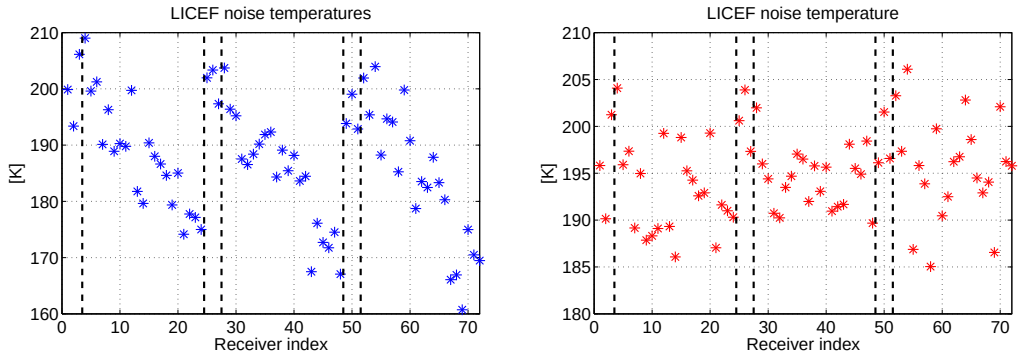

(a) Nominal NS configuration

(b) Redundant NS configuration

Figure 4.25: LICEF noise temperatures by distributed noise injection once amplitude correction factors have been applied.

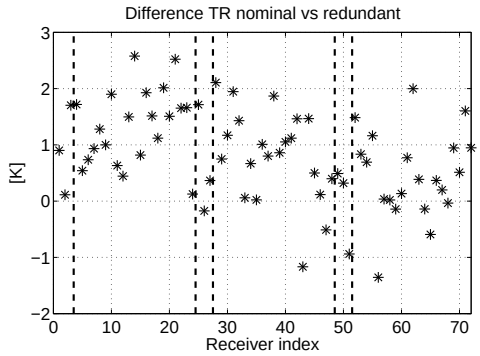

Figure 4.26: Difference of LICEF noise temperatures between nominal and redundant NS configurations once amplitude correction factors have been applied.

computed by the one-point approach (chapter 5) is analyzed. In this second method, receiver noise temperature accurately measured at calibration port by Mier Comunicaciones inside a climate chamber has been used. Note that one-point calibration approach is independent of the NDN characterization. Figure 4.27(a) shows the PMS gain relative difference before the amplitude correction factors application. The dependence of this magnitude with the LICEF position in the arm can be clearly observed. However, results once the correction have been applied show that the distributed calibration approach is independent on the arm position (Fig. 4.27(b)). The remaining difference (around 7%) is probably due to the absolute calibration errors in the NIR units. NIR absolute calibration is performed in-orbit by means of the external calibration events (sky views) [Brown *et al.*, 2008], which are not feasible on ground inside the anechoic chamber.

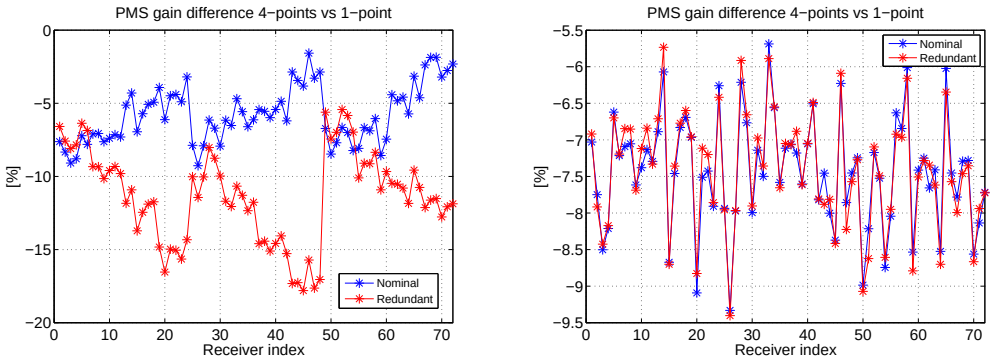

(a) (b)

Figure 4.27: PMS gain relative difference: 4-points method with respect to 1-point approach. (a) Before amplitude correction. (b) Once the correction has been applied.

4.4.5 Conclusions

The amplitude self-consistency tool has shown to be a quite useful utility to assess the performance of MIRAS amplitude calibration scheme along the mission. It has been shown that the NDN S-parameters presented small although non-negligible errors that have required further correction. This additional correction, the so-called CAS correction factors, are an output of the Calibration Consistency tool. Once this correction has been applied, residual amplitude errors after calibration have been reduced achieving the 1% amplitude calibration requirement. Note that ground consistency has been applied at the calibration plane (CIP) since only internal measurements were available. However, the same principle has been applied at the antenna plane to retrieve the flight CAS correction factors and antenna efficiency during Commissioning Phase tests [Corbella *et al.*, 2011, Durán, 2010].

In addition, the distributed calibration approach has been validated after applying the CAS correction factors. Both PMS gain and receiver noise temperatures have shown to be independent on the LICEF position in the arm and to have similar values for nominal and redundant calibration configurations, as expected.

4.5 Calibration of temperature phase drift

During the MIRAS instrument electrical test campaign, the phase of the local oscillator (LO) showed a significant dependence on the physical temperature, affecting the stability of the correlation phases. During the IVT characterization campaign, the correlation phases were very stable since the physical temperature of the receivers was also very stable (Fig. 4.28). However, during the instrument thermal characterization inside the LSS, LICEF physical temperatures were varied to emulate the space conditions. For this reason, thermal characterization measurements have been used to investigate the correlation phase drifts with physical temperature variations.

A comprehensive analysis of the correlation phases drifts with physical temperatures fluctuations during LSS measurements has been described in [Martín-Neira, 2007, González-Gambau *et al.*, 2008d]. One of the main outcomes of these studies is that baselines involving receivers within any segment present a small fluctuation in the correlation phase with the physical temperature variation (Fig. 4.29). The maximum peak-to-peak phase variation is found in some baselines within a segment in the Hub (up to 1 degree). The rest of baselines involving receivers in the same segment have fluctuations of the phase lower than 0.5 degrees. Nevertheless, the phases of baselines across segments are more affected by temperature changes (Fig. 4.30). Peak-to-peak phase variation for baselines across segments having a common noise source are listed in Table 4.4.

Considering from now on only the baselines across segments, it must be pointed out that correlation phases of different baselines involving the same two segments are very

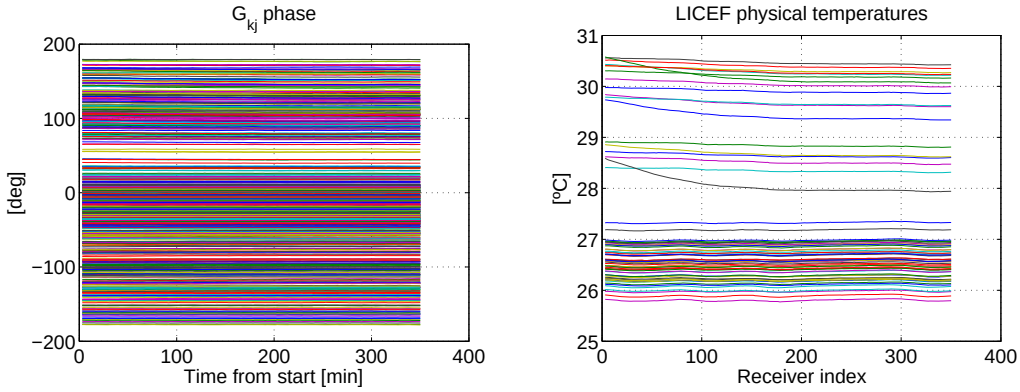

(a) Correlation phases drift.

(b) Receiver physical temperatures.

Figure 4.28: Stability of the G_{kj} phase during a test performed at Maxwell, in which the temperature of LICEFs was very stable.

Table 4.4: Peak-to-peak phase drift for baselines across segments.

Receiver k	Receiver j	Drift [deg]
H1	A1	16
H1	H2	12
H1	H3	4
A1	A2	4
A2	A3	4
H2	B1	4
H2	H3	8
B1	B2	3
B2	B3	3
H3	C1	10
C1	C2	3
C2	C3	2

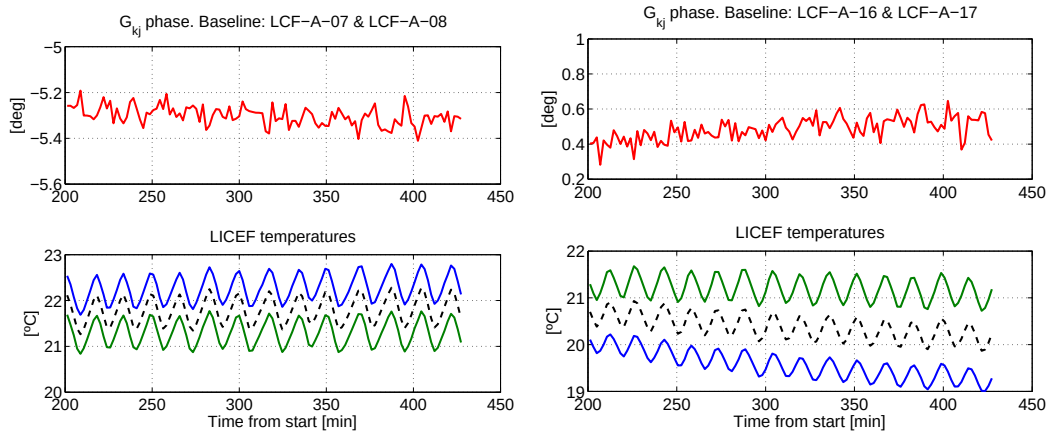

(a) (b)

Figure 4.29: Correlation phase drift of one baseline involving receivers in the first segment of arm A and another one involving receivers in the second segment (top plots). Physical temperature of both receivers forming the baseline and the average of both (bottom plots).

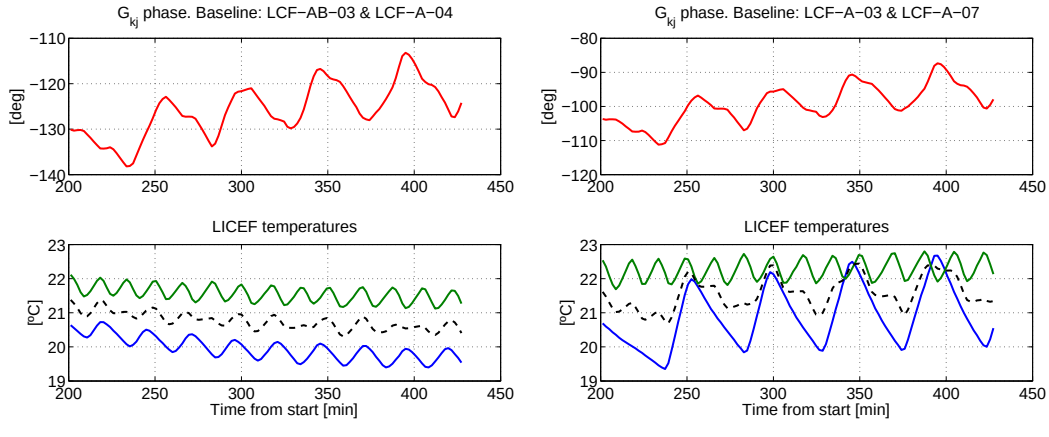

(a) (b)

Figure 4.30: Correlation phase drift of two baselines formed by receivers of the first segment in the hub and the first segment in the arm A (top plots). Physical temperature of both receivers forming the baseline and the average of both (bottom plots).

close to each other, even in the case where the profiles of the receiver physical temperatures are not similar (Fig. 4.30). All the previous results support the explanation that the cause of the phase drift is in the LO, which is common for the LICEF units in a segment, rather than at each particular receiver.

The instrumental phase to be calibrated is measured using two correlated noise injection levels. This phase can be split in a LICEF basis by applying matrix pseudo-inverse for each calibration sequence

$$\begin{pmatrix} \alpha_{1\,2} \\ \alpha_{1\,3} \\ \alpha_{1\,4} \\ \vdots \\ \alpha_{71\,72} \end{pmatrix} = \begin{pmatrix} 1 & -1 & 0 & 0 & \dots & 0 & 0 \\ 1 & 0 & -1 & 0 & \dots & 0 & 0 \\ 1 & 0 & 0 & -1 & \dots & 0 & 0 \\ \vdots & & & \vdots & & & \vdots \\ 0 & 0 & 0 & 0 & \dots & 1 & -1 \end{pmatrix} \begin{pmatrix} \alpha_1 \\ \alpha_2 \\ \alpha_3 \\ \alpha_4 \\ \vdots \\ \alpha_{71} \\ \alpha_{72} \end{pmatrix} \tag{4.11}$$

The matrix of the system in (4.11) has 612 rows (one for each baseline having a common noise source) and 72 columns (one for each receiver). The left-hand side column vector contains all the measured correlation phases. The system is solved after an iterative procedure to deal with phase wrapping in the α_{kj} measurements. It must be pointed out that the rank of the system is 71 since a constant phase term can be added to each individual phase. Therefore, when the absolute phases are estimated by computing the matrix pseudo-inverse, the retrieved phases always include an arbitrary constant phase term. As an example, the absolute phases of receivers in segment A1 after solving the system of equations in (4.11) are represented in Fig. 4.31(a). Note that memory track between consecutive calibrations is needed in order to remove the remaining phase jumps [González-Gambau *et al.*, 2008d]. Once this condition is applied in the resolution of the system, G_{kj} phase is continuous between calibrations, as it can be seen in Fig. 4.31(b).

Since only the differential phase drift between calibrations is relevant, the incremental phases from the first calibration sequence of receivers in segment A1 are represented in Fig. 4.32. What is apparent from this plot is that the phases of the six receivers in the segment have a very similar behavior.

In order to verify that phase drifts can be mainly assigned to the LO temperature drift, the incremental phases from the first calibration are plotted together per segments (Figs. 4.33 to 4.36, left-top plots). Physical temperature drifts of all receivers in the segment and its corresponding power divider physical temperature along the calibrations are also shown (Figs. 4.33 to 4.36, left-bottom plots). The reference receiver used in Figs. 4.33 to 4.36 is receiver LCF-C-20 (in the third segment of arm C). This receiver has been selected as the reference one because the LO phase variation between segment C3 and the others looks low (see Table 4.4). In any case, other references with a low

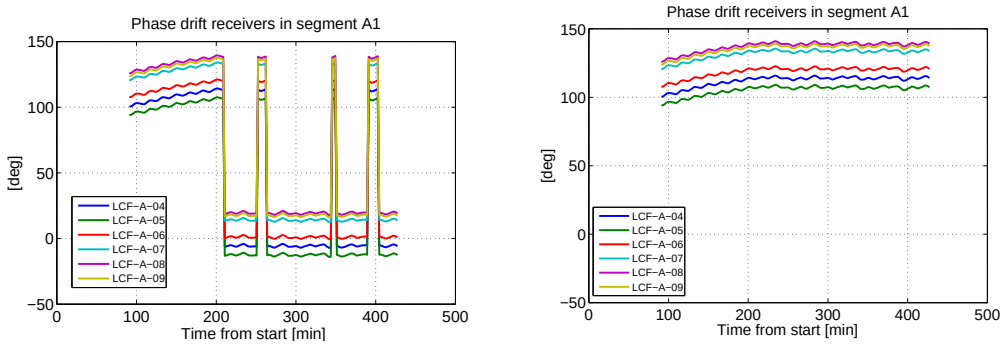

(a) Solving directly the system of equations proposed in (4.11).

(b) After applying memory track between consecutive calibrations.

Figure 4.31: Absolute phases of receivers in segment A1.

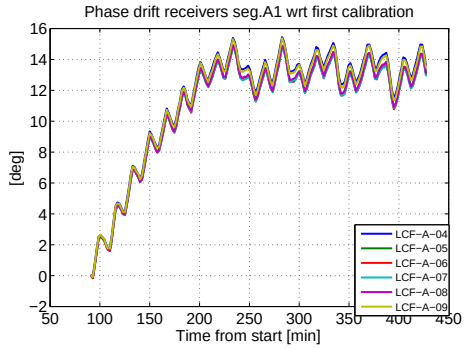

Figure 4.32: Incremental phase drift from first calibration sequence. Receivers in segment A1.

phase drift have been verified that produce similar results. Phase drift of receivers in a segment seems to roughly track the PD physical temperature drift in the case of the segments in the arms. These temperatures have been used to track the phase drift in this analysis due to the proximity with the LO, since physical temperature sensors are not available in the CMN. This approach has been found to perform quite satisfactorily in the arms. However, for receivers in the Hub, a clear relation between the phase drift and PD physical temperature drift can not be found. For these receivers (in segments H1, H2 and H3), the phase seems to track better the physical temperature drift of receivers LCF-AB-03, LCF-BC-03 and LCF-CA-03, respectively. In addition, phase drift for any single receiver is very low with respect to the absolute phase drift (Fig. 4.33 to 4.36, right plots). For receivers in segment A1 only [-0.3,0.5] over 25 degrees correspond to the individual contributions of LICEFs. From all the previous results, it can be concluded that the phase drift can be mainly ascribed to the LO phase drift due to temperature variations.

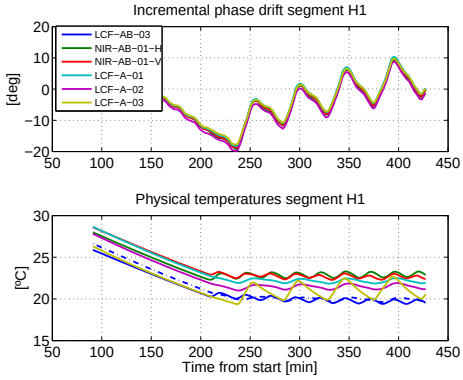

(a)

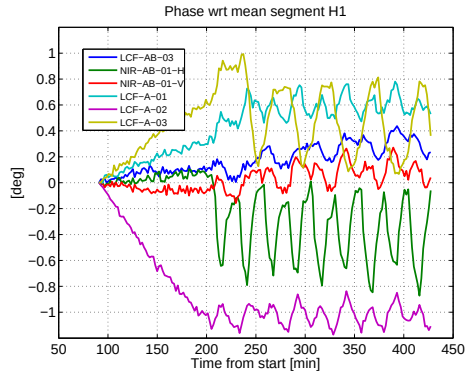

(b)

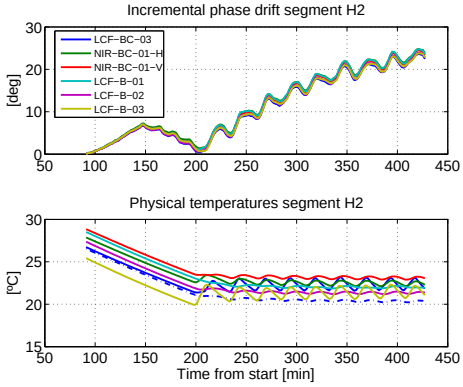

(c)

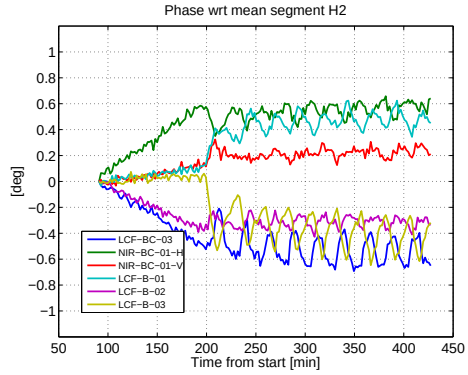

(d)

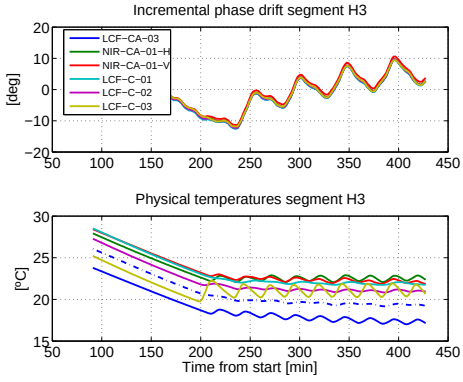

(e)

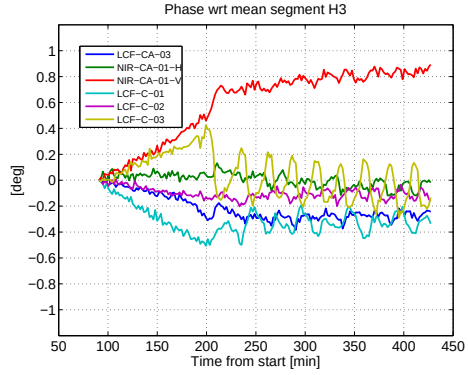

(f)

Figure 4.33: Phase drift of receivers in the Hub; (a) and (b) segment H1, (c) and (d) segment H2, (e) and (f) segment H3. Left plots: Incremental phase drift from first calibration for all receivers in the segment (top) (reference receiver: LCF-C-20). LICEFs and PD physical temperatures (bottom). Right plots: Phase difference with respect to the mean value of all receivers in that segment.

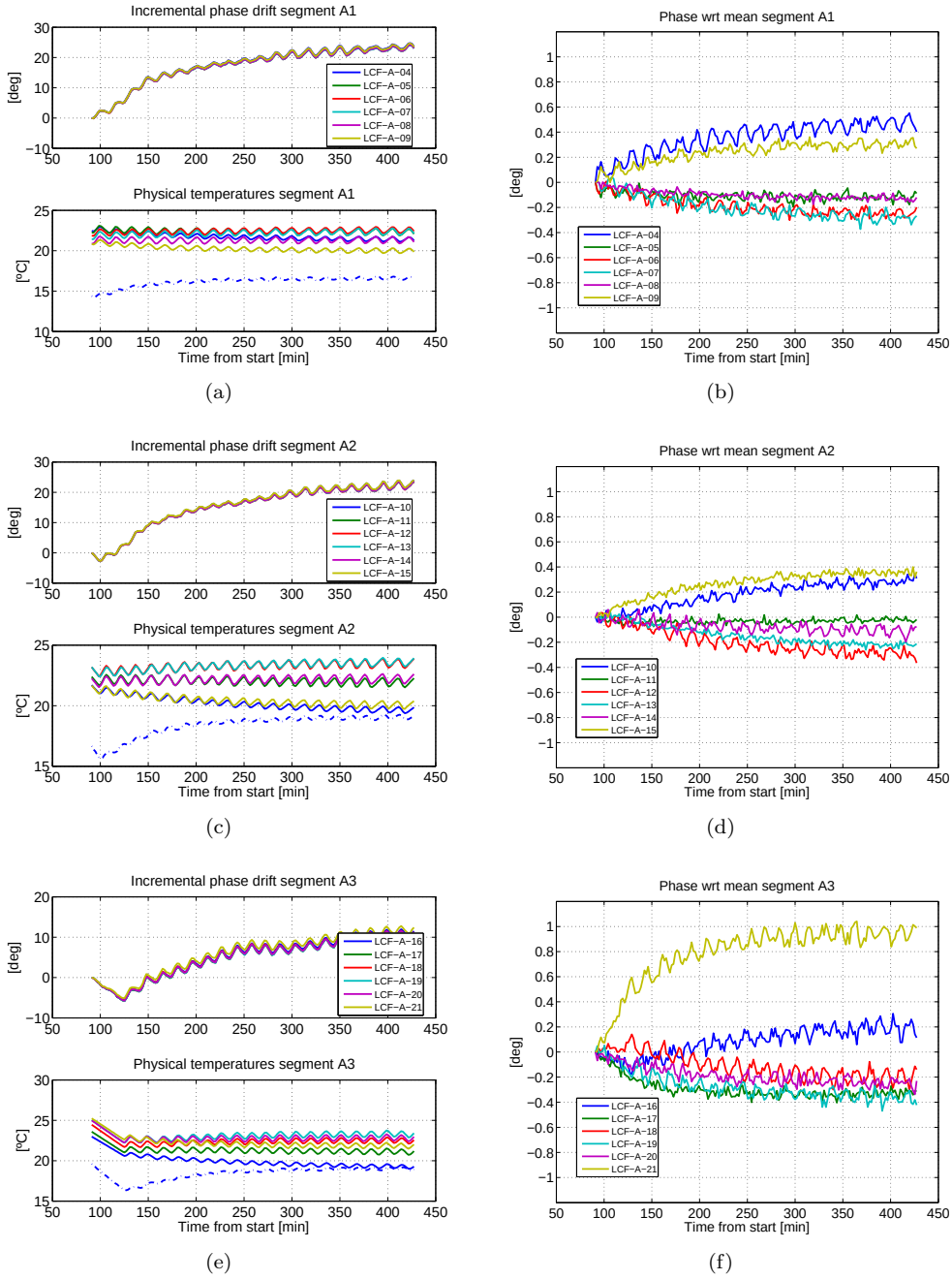

Figure 4.34: Phase drift of receivers in Arm A; (a) and (b) segment A1, (c) and (d) segment A2, (e) and (f) segment A3. Left plots: Incremental phase drift from first calibration for all receivers in the segment (top) (reference receiver: LCF-C-20). LICEFs and PD physical temperatures (bottom). Right plots: Phase difference with respect to the mean value of all receivers in that segment.

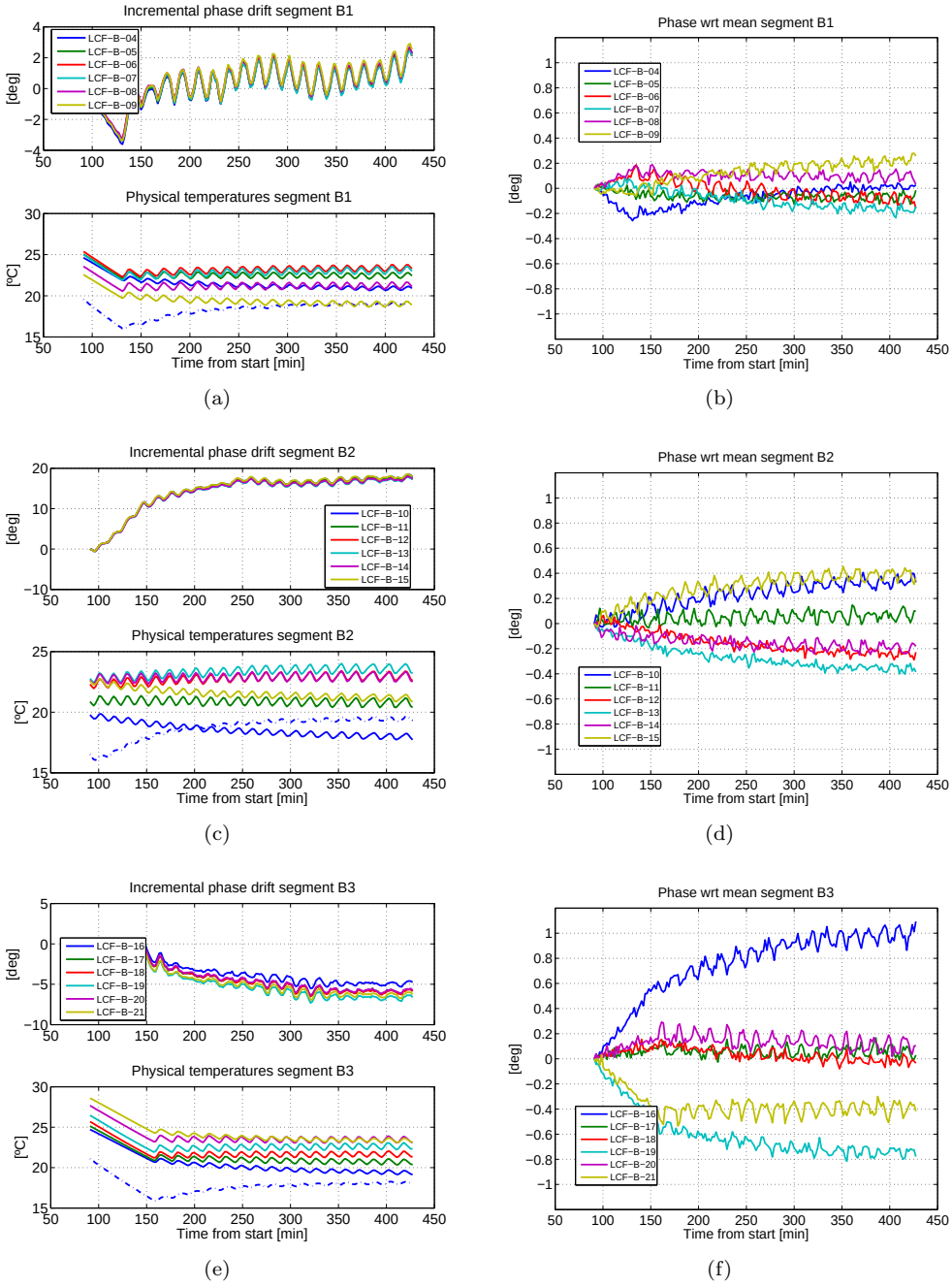

Figure 4.35: Phase drift of receivers in Arm B; (a) and (b) segment B1, (c) and (d) segment B2, (e) and (f) segment B3. Left plots: Incremental phase drift from first calibration for all receivers in the segment (top) (reference receiver: LCF-C-20). LICEFs and PD physical temperatures (bottom). Right plots: Phase difference with respect to the mean value of all receivers in that segment.

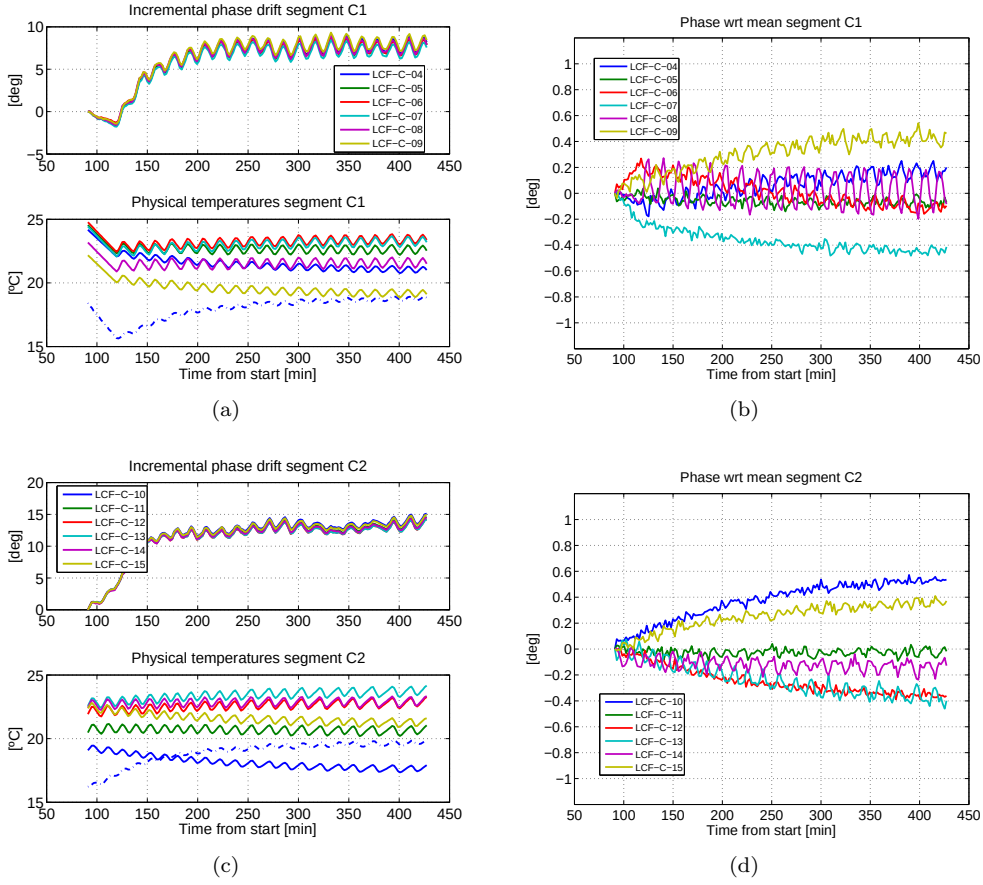

Figure 4.36: Phase drift of receivers in Arm C; (a) and (b) segment C1, (c) and (d) segment C2. Left plots: Incremental phase drift from first calibration for all receivers in the segment (top) (reference receiver: LCF-C-20). LICEFs and PD physical temperatures (bottom). Right plots: Phase difference with respect to the mean value of all receivers in that segment.

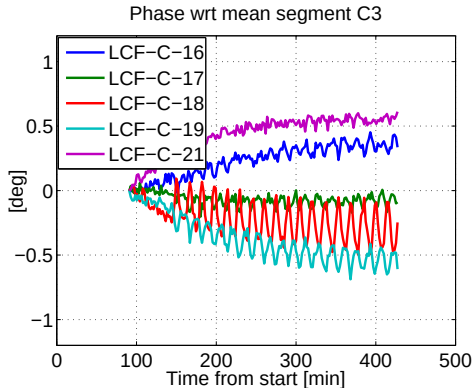

Figure 4.37: Incremental phase drift of receivers in segment C3. This CMN has been used as reference.

4.5.1 Phase track from physical temperature sensitivity

As mentioned in the previous section, each single phase drift includes a reference constant which masks the evolution of each individual phase. This is not a problem in a baseline basis since this constant is canceled out. Hence, next step in this analysis consists of tracking the LO phase by retrieving temperature sensitivity coefficients in a baseline basis [González-Gambau *et al.*, 2008d].

Correlation phases (α_{kj}) can be written as a function of the absolute phase sensitivities ($S_{Tph}^{\alpha_k}$, $S_{Tph}^{\alpha_j}$) and PD physical temperature drifts corresponding to receivers forming the baseline ($\Delta T_k, \Delta T_j$)

$$\begin{cases} \alpha_{1\,2} = S_{T_{ph}}^{\alpha_1} \cdot \Delta T_1 - S_{T_{ph}}^{\alpha_2} \cdot \Delta T_2 \\ \alpha_{1\,3} = S_{T_{ph}}^{\alpha_1} \cdot \Delta T_1 - S_{T_{ph}}^{\alpha_3} \cdot \Delta T_3 \\ \vdots \\ \alpha_{71\,72} = S_{T_{ph}}^{\alpha_{71}} \cdot \Delta T_{71} - S_{T_{ph}}^{\alpha_{72}} \cdot \Delta T_{72} \end{cases} \tag{4.12}$$

The retrieval of the absolute phase sensitivities to the physical temperature has been performed considering the following assumptions:

- Since LO physical temperatures are not available, physical temperatures and sensitivity coefficients are referred to the PD in the segment for the arms and receivers LCF-A-03, LCF-B-03, LCF-C-03 for the corresponding H1, H2 and H3 segments in the Hub.

- Since only the differential phase between calibrations is relevant, temperature and phase drifts are incremental from the first calibration.

- Equations of those baselines involving receivers in the same two segments have been averaged to a single equation (since the sensitivity is referred to the PD physical temperature, which is common for all receivers in a segment).

- Phase difference with respect to the mean of all receivers in a segment can be considered negligible (because it is much lower than the absolute phase drift, as it has been demonstrated in the previous section). Therefore, equations corresponding to baselines inside a segment have not been included in the linear regression to retrieve the absolute phase sensitivities.

Therefore, the system of equations to retrieve the 12 absolute phase (one per segment) sensitivities to the physical temperature drift is proposed in (4.13)

$$\begin{pmatrix} \alpha_{H1\,A1} \\ \alpha_{H1\,H2} \\ \alpha_{H1\,H3} \\ \vdots \\ \alpha_{C2\,C3} \end{pmatrix} = \begin{pmatrix} \Delta T_{H1} & -\Delta T_{A1} & 0 & 0 & \dots & 0 & 0 \\ \Delta T_{H1} & 0 & -\Delta T_{H2} & 0 & \dots & 0 & 0 \\ \Delta T_{H1} & 0 & 0 & -\Delta T_{H3} & \dots & 0 & 0 \\ \vdots & \vdots & \vdots & \vdots & \ddots & \vdots & \vdots \\ 0 & 0 & 0 & 0 & \dots & \Delta T_{C2} & -\Delta T_{C3} \end{pmatrix} \begin{pmatrix} S_{T_{ph}}^{\alpha_{H1}} \\ S_{T_{ph}}^{\alpha_{A1}} \\ S_{T_{ph}}^{\alpha_{H2}} \\ \vdots \\ S_{T_{ph}}^{\alpha_{C3}} \end{pmatrix} \tag{4.13}$$

Table 4.5: Absolute phase sensitivity coefficients to PD physical temperature, $S_{T_{ph}}^{\alpha}[deg/^{\circ}C]$.

$H1$	$A1$	$A2$	$A3$	$H2$	$B1$	$B2$	$B3$	$H3$	$C1$	$C2$	$C3$
2.1286	5.9779	4.7288	1.9762	−1.8238	1.1923	5.6996	1.6464	1.7794	0.6697	1.9652	2.2025

Figures 4.38 and 4.39 show plots of the original correlation phase and the retrieved one using the absolute phase sensitivities to temperature drift in Table 4.5 for the different sets of baselines between segments. After the analysis of the results, it can be concluded that an estimation of the LO phase drift sensitivity to temperature can be retrieved from receiver phase drift grouped by segments. However, since the physical temperature readings are not accurate enough (not close enough to the LO), phase tracking errors are slightly above the required accuracy for some of the segments, mainly in the hub.

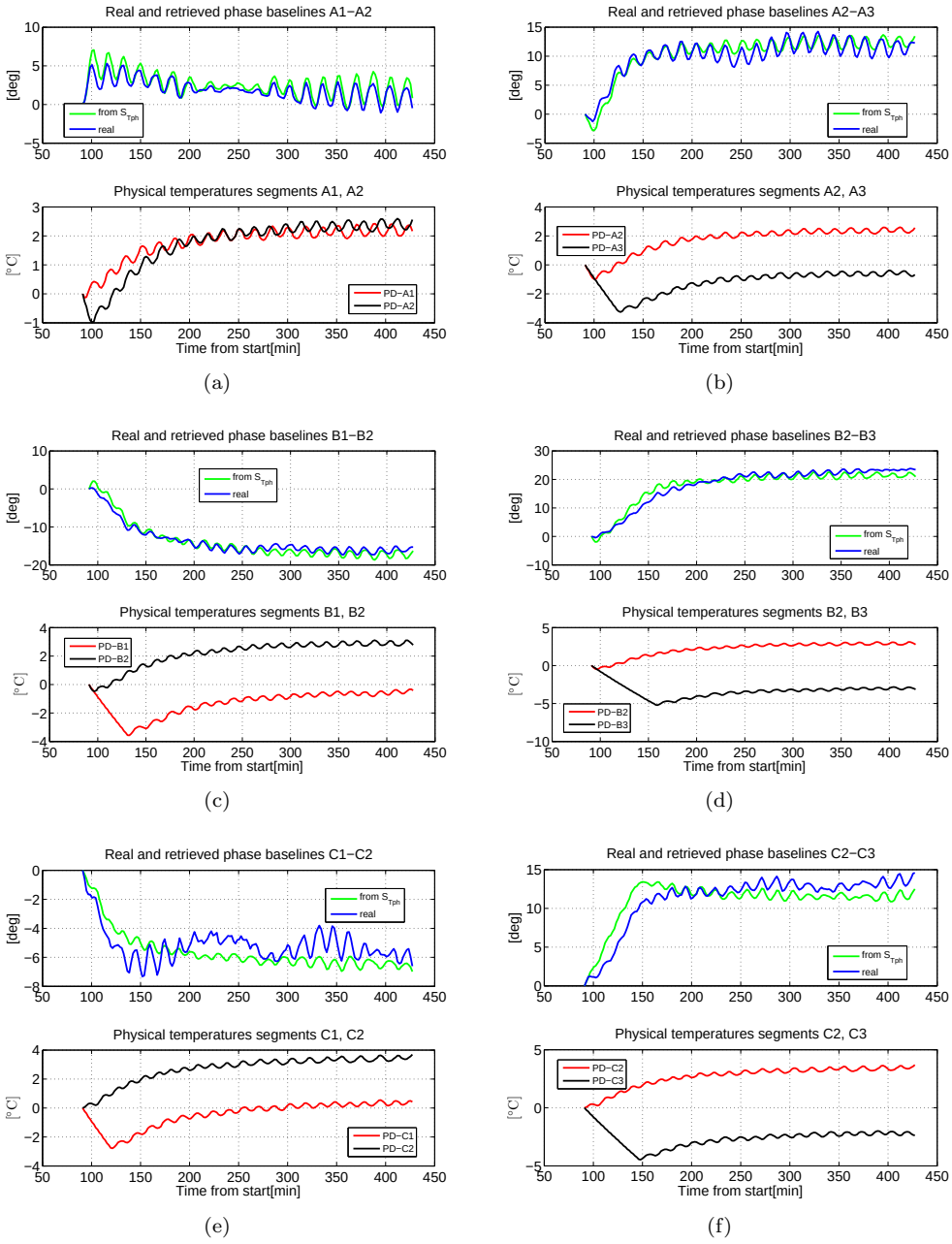

Figure 4.38: Top plots: Baseline phase (blue) and phase track using the absolute phase sensitivities to the physical temperature drifts (green) for baselines involving receivers in the arms. Bottom plots: Physical temperature variations in the corresponding segments. Baselines between segments: (a) A1-A2 (b) A2-A3 (c) B1-B2 (d) B2-B3 (e) C1-C2 (f) C2-C3.

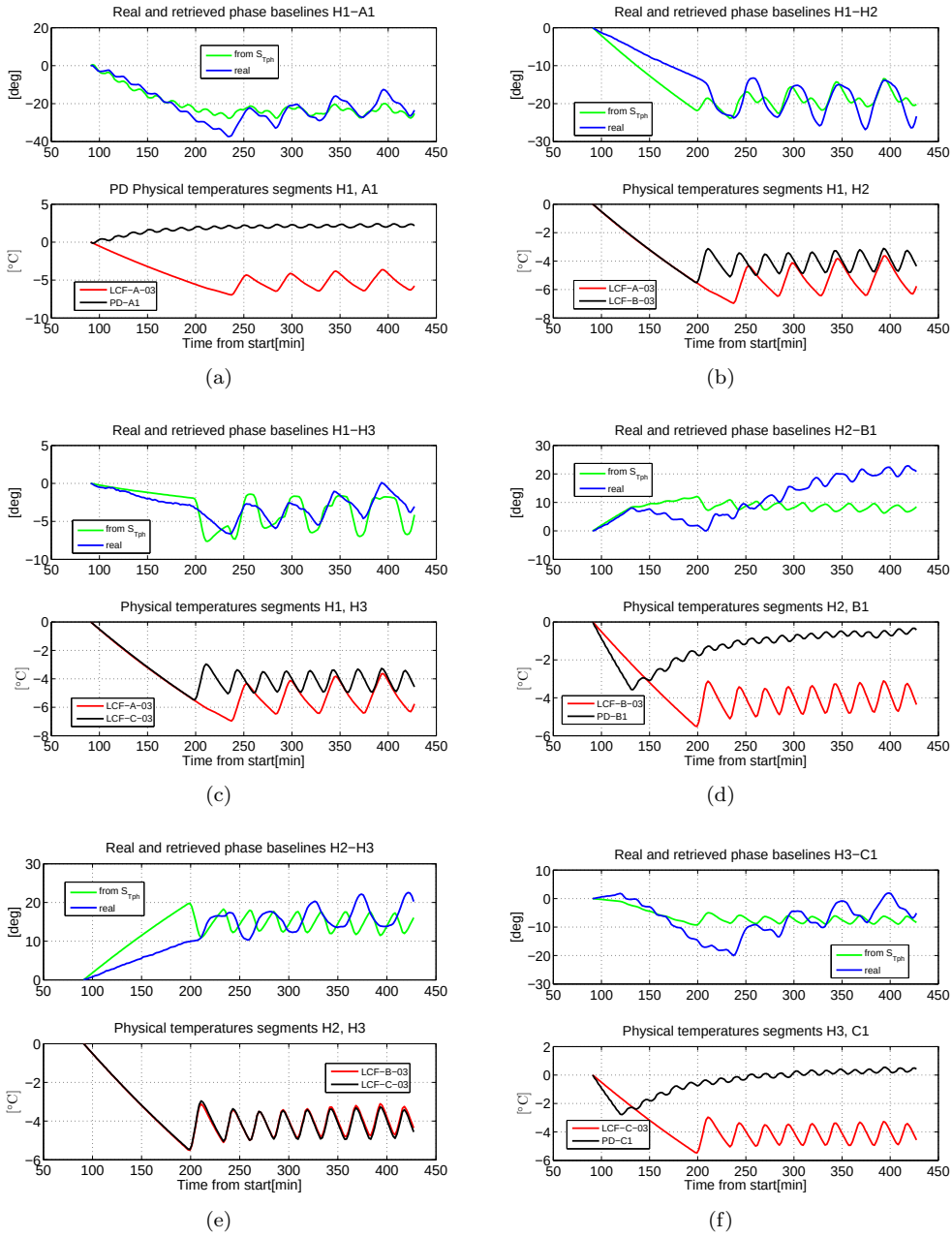

Figure 4.39: Top plots: Baseline phase (blue) and phase track using the absolute phase sensitivities to the physical temperature drifts (green) for baselines involving receivers in the Hub. Bottom plots: Physical temperature variations in the corresponding segments. Baselines between segments: (a) H1-A1 (b) H1-H2 (c) H1-H3 (d) H2-B1 (e) H2-H3 (f) H3-C1.

4.5.2 Conclusions

The correlation phase drift can be analyzed in a receiver basis (separable phases). Phase unwrap and memory track are required to retrieve a smooth and continuous phase drift assigned to each receiver. It has been confirmed that the phase drift is given in a CMN basis, due to LO phase drift. It has also been shown that differences in individual LICEF drifts within a segment can be considered almost negligible. The method developed in this work gives an estimation good enough to conclude that phase drift is basically caused by local oscillator sensitivity to physical temperature drift and it also may give an estimation of the expected baseline phase drift if different temperature gradients affect the segments. However, the physical temperatures readings are not accurate enough (sensors are not close enough to the LO) and therefore, phase tracking errors are slightly above the required accuracy (1 degree)[SMOS, 2003b, Torres *et al.*, 2007] for some of the segments, mainly in the hub. For this reason, an alternative phase calibration procedure is required: LO phase tracking calibrations by noise injection along the orbits [Brown *et al.*, 2008]. This method has allowed to track the phase drift during first Commissioning Phase and is currently implemented in SMOS Operational Phase to constrain phase errors below the 1 degree requirements at the cost of an increased percentage of time developed to calibration. In fact, at the current LO inter-calibration period of 10 minutes, phase tracking needs the bulk of the 1 % calibration time requirement.

4.6 Instrument stability

This section of the Thesis is devoted to assess the stability of the measurements provided by MIRAS. Long series of measurements (up to 12 hours) inside the empty Maxwell anechoic chamber (instrument measuring the chamber background) and at a constant temperature were performed during the IVT tests in order to assess the instrument stability. Long calibration sequences are interleaved with dual and full polarimetric measurements series. Therefore, the so-called ECCOS (Empty Chamber Correlation Offsets) were also measured with a large integration time. Every 1.2 seconds, MIRAS acquires a 2D image, generating 72 PMS voltage readings, 2556x2 correlator counts (real and imaginary part of complex correlations for the 2556 baselines), 6 NIR dicke pulse fraction, temperature readings (from sensors located in the receivers, in the calibration subsystem and NIRs) and control signals of the instrument operation modes among others. This fact implies that during a 12-hours test, MIRAS provides all these signals in approximately 36000 times. Due to the large amount of data to deal with, a smart data processing and visualization tool has been required [González-Gambau *et al.*, 2008a].

4.6.1 Data analysis and results

The main parameters to be analyzed in the stability measurements are the drift of the ECCOS, the antenna PMS voltage readings and the PMS calibration parameters (PMS gain, PMS offset and receiver noise temperature). Therefore, the tool envisaged to process this type of measurements must be able to:

- Assess the stability of the calibration parameters related to the PMS (gain, offset and receiver noise temperature). The variation of each parameter along time with respect to the mean value of all calibration sequences have been represented per segment (left plots in Fig. 4.41). The absolute values of these parameters have been also represented for all the calibration events (right plots in Fig. 4.41). Note that observing the physical temperature drift it can be clearly seen that the warming-up time of the instrument corresponds to approximately 200 minutes (see Fig. 4.40). This is the time at which the PMS calibration parameters can be considered stabilized.

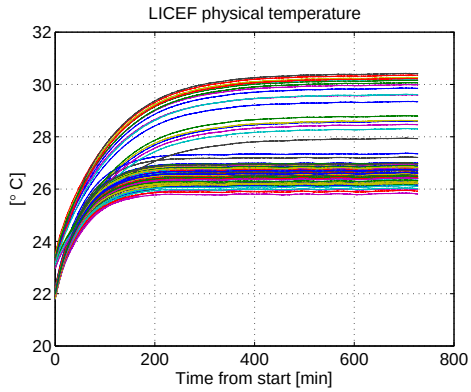

Figure 4.40: 12-hours stability measurements: LICEF physical temperatures.

- Show the stability of the antenna PMS voltage outputs. All consecutive antenna measurements in which the instrument settings are identical (horizontal and vertical polarization) are averaged and plotted per segment (sets of 25 measurements in horizontal/vertical polarization). In this way, all the measurements are reduced to a single plot to easily identify the proper behavior of the instrument (see first row in Fig. 4.42).

- Assess the ECCOS after some pre-processing to identify those baselines with the largest and the lowest drift due to the impossibility of representing the ECCOS of the 2556 baselines and their drift along time. Only the ten baselines with the largest (second row in Fig. 4.42) and the lowest standard deviation (last row in the same figure) are analyzed. ECCOS in each polarization are computed from the

antenna complex correlation measurements and subtracting the nearest correlation measurement during U-noise injection. The average of the different correlation measurements while injecting uncorrelated noise acquired in the test has not been carried out for long duration tests because it might introduce variations in their values.

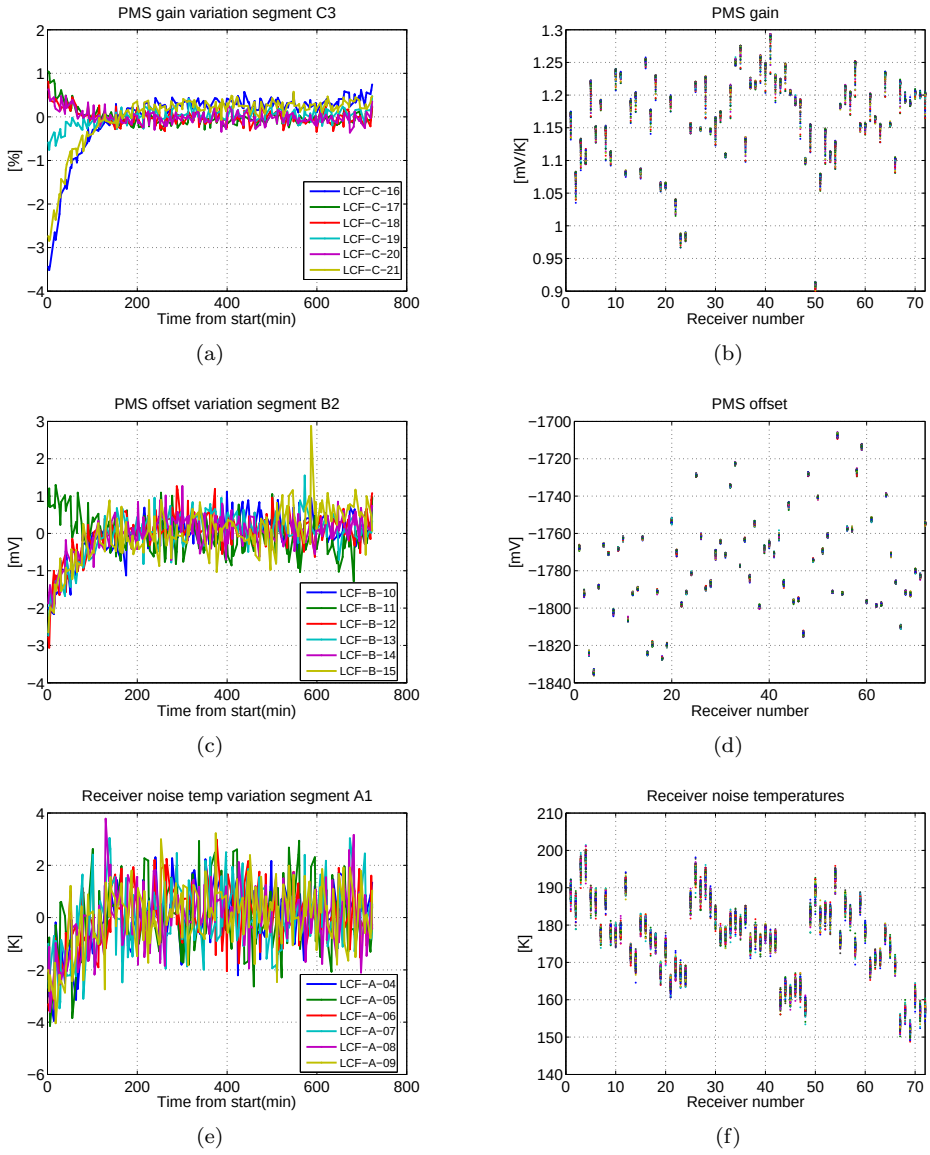

Figure 4.41: Stability plots of PMS calibration parameters. Left: error with respect to the mean value of all calibrations. Right: absolute value. (a) PMS gain segment C3, (b) PMS gain all receivers, (c) PMS offset segment B2, (d) PMS offset all receivers, (e) receiver noise temperature segment A1, (f) receiver noise temperature all receivers . Note that arm dependency of receiver temperature shown in this plot has been tracked down to the calibration system and corrected.

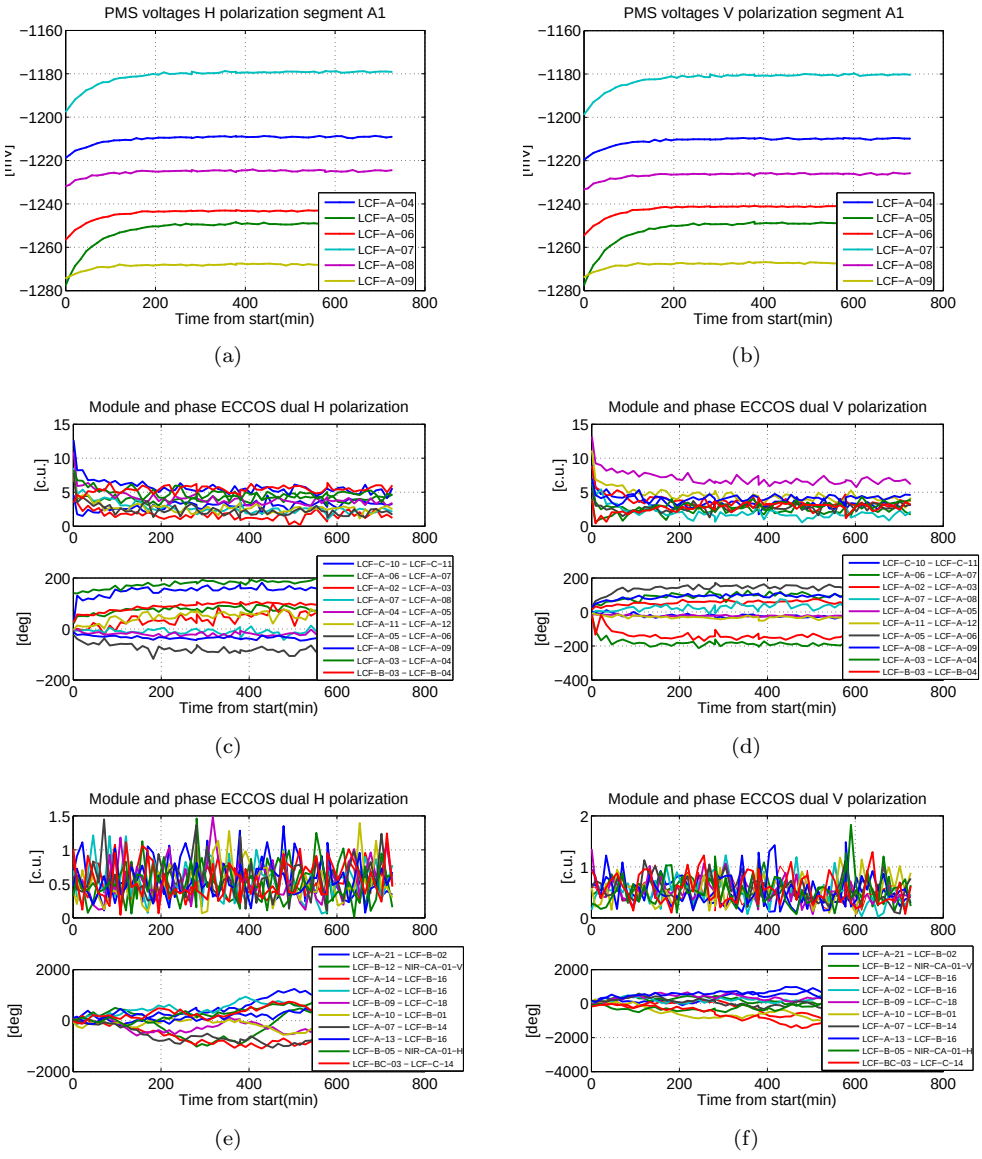

Figure 4.42: Stability plots of PMS voltage readings: (a) dual H polarization, (b) dual V polarization. ECCOS variation along time for the 10 baselines with the largest standard deviation: (c) dual H polarization, (d) dual V polarization. ECCOS variation along time for the 10 baselines with the lowest standard deviation: (e) dual H polarization, (f) dual V polarization.

4.6.2 Conclusions

From the analysis of these tests, some relevant conclusions must be pointed out. Empty chamber correlations offsets have been proved to be very low for baselines not sharing a common noise source or common local oscillator. For baselines connected through the distribution network, the residual offset has proved to be higher and this effect has a more important impact on baselines having a common local oscillator. In order to update the correlation offsets for in-orbit measurements, a calibration sequence where the instrument is only in U-injection mode is foreseen [Brown *et al.*, 2008]. The PMS calibration parameters are very stable along time and the antenna PMS voltages when the instrument is measuring the anechoic chamber background have the same behavior. It can be concluded that all receivers/baselines are stable and present a similar behavior. The frequency of the calibration events for each parameter need to be assessed during the first weeks of in-orbit operation but these outcomes suggest that the calibration events could be more spaced in time.

Chapter 5

One point calibration

The one-point calibration approach is an alternative method to the MIRAS amplitude calibration current baseline. The assessment of the one-point calibration performance is the goal of this chapter. Experimental analysis of the PMS absolute calibration using an all-LICEF mode has shown that it is a promising technique to be tested in-orbit. This technique has been also proposed for orbital PMS gain drift tracking during MIRAS/SMOS Commissioning Phase.

5.1 Introduction

The baseline amplitude calibration method uses the NIR and the NDN to calibrate the PMS using the internal calibration events (performed every 2 months) [Brown *et al.*, 2008] and compensates orbital temperature drifts by means of a sensitivity coefficient and the physical temperature readings of a probe placed at the LICEF front-end [Torres *et al.*, 2006]. However, ground tests have revealed some degree of hysteresis in the PMS drift with relation to the front-end physical temperature if fast and/or large temperature swing is present [Torres *et al.*, 2008]. To overcome this possible problem, the one-point calibration method has been developed as an alternative PMS gain calibration approach. Therefore, the one-point calibration is twofold:

1. PMS absolute calibration during external calibration events (deep sky views) as an alternative method to the current amplitude calibration baseline.

2. Orbital calibration as an alternative method to track the PMS gain drift due to the orbital temperature swing by means of periodic U-noise injection.

This alternative method proposes to calibrate PMS units at a more frequent rate (several calibration events per orbit) without using the reference radiometers to better

Table 5.1: PMS absolute calibration sequence.

Cold sky PMS validation sequence							
	Step	Epochs	LICEF	NIR	NS EVEN	NS ODD	Att.
PMS cold sky	1	4	U	LICEF-LU	OFF	OFF	L1
	2	8	Dual	LICEF-LA2	OFF	OFF	L1
	3	8	Dual	LICEF-LA	OFF	OFF	L0
	4	4	U	LICEF-LU	OFF	OFF	L0

Table 5.2: LO Phase tracking with U-noise calibration sequence.

LO Phase tracking with U-noise sequence						
Step	Epochs	LICEF	NIR	NS EVEN	NS ODD	Att.
1	1	U	LICEF-LU	OFF	OFF	L0
2	1	C	LICEF-LC	OFF	HOT	L0
3	1	C	LICEF-LC	HOT	OFF	L0

track the physical temperature orbital swing. PMS absolute calibration using the one-point approach is performed during the cold sky views switching between the measurement by the antenna (COLD temperature) and the internal matched load (switch in U-noise). Note that using this method it is not necessary a WARM external target. The Cold sky PMS calibration sequence is detailed in Table. 5.1 and it has been tested during in-orbit operation.

Regarding the orbital PMS gain drift tracking, periodic U-noise injection is needed to implement the one-point calibration approach. During the Commissioning Phase, a U-noise measurement was included in the Local Oscillator phase tracking calibration sequence in order to test the performance of this method (Table 5.2).

During the on-ground characterization of the instrument, this method has been used to compute the difference in the system temperatures between both noise injection levels (HOT and WARM) independently of the calibration subsystem. Therefore, this method has also contributed to the assessment of the residual systematic errors in the NDN S-parameters measurement, using the PMS Calibration Consistency Tool (see Chapter 4). This has led to the improvement of the current calibration baseline using CAS and NIR.

5.2 Description of the method

The relation between the PMS voltage and the input temperature, considering a PMS linear model, can be expressed as a function either of the system temperatures ($T^{AA}_{sys_k}$) or the antenna temperatures (T_A)

$$v^A_k = G^A_k T^{AA}_{sys_k} + v_{off_k} = G^A_k T_A + v'_{off_k}. \tag{5.1}$$

Note that in both expressions, the term of the PMS gain at the antenna plane (G^A_k) is the same and the relation between both offsets is

$$v'_{off_k} = v_{off_k} + G^A_k T^A_{R_k}, \tag{5.2}$$

where the term $T^A_{R_k}$ corresponds to the receiver noise temperature of LICEF k referred to the antenna plane.

Since the PMS offset can be independently estimated using the four-points method [Piironen, 2002], for the sake of simplicity it can be assumed that the instrumental offset equals to zero and the expression in (5.1) yields

$$v^A_k = G^A_k T^{AA}_{sys_k} = G^A_k \left(T_A + T^A_{R_k}\right). \tag{5.3}$$

The cold sky PMS calibration sequences are performed during the deep sky views programmed to calibrate the reference radiometers and compute the Flat Target Response [Brown *et al.*, 2008]. In addition, during these events, the PMS units are switched between the internal matched load (WARM temperature) and the antenna (see Table. 5.1), measuring the single external calibration target (known as COLD temperature).

For a better understanding, the scheme of the PMS front-end in Fig. 5.1 is used to illustrate the equivalent system temperatures computation for both switch positions.

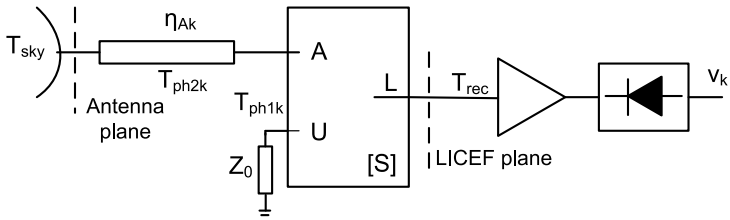

Figure 5.1: LICEF front-end scheme to illustrate the one-point calibration method, from [Torres *et al.*, 2006].

The equivalent system temperature at the switch output L when uncorrelated noise is injected to the receiver (WARM noise temperature, matched load), is given by

$$T^{UL}_{sys_k} = T_{ph1k} + T_{rec}, \tag{5.4}$$

where the first subscript indicates the switch position (U-load, WARM temperature) and the second one corresponds, in this case, to the switch output. This term can be expressed at the antenna plane by means of a plane translation as:

$$T_{sys_k}^{UA} = \frac{T_{ph1k} + T_{rec}}{\eta_{Ak}|S_{LAk}|^2}. \tag{5.5}$$

Following a similar reasoning, the system temperature while the instrument is measuring the cold sky (COLD temperature) can be written as

$$T_{sys_k}^{AA} = T_{sky} + \frac{T_{ph1k}\left(1 - |S_{LAk}|^2\right) + T_{rec}}{\eta_{Ak}|S_{LAk}|^2} + \frac{1 - \eta_{Ak}}{\eta_{Ak}} T_{ph2k}. \tag{5.6}$$

And the difference of the WARM and COLD system temperatures at the antenna plane yields

$$T_{sys_k}^{UA} - T_{sys_k}^{AA} = \frac{T_{ph1k} - T_{ph2k}}{\eta_{Ak}} + T_{ph2k} - T_{sky} = T_{phk_{eq}}^{A} - T_{sky}. \tag{5.7}$$

Once the equivalent system temperatures at the antenna plane have been computed, the PMS gain referred to the antenna plane only depends on the PMS voltages readings, the equivalent LICEF physical temperature at the antenna plane ($T_{phk_{eq}}^{A}$) and the sky temperature:

$$G_k^A = \frac{v_k^W - v_k^C}{T_{phk_{eq}}^{A} - T_{sky}}, \tag{5.8}$$

where v_k^W and v_k^C correspond to the WARM (switch in U-position) and COLD (measuring by the antenna) PMS readings, respectively.

It must be pointed out that in case of the thermal equilibrium (the switch and the antenna are at the same physical temperature), switching to the internal matched load is equivalent to placing an external target in front of the antenna at the same physical temperature (see Fig. 5.2). Then, the equivalent LICEF physical temperature at the antenna plane is T_{phk} and the expression in (5.7) simplifies to

$$T_{sys_k}^{UA} - T_{sys_k}^{AA} = T_{phk} - T_{sky}, \tag{5.9}$$

and therefore, the PMS gain is given by

$$G_k^A = \frac{v_k^W - v_k^C}{T_{phk} - T_{sky}}. \tag{5.10}$$

The receiver noise temperature measured during the PMS cold sky sequence can be written as

$$T_{R_k}^{A} = \frac{v_k^{C'} T_{phk} - v_k^{W'} T_{sky}}{v_k^W - v_k^C}. \tag{5.11}$$

Note that in expression (5.11), $v_k^{W'}$ and $v_k^{C'}$ correspond to the PMS voltage while U-noise injection and the voltage while the instrument is pointing to the cold sky, respectively, once the offset has been subtracted from them.

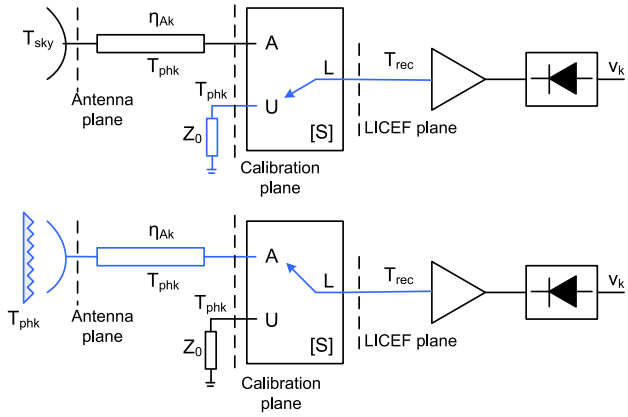

Figure 5.2: When the PMS front-end is in thermal equilibrium, switching to an internal load (top) is equivalent to placing an external target at the same temperature (bottom).

Both PMS gain and offset need to be corrected in temperature before applying them to the visibility denormalization (see section 3.5 in Chapter 3).

In order to track the PMS gain drift along the orbit, the most simple way to do it is using the U-noise injection, as proposed in [Torres *et al.*, 2008]. The PMS gain is retrieved as

$$G_{1_k}^A = \frac{v_k^U - v_{off_{1k}}}{T_{R1_k}^A + T_{ph1k}}, \tag{5.12}$$

where v_k^U is the PMS voltage when U-noise is injected at a physical temperature T_{ph1k}. Note that this term is equivalent to v_k^W and it is used to distinguish the U-noise injection during internal and external calibrations. $T_{R1_k}^A$ is the receiver noise temperature at the antenna plane at the U-noise injection temperature T_{ph1k}. It is corrected in temperature at the measurement time by means of the sensitivity coefficient to the physical temperature, $S_{T_{ph}}^{T_{R_k}^A}$, provided by the manufacturer at calibration plane and translated to the antenna plane using the following expression:

$$T_{R1_k}^A = T_{R0_k}^A + S_{T_{phk}}^{T_{R_k}^A} \left(T_{ph1k} - T_{ph0k}\right), \tag{5.13}$$

where $T_{R0_k}^A$ has been measured by the external PMS calibration at T_{ph0k} (5.13).

5.3 Assessment of the one-point calibration performance

One-point calibration performance has been analyzed in the framework of this Thesis. PMS absolute calibration using this technique has been evaluated by means of an experiment conceived to measure the Maxwell ceiling's antenna temperature using only the LICEFs (all-LICEF mode). The application of this alternative calibration approach to track orbital PMS gain drifts due to LICEF front-end temperature swing has been tested using both on-ground characterization and in-orbit measurements.

5.3.1 Estimation of Maxwell anechoic chamber's antenna temperature

During the IVT measurements in the Maxwell anechoic chamber facilities, physical temperature of the chamber was recorded by three temperature sensors. Two of them were located in the opposite corners of the ceiling and the third one was placed in the middle of one side of the ceiling, as shown in Fig. 5.3.

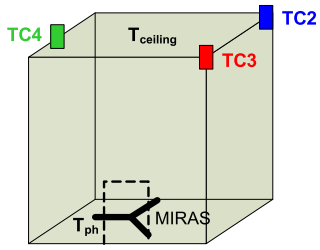

Figure 5.3: Scheme of the temperature sensors location during the IVT stability measurements.

The objective of this experiment consists of testing the absolute calibration of the receivers using only the LICEFs. To do that, brightness temperature of the Maxwell anechoic chamber has been estimated by means of the one-point calibration method and compared with the temperature recorded by the sensors.

Since during these measurements at the anechoic chamber the use of a cold target is not possible, the receiver noise temperature is not computed using the expression in 5.11, but measured at CIP at 21°C inside a climate chamber ($T^C_{R0_k}$) by the manufacturer (Mier Comunicaciones). It has been first corrected in temperature using the sensitivity coefficient to the physical temperature

$$T^C_{R1_k} = T^C_{R0_k} + S^{T^C_{R_k}}_{T_{ph}} \left(T_{ph1k} - T_{ph0k}\right), \tag{5.14}$$

where T_{ph1k} is the receiver physical temperature inside the Maxwell anechoic chamber and T_{ph0k} is $21°C$.

PMS gain at the calibration plane can be computed from PMS voltage when the instrument is in U-noise injection mode at a physical temperature T_{ph1k}

$$G^C_{1_k} = \frac{v^U_k - v_{off_{1k}}}{T^C_{R1_k} + T_{ph1k}}. \tag{5.15}$$

In order to compute the system temperature at the antenna plane, PMS gain and receiver noise temperature are first translated to that plane

$$G^A_{1_k} = G^C_{1_k} \frac{|S_{LAk}|^2}{|S_{LCk}|^2} \eta_{Ak} \tag{5.16}$$

$$T^A_{R1_k} = T^C_{R1_k} \frac{|S_{LCk}|^2}{|S_{LAk}|^2 \eta_{Ak}} + T_{ph1k} \left(\frac{|S_{LCk}|^2}{|S_{LAk}|^2 \eta_{Ak}} - 1 \right) \tag{5.17}$$

Using the PMS gain (5.16) and the receiver noise temperature (5.17) expressed at the antenna plane, the antenna temperature at the anechoic chamber can be estimated as

$$T_{A_k} = \frac{v^A_k - v_{off_{1k}}}{G^A_{1_k}} - T^A_{R1_k} \tag{5.18}$$

Stability measurements performed during the IVT campaign have been used to analyze the performance of the one-point calibration method. These tests include not only measurements of the anechoic chamber background (in dual and full polarization modes) but also interleaved long calibration sequences (around seven minutes) to assess the calibration parameters stability. This sequence is then cyclically repeated. All the analyzed stability measurements lasted about 12 hours. From measurements in full polarization mode, only those epochs with the three arms in the same polarization have been used, i.e. measurements equivalent to dual polarization mode.

In all the results that are presented hereafter, in addition to the antenna temperature measured by LICEFs, the maximum (always coincident with TC4 sensor), the minimum (always coincident with TC2) and the mean value of the temperatures provided by the three sensors are plotted along the complete test. Although the antenna temperature is normally expressed in Kelvin units, all the plots show the antenna temperature expressed in Celsius degrees for comparison to the sensor readings.

In a first stability test starting on 30^{th} of May 2007, the measurements were acquired while the instrument was still warming up (see Fig. 5.4). Receivers having a large variation in temperature correspond to the receivers in the Hub.

In order to estimate the ceiling temperature from LICEFs, first, the antenna temperature estimated by each LICEF has been averaged using a sliding window of 501 samples in order to smooth the signal for an easy comparison with the sensors readings. Antenna temperatures measured by all the 66 PMS units have been averaged (for horizontal and vertical polarizations) and compared to the maximum, the minimum and the mean value

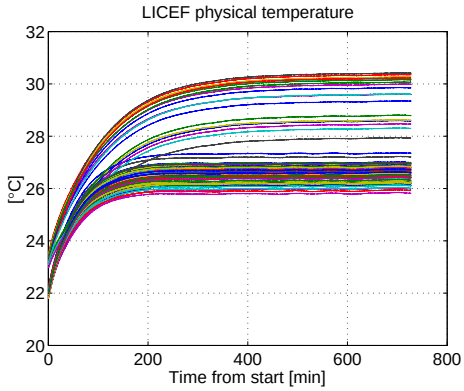

Figure 5.4: LICEFs physical temperature along the complete stability test starting on 2007-May-30. Receivers with a higher temperature variation correspond to receivers in the Hub. At the beginning of the test, the instrument was still warming up.

of the temperatures provided by the sensors (Fig. 5.5(a)). Then, the systematic error (bias) and the thermal noise are reduced by a factor larger than 8. It must be pointed out that the average of the antenna temperature estimated by the 66 LICEFs tracks the ceiling temperature recorded by the thermal sensors within a margin of 0.1-0.2 K and negligible bias. Note that at the beginning of the test, the ceiling temperature estimated by LICEFs is warming down about 0.5°C whereas the LICEF physical temperatures are warming up between 4.5 and 7°C (Fig. 5.4). Therefore, it can be concluded that the antenna temperature measured by the LICEFs does not show any dependency on their own physical temperature. Similar conclusions can be extracted from the results in other stability measurements performed in the following days (see Figs. 5.5(b) and 5.5(c)).

The average in time of the ceiling temperature estimation by each of the 66 receivers along the full stability test is represented in Fig. 5.6 for both polarizations (stars). The mean antenna temperature (both horizontal and vertical) is also plotted. For comparison purposes, the mean for the maximum and minimum temperatures registered by the three sensors along the full test are plotted as straight lines. From this result, it can be clearly seen that each LICEF unit presents some bias in the estimation of the ceiling's brightness temperature. Moreover, the dispersion of this bias is larger in vertical than in horizontal polarization. The origin of this dispersion is related to the uncertainty in the antenna efficiency. Note that 1% of error in the estimation of the antenna efficiency translates into a 2.93 K offset error in the estimation of the antenna temperature. Therefore, the dispersion which can be observed in Fig. 5.6 for vertical (3.5 K peak-to-peak) and horizontal (2 K peak-to-peak) are consistent with [Torres *et al.*, 2007]. This uncertainty affects only to the measurements inside the anechoic chamber, since the cold target is not feasible. Although the performance of each individual LICEF is not remarkable, the mean value of the 66 LICEFs allows tracking the ceiling's brightness temperature within a margin of 0.1-0.2 K and negligible bias.

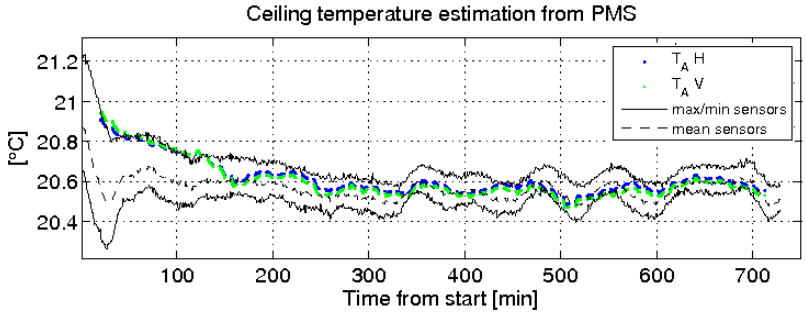

(a) Stability test start time: 2007-May-30 19:48:51

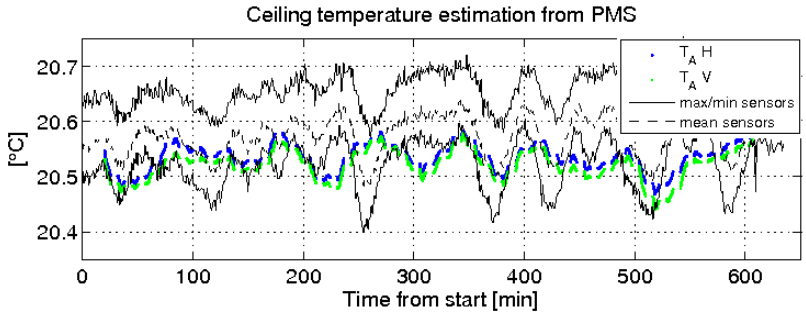

(b) Stability test start time: 2007-May-31 20:42:05

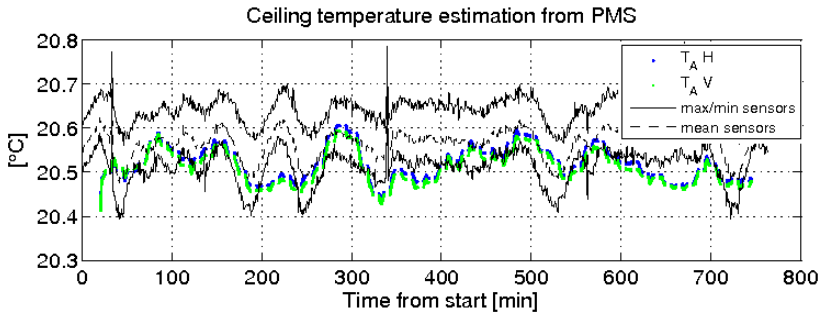

(c) Stability test start time: 2007-Jun-03 19:03:47

Figure 5.5: Ceiling temperature estimation by means of the one-point calibration in both polarizations. Maximum and minimum temperature values (black solid line) and the average of them (black dashed line) have been overlaid for comparison.

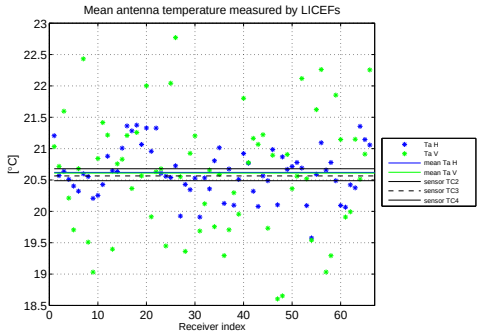

Figure 5.6: Mean ceiling temperature estimated by each of the 66 receivers in H (blue stars) and V (green stars) polarizations. Note that the mean temperature value for H (blue solid line) and V (green solid line) polarization are very similar. The temperatures registered by the three sensors along the complete test are plotted as straight lines.

A similar study has been performed using the reference radiometers to estimate the anechoic chamber ceiling's brightness temperature. Details of the antenna temperature measurement by NIRs can be found in [Colliander *et al.*, 2007a]. Although this is not an issue of this thesis work, the antenna temperatures estimated by NIRs provided by the MTS [Corbella *et al.*, 2008a] have been represented for comparison purposes. A

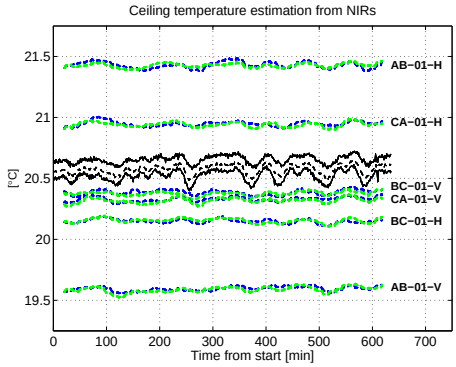

Figure 5.7: Ceiling temperature estimation by the 6 NIR channels. Maximum and minimum temperature values (black solid line) and the average of them (black dashed line) have been overlaid. Stability test start: 2007-Jun-03.

sliding window of 501 samples has been also applied to the antenna measurement of each NIR channel. Since the reference radiometers are continuously measuring in the same polarization, the number of measurements in H/V polarization is twice the number of the LICEF measurements. For this reason, the antenna temperature measured by each NIR channel has been filtered to have the same number of measurements than in the analysis with LICEFs. This is indicated in the legend of Figs. 5.8 and 5.9 as H-switch and V-switch. Ceiling temperature estimation by each NIR channel along the first stability

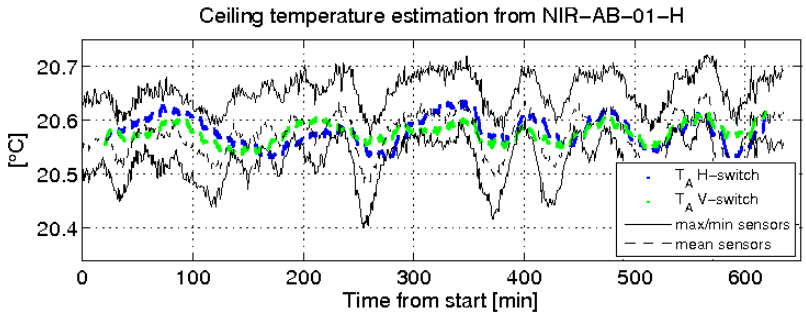

(a) Offset NIR-AB-01-H: -0.85 K

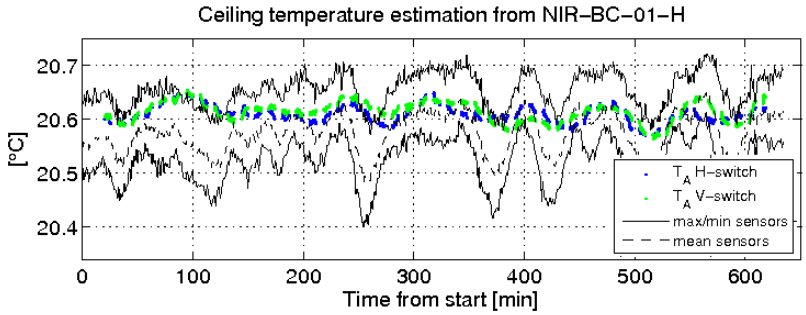

(b) Offset NIR-BC-01-H: 0.46 K

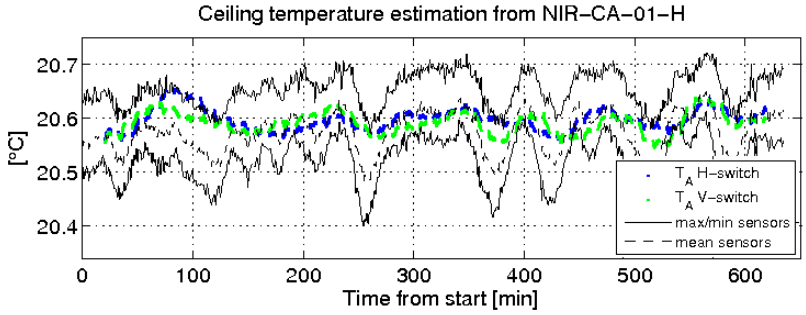

(c) Offset NIR-CA-01-H: -0.35 K

Figure 5.8: Ceiling temperature estimation from NIRs (H channels). Maximum and minimum temperature values (black solid line) and the average of them (black dashed line) have been overlaid.

measurement is shown in Fig. 5.7. Note that the NIRs are not well calibrated (ground calibration has been used [Colliander *et al.*, 2007b]) since a cold target is not feasible inside the anechoic chamber.

In order to evaluate the accuracy of the ceiling's brightness temperature estimation, an offset has been added to each NIR channel to overlap the NIR antenna temperature level and the sensors readings. Results are presented in Figs. 5.8 and 5.9 for NIR H and V channels, respectively. The absolute brightness temperature measured by the NIR channels varies within 1.2 K. Offsets are indicated in the caption of the figures. The estimation of each individual LICEF also presents a bias in this order of magnitude. However, the average of the 66 estimations results in a negligible bias. It can be concluded from the aforementioned results that the NIR antenna measurements track the small temperature variations in the sensor readings within a margin of 0.1 K. However, in terms of the absolute accuracy, these measurements present a bias which varies between 0.25-0.87 K, depending on the channel. These results are consistent with those obtained in [Colliander *et al.*, 2009].

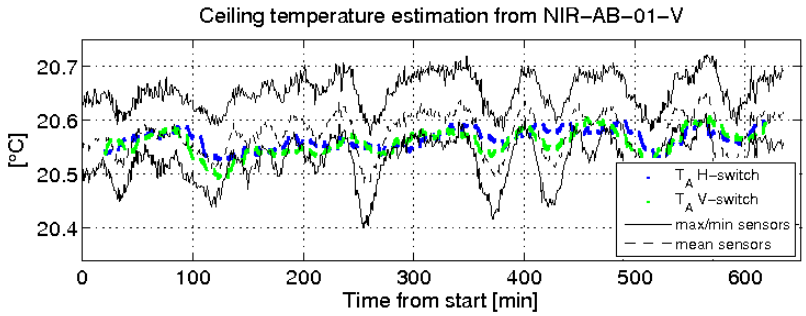

(a) Offset NIR-AB-01-V: 0.97 K

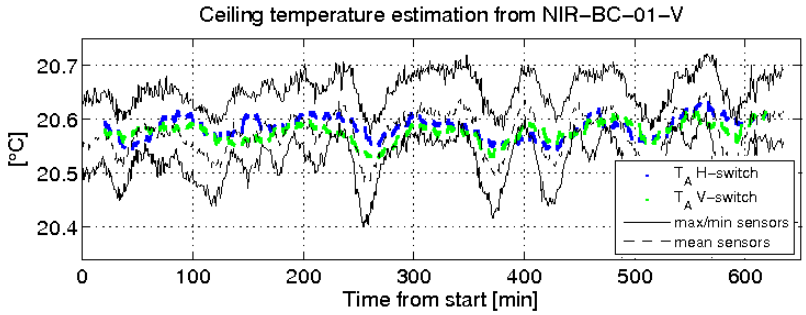

(b) Offset NIR-BC-01-V: 0.2 K

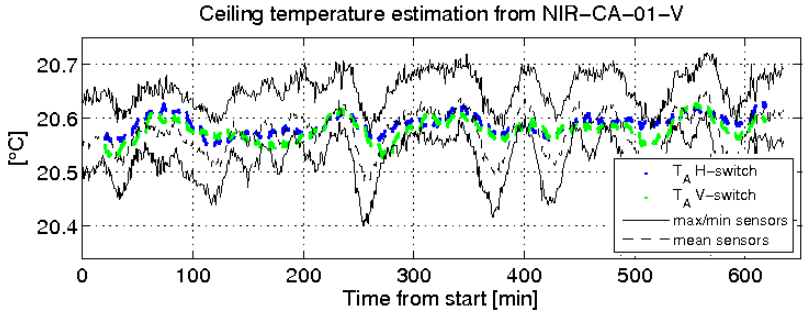

(c) Offset NIR-CA-01-V: 0.26 K

Figure 5.9: Ceiling temperature estimation from NIRs (V channels). Maximum and minimum temperature values (black solid line) and the average of them (black dashed line) have been overlaid.

5.3.2 PMS gain drift tracking by U-noise injection

As it was mentioned in the introduction of this chapter, MIRAS amplitude calibration baseline consists of using the CAS to calibrate the PMS and compensating its dependence on the temperature drift by means of the sensitivity coefficients computed in [Pablos, 2010] and the LICEF physical temperatures. During in-orbit measurements, LICEF physical temperature variation is regulated by the active thermal control. This way, orbital LICEF temperature drifts should be around 2°C peak-to-peak [McMullan *et al.*, 2008]. However, this small temperature drift (see Fig. 5.10) must be corrected in order to prevent a non-negligible PMS gain variation.

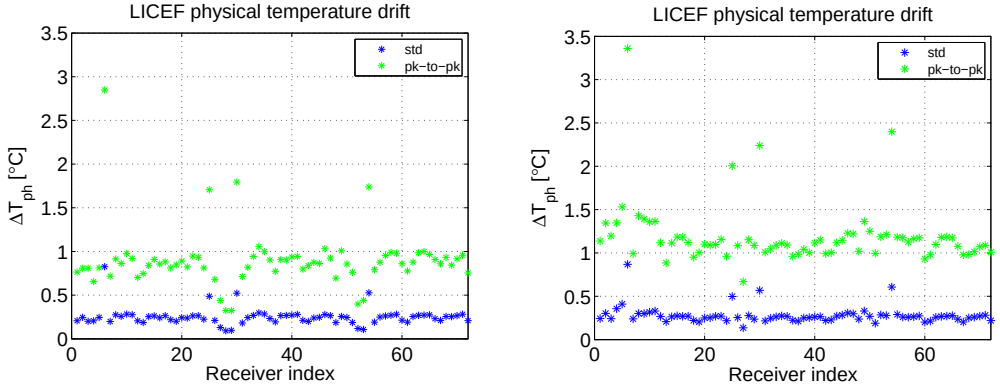

(a) LSS measurements

(b) In-flight measurements

Figure 5.10: LICEF physical temperature variation. Standard deviation (blue stars) and peak-to-peak variation (green stars) of the temperature drift.

PMS gain measurements have been compared with the predicted ones from the temperature readings and the sensitivity values (Fig. 5.11), obtained from on-ground characterization [Corbella *et al.*, 2009b, Pablos, 2010] and from in-flight data [Corbella *et al.*, 2011, Pablos, 2010]. The good agreement between the PMS gain measurements and the estimations can be clearly observed for both sensitivity coefficients for the bulk of the receivers. However, in the case of a few units, the PMS gain presents an hysteresis effect related to the front-end large temperature swings (Fig. 5.11(b)).

In order to prevent this problem, an alternative method based on tracking the PMS gain drift by means of periodic U-noise injection has been tested using on-ground data first and then when in-orbit data were available. On-ground dataset corresponds to measurements while the instrument was kept in calibration mode (long calibration events) during the LSS measurements. In-orbit dataset corresponds to one day of measurements while the instrument was continuously in internal calibration mode (short calibration events). U-noise measurement included in the internal calibration events is used to calibrate the PMS by means of the one-point approach. This way, PMS are calibrated using expressions in (5.12) and (5.13).

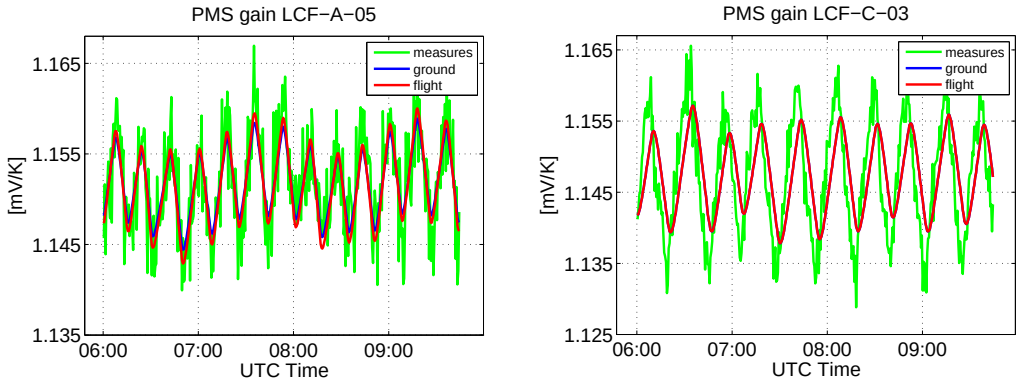

(a) (b)

Figure 5.11: In-orbit PMS gain track from calibrations by means of the four-points method (green line) and temperature correction to 21° C. Two sensitivities have been used: the sensitivity computed on-ground (blue line) and the one re-computed during in-orbit operation (red line).

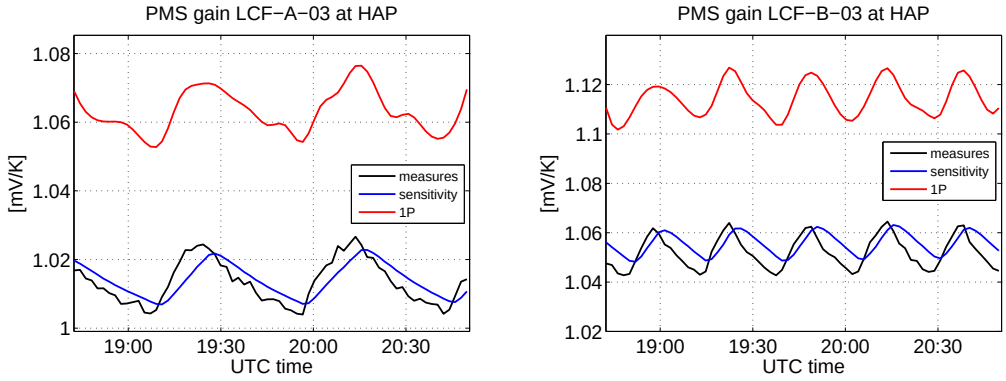

(a) (b)

Figure 5.12: PMS gain estimations using the current calibration baseline (black) in LSS test. PMS gain drift track using the sensitivity to compensate the temperature swing (blue) and by means of periodic U-noise injection (red). The last estimation presents a bias of around 5% since the NIR unit can not be calibrated on-ground and factory calibration parameters have been used. This problem is overcame during in-orbit operation since the NIRs are calibrated during deep sky views.

For those receivers presenting an hysteresis effect (LCF-A-03(6), LCF-B-03(30) and LCF-C-03(54)), which correspond to receivers with a larger temperature drift (see Fig.5.10), both methods to track the orbital PMS drift are compared. PMS calibrations computed using the current calibration baseline correspond to the black line in Fig. 5.12 and in left plots of Figs. 5.13 and 5.14. PMS gain estimations by means of the one-point calibration and using a spline interpolation between calibration events correspond to the red line. A calibration period of 6 minutes has been considered. The reason for analyzing that calibration period is that the U-noise measurement was foreseen to be included in the LO phase tracking calibration sequences, which at that moment were foreseen to be executed every 6 minutes. The blue line shows the PMS gain estimated from the mean value of the PMS gain for all the calibrations and corrected in temperature using the sensitivity coefficients measured in flight and the LICEF front-end temperature readings. Results from on-ground dataset are shown in Fig. 5.12. A bias of around 5% can be observed between both estimations since the NIR can not be calibrated on-ground and factory calibration parameters have been used instead. During in-orbit operation, the NIRs are calibrated during deep sky views, preventing this problem. However, an hysteresis effect between the PMS calibrations and the PMS gain tracking using the sensitivity coefficients can be clearly appreciated.

A similar analysis has been reproduced using in-orbit data. In this case, two inter-calibration periods have been considered: 6.16 minutes (Fig. 5.13) and 8.96 min (Fig. 5.14). As it can be seen from on-ground results, PMS gain track using periodic U-noise injection allows tracking the orbital PMS gain drift preventing the hysteresis effect. This is due to the fact that the receiver noise temperature presents a higher correlation to temperature drift than the PMS gain. Right plots in Figs. 5.13 and 5.14 show the error between each one of the estimations and the PMS gain calibrations. It can be observed that the error reduces using the one-point with respect to the nominal calibration for an inter-calibration period around 6 minutes (Fig. 5.13). However, when the time between calibrations increases to 9 minutes, the errors using both methods become comparable (Fig. 5.14).

Figure 5.15 shows the error in percent in the PMS gain estimations with respect to the calibration measurements. Each one of the estimations corresponds to:

- Mean PMS gain computed during a complete day in calibration mode (black stars). The error in this case is due to the temperature drift.
- PMS gain estimation applying the current calibration baseline, i.e. temperature drift compensation between calibration events by means of the PMS gain sensitivity to physical temperature.
- PMS gain estimation from one-point approach using periodic U-noise injection measurements during the calibration events (considering a calibration period of 6 minutes) and interpolating between calibration events.

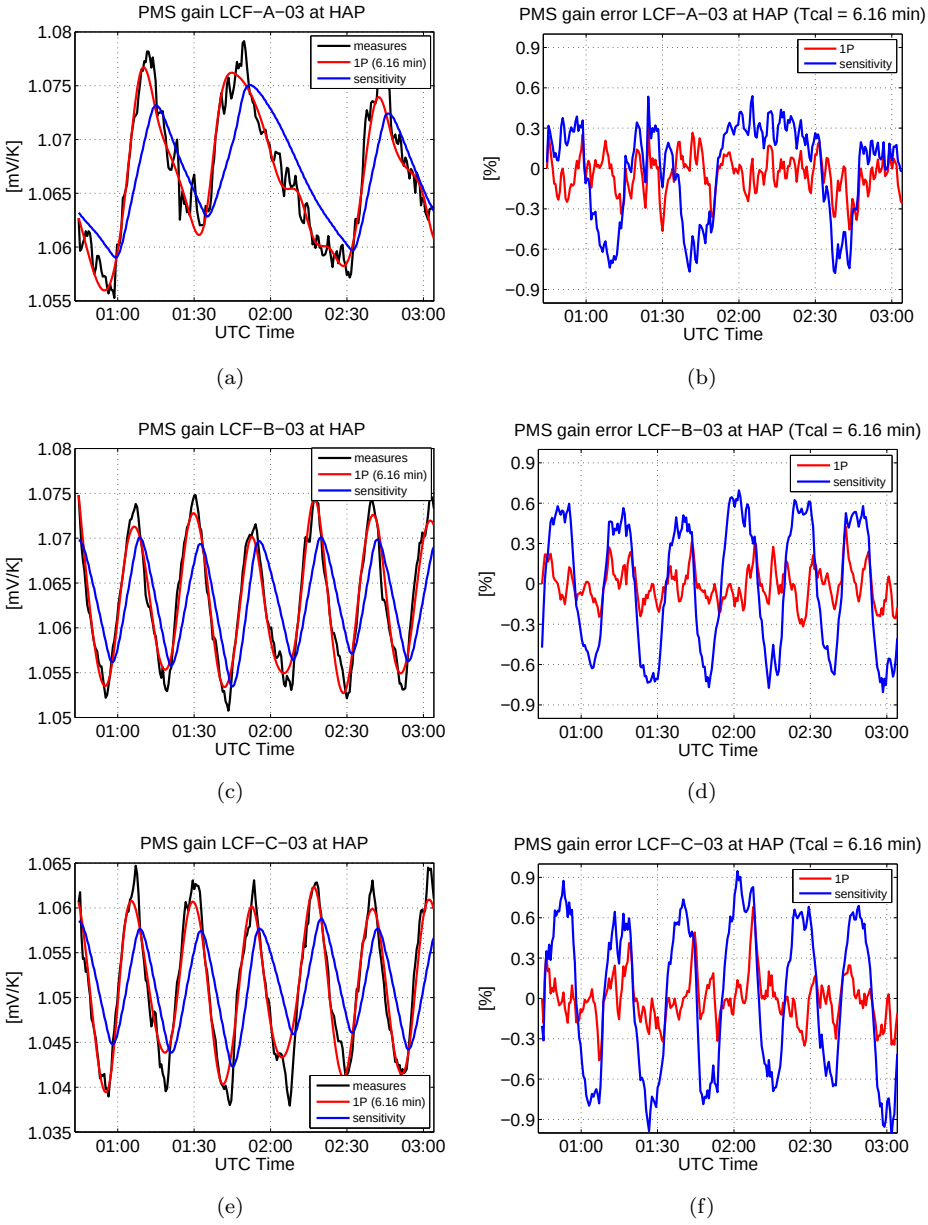

Figure 5.13: Left: PMS gain calibrations using current calibration baseline (black). Orbital PMS gain drift track using the sensitivity to compensate the temperature swing (blue) and by means of periodic U-noise injection, every 6.16 minutes (red). Right: PMS gain estimation error for both methods.

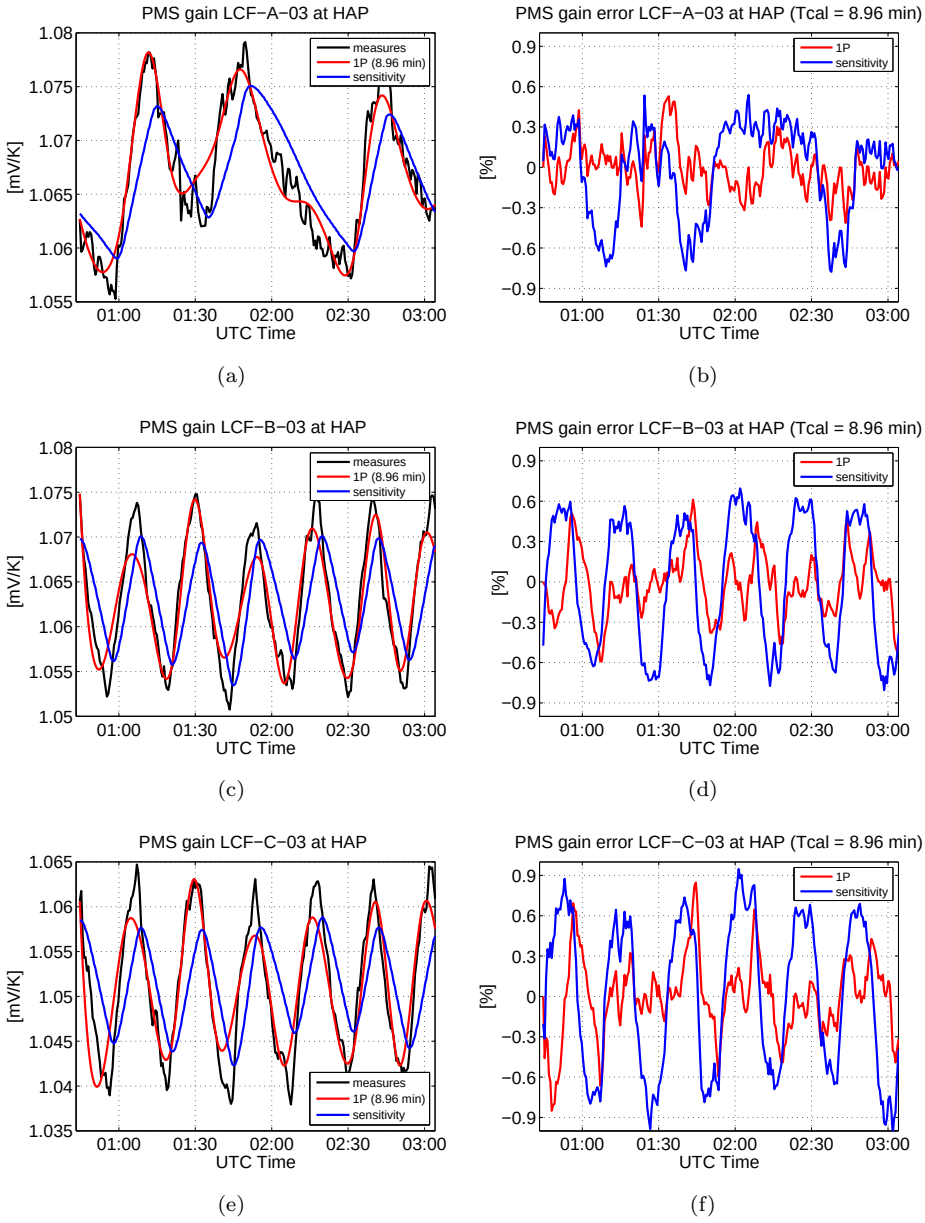

Figure 5.14: Left: PMS gain calibrations using current calibration baseline (black). Orbital PMS gain drift track using the sensitivity to compensate the temperature swing (blue) and by means of periodic U-noise injection, every 8.96 minutes (red). Right: PMS gain estimation error for both methods.

Note that hysteresis effect is minimum in the bulk of the receivers due to the small temperature excursion achieved by the thermal control. This effect is only clearly detected in units presenting a fast/large temperature swing (LCF-A-03(6), LCF-B-03(30) and LCF-C-03(54)) and, even in these units the error is well below 1% requirement [SMOS, 2003b, Torres *et al.*, 2007]). The LO calibration sequence takes a large fraction of the 1% calibration time requirement [SMOS, 2003a]. Hence, the U-noise measurement has been removed from the LO calibration sequence to keep it as short as possible in the operational mode.

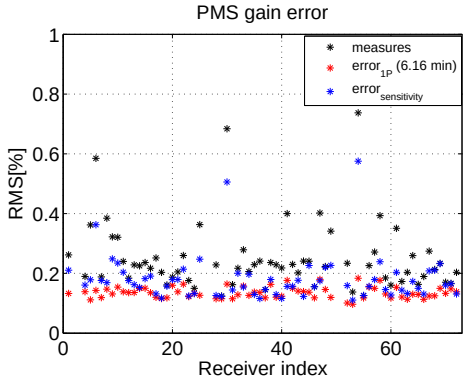

Figure 5.15: Error in the PMS gain estimation using: the calibration baseline (CAS+NIR and temperature correction) (blue stars) and using the one-point calibration and spline interpolation between calibration events (red stars). Black stars represent the error due to the temperature drift. The error at 6.16 minutes corresponds to the thermal noise error. That is, at this calibration rate, the systematic error due to orbital temperature swing has been reduced below the thermal noise level.

5.4 Conclusions

One-point calibration performance has been analyzed in the framework of this Thesis. Two applications of this method have been assessed: the PMS absolute calibration during deep sky views and the orbital PMS gain drift tracking using the U-noise injection.

Regarding the absolute calibration, an experiment to measure the Maxwell anechoic chamber's antenna temperature using only the LICEFs has been devised. Outcomes from this experiment reveal that each LICEF presents some bias in the retrieval of the antenna temperature. The dispersion of this bias is larger in vertical than in horizontal polarization. However, cold sky PMS one-point calibration at the antenna plane during the external maneuvers has been shown to correct this antenna efficiency dispersion. In addition, although the performance of each individual LICEF is not remarkable, the mean value of the 66 LICEFs allows tracking the ceiling's brightness temperature within a margin of 0.1-0.2 K and negligible bias. As a conclusion, these results suggest that the one-point calibration is a promising approach using an all-LICEF configuration to be tested during in-orbit operation.

This calibration approach has also been proposed as a method to track the PMS gain drifts due to orbital temperature swings, since it is not affected by thermal hysteresis as the sensitivity approach. However, this effect is minimum in the bulk of the receivers, affecting mainly to those units which present a fast/large temperature swing. Even in the case of these few receivers, the PMS gain error is well below the 1% amplitude error requirement [SMOS, 2003b, Torres *et al.*, 2007] and therefore, the temperature correction has been selected as the operational calibration baseline, in order to minimize the calibration time.

After the assessment of the one-point calibration performance, the in-orbit PMS cold sky calibration sequence was developed to be performed during the external calibration events [Brown *et al.*, 2008]. This method has been used as a back-up amplitude calibration method during the Commissioning phase activities and has also allowed validating the calibration subsystem, updating the CAS correction factors.

Chapter 6

MIRAS characterization during Commissioning Phase

This chapter summarizes the main investigations performed during the first in-orbit measurements in the framework of the MIRAS/SMOS Commissioning Phase. The objective of these analysis has been to complete the on-ground instrument characterization. Its main outcomes have been throughly detailed in Chapters 4 and 5. Tools and algorithms developed during this work and applied to the on-ground instrument assessment have been used and/or updated in order to complete the characterization of the system performance.

6.1 Introduction

The scope of this Thesis is the characterization of the MIRAS/SMOS payload. It has mainly contributed to the assessment of the system performance as well as to the development of different algorithms in order to achieve the electrical and technological mission requirements. Most of this work has been done in the framework of the MIRAS/SMOS Pre-Commissioning Phase activities. However, just after launch, several measurements devoted to check the behavior of the instrument during the in-orbit operation were performed. The tools and techniques developed for the on-ground system performance assessment have been adapted to fulfill in-orbit instrument characterization.

During the first part of the Commissioning Phase, many activities aimed at checking the instrument behavior in-flight were performed. These first tests were mainly devoted to:

- Assess the electrical and thermal stability of the instrument.
- Provide, for the first time, an absolute calibration by means of the external maneu-

vers.

- Correct the internal calibration data using the external measurements.
- Assess the frequency for the calibration events achieving the mission requirements while maximizing the observation time.
- Evaluate the possible RFI caused by the subsystems of the payload/platform.

In addition, other tests are devoted to the assessment of the instrument imaging capability, obtaining the first images both in dual and full polarization modes. During the second stage of the Commissioning, the main objective was to decide which configuration dual/full was selected for the operation mode, the instrument being switched between both modes every two weeks.

All these tests are throughly detailed in the *In-orbit Commissioning Plan document* [Brown & team, 2008] and the final objective is to obtain the Level 1B data products (brightness temperatures) with the required accuracy [SMOS, 2003b].

Concerning the analysis performed in the framework of this Thesis, it can be mainly focused on the following particular items:

- In-orbit EMC assessment of different payload/platform configurations.
- Assessment of the amplitude and phase calibration consistency.

The most representative investigations and outcomes of these analysis are detailed in the next sections.

6.2 In-orbit EMC assessment

A comprehensive analysis of the impact on system performance of different instrument/set up configurations was performed during the MIRAS on-ground characterization, first evaluating the EMC of the instrument itself and then when the integration with the platform was completed [González-Gambau *et al.*, 2008a,e]. This study was carried out using the Success Criteria tool, developed in the framework of this thesis (see Chapter 4).

During the first in-orbit measurements, several tests were devoted to evaluate the EMC of different subsystems of the payload/platform:

- S-band transmitter
- Solar Array Driver Mechanism (SADM)
- X-band transmitter
- Star tracker

Table 6.1: EMC tests performed during Commissioning Phase.

Date	Pointing	Duration	Target	Mode	Purpose	LO A2
14-Dec-2009	Zenith	1.1 orbits	One full sky circle	Dual	S-band RFI	unlocked
16-Dec-2009	Zenith	1.1 orbits	One full sky circle	Dual	S-band RFI	unlocked
23-Dec-2009	Inertial	Standard	Sun eclipsed-Galaxy	Dual	SADM	locked
07-Jan-2010	Inertial	Standard	Moon in AF-FoV	Dual	X-band + Star tracker RFI	locked

Details of each test are summarized in Table 6.1.

The analysis of these EMC tests has required an update on the Success criteria tool used during the on-ground characterization, both in IVT and RACT campaigns. During these measurements, the instrument was continuously measuring the anechoic chamber background, that is, a constant target. By contrast, for the analysis of the in-orbit EMC measurements it is necessary to distinguish between changes in the measurements due to the change of the target seen by the antenna and the possible RFI caused by the analyzed subsystems. For this reason, success criterion for the standard deviation has been applied, in this case, to the first-order difference of each snapshot with respect to the previous one, both for normalized correlations and PMS voltages. Note that in this way it is possible to estimate the standard deviation independently of the long-term variation. The standard deviation of the corresponding magnitude can be derived from the standard deviation of the first-order difference taking into account a factor $1/\sqrt{2}$.

In all the EMC tests, the state ON/OFF of the corresponding subsystem is provided by the platform. In this way, it is possible to separate those blocks of measurements in which a given subsystem is ON from the blocks of measurements where the subsystem has been switched OFF. Both polarizations in dual mode have been also separated in each block. The most representative results from this analysis are presented in this section.

Regarding the S-band transmitter test, data correspond to the 14^{th} and 16^{th} of December 2009 (performed during Week 3 of the IOCP, [Brown & team, 2008]), first and second 1.1 orbits respectively, where the instrument was pointing to the zenith and measuring in dual polarization mode. In both datasets, the local oscillator in the segment A2 was unlocked and therefore, both the PMS voltages from the receivers in this segment and the normalized correlations from those baselines involving receivers in the segment A2 have been discarded for this analysis. During these measurements, the S-band transmitter was switched ON/OFF every 5 minutes. An estimation of the standard deviation is computed for each block ON/OFF and for dual H and V polarization measurements (around 125 samples per block in each polarization). Finally, the success criteria for the standard deviation is applied to the mean value of all the standard deviation estimations along the 1.1 orbits.

In the case of the success criteria for the mean, the absolute value of the difference between the mean values of PMS voltages and the correlations for the ON and OFF transmitter status have been represented. However, in the case of the mean, the results of the Success Criteria tool are contaminated by the temperature drift and the changes in the image. Although these effects are partially corrected by computing the Success Criteria tool along a full orbit, it is not clear at all if their residual values could invalidate the results.

Similar results are obtained from the analysis of the two S-band transmitter EMC tests. The impact of the S-band transmitter status on science data from the second test is presented below. It can be clearly seen that some baselines are not in compliance with the success criteria neither for the mean (Fig. 6.1, first column) nor for the standard deviation (Fig. 6.1, second column). Concerning the success criteria for the mean, it must be pointed out that these magnitudes have not been corrected in temperature along the orbit.

Note that both the reference measurement (S-band transmitter ON) and the measurement under perturbation (S-band transmitter OFF) present artifacts. In order to find out the reason why the standard deviation of the normalized correlations presents a clear pattern, the different estimations of the standard deviation of the M_{kj} first-order difference are analyzed per each block ON/OFF separately. An example of two blocks presenting artifacts and another two in which no effect/perturbation can be observed are shown in Figs. 6.2 and 6.3, respectively. Both states of the transmitter and both polarizations are analyzed. The two red lines correspond to applying the success criteria to the block itself (these two lines correspond to the thresholds: $\overline{\mathrm{std}\,(X)} \pm 3 \cdot \mathrm{std}\,(\mathrm{std}\,(X))$), in order to assess if there is any effect in the block. These outcomes confirm that the artifacts are independent on the S-band transmitter state.

Although the measurements for all these EMC tests were performed while the instrument was pointing to the zenith/inertial position, the origin of the perturbations could have been due to radiation entering the secondary lobes. Plotting the satellite position over the Earth in latitude-longitude for each block separately (third row in Figs. 6.2 and 6.3) allows to assess if these artifacts are correlated with known regions affected by RFI over land/sea. In this way, this hypothesis has been discarded.

During both S-band transmitter EMC tests, the local oscillator of the segment A2 was unlocked. Measurements from two external tests where the A2 LO was locked were analyzed in order to assess this effect. In these measurements the S-band transmitter was always in the nominal configuration (ON). As it can be seen in Fig. 6.4, one of the external measurement also presents artifacts, although the pattern is different from those of the S-band transmitter test. The position of the Sun during the measurements is another issue investigated, not explaining the RFI pattern appeared in the S-band tests.

Finally, the success criteria has been applied to measurements not affected by these perturbations (block of measurements in Fig. 6.3). These measurements successfully

pass the success criterion for the standard deviation (Fig. 6.5, second column). Marginal effects in a few baselines can be found in the success criterion for the mean (first column of the same figure). Since the test has not been performed now including a full orbit, the residual errors due to temperature/image changes can be large and it is feasible that the non-compliance for these baselines is caused by this and not by the S-band transmitter. Comparison of these blocks of data does not show an impact of the S-band transmitter on the mean or the standard deviation of the normalized correlations.

In conclusion, a clear relation between the S-band transmitter status and the artifacts observed in the science data measured by the instrument can not be established. Some baselines are not in compliance with the success criteria independently on the S-band transmitter status. That is, artifacts can not be linked to the S-Band transmitter.

Relating to the X-band transmitter and the star tracker subsystems, both EMC measurements have been performed at the same time. During this EMC test, both subsystems were switched ON/OFF almost simultaneously. The analysis has been carried out using those epochs of the external calibration maneuver in dual mode corresponding to the FTR computation [Brown *et al.*, 2008]. The local oscillator of the A2 segment was locked during these measurements.

Normalized correlations pass the success criteria for the mean (Fig. 6.6, first column) and also for the standard deviation (Fig. 6.6, second column). Only some marginal non-compliant baselines can be observed in V polarization. Therefore, it can be concluded that both the star tracker and the X-band transmitter state produce a negligible impact in the statistic properties of the normalized complex correlations.

In case of the PMS voltages, marginal receivers are non-compliant with the success criterion for the mean (see Fig. 6.7, first column) due to the temperature/image change contribution between the different blocks that have been analyzed. Note that in this test, only the measurements corresponding to the FTR computation are used. Therefore, the effect of the temperature changes can not be compensated.

As a conclusion, the star tracker and X-band transmitter EMC test passes the success criteria for both the mean and the standard deviation for the normalized complex correlations. The temperature/image change contribution is only marginally affecting the success criteria test for the mean in the case of the PMS voltages. There is no effect in the success criterion for the standard deviation.

The objective of the SADM test was to check if the solar array rotation could potentially interfere with the instrument measurements. In order to do this analysis, measurements during a symmetrical period with regards to the external calibration maneuver center were performed in 5 positions of the solar arrays (90°, 95°, 90°, 85° and 90°). The reference position is at 90°. Results for the standard deviation of the normalized correlations first-order differences present artifacts independent on the rotation of the solar arrays, i.e. for all the positions mentioned before.

Figure 6.8 shows this magnitude for two of the positions: the reference one (first row)

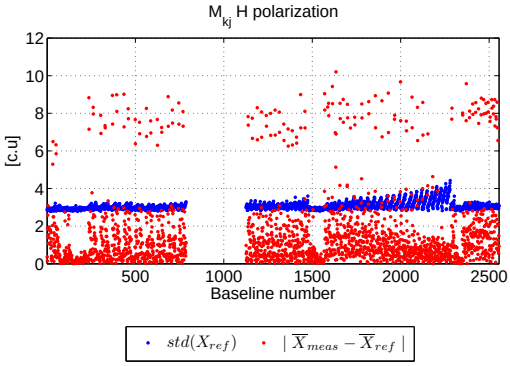

(a) Mean H polarization

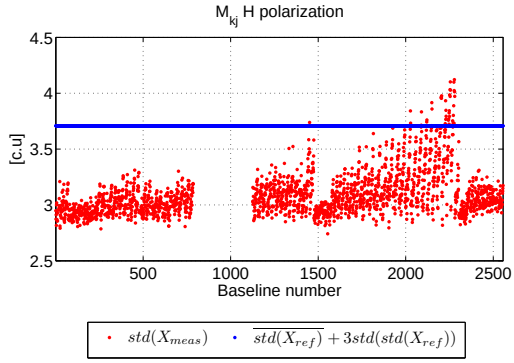

(b) Standard deviation H polarization

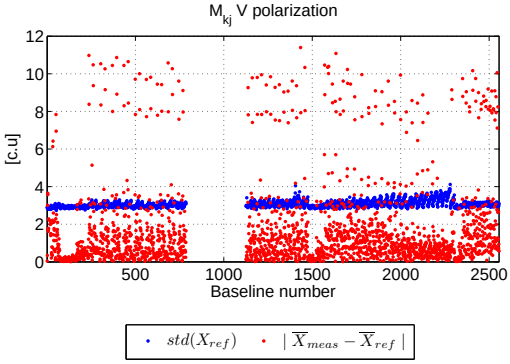

(c) Mean V polarization

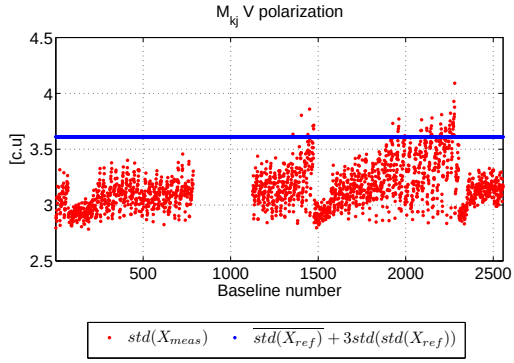

(d) Standard deviation V polarization

Figure 6.1: Success criteria for the normalized correlations during the second S-band transmitter test. It can be observed that both the reference measurement and the measurement acquired when the S-band transmitter was OFF present artifacts.

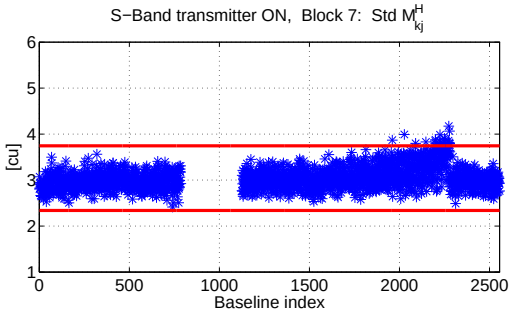

(a) S-band transmitter ON, H polarization

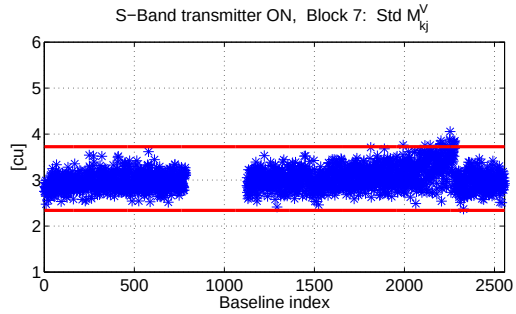

(b) S-band transmitter ON, V polarization

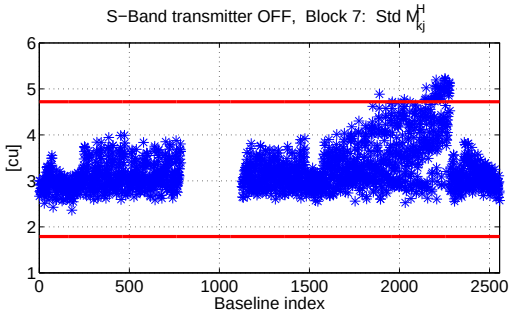

(c) S-band transmitter OFF, H polarization

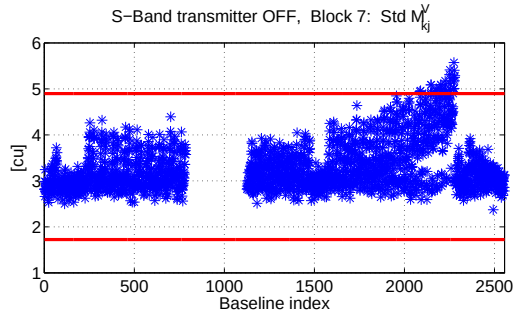

(d) S-band transmitter OFF, V polarization

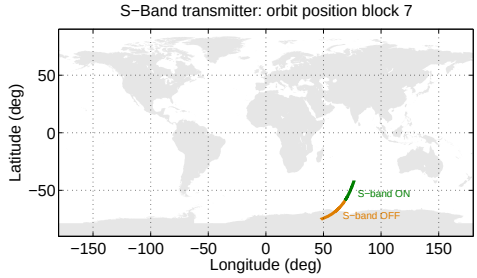

(e) Orbit position

Figure 6.2: Standard deviation of the normalized correlations in case of two blocks which present artifacts. Red lines represent $\overline{\mathrm{std}\,(X)} \pm 3 \cdot \mathrm{std}\,(\mathrm{std}\,(X))$ thresholds, in order to check if there is any artifact in the measurements. Top: S-band transmitter ON. Middle: S-band transmitter OFF. Bottom: Orbit position during the analyzed measurements. From these results, artifacts can not be linked to the S-Band transmitter status.

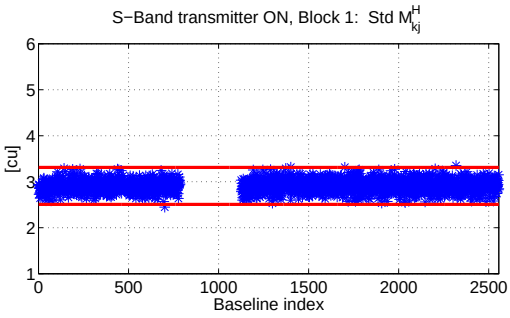

(a) S-band transmitter ON, H polarization

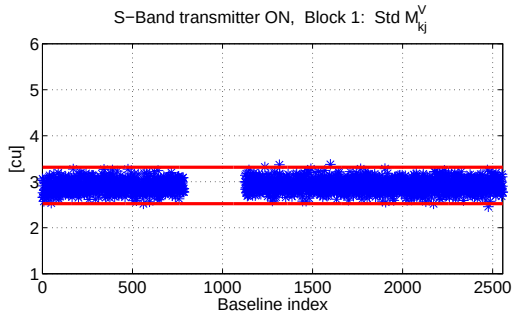

(b) S-band transmitter ON, V polarization

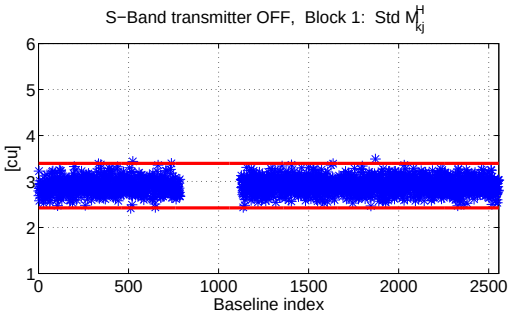

(c) S-band transmitter OFF, H polarization

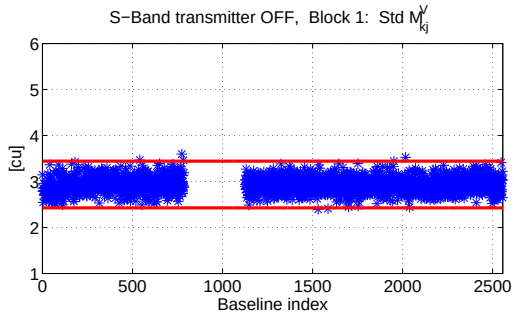

(d) S-band transmitter OFF, V polarization

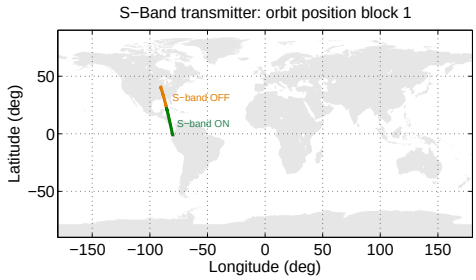

(e) Orbit position

Figure 6.3: Standard deviation of the normalized correlations in case of two blocks which do not present any artifact/perturbation. Red lines represent $\overline{\text{std}\,(X)} \pm 3 \cdot \text{std}\,(\text{std}\,(X))$ thresholds. Top: S-band transmitter ON. Middle: S-band transmitter OFF. Bottom: Orbit position during the analyzed measurements.

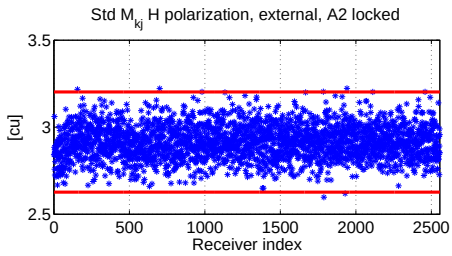

(a) H polarization, 8-Dec-2009

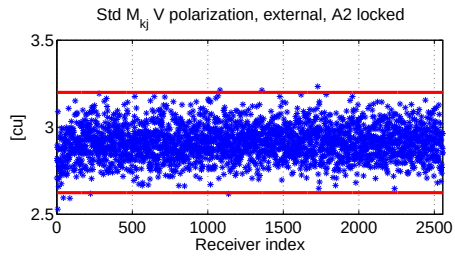

(b) V polarization, 8-Dec-2009

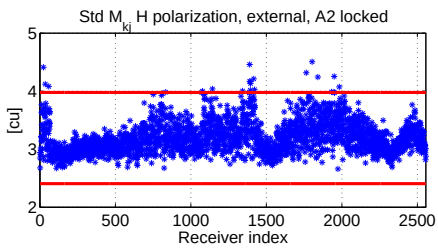

(c) H polarization, 23-Dec-2009

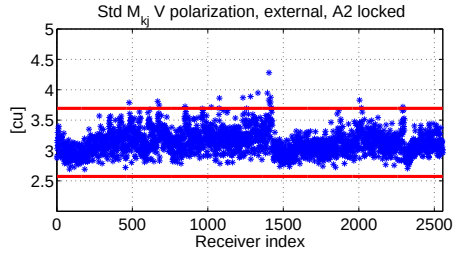

(d) V polarization, 23-Dec-2009

Figure 6.4: Standard deviation of M_{kj} first-order differences in two external tests with local oscillator of the A2 segment locked. This check allows to verify if these unlocks produce the perturbations. Red lines represent $\overline{\text{std}(X)} \pm 3 \cdot \text{std}(\text{std}(X))$, in order to check if there is any artifact in the measurements. Top: In 8-Dec-2009 dataset only marginal effects can be observed. Bottom: Artifacts are present in the external measurements performed on 23-Dec-2009.

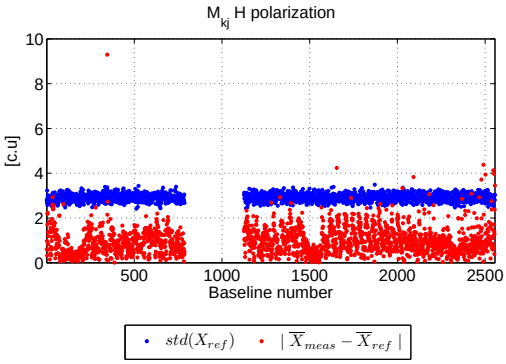

(a) Mean H polarization

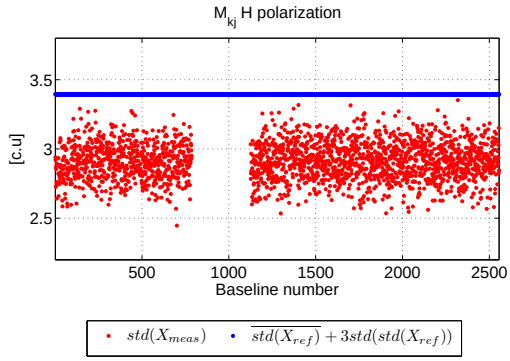

(b) Standard deviation H polarization

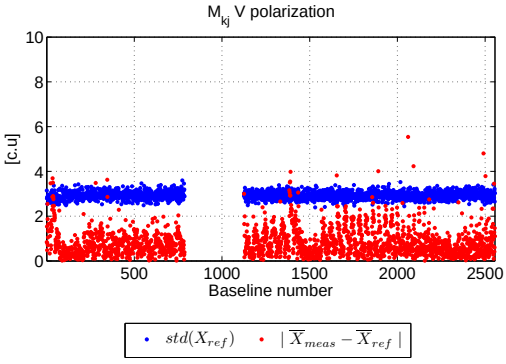

(c) Mean V polarization

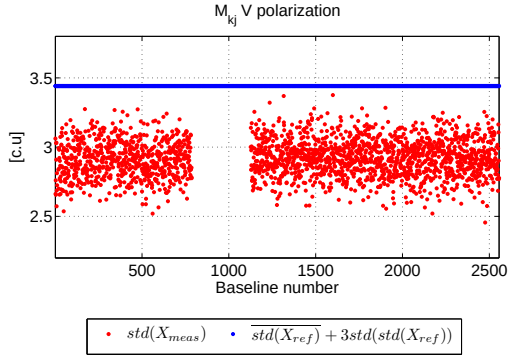

(d) Standard deviation V polarization

Figure 6.5: Success criteria for the normalized complex correlations in the S-band transmitter EMC test. Only one block of measurements clean of artifacts has been used to performed the comparison (block shown in Fig. 6.3). Left: success criteria for the mean. Since the test has not been computed including a full orbit, the residual error due to temperature and image changes is large and it cannot be concluded that the non-compliance is caused by the S-band transmitter. Right: success criteria for the standard deviation.

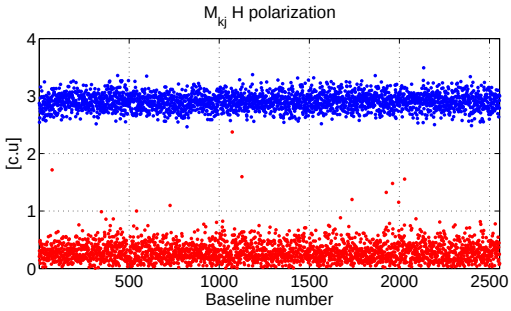

(a) Mean H polarization

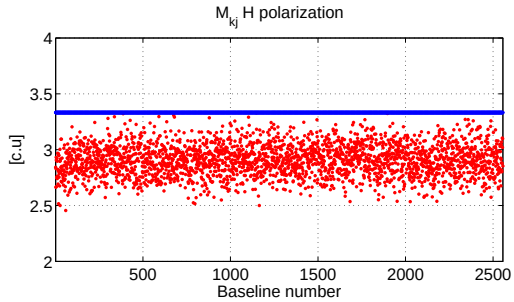

(b) Standard deviation H polarization

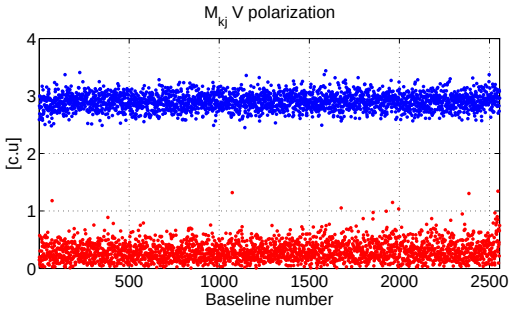

(c) Mean V polarization

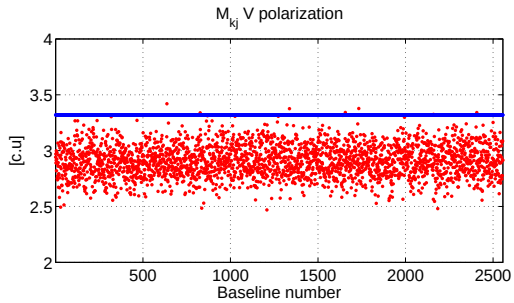

(d) Standard deviation V polarization

Figure 6.6: Success criteria for the normalized correlations during X-band transmitter and star tracker test. Only marginal baselines are non-compliant with the success criterion for the standard deviation in V polarization.

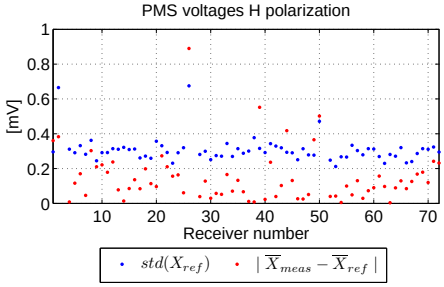

(a) Mean H polarization

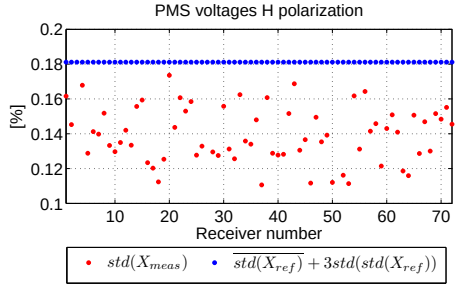

(b) Standard deviation H polarization

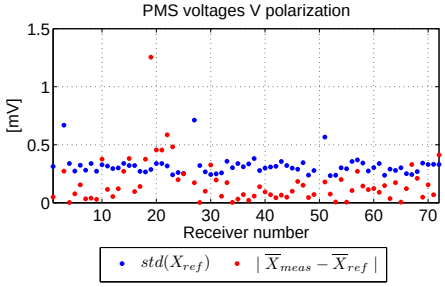

(c) Mean V polarization

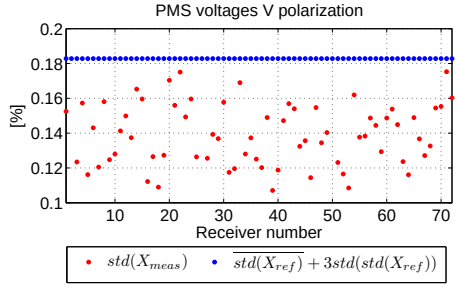

(d) Standard deviation V polarization

Figure 6.7: Success criteria for the PMS voltages during X-band transmitter and star tracker test. The temperature/image change contribution is only marginally affecting the success criteria test for the mean. There is no effect in the success criteria for the standard deviation.

and the measurements while the solar arrays are rotating +5° from the reference position (second row). As in the analysis of the S-band transmitter test, red lines correspond to the application of the success criteria for the measurement itself to assess if there is any undesired effect. The presence of artifacts/perturbations is evident for both positions of the solar arrays. Similar results are obtained for the rest of the positions, therefore, the use of the success criteria tool to assess the impact of this subsystem on the science data is not applicable.

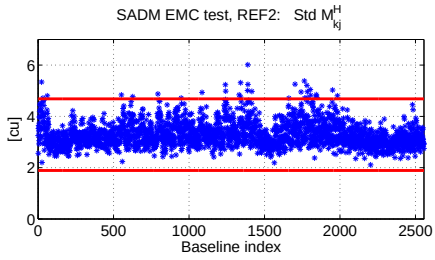

(a) Reference position, H polarization

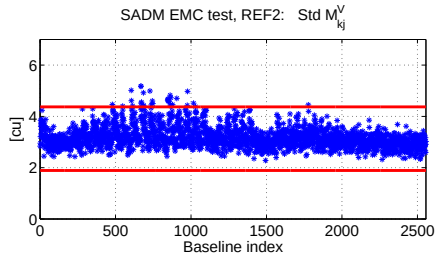

(b) Reference position, V polarization

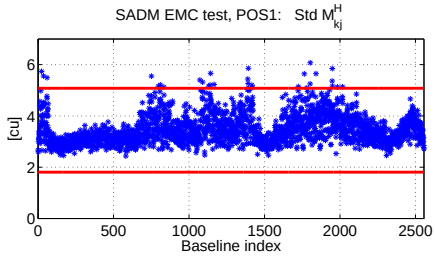

(c) 95° position, H polarization

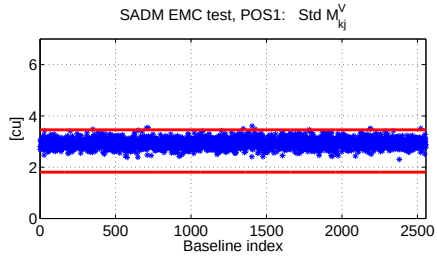

(d) 95° position, V polarization

Figure 6.8: Standard deviation of the normalized correlations during the solar arrays rotation test. Red lines represent $\overline{\text{std}(X)} \pm 3 \cdot \text{std}(\text{std}(X))$. Note that in this case, both the reference measurement (at 90°) and the movement up to 95° present artifacts/perturbations. Similar patterns are present in the rest of the positions. Therefore, the use of the success criteria to assess the impact of this subsystem on the science data is not applicable.

6.3 PMS in-orbit assessment

The PMS is the main contribution to visibility amplitude errors. Therefore, an accurate assessment of its in-orbit performance was undertaken during Commissioning Phase. MIRAS calibration baseline for the PMS offset is based on the values obtained by means of the internal correlated noise injection during the long calibration sequences [Brown *et al.*, 2008] and the in-orbit temperature drift correction [Torres *et al.*, 2006]. From the on-ground characterization tests (LSS measurements), it was evident that drifts of the PMS offsets were due to not only the temperature swings but also to another unknown effect. Figure 6.9 shows the PMS offset from continuous long calibrations and the offset estimations from the mean value and the sensitivity to physical temperature for two receivers. Offset estimations can not track the abrupt jumps present in the calibrations. The square waveform of the offset voltage leads to the hypothesis of these jumps being related to the on/off switching of the heaters.

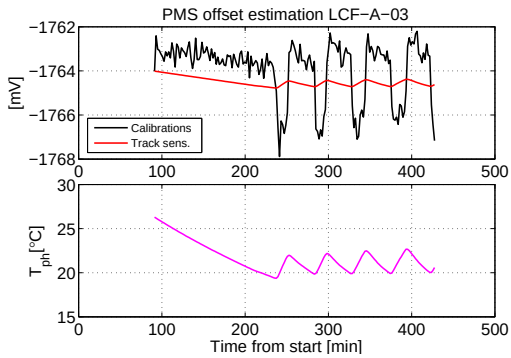

(a) LCF-A-03, dataset from LSS

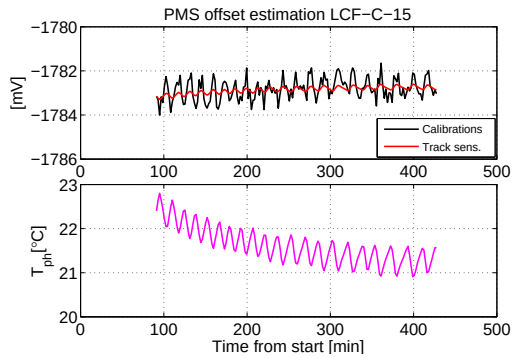

(b) LCF-C-15, dataset from LSS

Figure 6.9: Top: PMS offset calibrations and estimations using the mean value and correcting for temperature drifts using the sensitivity coefficients computed in [Pablos, 2010]. Bottom: LICEF physical temperature swing along the test.

In order to comprehensively analyze this effect, a single heater has been assigned to each receiver. In case of receivers in the arms, a clear correspondence between the signal changes of the heater which belongs to the same segment of the receiver can be found. On the contrary, for receivers in the Hub, this assignment is not so clear. An example of one receiver in the Hub (LCF-A-03) is shown in Fig. 6.10 along with the signals of all the heaters in the Hub. Two of them (heaters in segments H1 and H3) can be discarded since the first changes in the heater signal happen before the offset jumps start. In addition, the period of the switching on/off of the heater H2 matches exactly to the periodicity of the abrupt jumps observed in the offset voltage. Hence, the heater in segment H2 is affecting the offset jumps of receiver LCF-A-03.

However, a delay between the offset jumps and the heater state was present in the

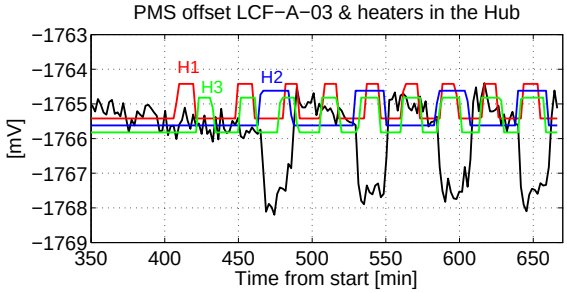

Figure 6.10: PMS offset calibrations (black line) and the heater signals overlapped in order to find the heater controlling these jumps. An example for a receiver in the hub (LCF-A-03).

Table 6.2: PMS offset special sequence.

PMS offset calibration. SEQUENCE E3							
	Step	Epochs	LICEF	NIR	NS EVEN	NS ODD	Att.
PMS Offset ODD	1	1	C	LICEF-LC	OFF	WARM	L1
	2	1	C	LICEF-LC2	OFF	HOT	L1
	3	1	C	LICEF-LC2	OFF	WARM	L0
	4	1	C	LICEF-LC	OFF	HOT	L0

on-ground datasets. Since the PMS offsets had been retrieved from long calibration sequences, the time between calibrations was around 2 minutes and it was not possible to evaluate the delay from these measurements. Then, it was necessary to implement a special sequence to characterize the delay and jumps in the offset voltage for each receiver with respect to the heater signal. This sequence only contains the four steps (4.8 seconds) with the instrument in correlated noise injection mode for the odd noise sources required to compute the offset by the 4-points method in all receivers [Piironen, 2002]. The sequence is detailed in Table 6.2. In case of the NIR receivers, the sequence has not been worked properly. For this reason, the delays and jumps have been retrieved from continuous short calibration sequences (every 35 seconds) performed along one day to evaluate the temperature behavior of the calibration parameters. Figure 6.11 shows the PMS offset calibrations for two different receivers: a receiver in the Hub, presenting abrupt jumps in the PMS voltages and other in the arm C, which presents moderate jumps in the offset voltage. In addition, the corresponding heater signals have been overlapped.

From the continuous execution of this sequence (every 4.8 seconds), a delay (in epochs) has been computed for each receiver in order to maximize the correlation between the

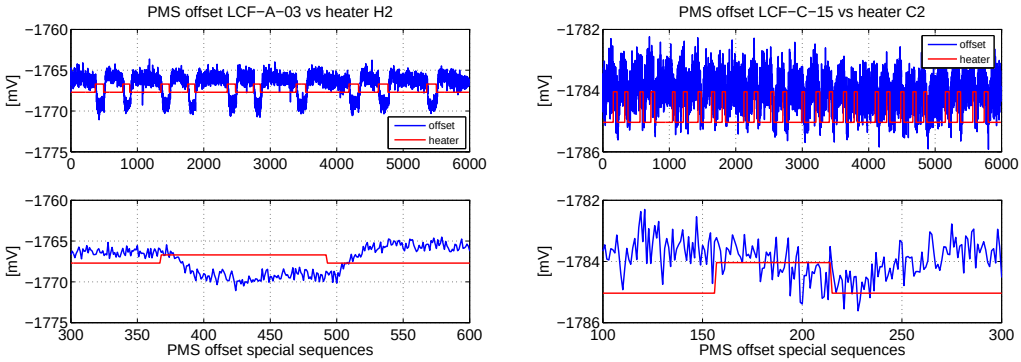

(a) LCF-A-03 (b) LCF-C-15

Figure 6.11: Top: PMS offset and heater signal. A clear correlation between both signals can be observed. Heater state (ON/OFF) corresponds to 1/0 values, respectively. Mean offset has been added to the heater state to overlap both signals. Bottom: Zoom of the top plot.

offset voltage jumps and the heater signal changes. Once these delays have been computed, heater signals are accordingly delayed. Then, jumps in the offset voltages are computed as the difference between the mean value for the offset calibrations when the associated heater is ON and the mean value for those calibrations with the corresponding heater OFF. Two tests performed more than two months apart, give very similar values for the delays and jumps. This electrical stability test [Brown & team, 2008] was repeated one year apart giving similar results. This means that the heater correction is very stable in time and therefore there is no need for recomputing it along the mission. This correction has been incorporated in the MTS [Corbella *et al.*, 2008a]. The correction is applied at the PMS voltage level before the application of all the calibration procedures [Corbella *et al.*, 2005], [Torres *et al.*, 2006].

In order to assess the improvement in the PMS estimations due to the heater correction, the rms error before/after the application of the delay and jumps have been represented in Fig. 6.12 both for the special sequences (left plot) and the long flight calibration segment sequence (right plot), i.e. 45 long calibration sequences and therefore 45 PMS offset estimations. The rms error decreases considerably when the heater offset correction is applied to the PMS offset special sequence and also for the long sequences, being in both cases well below the system requirements (1mV) [SMOS, 2003b],[Torres *et al.*, 2007]. The differences between the two datasets in PMS offset rms error after the correction is negligible (between left and right plots).

Offset voltages before and after applying the heater correction have been obtained for the PMS offset special sequence (Fig. 6.13) and for the long flight calibration segment sequence (Fig. 6.14). After applying the heater correction two kinds of errors can appear:

1. The offset presents an abrupt jump but the correction has not been applied yet.

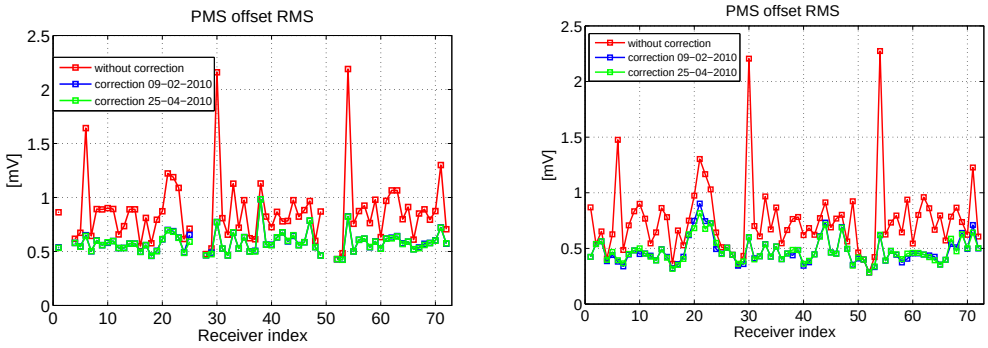

(a) Special test

(b) Long calibration sequences

Figure 6.12: PMS offset rms before and after the heater correction. Note that this correction allows to comply the MIRAS requirements for all the receivers, a PMS offset rms below 1 mV [SMOS, 2003b],[Torres *et al.*, 2007].

2. And the opposite situation: the correction has been applied but the jump has not occurred yet.

These effects can be appreciated only in Fig. 6.13, which corresponds to the PMS offset special calibration sequence. By contrast, these errors can not be observed in the 45 long calibration sequences due to the averaging of the epochs available to compute the offset. However, since the instrument performance is based on its large capability for averaging errors (both temporal and spatially), the result to be considered is the one giving the rms error after the correction (Fig. 6.12). This shows that the heater correction reduces rms error to the thermal noise level.

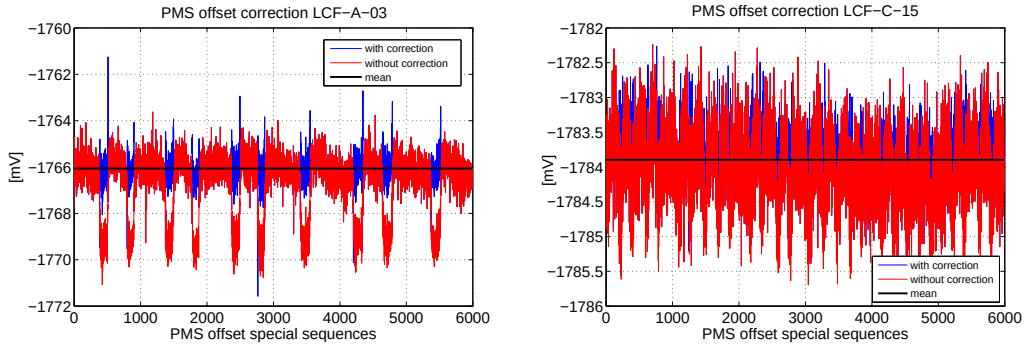

(a) LCF-A-03

(b) LCF-C-15

Figure 6.13: PMS offset correction for heater signal dependence during the PMS offset special test.

In conclusion, the heater correction is very stable in time. The differences between the two data sets in PMS offset rms error after the correction is negligible and rms deviation

resulting after both corrections is in the level of thermal noise. The fact that peak-to-peak deviation increases in the special calibration sequences means that in punctual moments the error is large.

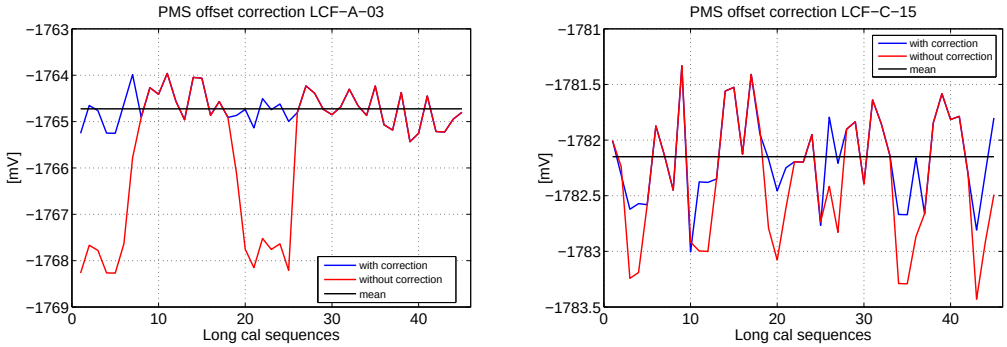

(a) LCF-A-03 (b) LCF-C-15

Figure 6.14: PMS offset correction for heater signal dependence during long calibration sequences. After correction, PMS offset for the bulk of the receivers shows the random fluctuation due to the thermal noise and a small dependence on physical temperature variation. This last drift is corrected using sensitivity coefficients [Torres *et al.*, 2006].

The heater correction has been also implemented in the official SMOS Level 1 data processing at the PMS voltage level. This correction has allowed tracking the PMS offset, within the SMOS mission requirements, from the values obtained by means of the long calibrations events and temperature correction between them.

6.4 Local oscillator phase track

A method to track the visibility phase variations with temperature swings has been developed and tested during the on-ground characterization (throughly detailed in chapter 4). This method has allowed to give an estimation of the LO phase good enough to conclude that phase drift is basically caused by LO sensitivity to physical temperature drift and it also may give an estimation of the expected baseline phase drift if different temperature gradients affect the segments. However, the physical temperatures readings are not accurate enough and therefore, phase tracking errors are slightly above the required accuracy [González-Gambau *et al.*, 2008d].

The conclusion of this analysis has led to propose an alternative phase calibration procedure: frequent calibrations by means of the correlated noise injection. However, it is necessary to evaluate the LO calibration frequency needed to estimate the phase with the required accuracy while maximizing the observation time.

During the first in-orbit measurements, the instrument was in the Switch-On and Data Acquisition Phase and calibration of the instrument was not possible. However, phases

could be estimated using physical temperature readings and the sensitivity coefficients computed on-ground [González-Gambau *et al.*, 2008d], providing a first guess on the in-flight LO phase track strategy.

A comprehensive analysis of the visibility phase drifts with the physical temperature swings has been performed using the electrical stability test (continuous short calibrations). The same tool developed for the analysis of the on-ground measurements has been used. In this case, the receiver LCF-C-06 has been used as a reference because it has the minor sensitivity and a low temperature variation. Only results for the segments in the Hub and for arm A are shown. Similar results are obtained for the rest of the receivers. Left plots in Figs. 6.15 and 6.16 present the incremental phase drift for all the receivers in a segment. Phase difference with respect to the mean value of all receivers in the segment is shown in right plots of the same figures. From these outcomes, the following conclusions can be pointed out:

- Phase drift can be mainly assigned to LO temperature drifts.
- Phase drift in temperature at LICEF level is very low for all the receivers, except for receiver NIR-AB-01-H, which presents abrupt jumps in the phase difference with respect to the mean value of all receivers in the segment. The rest of the receivers has a very good behavior, being 0.6 degrees the maximum phase difference.
- LICEF phase drift grouped in segments (12 CMNs) gives a simple way to monitor LO phase behavior, such as drifts, jumps and unlocks.
- Confirmation of the current calibration baseline: frequent calibrations by noise injection along the orbits (LO phase tracking) and interpolation between calibration events.

Currently, baselines involving the NIR-AB-01-H are not being used to obtain brightness temperatures to avoid these abrupt jumps in the phase. However, this is not a problem, since all of them are redundant baselines.

The point now is the assessment of the LO calibration frequency needed to calibrate the phase with the required accuracy. During March 2010, the LO calibration frequency was set to 2 minutes during a week. This test was performed to analyze the impact of the LO calibration frequency on the geophysical parameters retrieval [Gabarró *et al.*, 2011]. Using these measurements, LO calibration data have been decimated to study different intervals between calibrations: 4, 6, 10 and 12 minutes. The standard deviation of the visibility phase errors is shown in Fig. 6.17. The highest values correspond to baselines involving the receiver NIR-AB-01-H due to the oscillations in the phase of this receiver. The mean error (in all the cases below 0.02 degrees) can be considered negligible. For receiver, this rms error is divided by $\sqrt{2}$. It has been finally established in 10 minutes to keep residual rms phase error below the 1 degree requirement [SMOS, 2003b],[Torres *et al.*, 2007].

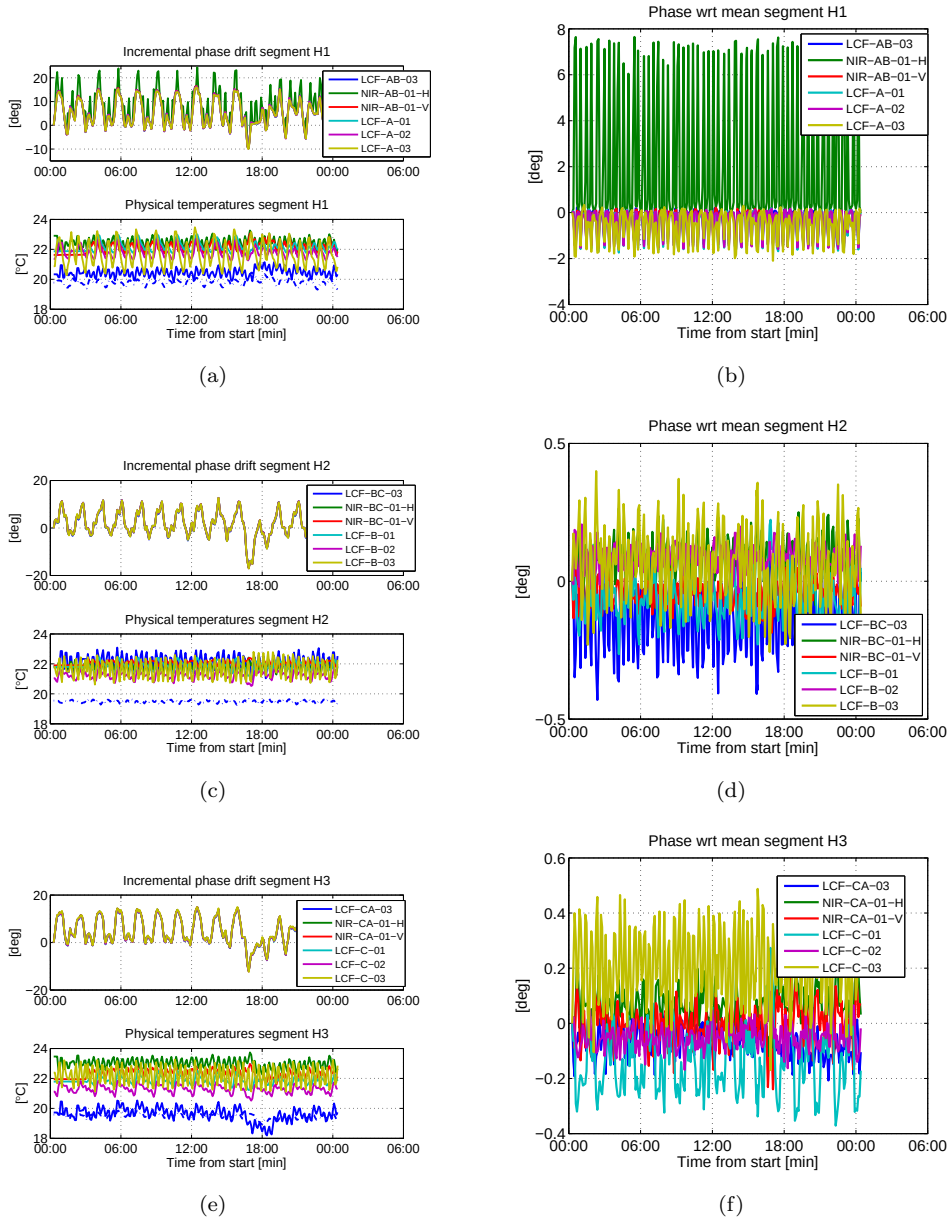

Figure 6.15: Phase drift of receivers in the Hub; (a) and (b) segment H1, (c) and (d) segment H2, (e) and (f) segment H3. Left plots: Incremental phase drift from first calibration for all receivers in the segment (top)(reference receiver: LCF-C-06). LICEFs and PD physical temperatures (bottom). Right plots: Phase difference with respect to the mean value of all receivers in the segment.

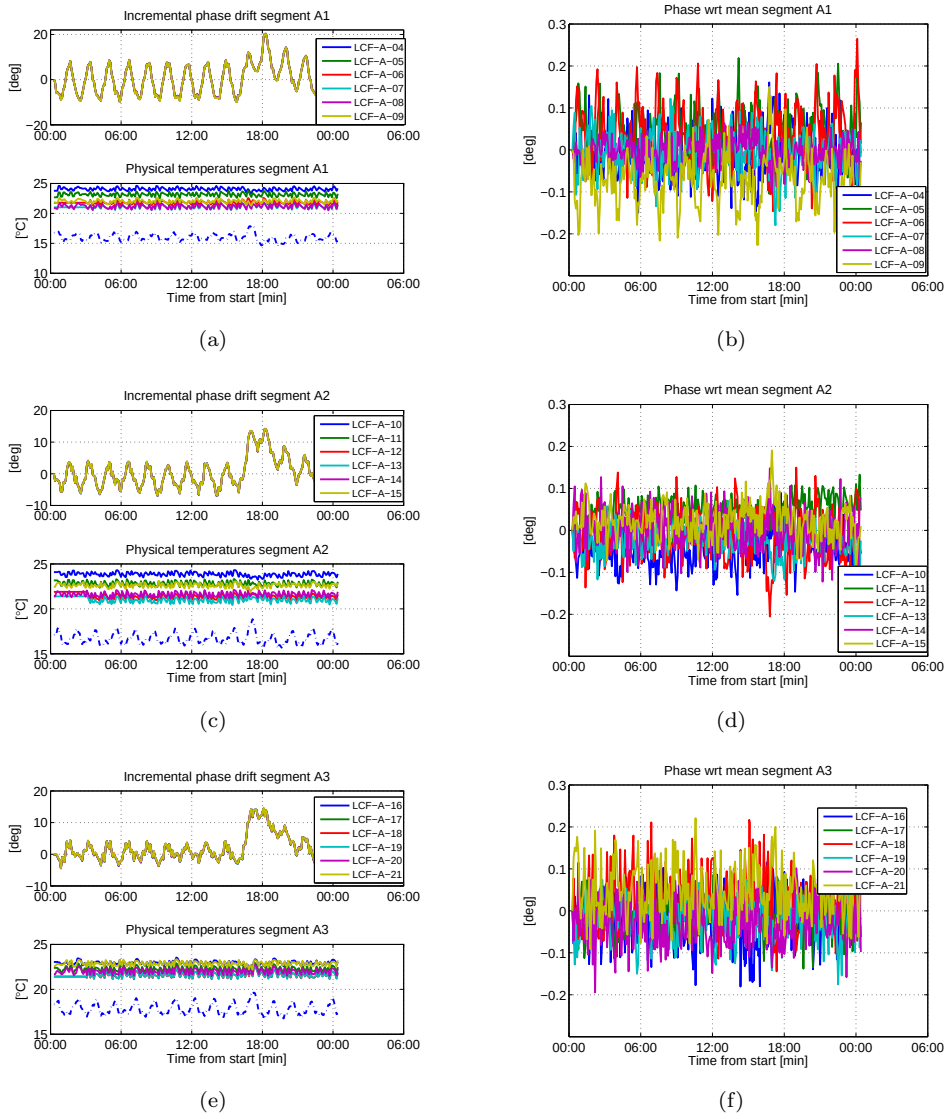

Figure 6.16: Phase drift of receivers in Arm A; (a) and (b) segment A1, (c) and (d) segment A2, (e) and (f) segment A3. Left plots: Incremental phase drift from first calibration for all receivers in the segment (top)(reference receiver: LCF-C-06). LICEFs and PD physical temperatures (bottom). Right plots: Phase difference with respect to the mean value of all receivers in the segment.

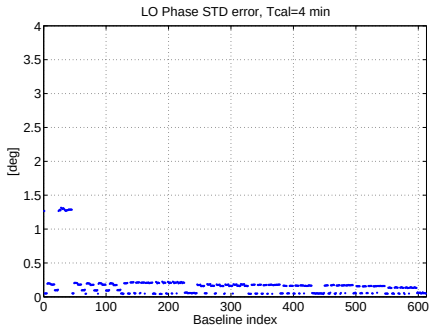

(a) LO calibration every 4 minutes

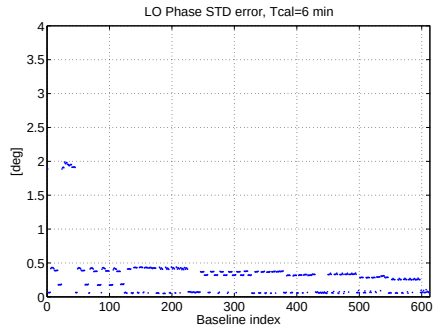

(b) LO calibration every 6 minutes

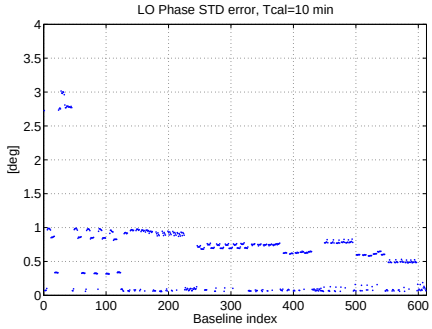

(c) LO calibration every 10 minutes

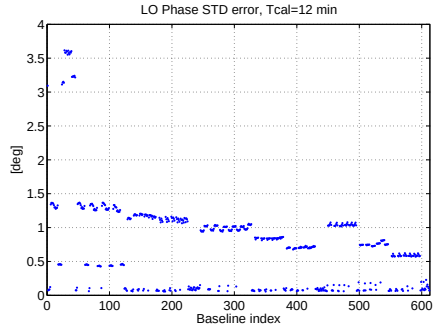

(d) LO calibration every 12 minutes

Figure 6.17: Std of the visibility phase errors for those baselines sharing a noise source. The LO phase is decimated at different frequencies in order to evaluate the optimal LO calibration frequency satisfying the required accuracy while maximizing the observation time.

6.5 Conclusions

In this chapter the first results of the in-orbit instrument characterization have been presented. This initial analysis has contributed to fulfill the MIRAS payload characterization. Some issues pending from the on-ground campaigns (in-orbit measurements were needed for further analysis) have been investigated, as in the case of the PMS offset dependence on the heater signal and the LO phase variation with temperature swings along the orbit. An important effort has also been made in the EMC analysis of different payload/platform subsystems. Specific tests and/or sequences proposed have been tested during these first measurements of the Commissioning Phase to address all these items. Tools and algorithms developed for the on-ground characterization have revealed to be very useful to perform these analysis.

Main outcomes show that the system performance of the instrument are consistent with the on-ground studies. As a conclusion from the in-orbit EMC tests assessment, both the star tracker and X-band transmitter EMC test pass the success criteria. S-band transmitters tests present artifacts in the MIRAS correlations both when the S-band transmitter is ON and when it is OFF. Therefore, these artifacts can not be linked with the S-band transmitter status and they seem to be external interferences.

Regarding the PMS in-orbit assessment, a correction of the PMS voltage levels has been devised using a special sequence during in-orbit measurements in order to estimate the delay and jumps affecting the PMS voltage of each LICEF. These values have been incorporated in the L1OP. This correction has allowed tracking the PMS offset, within the SMOS mission requirements, from the values obtained by means of the long calibrations events and temperature correction between them.

Finally, a comprehensive analysis of the visibility phase drifts with the physical temperature swings has been performed using the electrical stability test (continuous short calibrations). The same tool developed for the analysis of the on-ground measurements has been used. Results are consistent to the obtained ones on-ground. The phase drift can be mainly assigned to LO temperature drifts, being the LICEF contribution very low for all the receivers, except for receiver NIR-AB-01-H, which presents abrupt jumps. The current calibration baseline: frequent calibrations by noise injection along the orbits (LO phase tracking) and interpolation between calibration events has been confirmed.

Chapter 7

Conclusions and future lines

SMOS mission is expected to provide global maps of soil moisture and sea surface salinity with the accuracy required by the scientific community [SMOS, 2003a]. MIRAS compliance with scientific requirements is directly related to the instrumental errors in the visibility samples [SMOS, 2003b, Torres *et al.*, 2007].

This Thesis has mainly contributed to: (i) the characterization of the MIRAS system performance, and therefore, to the definition of tests, data processing methods and success criteria and (ii) fine-tuning the instrument in order to fully achieve the system requirements.

Most of the work has been performed in the framework of the MIRAS/SMOS Pre-Commissioning Phase activities (on-ground tests) and it has been completed during the first months of in-orbit operation, in the framework of the Commissioning Phase. Main conclusions from both parts of this study are discussed afterwards. Original contributions of this Thesis and the future research lines are also outlined in this chapter.

7.1 Main conclusions

The assessment of the MIRAS system performance has been carried out from on-ground characterization measurements, including all the activities undertaken within the IVT and RACT campaigns. These tests have shown that the payload is very stable and, in general, presents a very robust performance in front of electromagnetic perturbations and/or extreme operating conditions. However, these measurements have also revealed some anomalies, such as a variation of the visibility phase with temperature larger than expected, PMS gain and offset calibration errors slightly above the requirements and a small interference in the correlations measured by the instrument produced by the

nominal X-band transmitter. Therefore, the development of several calibration tools has been required in order to fully comply with the SMOS requirements.

Just after launch, specific tests and/or sequences devoted to check the behavior of the instrument during the in-orbit operation were performed. Calibration tools and algorithms developed for the on-ground system performance assessment have been adapted to fulfill the in-orbit characterization in order to prepare the instrument for the operational condition.

The main outcomes from this work can be summarized as follows:

- *MIRAS/SMOS RFI and EMC tests*
  MIRAS system performance changes in front of EM perturbations and/or extreme operating conditions have been analyzed by means of the Success Criteria tool. This analysis has been carried out at ESA's Maxwell anechoic chamber (Noordwijk, Holland) during the IVT tests first and then during the RACT tests at Thales Alenia Space (Cannes, France) once the instrument was integrated to the platform. Results concluded that neither subsystems of the payload nor the platform affect the MIRAS instrument measurements (correlations and/or PMS voltages). Marginal effects have been detected during the nominal X-band transmitter synchronization with the ground station. These interferences can be overcome using the redundant transmitter of the platform. This outcome has been one of the major reasons supporting the redundant operation mode of MIRAS after launch.

- *Amplitude calibration*
  The PMS is the major contributor to the visibility amplitude errors. The PMS Calibration Consistency tool has been developed to easily assess the self consistency of the amplitude calibration coefficients used in the MIRAS instrument. Initially, amplitude errors after PMS calibration of about 6% peak-to-peak in nominal configuration and 8% in the redundant one had been found. It has been shown that the NDN S-parameters presented non-negligible systematic errors, associated to each output of the NS. These errors are large with respect to 1% (1σ) amplitude errors in the calibration requirements. However, after applying the CAS correction factors computed using this tool, the error presents a random distribution with much lower dispersion (around 4% peak-to-peak), which are below 1% calibration requirements. These values have been included in the L1OP to be used when in-orbit calibration is not available. Nevertheless, CAS correction factors have been computed from on-ground measurements, where NIRs could not be calibrated. This correction has been further improved using the same principle during in-orbit operation, once NIR units have been calibrated during deep sky views to include the full path to the antenna phase center (switch and antenna loss) [Corbella *et al.*, 2011]. Besides, after applying the correction, the distributed calibration approach has been validated, being both the PMS gain and the receiver noise temperature independent on the

LICEF position in the arms and having similar values for nominal and redundant configuration, as expected.

- *Calibration of temperature phase drift*
  Visibility phase errors are decoupled into receiver phase errors that can be tracked in temperature. The system of equations to monitor the phase track deals with under determination, memory and phase wrapping problems. Due to the way of solving the equation system (pseudo inverse matrix) a reference phase remains undetermined. The evolution of each individual phase includes the drift of this reference constant. At baseline level this is not a problem since this constant is canceled out in a calibration basis. Therefore, a method to track the LO phase by retrieving the sensitivity coefficients to physical temperature in a baseline basis has been devised. This method gives an estimation of phase sensitivity to physical temperature good enough to conclude that phase drift is basically caused by local oscillator sensitivity to physical temperature. However, physical temperatures are not measured with enough accuracy since the sensors are not close enough to the LO. For this reason, phase tracking errors are slightly above phase errors requirements (1 degree), mainly for segments in the Hub. From these outcomes, LO phase tracking calibrations by correlated noise injection along the orbits are required. Since the calibration time is limited to the 1% of the mission time, the frequency of these calibration events need to be assessed in order to find a trade-off between phase errors and the observation time.

- *One point calibration assessment*
  MIRAS calibration current baseline proposes to use the NIR units as absolute reference for the PMS calibration and the sensitivity approach to correct drifts due to orbital temperature swing between calibration events. The performance of the one-point calibration approach has been assessed in order to validate this alternative calibration method for in-orbit operation. This method is two-fold: (i) absolute PMS calibration during the external maneuvers and (ii) tracking of the PMS gain drifts due to physical temperature orbital swing. A test to estimate the Maxwell ceiling's brightness temperature from the 66 receivers has been devised using the stability measurements of the IVT campaign. Outcomes from this experiment reveal that each single LICEF presents some bias in the estimation of the Maxwell ceiling's brightness temperature. However, the mean value of the whole set of 66 receivers reduces the systematic errors (bias) and thermal noise by an additional factor larger than eight, estimating the ceiling's temperature within an error margin of 0.1-0.2 K. This result reinforces the one-point calibration approach as a promising method to calibrate the PMS in an all-LICEF configuration. After the assessment of the one-point calibration performance, the in-orbit PMS cold sky calibration sequence has been prepared to be tested during the first external maneuvers.

Tests performed on ground have been used to test the U-noise injection to track the PMS gain drifts due to orbital temperature gradients. Results have shown that this method performs better than the temperature correction approach, mainly for those receivers presenting a larger temperature swing.

Therefore, the LO phase tracking calibration sequence (performed several times per orbit) has been modified to include a U-noise injection measurement, in order to test this approach with in-orbit measurements. The analysis of these measurements has shown low orbital temperature swings. Hence, even for those receivers presenting a thermal hysteresis effect, the amplitude error is well below the 1% calibration requirement when using the temperature correction between calibration events. For this reason, the U-noise injection measurement has been removed from the LO calibration events performed every 10 minutes, in order to minimize the calibration time.

- *In-orbit instrument performance assessment*
  Main issues addressed during this stage are the following:

  ◇ EMC assessment
  During the first in-orbit measurements, several tests were devoted to evaluate the EMC of different subsystems of the payload/platform, namely, the S-band and X-band transmitters, the star tracker and the SADM. In this case, an update of the Success Criteria tool was needed to be able to distinguish between changes in the measurements produced by a change in the target and those produced by any of the subsystems. From this analysis, it can be concluded that the star tracker/X-band transmitter EMC tests successfully pass the success criteria. In case of the S-band transmitter and SADM tests, some artifacts are clearly identified in the measurements. However, these interferences have appeared independently of the status of these subsystems.

  ◇ Amplitude and phase calibration consistency
  An accurate assessment of the PMS in-orbit performance has been undertaken also during Commissioning Phase. A special sequence has been used to assess the PMS voltage jumps linked to the heater signal. This behavior was detected in the tests performed on-ground, but it was necessary to develop a special sequence in order to correct them. From the analysis of these measurements, a correction of the PMS signal with the heater status has been developed. The heater correction has been also implemented in the L1OP at PMS voltage level. After applying this correction, the PMS offset is tracked from the values obtained by means of the long calibrations events and temperature correction between them, being within the system requirements.

  The visibility phase drifts with the physical temperature swings have been an-

alyzed using the electrical stability test. Results are consistent to the obtained ones on-ground. The phase drift can be mainly assigned to LO temperature drifts, being the LICEF contribution very low for all the receivers, except for receiver NIR-AB-01-H, which presents abrupt jumps. From these outcomes, the current calibration baseline being frequent calibrations by noise injection along the orbits and interpolation between calibration events, has been confirmed.

7.2 Original contributions

The original contributions of this Thesis have resulted in contributions to 4 journal papers and 21 international conferences (Appendix A). They can be summarized as follows:

- Definition and development of a Success Criteria tool for interferometric radiometers devoted to Earth observation. The tool is capable of assessing the impact in front of EM perturbations and/or extreme operating conditions from the payload itself or from the platform on the overall system performance [González-Gambau *et al.*, 2008a,e, Corbella *et al.*, 2009b].

- Definition of a method to check the consistency of the amplitude calibration in interferometric radiometers. The Calibration Consistency Tool is capable of estimating the PMS gain uncertainty and, therefore, the visibility amplitude errors after calibration, which are directly translated into image distortion in brightness temperatures [González-Gambau *et al.*, 2008b, Corbella *et al.*, 2009b].

- Proposal of a method to track visibility phase errors due to temperature gradients in interferometric radiometers in order to increase the inter-calibration period, thus maximizing the coverage. The method uses the sensitivity coefficients to physical temperature in a baseline basis [González-Gambau *et al.*, 2008d].

- Experimental validation of the one-point calibration approach as PMS absolute calibration method using an all-LICEF configuration [Torres *et al.*, 2008, Corbella *et al.*, 2009b].

- Proposal of tracking the PMS gain drifts due to orbital temperature swing using the U-noise injection at a frequent rate (several calibration events per orbit) instead of using the temperature correction approach [Torres *et al.*, 2010].

In addition, the main activities have been comprehensively detailed, as co-author, in a set of Technical Notes within the frame of several projects sponsored by the European Space Agency (Appendix A). The Master Thesis entitled "Sensitivity analysis of MIRAS/SMOS instrument calibration parameters" has been co-advised.

7.3 Future research lines

MIRAS has shown to be capable of producing brightness temperature images with the required accuracy for the Level 1B products (http://www.esa.int/esaLP/LPsmos.html). SMOS is an Earth Explorer mission and therefore a SMOS follow-on operational mission is currently under study. In the long term, based on the experience of the current mission, improvements in several technological and scientific aspects will be evaluated. In the frame of SMOS follow-on programs, the tests defined for the analysis of the MIRAS system performance and all the algorithms/calibration tools developed in this Thesis can be extrapolated to the MIRAS-2 instrument on-ground characterization.

Interferometric aperture synthesis in two dimensions is a new technology, first demonstrated in the SMOS Earth Explorer mission. However, in the last years an increasing interest on this technology is being observed. As it has been mentioned, there are currently several missions in progress devoted to Earth observation using this technology, such as GeoSTAR (JPL) or GAS (ESA), two geostationary atmospheric sounders. The application of these calibration tools in order to correct amplitude and phase errors in the visibility samples could be further investigated.

In the short term, support activities to SMOS higher level developers is a key activity for Level-1 instrument engineers, since the analysis and fine-tuning of the scientific SMOS products is very related to the quality (accuracy and stability) of the calibrated visibilities. This activity is currently foreseen at the SMOS Barcelona Expert Centre within a post-doc program.

Appendix A

List of publications

Journal papers

1. I. Ramos-Perez, X. Bosch-Lluis, A. Camps, **V. González**, N. Rodriguez-Alvarez, E. Valencia, H. Park, M. Vall llosera, and G. Forte. Optimum intercalibration time in synthetic aperture interferometric radiometers: Application to SMOS. *Geoscience and Remote Sensing Letters, IEEE*, PP(99):1 –4, 2012.

2. I. Corbella, F. Torres, N. Duffo, **V. González-Gambau**, M. Pablos, I. Durán, and M. Martín-Neira. MIRAS calibration and performance: results from the SMOS in-orbit commissioning phase. *IEEE Transactions on Geoscience and Remote Sensing*, PP(99):1 –9, 2011.

3. I. Corbella, F. Torres, N. Duffo, M. Martín-Neira, **V. González-Gambau**, A. Camps, and M. Vall-llossera. On-ground characterization of the SMOS payload. *IEEE Transactions on Geoscience and Remote Sensing*, 47, 2009.

4. M. Martín-Neira, I. Cabeza, C. Perez, M. A. Palacios, M. A. Guijarro, S. Ribó, I. Corbella, S. Blanch, F. Torres, N. Duffo, **V. González**, S. Beraza, A. Camps, M. Vall-llossera, S. Tauriainen, J. Pihlflyckt, J. P. Gonzalez, and F. Martín-Porqueras. AMIRAS: airborne MIRAS demonstrator. *IEEE Transactions on Geoscience and Remote Sensing*, 46(3):705–716, March 2008.

Conference papers

1. J. Gourrion, S. Guimbard, R. Sabia, C. Gabarro, **V. González**, S. Montero, M. Talone, M. Portabella, A. Turiel, F. Pérez, and J. Martínez. Reducing systematic errors on SMOS retrieved salinity: calibration of brightness temperature

images and forward model improvement. In *Geoscience and Remote Sensing Symposium (IGARSS), 2011 IEEE International*, pages 2397 –2400, july 2011.

2. I. Corbella, F. Torres, N. Duffo, I. Durán, M. Pablos, **V. González-Gambau.**, J. Closa, and M. Martín-Neira. SMOS-MIRAS calibration and performance. In *ESA Living Planet Symposium*, 2010.

3. M. Talone, J. Gourrion, **V. González**, R. Sabia, A. Camps, I. Corbella, A. Turiel, A. Monerris, and J. Font. SMOS brightness temperatures statistical characterization: methodology and first results after the commissioning phase. In *ESA Living Planet Symposium*, 2010.

4. I. Corbella, F. Torres, N. Duffo, **V. González-Gambau**, I. Duran, M. Pablos, and M. Martín-Neira. Some results on SMOS-MIRAS calibration and imaging. In *Geoscience and Remote Sensing Symposium (IGARSS), 2010 IEEE International*, pages 3768 –3771, july 2010.

5. M. Talone, J. Gourrion, R. Sabia, C. Gabarro, **V. González**, A. Camps, I. Corbella, A. Monerris, and J. Font. SMOS brightness temperatures validation: First results after the commisioning phase. In *Geoscience and Remote Sensing Symposium (IGARSS), 2010 IEEE International*, pages 4306 –4309, july 2010.

6. I. Corbella, F. Torres, N. Duffo, **V. González-Gambau**, M. Pablos, I. Duran, J. Closa, and M. Martín-Neira. SMOS calibration and level 1 data assessment. In *URSI Commission-F Microwave Signatures*, 2010.

7. I. Corbella, F. Torres, N. Duffo, **V. González-Gambau**, M. Pablos, I. Duran, and M. Martín-Neira. First results on MIRAS calibration and overall SMOS performance. In *Microwave Radiometry and Remote Sensing of the Environment (MicroRad), 2010 11th Specialist Meeting on*, pages 1 –4, march 2010.

8. F. Torres, I. Corbella, N. Duffo, **V. González-Gambau**, I. Durán, M. Pablos, and M. Martín-Neira. One point calibration in interferometric radiometers: MIRAS/SMOS preliminary results. In *Microwave Radiometry and Remote Sensing of the Environment (MicroRad), 2010 11th Specialist Meeting on*, pages 243 –246, march 2010.

9. I. Corbella, F. Torres, N. Duffo, **V. González**, A. Camps, and M. Vall-llossera. On-flight characterization of the SMOS payload during the commissioning phase. In *Geoscience and Remote Sensing Symposium,2009 IEEE International,IGARSS 2009*, volume 5, pages V–180 –V–183, july 2009.

10. F. Torres, I. Corbella, N. Duffo, and **V. González-Gambau** One point calibration in interferometric radiometers: error assessment. In *Geoscience and Remote Sensing*

Symposium,2009 IEEE International,IGARSS 2009, volume 3, pages III–1035 –III–1038, july 2009.

11. I. Corbella, F. Torres, M. Martín-Neira, N. Duffo, **V. González-Gambau**, A. Camps, and M. Vall-llossera. MIRAS characterization and monitoring during the SMOS in-orbit commissioning phase. In D. N. Arabelos & C. C. Tscherning, editor, *EGU General Assembly Conference*, volume 11 of *EGU General Assembly Conference Abstracts*, page 6759, April 2009.

12. **V. González-Gambau**, F. Torres, N. Duffo, and M. Martín-Neira. Calibration consistency tool for interferometric radiometers. In *Proc. IEEE International Geoscience and Remote Sensing Symposium IGARSS 2008*, volume 5, pages V–401–V–404, 7–11 July 2008.

13. **V. González-Gambau**, F. Torres, and N. Duffo. Phase calibration temperature track in interferometric radiometers devoted to earth observation. In *Proc. SPIE Europe Remote Sensing 2008*, 2008.

14. **V. González-Gambau**, F. Torres, F.J. Benito, J. Closa, and M. Martín-Neira. Analysis of EMC tests for interferometric radiometers. In *Proc. SPIE Europe Remote Sensing 2008*, 2008.

15. **V. González-Gambau**, F. Torres, F.J. Benito, J. Closa, and M. Martín-Neira. Success criteria tool in EMC tests for interferometric radiometers. In *Proc. IEEE International Geoscience and Remote Sensing Symposium IGARSS 2008*, 2008.

16. F. Torres, **V. González-Gambau**, and C. González-Haro. One-point calibration in interferometric radiometers devoted to Earth observation. In *Proc. SPIE Europe Remote Sensing 2008*, 2008.

17. I. Corbella, F. Torres, N. Duffo, **V. González**, A. Camps, and M. Vall-llossera. Fast processing tool for SMOS data. In *Proc. IEEE International Geoscience and Remote Sensing Symposium IGARSS 2008*, volume 2, pages II–1152–II–1155, 7–11 July 2008.

18. N. Duffo, I. Corbella, F. Torres, **V. González-Gambau**, and M. Martín-Neira. Interferometric radiometers: Fringe washing function estimation. In *Geoscience and Remote Sensing Symposium, 2008. IGARSS 2008. IEEE International*, volume 5, pages V –405 –V –408, july 2008.

19. I. Corbella, F. Torres, N. Duffo, M. Martín-Neira, **V. González**, A. Camps, and M. Vall-llossera. MIRAS ground characterization. In *Microwave Radiometry and Remote Sensing of the Environment, 2008. MICRORAD 2008*, pages 1 –4, march 2008.

20. I. Corbella, F. Torres, N. Duffo, A. Camps, M. Vall-llossera, and **V. González** MIRAS in-orbit calibration. In *Geoscience and Remote Sensing Symposium, 2007. IGARSS 2007. IEEE International*, pages 3622 –3625, july 2007.

21. N. Duffo, F. Torres, I. Corbella, **V. González**, S. Blanch, A. Camps, M. Vall-llossera, J.L. Alvarez, S. Ribo, and M. Martín-Neira. Some results of the MIRAS-SMOS demonstrator campaigns. In *Geoscience and Remote Sensing Symposium, 2007. IGARSS 2007. IEEE International*, pages 3639 –3642, july 2007.

Workshops

1. C. Gabarró, **V. González**, J. Martínez, I. Corbella, M. Portabella, N. Duffo, F. Torres, and J. Font. Assessment of the local oscillator calibration frequency impact on the SMOS SSS and RFI detection. In *SMOS Science Workshop, Arles (France)*, 2011.

2. **V. González-Gambau**, I. Corbella, F. Torres, N. Duffo, M. Pablos, I. Durán, and M. Martín-Neira. SMOS calibration and level 1 assessment. In *SMOS Validation and Retrieval Team Workshop, ESA-ESRIN, Frascati (Italy)*, 2010.

3. M. Talone, J. Gourrion, **V. González-Gambau**, R. Sabia, A. Camps, I. Corbella, C. Gabarró, A. Turiel, A. Monerris, and J. Font. SMOS brightness temperature bias mitigation. In *SMOS Validation and Retrieval Team Workshop, ESA-ESRIN, Frascati (Italy)*, 2010.

Technical reports

1. M. Pablos, **V. González-Gambau**, N. Duffo, F. Torres, and I. Corbella. Electrical stability 2: PMS gain sensitivity, SO-TN-UPC-PLM-0104. Technical report, Universitat Politècnica de Catalunya, May 2010.

2. M. Pablos, **V. González-Gambau**, N. Duffo, F. Torres, and I. Corbella. PMS heater offset correction, SO-TN-UPC-PLM-0102. Technical report, Universitat Politècnica de Catalunya, May 2010.

3. M. Pablos, **V. González-Gambau**, N. Duffo, F. Torres, and I. Corbella. Estimation of PMS gain sensitivity of SMOS flight data, SO-TN-UPC-PLM-0098. Technical report, Universitat Politècnica de Catalunya, April 2010.

4. I. Durán, **V. González-Gambau**, N. Duffo, F. Torres, and I. Corbella. External calibration factors, SO-TN-UPC-PLM-0097. Technical report, Universitat Politècnica de Catalunya, April 2010.

5. **V. González-Gambau**, F. Torres, N. Duffo, and I. Corbella. Star tracker and X-band in-orbit test, SO-TN-UPC-PLM-0099. Technical report, Universitat Politècnica de Catalunya, February 2010.

6. **V. González-Gambau**, F. Torres, N. Duffo, and I. Corbella. S-band transmitter analysis, SO-TN-UPC-PLM-0096. Technical report, Universitat Politècnica de Catalunya, January 2010.

7. M. Pablos, **V. González-Gambau**, N. Duffo, F. Torres, and I. Corbella. LO phase track analysis of SMOS flight data, SO-TN-UPC-PLM-0094. Technical report, Universitat Politècnica de Catalunya, January 2010.

8. I. Durán, **V. González-Gambau**, F. Torres, I. Corbella, and N. Duffo. In-orbit CAS validation SW, SO-TN-UPC-PLM-0091. Technical report, Universitat Politècnica de Catalunya, January 2010.

9. **V. González-Gambau**, F. Torres, N. Duffo, I. Corbella, A. Camps, and M. Vall-llossera. PMS and NIR calibration consistency tool, SO-TN-UPC-PLM-0069. Technical report, Universitat Politècnica de Catalunya, March 2009.

10. N. Duffo, **V. González-Gambau**, I. Corbella, F. Torres, A. Camps, and M. Vall-llossera. Distributed FWF assessment from IVT data, SO-TN-UPC-PLM-0066. Technical report, Universitat Politècnica de Catalunya, March 2009.

11. M. Pablos, **V. González-Gambau**, N. Duffo, F. Torres, and I. Corbella. Review of PMS sensitivity analysis in lSS tests, SO-TN-UPC-PLM-0079. Technical report, Universitat Politècnica de Catalunya, March 2009.

12. **V. González-Gambau**, N. Duffo, F. Torres, I. Corbella, A. Camps, and M. Vall-llossera. LO phase track analysis, SO-TN-UPC-PLM-0070. Technical report, Universitat Politècnica de Catalunya, February 2009.

13. I. Corbella, F. Torres, **V. González-Gambau**, N. Duffo, A. Camps, and M. Vall-llossera. Commissioning phase test plan, SO-TN-UPC-PLM-0077. Technical report, Universitat Politècnica de Catalunya, December 2008.

14. **V. González-Gambau**, I. Corbella, F. Torres, N. Duffo, A. Camps, and M. Vall-llossera. MIRAS Testing Software user guide, SO-TN-UPC-PLM-0075. Technical report, Universitat Politècnica de Catalunya, November 2008.

15. **V. González-Gambau**, I. Corbella, F. Torres, N. Duffo, A. Camps, and M. Vall-llossera. IVT-TS description, SO-TN-UPC-PLM-0059. Technical report, Universitat Politècnica de Catalunya, October 2007.

16. **V. González-Gambau**, I. Corbella, F. Torres, N. Duffo, A. Camps, and M. Vall-llossera. IVT tests detailed outputs, SO-TN-UPC-PLM-0055. Technical report, Universitat Politècnica de Catalunya, February 2007.

Appendix B

List of acronyms

AF-FOV	Alias Free-Field of View
AMIRAS	Airborne Microwave Imaging Radiometer by Aperture Synthesis
CAS	CAlibration Subsystem
CCU	Central Correlator Unit
CIP	Correlated noise Input Port
CMN	Control and Monitoring Node
CNES	Centre National d'Etudes Spatiales
CP34	Centro de Producción niveles 3 y 4
CSIC	Consejo Superior de Investigaciones Científicas
CSSAR	Center of Space Science and Applied Research
DICOS	DIgital COrrelator System
DPGS	Data Processing Ground Segment
EADS-CASA	European Aeronautic Defense and Space-Construcciones Aeronáuticas Sociedad Anónima
ECCOS	Empty Chamber Correlator Offsets
EGSE	Electronic Ground Segment Equipment
EMC	ElectroMagnetic Compatibility
ESA	European Space Agency
ESAC	European Space Astronomy Centre
ESTEC	European Space Research and Technology Centre
ESTAR	Electronically Steered Thinned Array Radiometer
FPIR	Full Polarization Interferometric Radiometer
FTR	Flat Target Response
FWF	Fringe Washing Function

GAS	Geostationary Atmospheric Sounder
GeoSTAR	Geostationary atmospheric sounder Steered Thinned Array Radiometer
GSFC	NASA Goddard Space Flight Center
IEEC	Institut d'Estudis Espacials de Catalunya
IOCP	In-Orbit Calibration Plan
IRTA	Institut de Recerca i Tecnologias Agroalimentàries
IVT	Image Validation Tests
L1PP	Level-1 Prototype Processor
L1OP	Level-1 Operational Processor
LICEF	LIght Cost-Effective Front end
LO	Local Oscillator
LSS	Large Space Simulator
LST/HUT	Laboratory of Space Technology/Helsinki University of Technology
LTA	Long Term Archive
MDPP-3	MIRAS Demonstrator Pilot Project, stage 3
MIRAS	Microwave Imaging Radiometer by Aperture Synthesis
MTS	MIRAS Testing Software
NASA	National Aeronautics and Space Administration
NDN	Noise Distribution Network
NIR	Noise Injection Radiometer
NRT	Near Real Time
NS	Noise Source
PATH	Precipitation and All-weather Temperature and Humidity
PD	Power Divider
PLM	PayLoad Module
PMS	Power Measurement System
PROTEUS	Plate-forme Reconfigurable pour l'Observation, les Télécommunications et les Usages Scientifiques
RFI	Radio Frequency Interference
RSLab	Remote Sensing Laboratory
SADM	Solar Array Driver Mechanism
SA-PAU	Synthetic Aperture Passive Advanced Unit
SMOS	Soil Moisture and Ocean Salinity
SMOS-BEC	SMOS Barcelona Expert Centre

TPR	Total Power Radiometer
TSC	Teoria del Senyal i Comunicacions
UPC	Universitat Politècnica de Catalunya
VLA	Very Large Array

List of Figures

List of Tables

Bibliography

Barre, H.M.J., Duesmann, B., & Kerr, Y.H. 2008. SMOS: the mission and the system. *IEEE Transactions on Geoscience and Remote Sensing*, **46**(3), 587 –593. 2.3

Benito, J., & team. 2007. *Image Validation Test (IVT) plan, SO-PR-CASA-PLM-1041.* Tech. rept. EADS CASA Espacio. 4.1.3

Beraza, S., González, V., Torres, F., Duffo, N., Corbella, I., Blanch, S., Camps, A., Vall-llossera, M., Alvarez, J.L., Ribó, S., & Martin-Neira, M. 2006 (31 2006-aug. 4). MIRAS-SMOS Demonstrator Test Campaigns at Polytechnic University of Catalonia. *Pages 1776 –1779 of: Proc. IEEE International Geoscience and Remote Sensing Symposium IGARSS 2006.* 2.2

Brown, M., & team, ESA. 2008. *In-Orbit Commissioning Phase (IOCP) plan, SO-PL-ESA-SYS-5505.* Tech. rept. ESA-ESTEC, Noordwijk, The Netherlands. 6.1, 6.2, 6.3

Brown, M.A., Torres, F., Corbella, I., & Colliander, A. 2008. SMOS calibration. *IEEE Transactions on Geoscience and Remote Sensing*, **46**(3), 646 –658. 1.4, 2.4.2, 2.4.2, 3.3.1, 3.4, 3.6, 3.6, 3.3, 1, 4.4.3, 4.4.4, 4.5.2, 4.6.2, 5.1, 5.2, 5.4, 6.2, 6.3, B

Butora, R., Martín-Neira, M., & Rivada-Antich, A.L. 2003. Fringe-Washing function calibration in aperture synthesis microwave radiometry. *Radio Science*, **38(2)**. 2.4.2, 3.6

Camps, A. 1996. *Application of interferometric radiometry to Earth observation.* Ph.D. thesis, Universitat Politècnica de Catalunya. http://www.tdx.cat/TDX-1020104-091741/. 1.1, 2.2, 2.4.1, 2.4.1

Camps, A., Bara, J., Corbella, I., & Torres, F. 1997. The processing of hexagonally sampled signals with standard rectangular techniques: application to 2-D large aperture synthesis interferometric radiometers. *IEEE Transactions on Geoscience and Remote Sensing*, **35**(1), 183 –190. 2.4.1

Camps, A., Vall-llossera, M., Corbella, I., Duffo, N., & Torres, F. 2008. Improved image reconstruction algorithms for aperture synthesis radiometers. *IEEE Transactions on Geoscience and Remote Sensing*, **46**(1), 146 –158. 2.4.1

CASA. 2007. *Usage of CAS on-ground measurements in L1 processing, SO-TN-CASA-PLM-1102*. Tech. rept. EADS-CASA Espacio. 2.4.2

Christensen, J., Carlstrom, A., Ekstrom, H., de Maagt, P., Colliander, A., Emrich, A., & Embretsen, J. 2007 (july). GAS: the Geostationary Atmospheric Sounder. *Pages 223 –226 of: Proc. IEEE International Geoscience and Remote Sensing Symposium IGARSS 2007*. 2.2

Colliander, A., Tauriainen, S., Auer, T.I., Kainulainen, J., Uusitalo, J., Toikka, M., & Hallikainen, M.T. 2005. MIRAS reference radiometer: a fully polarimetric noise injection radiometer. *IEEE Transactions on Geoscience and Remote Sensing*, **43**(5), 1135 – 1143. 2.4.2

Colliander, A., Ruokokoski, L., Suomela, J., Veijola, K., Kettunen, J., Kangas, V., Aalto, A., Levander, M., Greus, H., Hallikainen, M.T., & Lahtinen, J. 2007a. Development and calibration of SMOS reference radiometer. *IEEE Transactions on Geoscience and Remote Sensing*, **45**(7), 1967 –1977. 2.4.2, 2.4.2, 2.4.2, 2.15, 3.3.1, 5.3.1

Colliander, A., Lemmetyinen, J., Uusitalo, J., Suomela, J., Veijola, K., Kontu, A., Kemppainen, S., Pihlflyckt, J., Rautiainen, K., Hallikainen, M., & Lahtinen, J. 2007b (23–28 July). Ground calibration of SMOS: NIR and CAS. *Pages 3631–3634 of: Proc. IEEE International Geoscience and Remote Sensing Symposium IGARSS 2007*. 4.4.1, 5.3.1

Colliander, A., Martín-Neira, M., Closa, J., & Benito, J. 2009 (july). Satellite radiometer pre-launch sensitivity estimation using anechoic chamber and channel inter-comparison. *Pages V–176 –V–179 of: Proc. IEEE International Geoscience and Remote Sensing Symposium IGARSS 2009*, vol. 5. 5.3.1

Corbella, I., Camps, A., Torres, F., & Bara, J. 2000a. Analysis of noise-injection networks for interferometric-radiometer calibration. *IEEE Transactions on Microwave Theory and Techniques*, **48**(4), 545 –552. 3.3.2

Corbella, I., Torres, F., Camps, A., Bara, J., Duffo, N., & Vall-Ilossera, M. 2000b (24–28 July). L-band aperture synthesis radiometry: hardware requirements and system performance. *Pages 2975–2977 of: Proc. IEEE International Geoscience and Remote Sensing Symposium IGARSS 2000*, vol. 7. 1.1

Corbella, I., Duffo, N., Vall-llossera, M., Camps, A., & Torres, F. 2004. The visibility function in interferometric aperture synthesis radiometry. *IEEE Transactions on Geoscience and Remote Sensing*, **42**(8), 1677 – 1682. 2.4.1, 3.2

Corbella, I., Torres, F., Camps, A., Colliander, A., Martín-Neira, M., Ribó, S., Rautiainen, K., Duffo, N., & Vall-llossera, M. 2005. MIRAS end-to-end calibration: application to SMOS L1 processor. *IEEE Transactions on Geoscience and Remote Sensing*, **43**(5), 1126 – 1134. 2.4.2, 3.1, 4.2, 4.4, 6.3

Corbella, I., Torres, F., Duffo, N., Camps, A., Vall-Ilossera, M., & González, V. 2007 (23–28 July). MIRAS in-orbit calibration. *Pages 3622–3625 of: Proc. IEEE International Geoscience and Remote Sensing Symposium IGARSS 2007.* 3.6

Corbella, I., Torres, F., Duffo, N., González, V., Camps, A., & Vall-llossera, M. 2008a (7–11 July). Fast processing tool for SMOS data. *Pages II–1152–II–1155 of: Proc. IEEE International Geoscience and Remote Sensing Symposium IGARSS 2008*, vol. 2. 1.2, 4.2, 4.4, 4.5, 5.3.1, 6.3

Corbella, I., Torres, F., Benito, J., & Martín-Neira, M. 2008b (july). MIRAS-SMOS antenna relative phase calibration. *Pages 1 –4 of: Proc. IEEE Antennas and Propagation Society International Symposium, 2008.* 3.3, 3.3.2, 3, 4.4.2

Corbella, I., Torres, F., Camps, A., Duffo, N., & Vall-llossera, M. 2009a. Brightness temperature retrieval methods in synthetic aperture radiometers. *IEEE Transactions on Geoscience and Remote Sensing*, **47**(1), 285 –294. 1.1, 2.2, 2.2, 2.5, 2.4.1, 2.4.1, 2.4.1, 4.2

Corbella, I., Torres, F., Duffo, N., Martín-Neira, M., González-Gambau, V., Camps, A., & Vall-llossera, M. 2009b. On-ground characterization of the SMOS payload. *IEEE Transactions on Geoscience and Remote Sensing*, **47**(9), 3123 –3133. 3.5, 5.3.2, 1, 2, 4

Corbella, I., Torres, F., Duffo, N., González-Gambau, V., Pablos, M., Durán, I., & Martín-Neira, M. 2011. MIRAS calibration and performance: results from the SMOS in-orbit Commissioning Phase. *IEEE Transactions on Geoscience and Remote Sensing*, **49**(9), 3147 –3155. 3.5, 3.6, 4.4.2, 4.4.5, 5.3.2, 2

Duffo, N., Torres, F., Corbella, I., González, V., Blanch, S., Camps, A., Vall-Ilossera, M., Alvarez, J. L., Ribó, S., & Martín-Neira, M. 2007 (23–28 July). Some results of the MIRAS-SMOS demonstrator campaigns. *Pages 3639–3642 of: Proc. IEEE International Geoscience and Remote Sensing Symposium IGARSS 2007.* 2.2, 2.5

Duffo, N., Corbella, I., Torres, F., González, V., & Martín-Neira, M. 2008. Interferometric radiometers: Fringe-Washing function estimation. *In: Proc. IEEE International Geoscience and Remote Sensing Symposium IGARSS 2008.* 2.4.2, 3.6

Durán, Israel. 2010. *SMOS flight external calibration and monitoring.* M.Phil. thesis, Universitat Politècnica de Catalunya. 4.4.5

Font, J., Lagerloef, G.S.E., Le Vine, D.M., Camps, A., & Zanife, O.-Z. 2004. The determination of surface salinity with the European SMOS space mission. *IEEE Transactions on Geoscience and Remote Sensing*, **42**(10), 2196 – 2205. 1.1

Font, J., Camps, A., Borges, A., Martín-Neira, M., Boutin, J., Reul, N., Kerr, Y.H., Hahne, A., & Mecklenburg, S. 2010. SMOS: the challenging sea surface salinity measurement from space. *Proceedings of the IEEE*, **98**(5), 649 –665. 1.1, 2.3

Gabarró, C., González, V., Martínez, J., Corbella, I., Portabella, M., Duffo, N., Torres, F., & Font, J. 2011. Assessment of the local oscillator calibration frequency impact on the SMOS SSS and RFI detection. *In: SMOS Science Workshop, Arles (France).* 3.6, 6.4

González-Gambau, V., Torres, F., Benito, F.J., Closa, J., & Martín-Neira, M. 2008a. Analysis of EMC tests for interferometric radiometers. *In: Proc. SPIE Europe Remote Sensing 2008.* 4.3.2, 4.6, 6.2, 1

González-Gambau, V., Torres, F., Duffo, N., & Martín-Neira, M. 2008b (7–11 July). Calibration consistency tool for interferometric radiometers. *Pages V–401–V–404 of: Proc. IEEE International Geoscience and Remote Sensing Symposium IGARSS 2008*, vol. 5. 4.4.1, 2

González-Gambau, V., Corbella, I., Torres, F., Duffo, N., Camps, A., & Vall-Ilossera, M. 2008c. *MIRAS Testing Software (MTS) user guide, SO-TN-UPC-PLM-0075.* Tech. rept. UPC. 4.2

González-Gambau, V., Torres, F., & Duffo, N. 2008d. Phase calibration temperature track in interferometric radiometers devoted to Earth observation. *In: Proc. SPIE Europe Remote Sensing 2008.* 4.5, 4.5, 4.5.1, 6.4, 3

González-Gambau, V., Torres, F., Benito, F.J., Closa, J., & Martín-Neira, M. 2008e. Success criteria tool in EMC tests for interferometric radiometers. *In: Proc. IEEE International Geoscience and Remote Sensing Symposium IGARSS 2008.* 4.3.2, 6.2, 1

González-Haro, C., Torres, F., Duffo, N., Corbella, I., Vilaseca, R., de Paco, P., & Martín-Neira, M. 2009 (july). Linearity characterization of detectors for interferometric radiometers. *Pages IV–657 –IV–660 of: Proc. IEEE International Geoscience and Remote Sensing Symposium IGARSS 2009*, vol. 4. 3.3.1

Gutierrez, A., Barbosa, J., Almeida, N., Catarino, N., Freitas, J., Ventura, M., & Reis, J. 2007 (23–28 July). SMOS L1 Processor Prototype: from digital counts to brightness temperatures. *Pages 3626–3630 of: Proc. IEEE International Geoscience and Remote Sensing Symposium IGARSS 2007.* 1.2, 4.2.1

Kerr, Y.H., Waldteufel, P., Wigneron, J.-P., Martinuzzi, J., Font, J., & Berger, M. 2001. Soil moisture retrieval from space: the Soil Moisture and Ocean Salinity (SMOS) mission. *IEEE Transactions on Geoscience and Remote Sensing*, **39**(8), 1729 –1735. 1.1

Kerr, Y.H., Waldteufel, P., Wigneron, J.-P., Delwart, S., Cabot, F., Boutin, J., Escorihuela, M.-J., Font, J., Reul, N., Gruhier, C., Juglea, S.E., Drinkwater, M.R., Hahne, A., Martín-Neira, M., & Mecklenburg, S. 2010. The SMOS mission: new tool for monitoring key elements of the global water cycle. *Proceedings of the IEEE*, **98**(5), 666 –687. 1.1, 2.3

Lambrigtsen, B., Tanner, A., Gaier, T., Kangaslahti, P., & Brown, S. 2007 (july). Developing a GeoSTAR science mission. *Pages 5232 –5236 of: Proc. IEEE International Geoscience and Remote Sensing Symposium IGARSS 2007.* 2.2

Le Vine, D.M., & Abraham, S. 2004. Galactic noise and passive microwave remote sensing from space at L-band. *IEEE Transactions on Geoscience and Remote Sensing*, **42**(1), 119 – 129. 2.4.1

Le Vine, D.M., Swift, C.T., & Haken, M. 2001. Development of the synthetic aperture microwave radiometer, ESTAR. *IEEE Transactions on Geoscience and Remote Sensing*, **39**(1), 199 –202. 2.2

Le Vine, D.M., Jackson, T.J., & Haken, M. 2007. Initial Images of the Synthetic Aperture Radiometer 2D-STAR. *IEEE Transactions on Geoscience and Remote Sensing*, **45**(11), 3623 –3632. 2.2

Lemmetyinen, J., Uusitalo, J., Kainulainen, J., Rautiainen, K., Fabritius, N., Levander, M., Kangas, V., Greus, H., Pihlflyckt, J., Kontu, A., Kemppainen, S., Colliander, A., Hallikainen, M. T., & Lahtinen, J. 2007. SMOS calibration subsystem. *IEEE Transactions on Geoscience and Remote Sensing*, **45**(11), 3691–3700. 2.4.2, 2.4.2, 4.4.1

Martín-Neira, M. 2007. *Analysis of LO phase drift calibration, SO-TN-ESA-PLM-6052.* Tech. rept. ESA-ESTEC. 3.6, 4.5

Martín-Neira, M., & Goutoule, J.M. 1997. MIRAS: a two dimensional aperture synthesis radiometer for Soil Moisture and Ocean Salinity observations. *ESA Bulletin*, **92**, 95–104. 1.1, 2.2

Martín-Neira, M., Ribó, S., & Martin-Polegre, A. J. 2002. Polarimetric mode of MIRAS. *IEEE Transactions on Geoscience and Remote Sensing*, **40**(8), 1755–1768. 2.4.2, 2.1

Martín-Neira, M., Ribó, S., & Rautianen, K. 2004. 0-1 correction of comparator threshold in 1-bit interferometric radiometers. *In: Proc. IEEE 8th Specialist Meeting on Microwave Radiometry and Remote Sensing Applications.* 2.4.2, 3.1, 3.2, 4.2

Martín-Neira, M., Cabeza, I., Pérez, C., Palacios, M. A., Guijarro, M. A., Ribó, S., Corbella, I., Blanch, S., Torres, F., Duffo, N., González, V., Beraza, S., Camps, A., Vall-llossera, M., Tauriainen, S., Pihlflyckt, J., Gonzalez, J. P., & Martin-Porqueras, F. 2008a. AMIRAS: airborne MIRAS demonstrator. *IEEE Transactions on Geoscience and Remote Sensing*, **46**(3), 705–716. 2.2

Martín-Neira, M., Suess, M., Kainulainen, J., & Martín-Porqueras, F. 2008b. The Flat Target Transformation. *IEEE J. GRS*, **46**(3), 613–620. 2.4.1, 3.6

Martín-Neira, M., Corbella, I., Torres, F., Kainulainen, J., Oliva, R., Buenadicha, G., Nieto, S., Castro, R., Gutierrez, A., Barbosa, J., Cabot, F., Tenerelli, J., Reul, N., Spurgeon, P., Gourrion, J., Boutin, J., Closa, J., Camps, A., Anterrieu, E., Martín-Porqueras, F., & Daganzo, E. 2011. Overview MIRAS instrument performance and status of RFI. *In: SMOS Science Workshop.* 3.4

McMullan, K. D., Brown, M. A., Martín-Neira, M., Rits, W., Ekholm, S., Marti, J., & Lemanczyk, J. 2008. SMOS: the payload. *IEEE Transactions on Geoscience and Remote Sensing*, **46**(3), 594–605. 1.1, 2.2, 2.4.2, 2.10, 2.12, 2.14, 3.5, 5.3.2

Napier, P.J., Thompson, A.R., & Ekers, R.D. 1983. The very large array: Design and performance of a modern synthesis radio telescope. *Proceedings of the IEEE*, **71**(11), 1295 – 1320. 2.2

Pablos, M. 2010. *Sensitivity analysis of MIRAS/SMOS instrument calibration parameters.* M.Phil. thesis, Universitat Politècnica de Catalunya. 5.3.2, 5.3.2, 6.9

Piironen, P. 2002. *PMS offset determination using an IF attenuator.* Tech. rept. ESA-ESTEC, Noordwijk, The Netherlands. 3.1, 3.3.1, 5.2, 6.3

Ramos-Pérez, I., Camps, A., Bosch-Lluis, X., Marchan-Hernandez, J.F., Rodriguez-Alvarez, N., Valencia, E., Frascella, F., Campigotto, P., & Donadio, M. 2007 (july). Synthetic Aperture PAU: a new instrument to test potential improvements for future SMOSops. *Pages 247 –250 of: Proc. IEEE International Geoscience and Remote Sensing Symposium IGARSS 2007.* 2.2

Rautiainen, K., Kainulainen, J., Auer, T., Pihlflyckt, J., Kettunen, J., & Hallikainen, M.T. 2008. Helsinki University of Technology L-Band Airborne Synthetic Aperture Radiometer. *IEEE Transactions on Geoscience and Remote Sensing*, **46**(3), 717 –726. 2.2

Ribó i Vedrilla, Serni. 2005. *Calibration validation and polarimetry in 2D aperture synthesis. Application to MIRAS.* Ph.D. thesis, Universitat Politècnica de Catalunya. http://www.tdx.cat/TDX-0725105-154133/. 1.1, 2.2, 2.2, 2.4.2

Sanz, J.A., & team. 2007. *Heater control laws definition, SO-TN-CASA-PLM-0657.* Tech. rept. EADS-CASA Espacio. 2.4.2

Silvestrin, P., Berger, M., Kerr, Y., & Font, J. 2001. ESA's second Earth explorer opportunity mission: the Soil Moisture and Ocean Salinity mission-SMOS. *IEEE Geoscience and Remote Sensing Newsletter*, **118**, 11–14. 1.1, 2.3

Skou, N. 1989. *Microwave radiometer systems: design and analysis.* Artech House. 2.1.3, 2.3

SMOS. 2003a. *Mission objectives and scientific requirements of the SMOS mission, MRD, Version 5.* Tech. rept. European Space Agency. 1.1, 2.3, 4.1, 5.3.2, 7

SMOS. 2003b. *SMOS system requirements document, SO-RS-ESA-SYS-0555.* Tech. rept. ESA. 1.1, 1.4, 3.6, 4, 5, 4.4.2, 4.5.2, 5.3.2, 5.4, 6.1, 6.3, 6.12, 6.4, 7

Swift, C.T., & McIntosh, R.E. 1983. Considerations for microwave remote sensing of ocean-surface salinity. *IEEE Trans. Geoscience Electronics*, **4**, 480–491. 1.1, 2.2

Thompson, A.R., Moran, J.M., & Swenson, G.W. 1986. *Interferometry and synthesis in radio astronomy.* John Wiley and Sons. 1.1, 2.2

Torres, F., Camps, A., Bará, J., Corbella, I., & Ferrero, R. 1996. On board phase and modulus calibration of large aperture synthesis radiometers: study applied to MIRAS. *IEEE Transactions on Geoscience and Remote Sensing*, **34**, 1000–1009. 2.4.2, 2.4.2, 3.3.3, 4.4.1

Torres, F., Duffo, N., Corbella, I., Camps, A., Vallllossera, M., & Sagues, L. 2003. Dynamic range and linearity trade-off in detectors for interferometric radiometers. *Electronics Letters*, **39**(25), 1852 – 1854. 3.1

Torres, F., Duffo, N., Corbella, I., Camps, A., & Vall-llossera, M. 2004. MIRAS-SMOS, the relative instrumental error correction approach. *In: Proc. IEEE 8th Specialist Meeting on Microwave Radiometry and Remote Sensing Applications.* 3.3.1, 3.2

Torres, F., Corbella, I., Camps, A., Duffo, N., Vall-llossera, M., Beraza, S., Gutierrez, C., & Martín-Neira, M. 2006. Denormalization of visibilities for in-orbit calibration of interferometric radiometers. *IEEE Transactions on Geoscience and Remote Sensing*, **44**(10), 2679–2686. 3.1, 3.3.1, 3.5, 4.2, 4.3, 5.1, 5.1, 6.3, 6.3, 6.14

Torres, F., Corbella, I., Camps, A., Duffo, N., & Vall-Ilossera, M. 2007. *Error budget map to SRD (PRS), SO-TN-UPC-PLM-0007.* Tech. rept. UPC. 1.1, 5, 4.4.2, 4.5.2, 5.3.1, 5.3.2, 5.4, 6.3, 6.12, 6.4, 7

Torres, F., González-Gambau, V., & González-Haro, C. 2008. One-point calibration in interferometric radiometers devoted to Earth observation. *In: Proc. SPIE Europe Remote Sensing 2008.* 4.4.2, 5.1, 5.2, 4

Torres, F., Corbella, I., Duffo, N., González-Gambau, V., Durán, I., Pablos, M., & Martín-Neira, M. 2010 (march). One point calibration in interferometric radiometers: MIRAS/SMOS preliminary results. *Pages 243 –246 of: Proc. IEEE 11th Specialist Meeting on Microwave Radiometry and Remote Sensing of the Environment (MicroRad), 2010.* 5

Ulaby, F.T., Moore, R.K., & Fung, A.K. 1981. *Microwave remote sensing: active and passive. Vol I. Microwave remote sensing fundamentals and radiometry.* Addison-Wesley. 2.2, 2.1.3

Yan, Jingye, Wu, Ji, & Martin-Neira, M. 2007 (july). FPIR: A one dimensional full polarization interferometric radiometer. *Pages 4408 –4411 of: Proc. IEEE International Geoscience and Remote Sensing Symposium IGARSS 2007.* 2.2

Agradecimientos

Es un placer poder agradecer a todos los que han hecho posible de un modo u otro la realización de esta tesis.

En primer lugar, me gustaría dar las gracias a mis directores de tesis, Xicu Torres y Nuria Duffo, porque desde el principio han sido una referencia a seguir en el mundo de la investigación. Gracias por contagiarme vuestro espíritu de trabajo. Ha sido un verdadero placer trabajar con vosotros. Me gustaría también agradecer a Ignasi Corbella todos estos años de dedicación, guía y consejos. Han sido años de trabajo codo con codo y contigo, el trabajo diario se ha hecho más sencillo. Gracias a los tres, porque en definitiva, me habéis hecho sentir una más en el equipo de trabajo.

No me puedo olvidar de los buenos consejos y de los ánimos que en todo momento me han dado Mercè Vall-llosera y Adriano Camps. Siempre han tenido una palabra amable cuando la he necesitado.

Durante la realización de esta tesis, han sido muchas las campañas, collocations, progress meetings... Ha sido una experiencia muy enriquecedora poder compartirlas con Manuel Martín-Neira, Josep Closa, Antonio Gutierrez y Jose Barbosa. Porque de ellos también he aprendido el trabajo en equipo universidad-empresa. Aunque han sido días y días de duro trabajo, siempre hemos sabido llevarlo con una sonrisa.

La última parte de esta tesis la he realizado en el SMOS Barcelona Expert Centre, donde me han dado la oportunidad de poder acabar la escritura de este documento y a la vez poder formar parte de un equipo de trabajo fantástico. Muchas gracias Jordi, por tu paciencia y comprensión. Es muy gratificante trabajar cada día con todos vosotros, y sentirme una más en los salty thursdays.

Compañeros del despacho D3-212 y D3-116, ha sido un placer compartir con vosotros estos años de doctorado. Ha habido de todo, momentos de risas y momentos de lágrimas, pero de lo que estoy segura es de que ha sido más llevadero junto a vosotros. Compañeros del BEC, ha sido un placer compartir despacho con vosotros durante estos dos últimos años y lo seguirá siendo a partir de ahora. Compañeros de cafés, es un placer poder desconectar cada día de trabajo con vosotros.

Por último, no puedo terminar estos agradecimientos sin dar las gracias a mi familia y amigos. Gracias a mis padres, Clara y Sebastián y a mi hermano Miguel por haberme

apoyado desde el principio y sin reservas en esta andadura, como siempre me habéis apoyado en todo. Sin vosotros nada de esto hubiese sido posible. Y quiero agradecer a todos mis amigos su apoyo incondicional. En especial, me gustaría agradecer a Laura, Vero, Óscar, María, Gemma, Anna, Jordi, Raúl, Nacho, Gemma y Marta, porque me han apoyado y me han entendido durante durante todos estos años.